



**HAL**  
open science

# Application of attosecond pulses to high harmonic spectroscopy of molecules

Nan Lin

► **To cite this version:**

Nan Lin. Application of attosecond pulses to high harmonic spectroscopy of molecules. Other [cond-mat.other]. Université Paris Sud - Paris XI, 2013. English. NNT : 2013PA112355 . tel-01064138

**HAL Id: tel-01064138**

**<https://theses.hal.science/tel-01064138>**

Submitted on 15 Sep 2014

**HAL** is a multi-disciplinary open access archive for the deposit and dissemination of scientific research documents, whether they are published or not. The documents may come from teaching and research institutions in France or abroad, or from public or private research centers.

L'archive ouverte pluridisciplinaire **HAL**, est destinée au dépôt et à la diffusion de documents scientifiques de niveau recherche, publiés ou non, émanant des établissements d'enseignement et de recherche français ou étrangers, des laboratoires publics ou privés.

UNIVERSITE PARIS-SUD

ÉCOLE DOCTORALE : *Ondes et Matière*

*Effectuée au Service des Photons, Atomes et Molécules, IRAMIS, DSM  
Commissariat à l'Energie Atomique, Saclay.*

DISCIPLINE Lasers et Matière

THÈSE DE DOCTORAT

soutenue le 16/12/2013

par

Nan LIN

APPLICATION OF ATTOSECOND PULSES TO HIGH  
HARMONIC SPECTROSCOPY OF MOLECULES

**Directeur de thèse :**

M. Pascal SALIÈRES

Chercheur (CEA)

**Composition du jury :**

*Président du jury :*

Mme Annie KLISNICK

Directeur de Recherche (CNRS/Univ. Paris Sud)

*Rapporteurs :*

Mme Valerie BLANCHET

Chargée de Recherche (CELIA Bordeaux)

M. Pierre AGOSTINI

Professeur (Ohio State Univ.)

*Examineurs :*

Mme Amelle ZAÏR

Chercheur (Imperial College London)

M. Philippe ZEITOUN

Directeur de Recherche (LOA)

APPLICATION OF ATTOSECOND PULSES TO HIGH HARMONIC SPECTROSCOPY OF MOLECULES

© 2013 Nan Lin  
All rights reserved  
Printed in Paris, 2013

Commissariat à l'Énergie Atomique  
Direction Science de la Matière  
Institut Rayonnement Matière Saclay  
Service des Photons, Atomes et Molécules  
Bâtiment 522  
F-91191 Gif-sur-Yvette  
France

<http://iramis.cea.fr/spam/MEC/>

This thesis was typeset with the L<sup>A</sup>T<sub>E</sub>X-system and the memoir class, using a model developed by Stefan Haessler, Zsolt Diveki and the smart people of the Atomfysik division at Lund University.

# ABSTRACT

---

---

High-order Harmonic Generation (HHG) is an extreme nonlinear process that can be intuitively understood as the sequence of 3 steps: i) tunnel ionization of the target atom/molecule, creating an electronic wave packet (EWP) in the continuum, ii) acceleration of the EWP by the strong laser field and iii) recombination to the core with emission of an attosecond burst of XUV coherent light. HHG thus provides a tunable ultrashort tabletop source of XUV/Soft X-ray radiation on attosecond time scale for applications (direct scheme). At the same time, it encodes coherently in the XUV radiation the structure and dynamical charge rearrangement of the radiating atoms/molecules (self-probing scheme or High Harmonic Spectroscopy). This thesis is dedicated to both application schemes in attophysics based on advanced characterization and control of the attosecond emission.

In the so-called self-probing scheme, the last step of HHG, the electron-ion re-collision can be considered as a probe process and the emission may encode fruitful information on the recombining system, including molecular structure and dynamics. In the first part, we performed high harmonic spectroscopy of  $\text{N}_2\text{O}$  and  $\text{CO}_2$  molecules that are (laser-)aligned with respect to the polarization of the driving laser. We implemented two methods based on optical and quantum interferometry respectively in order to characterize the amplitude and phase of the attosecond emission as a function of both photon energy and alignment angle. We discovered new effects in the high harmonic generation which could not be explained by the structure of the highest occupied molecular orbital (HOMO). Instead, we found that during the interaction with the laser field, two electronic states are coherently excited in the molecular ion and form a hole wave packet moving on an attosecond timescale in the molecule after tunnel ionization. We focused on exploring this coherent electronic motion inside the molecule, and compared the measurements in  $\text{N}_2\text{O}$  and  $\text{CO}_2$ . The striking difference in the harmonic phase behavior led us to the development of a multi-channel model allowing the extraction of the relative weight and phase of the two channels involved in the emission. Moreover, we studied the attosecond profile of the pulses emitted by these two molecules, and we proposed a simple but flexible way for performing attosecond pulse shaping. In the second part, high harmonic spectroscopy was extended to other molecular systems, including some relatively complex molecules, e.g.,  $\text{SF}_6$  and small hydrocarbons (methane, ethane, ethylene, acetylene). It revealed many interesting results such as phase distortions not previously reported.

For the direct scheme, we photoionized rare gas atoms using well characterized attosecond pulses of XUV coherent radiation combined with an infrared (IR) laser dressing field with controlled time delay, stabilized down to about  $\pm 60$  as. We evidenced marked differences in the measured angular distributions of the photoelectrons, depending on the number of IR photons exchanged. Joined to a theoretical interpretation, these observations bring new insights into the dynamics of this class of multi-color photoionization processes that are a key step towards studying photoionization in the time domain, with attosecond time resolution.



# SYNTHÈSE

---

La génération d'harmoniques d'ordre élevé (HHG) est un processus non linéaire extrême qui peut être compris intuitivement par la séquence de trois étapes: i) ionisation tunnel de la cible atome/ molécule et création d'un paquet d'ondes électronique (EWP) dans le continuum, ii) accélération de l'EWP par le champ laser intense et iii) recombinaison avec le cœur ionique et émission d'une impulsion attoseconde de lumière cohérente dans l'extrême UV (XUV). La HHG fournit ainsi une source ultracourte accordable dans l'XUV/ rayons X mous à l'échelle de temps attoseconde pour les applications (schéma direct). Dans le même temps, elle encode de manière cohérente dans le rayonnement XUV émis la structure et la dynamique de réarrangement de charge des atomes/molécules qui rayonnent (schéma auto-sonde ou Spectroscopie d'harmoniques d'ordre élevé). Cette thèse est consacrée à ces deux schémas d'application en attophysique, basés sur une caractérisation et un contrôle avancés de l'émission attoseconde.

Dans ce qu'on appelle le schème "auto-sonde", la dernière étape de la HHG, la recombinaison électron-ion peut être considérée comme un procédé de sonde et l'émission peut coder des informations fructueuses sur le système se recombinant, telles que la structure moléculaire et la dynamique. Dans la première partie, nous avons effectué la spectroscopie harmonique de molécules  $N_2O$  et  $CO_2$  qui sont alignées par rapport à la polarisation du laser générateur. Nous avons implémenté deux méthodes basées respectivement sur l'interférométrie optique et quantique afin de caractériser l'amplitude et la phase de l'émission attoseconde en fonction à la fois de l'énergie des photons et de l'angle d'alignement. Nous avons découvert de nouveaux effets dans la génération d'harmoniques qui ne peuvent pas être expliqués par la structure de l'orbitale moléculaire la plus haute occupée (HOMO). Au lieu de cela, nous avons trouvé que pendant l'interaction avec le champ laser, deux états électroniques sont excités de manière cohérente dans l'ion moléculaire, formant un paquet d'ondes de « trou » se déplaçant à une échelle de temps attoseconde dans la molécule après ionisation tunnel. Nous nous sommes concentrés sur l'exploration de ce mouvement électronique cohérent à l'intérieur de la molécule, et comparé les mesures de  $N_2O$  et  $CO_2$ . La différence frappante dans la phase harmonique nous a conduits à l'élaboration d'un modèle multi-canal permettant l'extraction de l'amplitude et de la phase relative des deux canaux impliqués dans l'émission. En outre, nous avons étudié le profil des impulsions attosecondes émises par ces deux molécules, et nous avons proposé un moyen simple mais flexible pour la réalisation de la mise en forme d'impulsions attosecondes. Dans la deuxième partie, la spectroscopie harmonique a été étendue à d'autres systèmes moléculaires, y compris certaines molécules relativement complexes, par exemple,  $SF_6$  et petits hydrocarbures (méthane, éthane, éthylène, acétylène). Elle a révélé de nombreux résultats intéressants tels que des distorsions de phase observées pour la première fois.

Dans le schéma direct, nous avons photoionisé des atomes de gaz rares en utilisant des impulsions attosecondes bien caractérisées combinées avec un laser infrarouge d'habituelle avec un délai contrôlé, stabilisé à environ  $\pm 60$  as. Nous avons mesuré des différences marquées dans les distributions angulaires des photoélectrons, en fonction du nombre de photons IR échangés. Jointes à notre interprétation théorique, ces observations apportent de nouvelles connaissances sur la dynamique de cette classe de processus de photo-ionisation multi-couleurs qui sont une étape clé vers l'étude de la photo-ionisation dans le domaine temporel avec une résolution attoseconde.



# ABBREVIATIONS

---

---

APT	Attosecond Pulse Train
BO	Born-Oppenheimer
DME	Dipole Matrix Element
EWP	Electron Wave Packet
FFT	Fast Fourier Transform
FWHM	Full Width at Half Maximum
HF	Hartree-Fock
IR	Infra Red
LCAO	Linear Combination of Atomic Orbitals
MO	Molecular Orbital
RABITT	Reconstruction of Attosecond harmonic Beating by Interference of Two-photon Transitions
TSI	Two Source Interferometry
SFA	Strong Field Approximation
TDSE	Time Dependent Schrödinger Equation
XUV	eXtreme Ultra Violet
PG	Polarization Gating
DOG	Double Optical Gating
GDOG	Generalized Double Optical Gating
SPIDER	Spectral Phase Interferometry for Direct Electric-field Reconstruction





# CONTENTS

---

---

<b>Introduction</b>	<b>1</b>
<b>1 Theoretical elements of High-order Harmonic Generation</b>	<b>7</b>
1.1 The time-dependent Schrödinger equation . . . . .	8
1.2 Semi-classical three-step model . . . . .	9
1.2.1 Tunnel ionization . . . . .	9
1.2.2 Acceleration . . . . .	11
1.2.3 Recombination . . . . .	12
1.2.4 3-Dimensional steering of the electron motion . . . . .	13
1.3 Quantum model based on the strong field approximation . . . . .	15
1.4 Propagation effects . . . . .	21
1.5 Time profile of the XUV emission . . . . .	23
1.6 Isolated attosecond pulse generation: towards to attosecond pump/probe scheme . . . . .	25
1.6.1 Post pulse compression . . . . .	26
1.6.2 Optical gating technique . . . . .	30
1.7 High-order Harmonic Generation from molecules . . . . .	33
<b>2 Experimental tools for attosecond physics</b>	<b>37</b>
2.1 Attosecond pulse generation . . . . .	39
2.2 Molecular alignment . . . . .	41
2.3 Characterization of High-order Harmonic Generation . . . . .	47
2.3.1 Reconstruction of Attosecond Burst By Interference of Two-photon transition (RABBIT) . . . . .	48
2.3.2 Two Source Interferometry (TSI) . . . . .	54
2.4 The experimental setups : optical lines . . . . .	56
2.4.1 The RABBIT and Two-color photoionization optical line . . . . .	56
2.4.2 The 2-source optical line . . . . .	57
<b>3 The fundamentals of High-order Harmonic Spectroscopy</b>	<b>59</b>
3.1 Combining attosecond and Ångström resolutions . . . . .	61
3.2 Accessing the recombination dipole moment . . . . .	63
3.3 Molecular orbital tomography . . . . .	65
3.4 Two-center interference model . . . . .	66
3.5 Multi-channel harmonic generation . . . . .	67
<b>4 High-harmonic Spectroscopy of N<sub>2</sub>O and CO<sub>2</sub></b>	<b>69</b>
4.1 Comparison of N <sub>2</sub> O and CO <sub>2</sub> . . . . .	73
4.2 Structural or dynamical interferences? . . . . .	75
4.3 Combining TSI with RABBIT . . . . .	81
4.4 Experimental comparison of the harmonic emission from N <sub>2</sub> O and CO <sub>2</sub> . . . . .	84
4.5 Modeling harmonic generation from N <sub>2</sub> O and CO <sub>2</sub> . . . . .	85
4.6 Improving the model . . . . .	90
4.7 Coherent control of attosecond emission . . . . .	101
4.8 Conclusions . . . . .	107
<b>5 High Harmonic Spectroscopy in N<sub>2</sub>, SF<sub>6</sub> and hydrocarbons</b>	<b>109</b>
5.1 HHS in aligned N <sub>2</sub> . . . . .	111
5.2 HHS in hydrocarbon molecules . . . . .	117
5.3 HHS in SF <sub>6</sub> . . . . .	130
5.4 Conclusions . . . . .	150

<b>6</b>	<b>The application of attosecond pulses: two-color multi-photon ionization</b>	<b>151</b>
6.1	Multi-photon and multi-color photoionization of rare gas atoms . . . . .	153
6.2	The 2012 experiment . . . . .	154
<b>7</b>	<b>Conclusions and outlook</b>	<b>159</b>
<b>A</b>	<b>Atomic Units</b>	<b>163</b>
<b>B</b>	<b>Symmetry properties of the Fourier transform: Oddness and Imaginarity</b>	<b>165</b>
B.1	Considering the Plane Wave dipole for N <sub>2</sub> O . . . . .	166
	<b>Acknowledgments</b>	<b>169</b>
	<b>References</b>	<b>170</b>

**Papers**

---

<b>I</b>	<b>Attosecond evolution of energy- and angle-resolved photoemission spectra in two-color (IR + XUV) ionization of rare gases</b>	<b>183</b>
<b>II</b>	<b>Electron trajectory control of odd and even ordered harmonics in high harmonic generation using an orthogonally polarised second harmonic field</b>	<b>191</b>

# INTRODUCTION

---

Over the last centuries, humankind has developed a passion for the exploration of fast phenomena beyond the observation capability of the human eye, i.e. faster than the blink of an eye ( $\sim 0.1s$ ). In 1878, Eadweard Muybridge photographed a galloping horse, thus giving an end to the long debate whether or not there is a moment when all four hooves are off the ground. Etienne-Jules Marey recorded images of a falling cat in 1894 that helped us understand the special ability of the cat to orient itself as it falls in order to land on its feet. These two pioneers pushed human observation towards the time scale of *millisecond*( $10^{-3}s$ ). Later on, using flash lamps, Harold Edgerton successfully took the picture of a shooting bullet (1962) into a playing card which is on *microsecond*( $10^{-6}s$ ) timescale [1].

Since the invention of laser by Maiman in 1960, it quickly became an ideal tool to study ultrafast processes. Indeed, the laser pulse can serve as a flash or a fast shutter in photography. Thanks to the fast evolution of laser techniques during the last half century, the definition of 'ultrafast' has been always refreshed [2]. Just one year after the first laser, Hellwarth and McClung [3] reduced the pulse duration to *10nanosecond*( $10^{-9}s$ ) by inventing the Q-switch. Then mode-locking (DeMaria et al. [4]) accompanied by broad-gain dye laser media (Shank and Ippen [5]) further reduced the duration to less than *1picosecond*( $10^{-12}s$ ). With the invention of the ring cavity with dispersion management, the pulse duration was further decreased to reach the *femtosecond*( $10^{-15}s$ ) timescale (Fork et al. [6]). By the end of the 1990s, the innovations introduced by Kerr-lens mode-locking, self-phase modulation, spectral broadening, the availability of chirped, ultra-broad band mirrors and pulse compression together pushed the pulse duration towards the ultimate limit of the optical cycle, with the generation of pulses as short as two optical cycles (Steinmeyer et al. [7]). However, it became clear that with the currently used Ti:sapphire laser, the pulse duration could not be reduced below the optical period in the IR ( $2.7fs$ ).

The time-resolved investigations with extreme temporal resolution provide important information for the understanding of many basic processes. The 1999 Nobel Prize in Chemistry was awarded to Ahmed Zewail for his pioneering work on the transition states of chemical reactions using femtosecond spectroscopy [1]. The rotation of molecules is typically on a few picosecond timescale, while molecular vibration is on a few femtosecond timescale. But the intra-atomic/molecular electronic dynamics, which are the basic phe-

phenomena at play in biology, chemistry and physics [8], can occur on a timescale as fast as attosecond, i.e.  $10^{-18}$ s. The observation and understanding of electron dynamics can teach us how to control matter at this most fundamental level.

### **High-order Harmonic Generation**

With the natural limitation of the pulse duration for Ti:sapphire laser on one hand, the demand of creating attosecond pulses on the other hand, people had to find a new scheme for this purpose. The evolution in laser technology has not only shortened the pulse length in the time domain, but also increased the pulse energy significantly [9], leading to intensities in the focal spot higher than  $10^{15} \text{W/cm}^2$ . Such intensity is already comparable with the static Coulomb field experienced by an outer-shell electron in an atom, therefore the light-matter interaction can not be seen as a perturbative process anymore. Ferry et al in Saclay [10] and McPherson in Chicago [11] performed experiments in this non-perturbative regime by focusing strong laser light into atomic gas jets and both of them found striking results. When detecting the radiation emitted on the laser axis, they measured spectra made of discrete lines at the multiple frequencies of the laser frequency, so-called harmonic frequencies. As well known in perturbative optics, the intensity of the first harmonic orders decreased quickly. However, they were followed by a plateau region with almost constant intensity and a sudden cut-off with exponential decrease. This unique high-order nonlinear process is called High-order Harmonic Generation (HHG). Extremely high orders have been generated since the plateau has been shown to extend until the keV range [12].

The underlying physics can be understood with a model in three separate steps [13][14][15]. (i) an electron is able to tunnel out because of the strong electric field of the laser that distorts the potential barrier. (ii) The freed electron is then accelerated by the strong laser field and driven back to its parent ion. (iii) Finally, it recollides with its parent-atom/molecule, converting the kinetic energy into XUV emission. The whole process is directly laser driven and thus fully coherent.

The unique properties of HHG have found applications in very diverse fields. To name just a few: the harmonics can be used as a seed for the Free Electron Lasers in order to improve their temporal coherence (Lambert et al. [16][17]). They also can be applied to coherent lensless diffraction imaging of nanostructures with a spatial resolution of few tens of nm (Gauthier et al. [18], Morlens et al. [19], Ravasio et al. [20], Sandberg et al. [21]). Moreover, their broadband spectrum should result in attosecond pulses if the different harmonics were perfectly phase locked. This was theoretically studied by Farkas and Toth [22]. And this characteristic was confirmed in 2001 for Attosecond Pulse Trains (APT) by (Paul et al. [23]) and for single attosecond pulses (SAP) by (Hentschel et al. [24]). Therefore, a whole new world was opened to research while entering the attosecond timescale.

## Attosecond research

Nowadays attosecond research has two major directions [25]. The first one is the direct scheme of transferring the femtosecond spectroscopy to attosecond resolution. The HHG process provides a source of ultra-short XUV pulses, used to pump or probe atoms/molecules by exciting or photoionizing them. One then detects the ejected photoelectrons which carry information about the intra-atomic/ molecular dynamics. A number of field-driven[26][27][28][29] and intrinsic [30][31][32][33] processes with attosecond dynamics have already been studied in atoms, molecules and solids using direct schemes. The study of multi-photon ionization with an attosecond precision control that will be developed in Chapter 6 is a good example of the application of attosecond pulses. The second one is known as “High Harmonic Spectroscopy (HHS)”, where the recolliding electron wave packet takes the role of an ultra-short probe pulse, while the emitted XUV light carries information about the generating atom or molecule. In such a “self-probing” scheme, the harmonic signal is analyzed to retrieve temporal and structural insight into the generating system itself. The major parts of the thesis, chapter 4 and 5 are dedicated to this research.

The theoretical and experimental development of high degree optical molecular alignment in field free conditions (Rosca-Pruna and Vrakking [34], Seideman [35], Stapelfeldt and Seideman [36]) quickly attracted the interest for investigating the molecular structures from the HHG. The group at Imperial College London [37][38] was the first to implement the molecular alignment technique in HHG, where they obtained clear angular dependent harmonic signal. This dependence gives a hint on the structure of molecular orbitals (Lein et al. [39][40]). Later, Itatani et al. [41] proposed a scheme for the reconstruction of the Highest Occupied Molecular Orbital (HOMO) based on the tomographic characterization of the recombination dipole moment. The following experiments in CEA-Saclay and Milano successfully demonstrated the reconstruction of molecular orbitals for  $N_2$  [42] and  $CO_2$  [43], respectively. The tomographic reconstruction relies on the fact that the orbital structure is encoded in the recombination dipole in the form of a so-called structural interference. Manfred Lein evidenced it theoretically in the simple case of the ‘two-center’ like orbital of  $H_2^+$  [39], where he found that a destructive interference could happen between the recolliding electron wave and the bound-state wavefunction during the recombination step of HHG. And this ‘structural interference’ leaves a clear signature in the XUV emission. Many groups indeed observed a destructive interference in the harmonic emission from  $CO_2$  molecules that are aligned parallel to the laser polarization (Kanai et al. [44], Vozzi et al. [45], Boutu et al. [46]). However, they were found at different positions in energy by the different groups. The reason for this contradiction is due to the complicated electron dynamics occurring in the molecules during the high harmonic generation process. Smirnova et al. ([47][48]) and McFarland et al. ([49]) proposed that multiple orbitals could contribute to HHG: not only the HOMO as previously thought, but also lower lying orbitals. Therefore

the HHG from different orbitals may interfere, inducing laser intensity dependent electron dynamics [47], which well explained the different positions of destructive interference in CO<sub>2</sub>. This kind of interference is called dynamical interference. The study of multi-orbital contributions to HHG gives access to the time resolved behavior of the multi-electron rearrangement upon the ionization process as well as to the hole dynamics in the cation during the electron excursion in the continuum [42][47][50]. In addition, the motion of nuclei on the attosecond time scale can be encoded in HHG. This is because the tunnel ionization of an electron may lead to bond weakening, especially in molecules containing light atoms such as protons. Baker et al. [51][52] investigated the harmonic spectrum by comparing H<sub>2</sub>/D<sub>2</sub> and CH<sub>4</sub>/CD<sub>4</sub> and found clear signatures of nuclear dynamics in the harmonic amplitudes. Kanai et al. [53], Haessler et al. [54] measured the spectral phase for H<sub>2</sub>/D<sub>2</sub>, but the predicted phase variation seemed to be too small to be observed.

### **Overview of this Thesis**

This thesis is concerned with how molecules and their dynamics can be studied using the process of HHG. The work started in 2010 at a time where only simple molecules such as N<sub>2</sub> and CO<sub>2</sub> had been investigated. It was long considered a theoretical challenge to extend the HHG study to complex molecules due to the complicated underlying physics. This exciting question thus determined the main direction of this thesis: to perform measurements that would help to assess and improve the existing models and to obtain truly experimental evidence of the molecular structure and dynamics based on a much reduced set of assumptions.

Chapter 1 concentrates on stating the theoretical background of HHG. The fundamental principles of attosecond physics needed for the later theoretical and experimental investigations are introduced. The technical developments towards isolated attosecond pulse production are also detailed.

Chapter 2 covers the description of the experimental tools used in attosecond physics. The required techniques for the thesis are discussed, i.e. molecular alignment and attosecond pulse characterization techniques.

Chapter 3 is dedicated to the fundamental elements of High Harmonic Spectroscopy. It discusses the advantages of this method and what kind of information we can get access to.

Chapter 4 is the main part of the thesis. The measurements performed by two different methods for advanced characterization of the attosecond emission from aligned molecules (N<sub>2</sub>O and CO<sub>2</sub>) are presented. The significant differences in the measurements for N<sub>2</sub>O and CO<sub>2</sub> are discussed. And a model is developed to understand the underlying physics; it provides an excellent agreement with the experimental results as well as explains the differences between the two molecules. We can extract the contribution ratio between the two generation channels. Interestingly, we are able to demonstrate that harmonic emission

from a lower lying orbital can be larger than that from the highest occupied molecular orbital. In the second part of this chapter, the attosecond pulse shaping technique by using aligned molecules is presented.

Chapter 5 is dedicated to the extension of High Harmonic Spectroscopy to various molecules, including some "complex" molecules such as hydrocarbons or SF<sub>6</sub>. Plenty of unreported results will be shown. In particular, we measure phase deviations related to both nuclear and electronic dynamics.

Chapter 6 presents a direct application of attosecond pulses to the study of two-color multi-photon ionization. We will measure the distortion of the angular distribution of the ejected electrons as a function of the delay between the two color fields with attosecond precision.

Finally, the manuscript ends with general conclusions drawn from the work done during the three years of this thesis, together with an outlook on future developments.





---

# THEORETICAL ELEMENTS OF HIGH-ORDER HARMONIC GENERATION

---

In this chapter, we will describe a number of essential theoretical elements in Attophysics that are necessary for this thesis. First of all, we present in Section 1.1 the time-dependent Schrödinger equation (TDSE) that has to be solved for accessing the atomic/molecular dynamics in strong fields. We point out the difficulty of solving it for multi-electron systems due to the high dimensionality of the problem and the simplification introduced by the single-active electron approximation. Very detailed physical insight into high-harmonic generation (HHG) can be obtained with a simple semi-classical three-step model that will be introduced in Section 1.2. We will also discuss the specific case of HHG in the presence of the 800nm driving light and its orthogonally polarized second harmonic field, the basic idea in Paper II. Next, a quantum approach by solving TDSE with Strong Field Approximation will be described in Section 1.3, which recovers the assumptions of the semi-classical model. Later on, we will present how the macroscopic XUV emission is built up from the single atom/molecule response in Section 1.4.

We then turn to the study of the time profile of the XUV emission in Section 1.5 and to the generation of isolated attosecond pulses in Section 1.6. The current techniques for the latter purpose are given. For the post pulse compression, we will introduce the mechanism of the spectral broadening, the setup and the first results obtained during my thesis. For the optical gating methods, we will compare the different schemes in terms of their limitations and propose the Generalized Double Optical Gating for our laser system.

Finally, we will discuss in Section 1.7 the specificity of HHG from molecules. We explain the difficulties of the calculation of both the ionization and the recombination steps. The consequences on HHG of the structure of the highest occupied molecular orbital and of the existence of close lying ionization channels will be discussed.

## RÉSUMÉ DU CHAPITRE

Dans ce chapitre, nous allons décrire un certain nombre d'éléments théoriques essentiels dans la physique attoseconde qui sont nécessaires pour cette thèse. Tout d'abord, nous présentons dans la Section 1.1 l'équation de Schrödinger dépendant du temps (TDSE) qui doit être résolue pour accéder à la dynamique atomique/moléculaire dans des champs forts. Nous faisons remarquer la difficulté de la résoudre pour les systèmes multi-électrons en raison de la grande dimensionalité du problème et présentons la simplification apportée par l'approximation de l'électron mono-actif. La compréhension de la physique du processus de la génération d'harmoniques d'ordres élevés (HHG) peut être obtenue avec un modèle simple en trois étapes semi-classique qui sera présenté dans la section 1.2. Nous discuterons également le cas spécifique de la HHG en présence du champ électrique du laser à 800 nm et de son deuxième harmonique polarisé orthogonalement, l'idée de base discutée dans l'article II. Ensuite, une approche quantique de la résolution de la TDSE dans l'approximation du champ fort sera décrite dans la section 1.3, qui retrouve les hypothèses du modèle semi-classique. Plus tard, nous allons présenter comment l'émission XUV macroscopique est construite à partir de la réponse atome/molécule unique à la section 1.4.

Nous passons ensuite à l'étude du profil temporel de l'émission XUV dans la section 1.5 et à la génération d'impulsions attosecondes isolées dans la section 1.6. Les techniques actuelles utilisées à cette fin sont données. Pour la post-compression d'impulsions, nous allons introduire le mécanisme de l'élargissement spectral, la configuration et les premiers résultats obtenus au cours de ma thèse. Pour les méthodes de filtrage temporel («gating»), nous allons comparer les différents régimes en fonction de leurs limites et proposer un 'Generalized Double Optical Gating' pour notre système laser.

Enfin, nous allons discuter à la section 1.7 la spécificité de la HHG dans les molécules. Nous expliquons les difficultés du calcul à la fois des étapes de l'ionisation et de la recombinaison. Les conséquences sur la HHG de la structure de l'orbitale moléculaire occupée la plus élevée et de l'existence de plusieurs canaux d'ionisation seront discutés.

### 1.1 The time-dependent Schrödinger equation

The most important theoretical tool for describing quantum mechanical behavior in general is the time-dependent Schrödinger equation (TDSE). In single active electron approximation, the three dimensional time-dependent wave function  $\psi(\mathbf{r}, t)$  that exposed to time dependent potential in strong laser field with length gauge by using atomic units ( $m = e = \hbar = 1$ ) can be written as:

$$i \frac{\partial}{\partial t} \psi(\mathbf{r}, t) = \left[ -\frac{1}{2} \nabla^2 + V_0(\mathbf{r}) + \mathbf{r} \cdot \mathbf{E}(t) \right] \psi(\mathbf{r}, t) \quad (1.1)$$

with  $V(\mathbf{r}, t) = V_0(\mathbf{r}) + \mathbf{r}E(t)$  being the time-dependent potential.  $V_0(\mathbf{r})$  is the static intra-atomic/molecular potential. In strong field (intensity of  $10^{14} - 10^{16} \text{W/cm}^2$ ), electronic wave function is extremely distorted by the laser field since its strength is comparable to the intra-atomic/molecular electric field. Its influence cannot be treated as a perturbation in this case. Thus the interaction with the laser  $\mathbf{r}E(t)$  is also considered[55][56], where  $E(t)$  is the electric field of the laser.

The exact solution of the electronic wave function can be obtained by the integration of the equation. By splitting the time step small enough, the numerical solution of the TDSE for single electron can be very precise. However, the full numerical solution for multi-electron systems would be extremely complicated due to the high dimensionality of the problem (We have to look for a seven dimensional function  $(x_1, y_1, z_1, x_2, y_2, z_2, t)$  to describe the two-electron system), which makes the TDSE is intractable for multielectron atoms/molecules. Thus, single active electron approximation (usually from the highest occupied orbital) under a pseudo-potential is often applied[57]. There are attempts to solve the problem in many electron systems [58][59][60].

## 1.2 Semi-classical three-step model

On one hand, the solution of TDSE for multi-electron systems is difficult to get. On the other hand, people also would like to understand the physics insight of HHG which cannot be obtained from TDSE. Therefore, a simple semi-classical three-step model was developed[13][14]. When a strong laser field interacts with atom or molecule, its potential barrier is suppressed. Therefore the electron can tunnel ionize out from its parent atom/molecule with initially zero velocity(i). Then the free electron is accelerated away from the ion by the laser field, and its acceleration reverses when the laser field changes the direction of the oscillation (ii). Eventually, the electron gets chance to recollide with its parent ion, at which moment converts the kinetic energy into an extreme ultraviolet photon. In this model, the electron is treated by quantum mechanics at the instant of ionization, but its dynamics after is considered classically: the electron is considered as a classical point charge, and during the second step one considers the driving laser field to completely govern its evolution. The HHG process can be repeated each half cycle of the laser oscillation producing a train of pulses. The process is triggered by the laser's electric field, hence all the emitted harmonics are coherent. From now on we will concentrate on each step to explore HHG.

### 1.2.1 Tunnel ionization

The tunnel ionization process is very important in HHG, because it is not only the basis for all subsequent physical processes but also the source of the extreme non-linearity required to push the pulse duration to attosecond regime. To understand the mechanism of tun-

nel ionization, we start with the comparison of different ionization schemes, in the case of hydrogen like atoms interacting with an infra-red laser field.

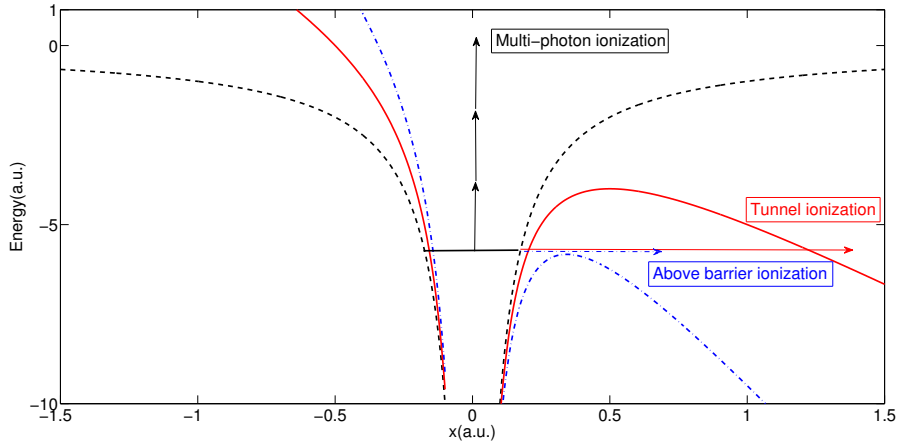


Figure 1.1: Different ionization schemes. The horizontal black line indicates the atomic ground state. Multi-photon ionization dominates when the external electric field is negligible as presented by the black dashed line. With the increase of the laser intensity, the Coulomb potential barrier is lowered so that the tunnel ionization happens as shown by the red solid line. A sufficiently intense electric field completely suppresses the potential barrier, in which case the Above Barrier Ionization takes place, see the blue dash-dotted line.

In strong field physics, the barrier formed by the coulomb potential  $V_0(x)$  is modified by the electric field linear polarized along  $\hat{x}$  direction:

$$\mathbf{E}(t) = E_0 \cos(\omega_0 t) \hat{x} \quad (1.2)$$

$E_0$  is the amplitude and  $\omega_0$  is the angular frequency of the laser. The total potential  $V(x, t)$  felt by the electron (in length gauge) is:

$$V(x, t) = V_0(x) + xE(t) \quad (1.3)$$

where  $V_0(x) = -Z_{eff}/x$  and  $Z_{eff}$  is the effective nuclear charge. Figure 1.1 shows different schemes of ionization due to the influence of the laser. The electron can be ionized from the simultaneous absorption of several photons corresponding to an energy greater than the ionization potential, which is referred as Multi-photon ionization. If the absorbed number of photons is larger than the minimum number required to reach the ionization threshold, Above Threshold Ionization takes place. When the electric field is comparable to the binding electric field between the nucleus and the electron, it distorts the potential (see the red solid line). Therefore, the electron gets a given probability to tunnel through a barrier that it classically could not surmount. This tunnel ionization effect is a quantum phenomenon (the wave function tunnels into the continuum) that depends on the height and the width of

the barrier and on the time during which the barrier is lowered. By continuously increasing the driving intensity, the potential barrier can be suppressed completely so that the electron gets free (see the blue dash-dotted line). This kind of ionization is called Above Barrier Ionization. The maximum laser intensity (referred to as saturation intensity  $I_{BS} = E_{BS}^2/(8\pi)$ ), that can be applied before reaching the barrier suppression ionization can be found by determining the position ( $x_0$ ) of the inflection point on the potential barrier. By deriving the equation 1.3 with respect to the position, one finds that  $x_0 = \sqrt{\frac{Z_{eff}}{E_{BS}}}$ . The saturation intensity is found by substituting the  $x_0$  back to eq. 1.3:

$$E_{BS} = \frac{I_p^2}{4Z_{eff}}, \quad I_{BS} = \frac{I_p^4}{128\pi Z_{eff}^2}, \quad I_{BS}[\text{W/cm}^2] = 4 \times 10^9 \frac{I_p^4[\text{eV}]}{Z_{eff}^2}. \quad (1.4)$$

For the rare gases krypton and argon, where  $Z_{eff} = 1$ , this implies  $I_{BS}^{Kr} = 1.5 \times 10^{14} \text{ W/cm}^2$  and  $I_{BS}^{Ar} = 2.5 \times 10^{14} \text{ W/cm}^2$ . These results already foresee the magnitude of the laser intensities that should be applied when generating harmonics.

The image above for a quasi-static field should be complemented in the case of an oscillating laser field due to the fact that tunnel ionization also depends on the time during which the barrier is lowered, proportional to the laser field.

To distinguish various ionization regimes of the light matter interaction, we then introduce the Keldysh parameter [61]:

$$\gamma = \sqrt{\frac{I_p}{2U_p}} = \omega_0 \sqrt{\frac{2I_p}{I}} = \frac{T_{tunnel}}{T_0} \quad (1.5)$$

where  $I_p$  is the ionization potential,  $I = E^2$  is the intensity of the laser field,  $U_p = E^2/4\omega_0^2$  is the ponderomotive potential, i.e. the mean quiver energy of a free electron in the laser field.  $T_{tunnel} = 2\pi \frac{\sqrt{2m_e I_p}}{eE}$  is the ionization time the electron takes to tunnel through the barrier.  $\gamma$  measures the ratio between the time needed for an electron to cross the Coulomb barrier, and the period of the oscillation,  $T_0 = 2\pi/\omega_0$ . As would be expected, a value of  $\gamma \gg 1$  indicates multi-photon ionization, and,  $\gamma \ll 1$  implies tunnel ionization.

## 1.2.2 Acceleration

Upon the instant of tunnel ionization ( $t_i$ ), the electron being born in the continuum with initially zero velocity. From this moment on, the electron is considered as a classical point charge, and during the second step one considers the driving laser field,  $E(t) = E_0 \cos(\omega_0 t) \hat{x}$ , to completely govern its evolution by assuming no influence of the atomic potential. For the sake of simplicity we assume that the position of the electron at  $t_i$  corresponds to the position of the atom,  $x_0 = 0$ . It is considered to be an acceptable approximation, since as we will see below, the length of the trajectory on which the electron is steered until it comes back to the vicinity of the atom, is much larger than the exit point of the tunnel ionization.

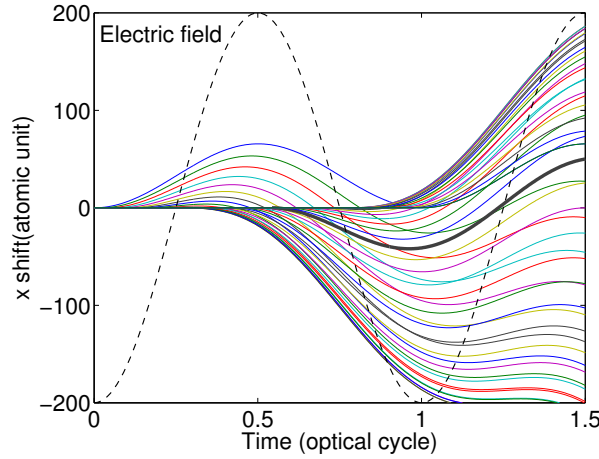


Figure 1.2: Electron oscillation after ionization driven by the laser field (see the black dash line). The center wavelength used for the calculation is 800nm and the intensity is  $2.5 \times 10^{14} \text{W/cm}^2$

Therefore, the velocity and displacement of the electron can be calculated from Equation 1.2,

$$v_x(t) = v_0 + \int_{t_i}^t E(t) dt \quad (1.6)$$

$$x(t) = x_0 + \int_{t_i}^t v_x(t) dt \quad (1.7)$$

With the initially conditions  $v_0 = 0$  and  $x_0 = 0$ . Thus

$$v_x(t) = \frac{E_0}{\omega_0} [\sin(\omega_0 t) - \sin(\omega_0 t_i)] \quad (1.8)$$

$$x(t) = \frac{E_0}{\omega_0^2} [\cos(\omega_0 t_i) - \cos(\omega_0 t)] - \frac{E_0}{\omega_0} \sin(\omega_0 t_i)(t - t_i) \quad (1.9)$$

From Equation 1.9, the electron trajectories that correspond to different tunnel ionization moments ( $t_i$ ) can be obtained, as shown in Figure 1.2. The electron reverses its acceleration direction when the electric field changes its sign, but not all the electrons are driven back to the ion at  $x = 0$ . For  $t_i$  within the first and third quarter of the laser oscillation period, the electrons do return to the core ( $[0, T_0/4]$  &  $[T_0/2, 3T_0/4]$ ). The electrons just drift away if the ionization occurs at any other time of the cycle. Moreover, some trajectories indicate several recollisions. However electron wave packet spreading increases with time so that it reduces the importance of the later collisions. Phase matching effects also decrease the contribution of longer trajectories to the macroscopic signal. Therefore, we only consider the first recollisions.

### 1.2.3 Recombination

In the last step, the electron recollides with its parent ion with which it can recombine and convert its kinetic energy into high energy photon emission. The time of this event is

defined as recombination time  $t_r$ . By solving  $x(t) = 0$  from Equation 1.9, we find  $t_i$  and  $t_r$  in pairs. The kinetic energy of the recolliding electron can be calculated from  $v_x^2(t_r)/2$ . The relation between electron kinetic energy, ionization time and recombination time is showed in Figure 1.3. from which we find that the maximum energy that an electron can get is  $3.17U_p$ . Therefore, the highest harmonic energy is

$$E_{cutoff} = I_p + E_k = I_p + 3.17U_p \quad (1.10)$$

This cut-off law, which is the intensity and medium dependent, provides us fruitful information of High-order Harmonic Generation [56]. The maximum order of HHG depends on the ionization potential of the generating medium. Moreover, the cut-off position varies with the laser intensity and wavelength due to  $U_p \propto I\lambda^2$ . Hence, one can achieve higher harmonic order emission either by increasing the intensity of the laser,  $I$ , but  $I_p$  determines an upper applicable limit (see section 1.2.1), or by increasing the lasers wavelength,  $\lambda$ , towards the MIR domain. The latter parameter gives more flexibility. Popmintchev et al. showed that the cutoff position is extended to more than  $1.6keV$  region (up to orders greater than 5000) by using a wavelength of  $3.9\mu m$  laser [12]. But the price to pay is the drop of the HHG efficiency. By increasing  $\lambda$  the excursion time  $\tau = t_r - t_i$  of the electron wave packet increases, leading to enhanced spreading that causes low XUV emission signal during the recombination. The exact scaling of the efficiency is not clear yet, but depending on the theory (experiment) it may be  $\propto \lambda^{-(5-9)}$  [62][63][64][65]. With good phase matching conditions one may shift this rate back towards  $\propto \lambda^{-2}$  dependence [66].

For energies below the cutoff, we find that there are two trajectories corresponding the same energy from Figure 1.3. The one which ionizes later and recombines earlier, therefore corresponding to smaller propagation time in the electric field, is defined as short trajectory. The other one spends more time in the electric field upon ionization, so it is called long trajectory. With increasing energy, the recombination time of short trajectories increases but that of long trajectories decreases. Eventually, they overlap at the maximum energy.

### 1.2.4 3-Dimensional steering of the electron motion

The electron trajectory after ionization is driven by the laser field, which is in 2-Dimension in the discussion above. If the field is elliptically polarized, we can 3-Dimensionally determine the direction of electron traveling. This kind of control can be done by using either elliptically polarized light or a perpendicularly polarized two-color field. Compared to the former, the latter one provides more freedom since the relative amplitude and phase can be manipulated separately. The electric field of orthogonally polarized  $800nm$  and  $400nm$  laser pulses is:

$$E(t) = E_x \cos(\omega_0 t) \hat{x} + E_y \cos(2\omega_0 t + \Delta\phi) \hat{y} \quad (1.11)$$

where  $\hat{x}$  and  $\hat{y}$  are the direction of the polarization of the fundamental field and of its second harmonic, respectively.  $E_x$  and  $E_y$  are their amplitudes.  $\Delta\phi$  is the phase difference between



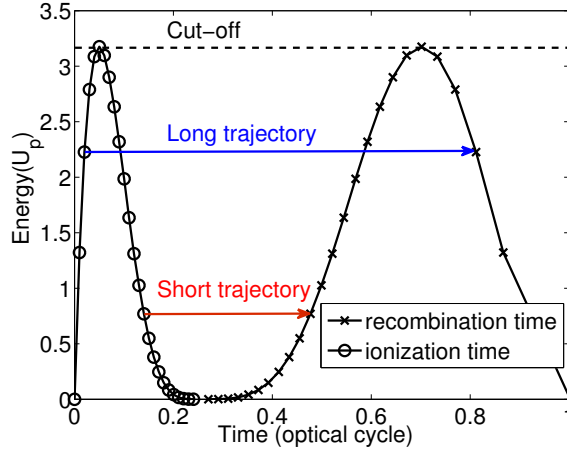


Figure 1.3: Classical calculation of ionization and recombination times as a function of the electron recollision energy, for an 800nm laser and an intensity of  $I = 2.5 \times 10^{14} \text{W/cm}^2$ . One example of long and short trajectories is showed by the blue and the red line, respectively. The cut-off position is marked by the black dashed line.

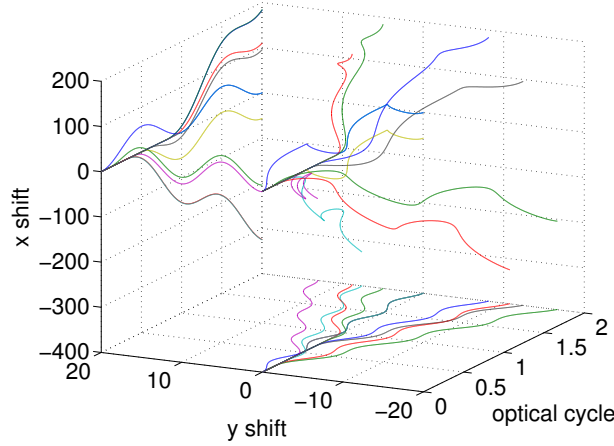


Figure 1.4: The 3-Dimensional electron trajectories after ionization in orthogonal two color fields (800 + 400nm) with  $\Delta\phi = 0$ .

the two color fields. As discussed in section 1.2.2, we can get the equations of the electron motion:

$$x(t) = \frac{E_x}{\omega_0^2} [\cos(\omega_0 t_i) - \cos(\omega_0 t)] - \frac{E_x}{\omega_0} \sin(\omega_0 t_i)(t - t_i) \quad (1.12)$$

$$y(t) = \frac{E_y}{4\omega_0^2} [\cos(2\omega_0 t_i + \Delta\phi) - \cos(2\omega_0 t + \Delta\phi)] - \frac{E_y}{2\omega_0} \sin(2\omega_0 t_i + \Delta\phi)(t - t_i) \quad (1.13)$$

The electron motion calculated from Equations 1.12 and 1.13 is showed in Figure 1.4. By adding a 400nm field, the electrons are driven laterally therefore their trajectories are more complex and the efficiency of electron-ion recollision drops dramatically so that only the electrons ionized within a short time interval can eventually recombine to the core. In this

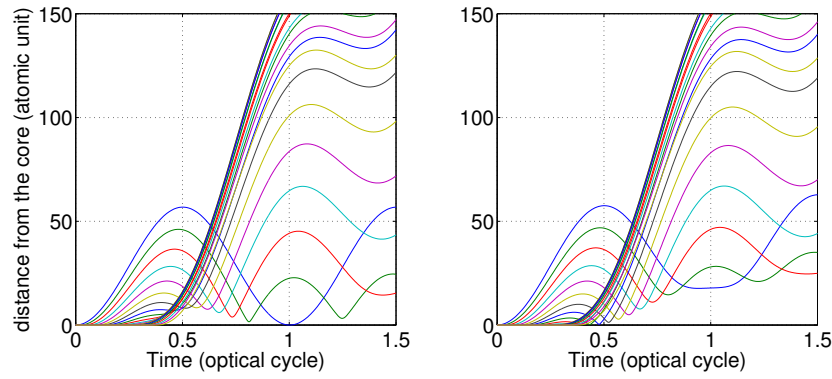


Figure 1.5: Oscillatory motion of the continuum electrons driven by an orthogonal two color fields when their relative phase difference  $\Delta\phi = 0$ (left) or  $\Delta\phi = \pi$ (right).

case, this two color fields can be treated as a time gate of the ionization and recombination instants because only the pairs of ionizations times,  $t_i$  and recollision times  $t_r$ , which have closed trajectories contribute to HHG. Figure 1.5 shows the different trajectories for different relative phase differences between 800nm laser field and its second harmonic. When  $\Delta\phi = 0$ , showed in the left picture, the electrons that ionized early within one optical cycle come back to the parent ion at a time close to  $T$  (one optical cycle). Thus, only long trajectories are selected. As for  $\Delta\phi = \pi$  in the right figure, the electrons that travel less time get the chance to recombine. The short trajectories are then chosen.

### 1.3 Quantum model based on the strong field approximation

Although the three-step model gives a very intuitive explanation for the experimental observation, it doesn't explain all the short comings for a complete picture, one needs to solve the TDSE. However, numerical solving TDSE is time consuming and it is not easy to understand the physics behind it. Thus based on the semi-classical model, Lewenstein et al. [15] developed a quantum approach by solving TDSE within the Strong Field Approximation. This model is built on the basis of the following assumptions:

- (i) Among the bound states, only the ground state contributes to high-order harmonic radiation. The other bound states are neglected.
- (ii) The depletion of the ground state is considered negligible in a first step.
- (iii) The electrons in the continuum states are seen as free electrons that are only affected by the laser field, and ignore the Coulomb potential of the ionic core.

According to the assumptions, the time-dependent wave function can be written as a superposition of ground state  $|0\rangle$  and continuum states  $|\mathbf{v}\rangle$ .

$$|\Psi(t)\rangle = e^{iI_p t} \left( \mathbf{a}(t) |0\rangle + \int d^3\mathbf{v} \mathbf{b}(\mathbf{v}, t) |\mathbf{v}\rangle \right) \quad (1.14)$$

where  $\mathbf{a}(t) \simeq 1$  is the complex amplitude of the ground state and  $\mathbf{b}(\mathbf{v}, t)$  is the time dependent amplitude and phase of the corresponding continuum state that has a velocity of  $\mathbf{v}$ . The TDSE for the single active electron writes (in length gauge) as Equation 1.1. So  $\mathbf{b}(\mathbf{v}, t)$  is obtained by solving

$$\mathbf{b}(\mathbf{v}, t) = i \int_0^t dt' \mathbf{E}(t') d_x(\mathbf{v} + \mathbf{A}(t) - \mathbf{A}(t')) \exp \left\{ -i \int_{t'}^t dt'' [(\mathbf{v} + \mathbf{A}(t) - \mathbf{A}(t''))^2 / 2 + I_p] \right\} \quad (1.15)$$

where  $\mathbf{A}(t) = (-\frac{E}{\omega} \sin(\omega t), 0, 0)$  is the vector potential of the electric field. Therefore, the nonlinear dipole moment  $d(t) = \langle \Psi(t) | x | \Psi(t) \rangle$  can be calculated by neglecting the continuum-continuum transitions:

$$d(t) = i \int_{-\infty}^t dt_i \int d^3 \mathbf{p} \mathbf{E}(t_i) d_x[\mathbf{p} + \mathbf{A}(t_i)] \exp[-iS(\mathbf{p}, t, t_i)] d_x^*[\mathbf{p} + \mathbf{A}(t)] + c.c. \quad (1.16)$$

where  $\mathbf{p} = \mathbf{v} + \mathbf{A}(t)$  is the canonical momentum,  $S(\mathbf{p}, t, t_i)$  is the quasi classical action

$$S(\mathbf{p}, t, t_i) = - \int_{t_i}^t dt'' \left( \frac{[\mathbf{p} + \mathbf{A}(t'')]^2}{2} + I_p \right) \quad (1.17)$$

and  $d_x$  is the dipole matrix element for bound-free transitions, that writes for hydrogen like atoms:

$$d_x(\mathbf{p}) = i \frac{2^{7/2} (2I_p)^{5/4}}{\pi} \frac{\mathbf{p}}{(\mathbf{p}^2 + 2I_p)^3} \quad (1.18)$$

As we can see from the dipole expression in Equation 1.16, it has a clear physical explanation. First,  $\mathbf{E}(t_i) d_x[\mathbf{p} + \mathbf{A}(t_i)]$  represents the probability amplitude for the laser-induced transition to the continuum state with momentum  $\mathbf{p}$  at time  $t_i$ . Next, the electron wave packet gains kinetic energy during the laser oscillation and obtains an extra phase  $S(\mathbf{p}, t, t_i)$ . Finally,  $d_x^*[\mathbf{p} + \mathbf{A}(t)]$  indicates that the electronic wave function eventually recombines to the ground state at time  $t$  and releases the energy in the form of photon emission, producing HHG.

The harmonic dipole  $d(\omega)$  can be obtained by the Fourier transform of the time dependent dipole:

$$d(\omega) = \mathcal{F}_{t \rightarrow \omega} [d(t)] \quad (1.19)$$

$$= i \int dt \int_{-\infty}^t dt_i \int d^3 \mathbf{p} \mathbf{E}(t_i) d_x[\mathbf{p} + \mathbf{A}(t_i)] \exp[-i\phi_{xuv}(\mathbf{p}, t, t_i)] d_x^*[\mathbf{p} + \mathbf{A}(t)] + c.c. \quad (1.20)$$

with

$$\phi_{xuv}(\mathbf{p}, t, t_i) = S(\mathbf{p}, t, t_i) + \omega t \quad (1.21)$$

is the Legendre transformed action. Equation 1.20 is an integration over an infinite number of triplets  $(\mathbf{p}, t, t_i)$ , which correspond to quantum orbits. Therefore the calculation is still time consuming.

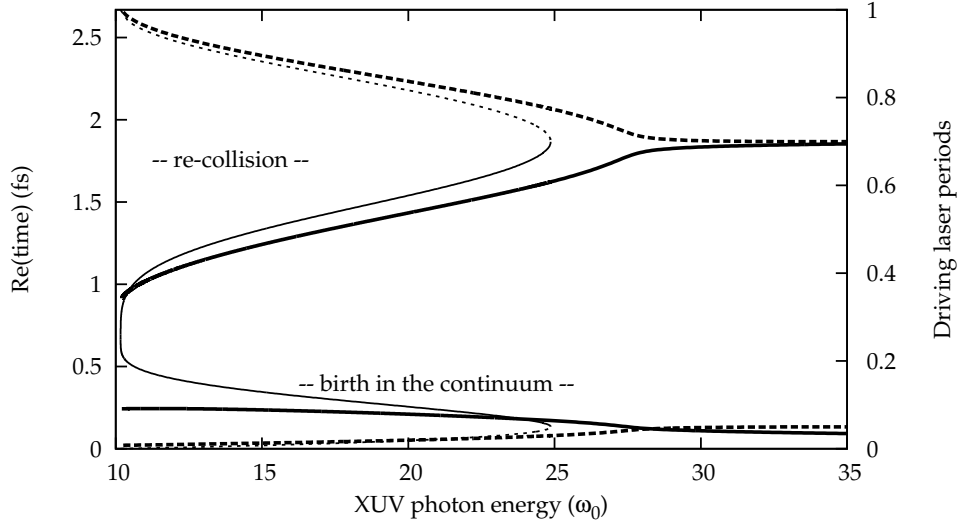


Figure 1.6: Ionization and recombination times as a function of photon energy. Thick and thin lines correspond to quantum and classical calculations respectively. Full and dashed lines mark the short and long trajectories. The calculation was performed in argon,  $I_p = 15.7eV$ , with an  $800nm$  laser and an intensity of  $I = 1.2 \times 10^{14}W/cm^2$ .

### Saddle point approximation

Even though there is an infinite number of quantum paths, the weights of their contribution are different. As discussed in Lewenstein et al. [15], Salières et al. [67], Priori et al. [68] and Sansone et al. [69], the main contribution to the integration in Equation 1.16 is from the stationary points of the quasi-classical action. Therefore, it can be further simplified by using saddle point approximation. In the first step, saddle point method is only performed on the integral of the momentum ( $\mathbf{p}$ ), which corresponds to the most troublesome integration.

$$d(t) = i \int_{-\infty}^t dt_i \left[ \frac{\pi}{\epsilon + i(t-t_i)/2} \right]^{3/2} \mathbf{E}(t_i) d_x [\mathbf{p}_{st} + \mathbf{A}(t_i)] \exp[-iS_{st}(\mathbf{p}, t, t_i)] d_x^* [\mathbf{p}_{st} + \mathbf{A}(t)] + c.c. \quad (1.22)$$

where  $\epsilon$  is an extremely small positive regularization constant and  $\mathbf{p}_{st}$  and  $S_{st}$  are the stationary value of the momentum and the action, respectively.

$$\mathbf{p}_{st}(t, t_i) = \frac{1}{t-t_i} \int_{t_i}^t \mathbf{A}(t') dt' \quad (1.23)$$

$$S_{st}(t, t_i) = (t-t_i)I_p - \frac{1}{2} \mathbf{p}_{st}^2(t-t_i) + \frac{1}{2} \int_{t_i}^t \mathbf{A}^2(t') dt' \quad (1.24)$$

Now we apply the same method to evaluate the remaining integrals over  $\mathbf{p}$ ,  $t$  and  $t_i$ . Therefore we get three saddle-point equations, obtained by equating to zero the derivatives of the Legendre transformed action, with respect to the canonical momentum  $\mathbf{p}$ , ionization time

$t_i$  and the recombination time  $t$ :

$$\nabla_{\mathbf{p}_{st}} \varphi_{xuv}(\mathbf{p}_{st}, t, t_i) = x(t_r) - x(t_i) = \int_{t_i}^t [\mathbf{p}_{st} + \mathbf{A}(t')] dt' = 0 \quad (1.25)$$

$$\frac{\partial \varphi_{xuv}(\mathbf{p}_{st}, t, t_i)}{t_i} = \frac{[\mathbf{p}_{st} + \mathbf{A}(t_i)]^2}{2} + I_p = 0 \quad (1.26)$$

$$\frac{\partial \varphi_{xuv}(\mathbf{p}_{st}, t, t_i)}{t} = \omega - \frac{[\mathbf{p}_{st} + \mathbf{A}(t)]^2}{2} - I_p = 0 \quad (1.27)$$

These three conditions correspond elegantly to the assumptions made in the classical description of HHG: Equation 1.25 states that the dominating quantum paths correspond to closed trajectories. Equation 1.26 means the kinetic energy of the tunneling electron is negative at the ionization time  $t_i$  so that the real part of the initial velocity is 0, as it is foreseen by the classical description. This imaginary-valued velocity can be obtained if  $t_i$  is complex, which can be seen as a trace of the tunnel ionization process [70]. This has important consequences since all quantities will then be complex. In particular, the imaginary part of the action will give the well known Keldysh exponential factor characteristics of tunnel ionization. Finally, Equation 1.27 implies that the energy of the emitted photon is the sum of the electron kinetic energy and the binding energy, which corresponds to the energy conservation law. We get triplets  $(\mathbf{p}, t, t_i)$  by solving these three equations, from which we find the relation between  $t_i$ ,  $t$  and the photon energy, see Figure 1.6 (calculated by Thierry Auguste). The simple semi-classical model turns out to be in reasonable agreement in the plateau region but, obviously, the more rigorous quantum-mechanical calculation yields a more precise description, i.e. the quantum calculation leads to the generation of higher harmonic orders than the classical simulation by taking the effects of quantum tunneling and quantum diffusion into account [15]. The cutoff energy that given from the quantum calculation  $E_{max} \simeq 3.17U_p + 1.32I_p$  for  $I_p \ll U_p$ .

In the spirit of Feynman's path integrals (Salières et al. [67]),  $d(\omega)$  can be written as a sum over all the quantum paths:

$$\begin{aligned} d(\omega, I) &= \sum_n |x_n(\omega, I)| \exp[i\phi_{xuv}^n(\omega, I)] \\ &= \sum_n \frac{i2\pi}{\sqrt{\det(S'')}} \left[ \frac{\pi}{\epsilon + i(t - t_i)/2} \right]^{3/2} \mathbf{E}(t_i) d_x[\mathbf{p}_{st} + \mathbf{A}(t_i)] \exp[-iS_{st}(\mathbf{p}, t, t_i) - i\omega t] d_x^*[\mathbf{p}_{st} + \mathbf{A}(t)] + c.c. \end{aligned} \quad (1.28)$$

where  $I$  is the driving laser intensity.  $|x_n(\omega, I)|$  is the amplitude and  $\phi_{xuv}^n(\omega, I)$  is the phase, which is given by the action along the path (see Equation 1.21);  $\det(S'')$  is the determinant of the  $2 \times 2$  matrix of the second derivatives of  $\varphi_{xuv}(\mathbf{p}, t, t_i)$  with respect to  $t$  and  $t_i$ . In Equation 1.29, the sum extends over all quantum orbits satisfying the saddle point equations 1.25 - 1.27. However, the main contributions are given by  $n = 1, 2$ , i.e. the short and long trajectories. This is because for bigger excursion times  $\tau = t - t_i$ , the electron wave packet spreads more ( $\tau^{-3/2}$ ) as indicated in Equation 1.29.

For a given laser intensity  $I$ , different harmonic orders correspond to different return kinetic energies and thus to different electron trajectories (and emission times) within a laser cycle (see Figure 1.6). The first derivative  $\frac{\partial \phi_{xuv}^n(\omega)}{\partial \omega}$ , which is the group delay, is equal to the real part of the recombination time  $t$  of the trajectory corresponding to the emission of the considered harmonic, also called emission time  $t_e$  see section 1.5. Around the center of the leading and the falling edges,  $t_e$  is a linear function of the harmonic energy. This corresponds to a constant Group Delay Dispersion (GDD), or chirp in the temporal domain. This GDD is called the attochirp ( $\Delta t_e$ ). Short trajectories have positive, while long trajectories have negative chirp. Therefore, the attosecond pulse constructed by the emitted harmonics is intrinsically not Fourier limited [71].

It worth to note that the phase  $\phi_{xuv}^n(\omega, I)$  depends on the intensity  $I$  as well, which varies almost linearly with intensity with a slope in the plateau region [72]

$$-\alpha_n(\omega) = \frac{\partial \phi_{xuv}^n(\omega)}{\partial I} \quad (1.30)$$

where  $\alpha_n(\omega)$  is the trajectory dependent coefficient.

The harmonic generation by a driving laser that has an envelop of many cycle pulses induces a change in time (from a cycle to the next) of the relevant electron trajectories in order to maintain the same return kinetic energy (and thus the emitted XUV photon energy). The phase within the harmonic order (harmonic phase), given by the action along these different electron trajectories, is thus temporally modulated. This consequently produces another chirp - harmonic chirp. At constant laser intensity, there is no harmonic chirp [72].

Both chirps always present together during the process of High order Harmonic Generation. However, the harmonic chirp is in the time scale of the laser envelop, while the attochirp is with half optical period (half laser cycle).

### Ammosov-Delone-Krainov (ADK) model

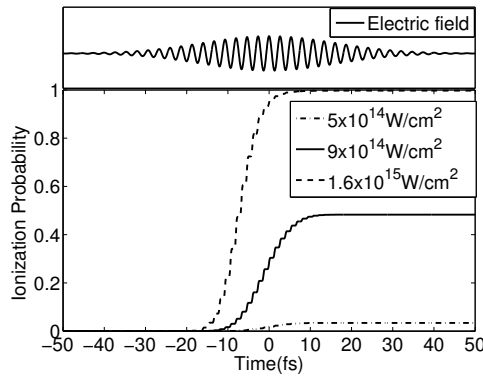


Figure 1.7: ADK calculation of the ionization probability for neon: electric field (top) , ionization probability for various generation intensities (bottom).

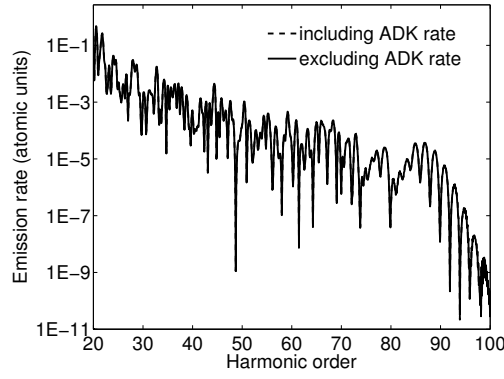


Figure 1.8: Single atom harmonic emission rate calculated by Lewenstein model. Parameters used in the calculations: laser wavelength  $744\text{nm}$ ; pulse duration  $6\text{fs}$ ; intensity  $6.2 \times 10^{14}\text{W/cm}^2$ ; neon gas.

In the experiments, the ionization cannot be ignored and ionization rate is usually high especially in the strong field regime. Therefore the second assumption ii) of section 1.3 has to be corrected in order to correctly describe HHG. The single atom response (eq. 1.22) can be written by taking the ionization rate into account. Here we take the Lewenstein integral as an example:

$$d(t) = i \int_{-\infty}^t dt_i \left[ \frac{\pi}{\epsilon + i(t-t_i)/2} \right]^{3/2} \mathbf{E}(t_i) d_x[\mathbf{p}_{st} + \mathbf{A}(t_i)] \exp[-iS_{st}(\mathbf{p}, t, t_i)] d_x^*[\mathbf{p}_{st} + \mathbf{A}(t)] \\ \times \exp\left[-\int_{-\infty}^t w(t_i) dt_i\right] + c.c. \quad (1.31)$$

The ionization rate  $w(t)$  in Equation 1.31 can be calculated using the Ammosov-Delone-Krainov (ADK) model [13][73].

$$w(t) = \omega_s |C_{n^*l^*}|^2 G_{lm}(4\omega_s/\omega_t)^{2n^*-|m|-1} \exp(4\omega_s/3\omega_t) \quad (1.32)$$

where  $\omega_s = I_p/\hbar$ ,  $\omega_t = e |\mathbf{E}(t)| / \sqrt{2m_e I_p}$ ,  $|C_{n^*l^*}|^2 = 2^{2n^*} / [n^* \Gamma(n^* + l^* + 1) \Gamma(n^* - l^*)]$ ,  $G_{lm} = (2l+1)(l+|m|)! / [2^{|m|} |m|!(l-|m|)!]$ ,  $n^* = Z/\sqrt{I_{p0}/I_p}$  is the effective principle quantum number,  $I_{p0}$  is the ionization potential of hydrogen atom,  $Z$  is the nuclear charge,  $l$  and  $m$  indicate the azimuthal quantum number and magnetic quantum number, respectively.  $l^*$  is the effective azimuthal quantum number, which is equal to 0 when  $l \ll n$ , otherwise  $l^* = n^* - 1$ .

Once the rate is known, the ionization probability is calculated as:

$$P(t) = 1 - \exp\left(\int_{-\infty}^t -w(t') dt'\right) \quad (1.33)$$

Figure 1.7 shows the calculation of the ionization probability by using ADK model. With increasing driving intensity, the depletion effect of the ground state becomes increasingly obvious. Therefore, the ionization cannot be ignored at high intensity. Now we can calculate the time dependent dipole  $d(t)$  by Equation 1.31 and the harmonic dipole  $d(\omega)$  by

Equation 1.19. The harmonic spectrum can be obtained from the Fourier transform of the dipole acceleration, which will be discussed later in the next section. Here, we would like to introduce the harmonic emission rate that is obtained by Milošević et al. [74] in order to check our SFA calculation to Sansone et al. [69]

$$\Gamma_{xuv}(\omega) \propto \omega^3 |d(\omega)|^2 \quad (1.34)$$

Figure 1.8 shows the harmonic emission rate of single atom response in neon gas for a 6 fs, 744 nm laser pulse and an intensity of  $I = 6.2 \times 10^{14} \text{ W/cm}^2$  both for including and excluding ADK rate. Two calculations give similar results, meaning that the ionization is negligible in these experimental conditions. Especially, our simulation is comparable to that of Sansone et al. [69] using the same parameters. As we can see, there is a broad plateau ending at harmonic order 85 in the spectrum. In the cutoff, the emission rate decreases exponentially.

### Calculating the XUV spectrum - different dipole operator

The harmonic emission can be calculated from the Fourier transform of the dipole acceleration:

$$\epsilon_{xuv}(\omega) = \mathcal{F}_{t \rightarrow \omega} [\langle \psi(\mathbf{r}, t) | \hat{\mathbf{a}} | \psi(\mathbf{r}, t) \rangle] \quad (1.35)$$

Via Ehrenfest theorem, the dipole acceleration operator can be replaced by different forms of operators, i.e. velocity form  $\hat{\mathbf{p}}$  and length form  $\hat{\mathbf{r}}$ . Depending on the selection, the harmonic spectrum can be written as:

$$\epsilon_{xuv}(\omega) = \mathcal{F}_{t \rightarrow \omega} \left[ \frac{d}{dt} \langle \psi(\mathbf{r}, t) | \hat{\mathbf{p}} | \psi(\mathbf{r}, t) \rangle \right] = i\omega \mathcal{F}_{t \rightarrow \omega} [\langle \psi(\mathbf{r}, t) | \hat{\mathbf{p}} | \psi(\mathbf{r}, t) \rangle] \quad (1.36)$$

$$\epsilon_{xuv}(\omega) = \mathcal{F}_{t \rightarrow \omega} \left[ \frac{d^2}{dt^2} \langle \psi(\mathbf{r}, t) | \hat{\mathbf{r}} | \psi(\mathbf{r}, t) \rangle \right] = -\omega^2 \mathcal{F}_{t \rightarrow \omega} [\langle \psi(\mathbf{r}, t) | \hat{\mathbf{r}} | \psi(\mathbf{r}, t) \rangle] \quad (1.37)$$

The resulting harmonic yield should be identical if  $\psi(t)$  is the exact wave function. However, due to the different approximations that we made during the calculation, Equation 1.36 and 1.37 are not equivalent any more, and the results vary with the dipole form. There is a long debate of which form is the best choice. Many studies have investigated which combination of gauge and dipole form is more efficient and precise. (Han et al. [75], Bandrauk et al. [76]) The discussion in above sections is in length form, including Lewenstein's original paper [15]. Gordon et al. [77] claims that the length form should be preferred whereas Chirilă et al. [78] are supporting the velocity form. Concerning the comparison with the macroscopic harmonic field Baggesen et al. [79] claims that the velocity form should be the reference.

## 1.4 Propagation effects

So far we have discussed the single atom/molecule response, however the HHG results from the emission of a macroscopic sample so one should consider the propagation of the



laser pulse and high harmonic in the gas medium (Antoine et al.[80] and Ruchon et al. [81]). The traveling equation for light in the medium can be obtained from the Maxwell's equations. In cylindrical coordinates, based on the usual symmetry of the system, the population equation reads:

$$\nabla^2 \mathbf{E}(\mathbf{r}, \mathbf{z}, t) - \frac{1}{c^2} \frac{\partial^2 \mathbf{E}(\mathbf{r}, \mathbf{z}, t)}{\partial t^2} = \mu_0 \frac{\partial^2 \mathbf{P}(\mathbf{r}, \mathbf{z}, t)}{\partial t^2} \quad (1.38)$$

where  $\mathbf{E}(\mathbf{r}, \mathbf{z}, t)$  is the electric field,  $\mathbf{P}(\mathbf{r}, \mathbf{z}, t)$  is the electronic polarization and  $\mu_0$  is the permeability of free space. The fundamental driving laser field and the generated high harmonics have quite different response to the medium. Their propagation effects can be calculated by the decoupled equations [68][82][83]:

$$\nabla^2 \mathbf{E}_L(\mathbf{r}, \mathbf{z}, t) - \frac{1}{c^2} \frac{\partial^2 \mathbf{E}_L(\mathbf{r}, \mathbf{z}, t)}{\partial t^2} = \frac{\Omega_p}{c^2} \mathbf{E}_L(\mathbf{r}, \mathbf{z}, t) \quad (1.39)$$

$$\nabla^2 \mathbf{E}_H(\mathbf{r}, \mathbf{z}, t) - \frac{1}{c^2} \frac{\partial^2 \mathbf{E}_H(\mathbf{r}, \mathbf{z}, t)}{\partial t^2} = \mu_0 \frac{\partial^2 \mathbf{P}_{NL}(\mathbf{r}, \mathbf{z}, t)}{\partial t^2} \quad (1.40)$$

where  $\mathbf{E}_L(\mathbf{r}, \mathbf{z}, t)$  and  $\mathbf{E}_H(\mathbf{r}, \mathbf{z}, t)$  represent the electric field of the laser and of the high order harmonics, respectively.  $\Omega_p = e\sqrt{\frac{n_e(\mathbf{r}, \mathbf{z}, t)}{m\epsilon_0}}$  is the plasma frequency. The free electron density  $n_e(\mathbf{r}, \mathbf{z}, t) = n_0 \left[ 1 - \exp\left(-\int_{-\infty}^t \omega(t')t'\right) \right]$ , with  $n_0$  is the neutral atom density.  $\mathbf{P}_{NL} = [n_0 - n_e(\mathbf{r}, \mathbf{z}, t)]d(\mathbf{r}, \mathbf{z}, t)$  is the nonlinear polarization generated by the gas, where  $d(\mathbf{r}, \mathbf{z}, t)$  can be obtained by Equation 1.31.

Equation 1.39 takes into account both temporal plasma-induced phase modulation and spatial plasma lensing effect on the driving laser, while it does not consider the linear gas dispersion and the depletion of the fundamental beam during the HHG process, which is valid at low gas pressure and low generating laser intensity. Equation 1.40 neglects the free electron dispersion because the plasma frequency is much lower than that of high harmonics. For the sake of simplicity, we move the coordinate ( $z' = z$  and  $t' = t - z/c$ ) and assume the field is emitted close to the propagation axis (paraxial approximation). Numerically solving these equations is generally carried out in the frequency domain by Fourier transforming the two sides of the equations:

$$\nabla_{\perp}^2 \tilde{\mathbf{E}}_L(\mathbf{r}, \mathbf{z}', \omega) - \frac{2i\omega}{c} \frac{\partial \tilde{\mathbf{E}}_L(\mathbf{r}, \mathbf{z}', \omega)}{\partial z'} = \tilde{\mathbf{G}}(\mathbf{r}, \mathbf{z}', \omega) \quad (1.41)$$

$$\nabla_{\perp}^2 \tilde{\mathbf{E}}_H(\mathbf{r}, \mathbf{z}', \omega) - \frac{2i\omega}{c} \frac{\partial \tilde{\mathbf{E}}_H(\mathbf{r}, \mathbf{z}', \omega)}{\partial z'} = -\omega^2 \mu_0 \tilde{\mathbf{P}}_{NL}(\mathbf{r}, \mathbf{z}', \omega) \quad (1.42)$$

with  $\tilde{\mathbf{E}}_L, \tilde{\mathbf{E}}_H, \tilde{\mathbf{G}}$  and  $\tilde{\mathbf{P}}_{NL}$  being the Fourier transform of  $\mathbf{E}_L, \mathbf{E}_H, \frac{\Omega_p}{c^2} \mathbf{E}_L, \mathbf{P}_{NL}$ . L'Huillier et al. [84] gave the solution of Equation 1.42 with a nonlinear polarization source  $\mathbf{P}_{NL}$ :

$$\mathbf{E}_H(\mathbf{r}', \omega) \propto \sum_n \int \frac{e^{ik(\omega)|\mathbf{r}'-\mathbf{r}|}}{|\mathbf{r}'-\mathbf{r}|} n(\mathbf{r}) |x_n(\omega, I(\mathbf{r}))| \exp[i\phi_{xuv}^n(\omega, I(\mathbf{r}))] d^3\mathbf{r} \quad (1.43)$$

The most important barrier for attosecond science as an emerging field is the low flux that can be generated particularly at shorter wavelengths. To enhance the high harmonic conversion efficiency from the driving laser, it is important to make sure that constructive interference can be obtained in the forward direction, which means that the phase difference

between newly generated field  $\epsilon_{xuv}(\omega, I(\mathbf{r}))$  and the propagated field  $E_{xuv}(\omega, \mathbf{r})$  is as small as possible. This requires good phase matching conditions, different from the case of low order harmonic generation because of an additional factor (Balcou et al. [85] and Salières et al. [86]):

$$\mathbf{k}_q = q\mathbf{k}_L + \vec{\nabla} \phi_{xuv}^n(q, I(\mathbf{r})) \quad (1.44)$$

where  $q$  is the harmonic order,  $\mathbf{k}_q$  and  $\mathbf{k}_L$  are the wavenumber vectors of the harmonic and laser field, respectively. And the last factor is the spatial phase mismatch of the harmonic dipole response  $\vec{\nabla} \phi_{xuv}^n(q, I(\mathbf{r})) = -\alpha_n(q) \vec{\nabla} I(\mathbf{r})$ .  $\alpha_n(q)$  is the trajectory dependent coefficient that was introduced in Equation 1.30. Minimization of the phase mismatch in HHG has been studied extensively [87][88][89][90][91]. For increasing  $n$ , it gets bigger and bigger so that phase matching condition is difficult to reach. That is why we only consider short and long trajectories in the macroscopic signal.

Besides the dipole phase, there are three other essential contributions to the phase mismatch along the laser propagation that affect the wave vectors [92]: i) the geometrical phase mismatch (Gouy phase shift which produces  $\pi$  phase difference through the laser focus [93]), ii) the neutral gas dispersion phase mismatch and iii) the plasma dispersion phase mismatch. The phase matching of HHG can be achieved by balancing the various terms for a zero phase mismatch. The relative importance of these terms depends on the geometry of HHG. Salières et al. [94] find that when the laser is focused sufficiently before the generating medium, the harmonic phase variation is minimal on axis, which is due to the dipole phase compensating the phase mismatch caused by the other terms. This is true for the short trajectories that therefore give the dominant contribution to HHG. On the other hand, when the laser is focused after the medium, efficient phase matching for the long trajectories can be obtained off-axis. Once we reach good phase matching conditions, the macroscopic signal can be treated as a replica of the single atom/molecule response, which is supported by theoretical investigations (Ruchon et al. [95]) and numerous experimental results [72][96][97][98][99].

## 1.5 Time profile of the XUV emission

As discussed above, in specific conditions phase matching can retain one of the classes of quantum paths that contribute to HHG. In this thesis, all the studies are done in the experimental conditions that optimize only the short trajectories, leading to the simplification of eq. 1.28 for the harmonic dipole to  $d(\omega, I) = |x(\omega, I)| \exp[i\phi_{xuv}(\omega, I)]$ . For atoms, the phase of the recombination dipole moment varies slowly, so the main variation comes from  $\phi_{xuv}(\omega, I)$ . By using Equations 1.21 and 1.25 - 1.27, we obtain (Mairesse et al. [96]):

$$\frac{d\phi_{XUV}}{d\omega} = \underbrace{\frac{\partial\phi_{XUV}}{\partial\omega}}_{=t_r} + \underbrace{\frac{\partial\phi_{XUV}}{\partial t_i}}_{=0} \frac{\partial t_i}{\partial\omega} + \underbrace{\nabla_p \phi_{XUV}}_{=0} \frac{\partial p}{\partial\omega} + \underbrace{\frac{\partial\phi_{XUV}}{\partial t_r}}_{=0} \frac{\partial t_r}{\partial\omega} = t_r. \quad (1.45)$$

As a result, the group delay of the emitted XUV wave packet is equivalent to the recombination time  $t_r$ . Fourier limited pulse duration can be achieved if the group delay dispersion is 0, meaning that all harmonics should be emitted at the same time. Figure 1.6 shows that this is the case only for harmonics in the cutoff region where the generation efficiency drops exponentially, preventing the generation of really short attosecond pulses. In the plateau, the recombination time depends almost linearly on the harmonic order so that the emitted XUV wave packet is chirped. The positive group delay dispersion ( $\text{chirp} > 0$ ) results in a red shifted instantaneous frequency on the leading edge and blue shifted on the falling edge. The effect of negative GDD ( $\text{chirp} < 0$ ) is inverse. Short trajectories have positive, while long trajectories have negative chirp.

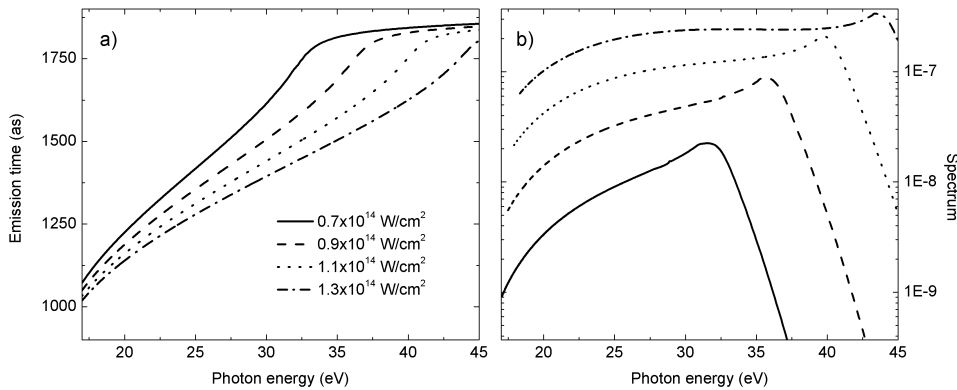


Figure 1.9: Short trajectory emission times (or group delays) a) and harmonic intensity b) as a function of photon energy for different laser intensities. The calculations were done for argon, with an  $I_p = 15.58$ . The center wavelength of the generating laser is at  $800\text{nm}$  [71].

The recombination time depends on the driving laser intensity, which leads to a direct influence on the attosecond generation. An example for this is shown in Figure 1.9: The GDD of the XUV emission, i.e. the slope of the group delay in the region before the cut-off, is inversely proportional to the laser intensity. At the same time, the cut-off position increases.

In the above considerations, a temporally constant laser intensity has always been assumed. In the experiments, the intensity variation in the envelope results in amplitude and phase changes in the XUV bursts at each half cycle of the laser, leading to features of the XUV emission on the femtosecond scale as well. Roughly, the attosecond XUV bursts, produced in each laser half-cycle, will vary according to the varying intensity envelope as already discussed in section 1.3. This thesis, however, will be concerned with the sub-laser-cycle structure of the XUV emission. The measurements are an average over the optical cycles with varying amplitude.

## 1.6 Isolated attosecond pulse generation: towards to attosecond pump/probe scheme

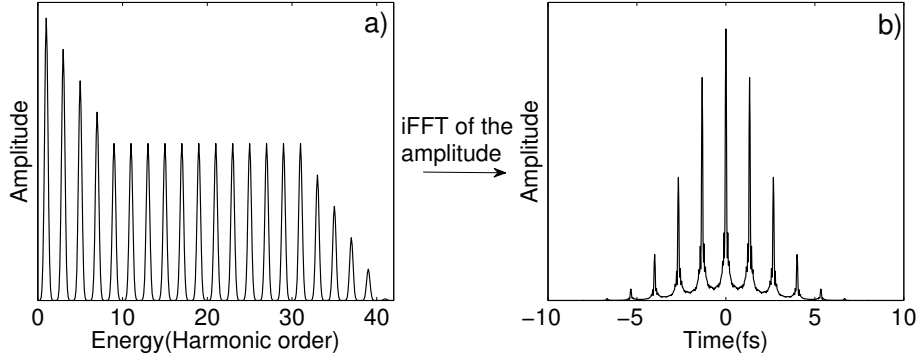


Figure 1.10: Time versus Frequency Domain. a) Schematic HHG spectrum, b) corresponding attosecond pulse train in the case of a Fourier-limited emission.

All the discussion above is based on the use of long driving pulses, i.e. many cycles of laser oscillation, in which case HHG is a periodical process that happens coherently within each half cycle of oscillation ( $T_0/2$ ), leading to the emission of an attosecond pulse train. A typical harmonic spectrum generated by a multi-cycle driving pulse is presented in Figure 1.10 a), only discrete harmonics spaced by two fundamental photon energies are generated ( $2\pi/T_0/2 = 2\omega_0$ ). The frequency spacing combined with inversion symmetry considerations imply that only odd harmonics of the fundamental laser frequency  $\omega_0$  are observed. At the photon energies corresponding to even harmonics destructive interference occurs between the emission from subsequent half cycles. Such a spectrum corresponds to a train of attosecond pulses that emitted at each half cycle of the driving laser field in the case of Fourier-transform-limited emission (see Figure 1.10). Antoine et al. [100] found that the duration of the generated pulses ( $\tau_{xuv}$ ) is proportional to the fundamental laser period ( $T_0$ ) and inversely proportional to the number of phase locked harmonics ( $N$ ):  $\tau_{xuv} \simeq \frac{T_0}{2N}$ . However, due to the intrinsic chirp of HHG, the phase between harmonics may not be locked, the attosecond pulses may be broadened.

Attosecond pulse trains are useful in attosecond spectroscopy for probing ultrafast processes occurring with the same periodicity ( $T_0/2$ ), such as those induced by the strong laser field (Schafer et al. [101] and Johnsson et al. [102]). However, for the general case of attosecond pump/probe spectroscopy, the generation of intense isolated attosecond pulses is required [9][103][8]. In order to generate a single attosecond pulse in the time domain, we have to obtain a continuum spectrum instead of discrete peaks in the spectrum domain. The width of the harmonic is defined by the envelop of the driving pulse, so reducing the number of optical cycles in the driving field will increase the width of each peak, meaning

pulse compression technique has to be performed [104]. But it is very difficult to make the driving pulse duration close to half of an optical cycle even by using post compression, which is the requirement to generate super continuum spectrum. Thanks to the intensity dependent process of HHG, the highest orders in the cutoff region are generated only by the center cycles of the driving laser, while the lower orders in the plateau are generated by the pre and post cycles. Thus, if we can select only a single cycle to contribute to the generation of the cutoff region, the super continuum is obtained by filtering out the harmonics in the plateau region. This pulse selection can be done by using optical gating methods. Finally, controlling the carrier envelop phase (CEP) is also crucial for the isolated attosecond pulse generation since it influences how many peaks within the optical gate [105]. This section will detail the developments performed together with the laser team on the laser systems in CEA-Saclay towards intense single attosecond pulse generation.

### 1.6.1 Post pulse compression

In order to achieve shorter pulse in time, the spectrum has to be broader. Thus the principle of pulse compression is to induce spectral bandwidth broadening first by a nonlinear laser-matter interaction effect called self phase modulation (SPM) [106]. However, SPM produces positive chirp so that subsequent dispersive compression has to be done by using optical devices with negative Group Delay Dispersion.

There are many successful techniques proposed to broaden the spectrum, e.g. by using self-guided filament [107], hollow core fiber [108][109][110] or fast gas ionization in a capillary [111]. The spectral broadening by using a gas-filled hollow core fiber has proved its stability over almost two decades. It has been well developed and used to generate few-optical-cycle pulses at a submillijoule [112][113] or even multimillijoule energy [114][115][116][117] combining with chirped-mirror pairs as the dispersive compression devices. The choice of the rare gas filling provides us some freedom for the nonlinearity. Moreover, the control of the gas pressure offers the possibility to linear tune the nonlinearity. Therefore, we are going to concentrate on this method for the post-compression of the driving laser pulse duration.

#### Mode coupling

The propagation of light in the hollow core fiber can be thought of as grazing incidence reflections at the inner surface of the core. The transmission of higher order mode is greatly suppressed due to their big losses. As a result, only the lowest loss mode can propagate through a sufficiently long fiber, which is the fundamental hybrid mode  $EH_{11}$  [110]:

$$I(r) = I_0 \cdot J_0^2\left(2.405 \frac{r}{a}\right) \quad (1.46)$$

where  $r$  is the radial coordinate,  $I_0$  the peak intensity,  $J_0(r)$  is the zero order Bessel function and  $a$  the inner core radius. Nisoli et al. [110] calculated that the most efficient coupling

between a Gaussian beam and the  $EH_{11}$  mode can be achieved when the ratio of the  $1/e^2$  radius in the focal plane (Gaussian beam waist) and the radius of the inner core of the fiber are related by  $w_0/a = 0.65$ .

### Nonlinear propagation and spectral broadening

The electric field of the mode propagating in the hollow fiber can be written as [118]:

$$E(\mathbf{r}, \omega) = F(x, y)A(z, \omega)\exp[i\beta(\omega)z] \quad (1.47)$$

with  $z$  being the laser propagation direction,  $F(x, y)$  accounts for the transverse mode distribution,  $A(z, \omega)$  is the amplitude of the mode and  $\beta(\omega)$  is the propagation constant. In the first-order perturbation theory, the modal distribution is not affected by the nonlinear perturbation of the refractive index ( $\Delta n = n_2 |E|^2$ ) [110] with  $n_2$  being the nonlinear index coefficient. Thus, the Equation 1.47 can be simplified to a one spatial dimension quantity problem after integration over the transverse coordinates. If  $A(z, \omega)$  is known, the time propagation of the mode amplitude through the fiber  $A(z, t)$  can be obtained from its inverse Fourier transform. By using the retarded frame  $T = t - z/v_g$ , where  $v_g$  is the group velocity of the pulse, and normalized amplitude  $U(z, T) = A(z, T)/\sqrt{P_0}$ , where  $P_0$  is the pulse peak power, the Maxwell equation for describing the propagation of optical pulses through the fiber can be written as [119]:

$$\frac{\partial U}{\partial z} + \frac{\alpha}{2}U + \frac{i}{2}\beta_2 \frac{\partial^2 U}{\partial T^2} - \frac{1}{6}\beta_3 \frac{\partial^3 U}{\partial T^3} = i\gamma P_0 \left[ |U|^2 U + \frac{i}{\omega_0} \frac{\partial}{\partial T} (|U|^2 U) \right] \quad (1.48)$$

with  $\alpha/2$  being the field attenuation factor [120]:

$$\frac{\alpha}{2} = \left( \frac{2.405}{2\pi} \right)^2 \frac{\lambda_0^2}{2a^3} \frac{\nu^2 + 1}{\sqrt{\nu^2 - 1}} \quad (1.49)$$

$\lambda_0 = 2\pi c/\omega_0$  is the laser wavelength in the gas and  $\nu$  is the ratio between the refractive indices of the fiber (fused silica) and propagation (gas) media. Moreover, the group velocity dispersion (GVD) and the third order dispersion correspond to

$$\beta_n = \left( \frac{d^n \beta}{d\omega^n} \right)_{\omega=\omega_0}, \quad (n = 2, 3) \quad (1.50)$$

Eventually, the nonlinear coefficient  $\gamma$  in Equation 1.48 is given by

$$\gamma = \frac{n_2 \omega_0}{c A_{eff}} \quad (1.51)$$

where  $A_{eff} \simeq 0.48\pi a^2$  is the effective mode area. The first term in the squared bracket of Equation 1.48 is related to the SPM process, the second one describes self-steepening, which leads to an asymmetry in the SPM-broadened spectra.

Vozzi et al. [119] performed the integration of the propagation equation 1.48 with the split-step Fourier method in which time derivatives are evaluated in the frequency domain

accessed with a fast-Fourier-transform algorithm. By assuming an input normalized field amplitude of the form:

$$U(0, T) = \exp\left(-\frac{T^2}{2T_0^2}\right) \quad (1.52)$$

The output field amplitude for a gas-filled fiber with length  $L$  is given by

$$A(L, T) = \exp\left(-\frac{\alpha}{2} - \frac{T^2}{2T_0^2} + i\varphi_m e^{-T^2/T_0^2}\right) \quad (1.53)$$

where  $\varphi_m = \gamma P_0 L_{eff}$  is the maximum phase shift and  $L_{eff} = [1 - \exp(-\alpha L)]/\alpha$ . A simple version of the broadening factor can be written as the ratio of the broadened spectral width  $\Delta\omega$  with the initial width  $\Delta\omega_0$  [119]:

$$F_b = \frac{\Delta\omega}{\Delta\omega_0} = \left(1 + \frac{4}{3\sqrt{3}}\varphi_m^2\right)^{1/2} \quad (1.54)$$

In principle, increasing one or many factors ( $\gamma, P_0, L_{eff}$ ) of the maximal phase shift  $\varphi_m$  produces a bigger broadening factor. However, there is always a compromise between an efficient spectral broadening and a good transmission efficiency. The nonlinear coefficient  $\gamma$  can be increased by using a fiber with a smaller core diameter, but the attenuation factor is increased in the same time which reduces the transmission of the coupling field.  $P_0$  can be increased by enhancing the intensity at the entrance of the fiber, but it induces ionization of the medium which reduces the laser coupling in the fiber. And the effective length  $L_{eff}$  can be increased by using a longer fiber, but the transmission of the laser field is also reduced. Therefore, to design a proper scheme of post-compression for specific laser system that has a sufficient broadening factor as well as a transmission rate is desired.

### Setup design

Although spectral broadening by self-phase modulation in a gas filled hollow core fiber is widely used, a broad spectrum with a high output flux ( $> 1mJ$ ) is still difficult to obtain. We are highly interested in coupling high input energy ( $4 - 5mJ$ ) combined with high energy transmission. In order to avoid the ionization at the entrance of the fiber, we use neon gas as the filling in the hollow core because its relative high ionization potential ( $21.6eV$ ), and the diameter of the fiber core is selected to be big. In addition, we also design a pressure gradient scheme [115][116][121], which has a small pressure in the fiber entrance and the pressure goes up gradually to the end of the fiber. In this way, the ionization in the entrance is highly reduced while still keeping efficient spectral broadening.

The setup is presented in Figure 1.11. A part of the energy from PLFA system (Laser facility used for the experiments, which will be presented in details in Chapter 2) is focused by a  $3m$  focal lens to the fiber entrance with a beam waist ( $1/e^2$ ) of  $\sim 160\mu m$  in order to achieve good coupling efficiency for the  $EH_{11}$  mode. The vacuum tube for holding the hollow core fiber is  $\sim 5m$  long, and the entrance window is set close to the lens for preventing material damage. The fiber is  $\sim 1.2m$  long with a  $500\mu m$  inner core diameter. The vacuum

tube is divided into two sections. The gas, which is provided from the optical-output side, flows through the fiber and is pumped away at the optical-input side of the hollow fiber. The neon pressure at the optical-end side is adjustable, while the optical input side is maintained under low pressure. The transmitted beam is divergent, which is collimated by a concave mirror. The positive chirp is then compensated by reflection on chirped mirror pairs.

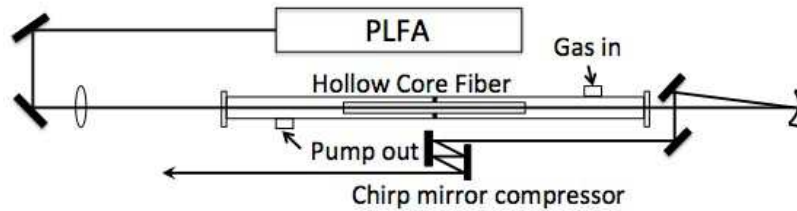


Figure 1.11: Schematic diagram of the pulse compression setup using the pressure gradient method. The gas is injected through the exit end of the optical fiber, and is pumped away at the entry end.

### Experimental results

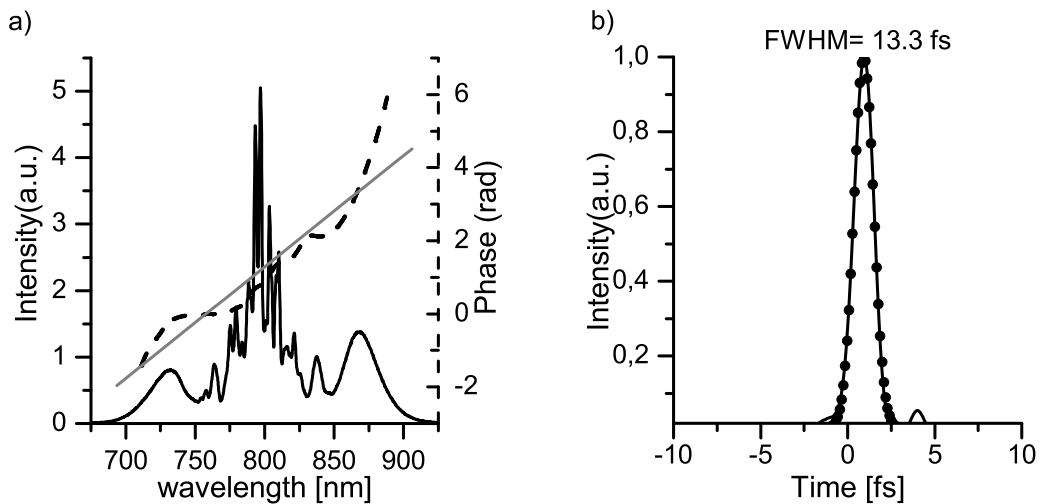


Figure 1.12: a) Broadened pulse spectrum obtained with 4mJ, 45fs input pulse in Neon at 2.2bar (black solid line) and spectral phase retrieved by SPIDER (black dash line). The gray line is a linear fit of the phase. b) Pulse temporal profile (solid line) and its Gaussian fit with FWHM=13.3fs (black dots).

Figure 1.12 shows the experimental results. The input laser pulse has an energy of 4mJ and a pulse duration of 45 fs. The pressure at the fiber entrance is  $\sim 10^3$  mbar and gradually increases to 2.2bar until the end of the fiber. The output laser pulse is characterized by



SPIDER after the compensation of chirp mirror pairs. We routinely generate  $1.6\text{mJ}$  pulses after 24 bounces of chirp mirrors with a total GDD of  $\sim 480\text{fs}^2$ . The spectrum and the phase are presented in a). The reconstructed laser pulse is showed by solid line in b) and the pulse duration is  $13.3\text{fs}$  from the gaussian fit.

Although the results are good, it is not ready to use it for generating harmonics because of the instability of the beam pointing. The new design of the fiber mounting as well as the development of the beam pointing stabilization system is under developing by the laser team. Also, the quality of the fiber was not realistic. The fiber with a flat core is still difficult to be produced. The maximum coupling efficiency is only about 80%. Recently, I have tested the new fibers, which provides  $\sim 95\%$  transmission efficiency for HeNe laser seed. Therefore, a reliable post-compression scheme will be achieved soon.

### 1.6.2 Optical gating technique

The pulse duration of our PLFA laser system is around  $45\text{fs}$  and  $\sim 13\text{fs}$  after pulse compression, which is still too long to generate isolated attosecond pulses. Thus, additional gating method is required. Two Color Gating (TCG), a method based on breaking the medium symmetry by using a mixing of a fundamental  $800\text{nm}$  laser field and a second laser field of different wavelength, indeed broadens the harmonics but do not guarantee an isolated attosecond pulse generation for “long” driving pulses. Many theoretical proposals in this scheme such as using of a very strong detuned second harmonic [122] or adding mid-infrared beam as the second color [123], are relatively difficult to implement in the experiments. Another gating technique is called Polarization Gating (PG), which is based on the confinement of the harmonic generation within a temporal gate. This is done by two counter-circularly polarized laser pulses that are delayed in time [26]. Harmonic generation is efficient only close to the linear polarization: when the ellipticity of the generating laser increases, the harmonic efficiency drops quickly [124]. This is because the perpendicular component of the field would drive the electrons sideways, so that they miss the core at return. Thus only the linearly polarized part in the middle of the combined field contributes to HHG. However, the driving pulse duration for PG has to be as short as  $\sim 5\text{fs}$  due to the depletion of the ground state. This is because the long leading edge of the relative long pulse fully ionizes the medium, which cause no atoms or molecules left for the center pulse to generate harmonics. Thus it is impractical for our setup. Therefore, Chang et al. proposed a method combining both TCG and PG in order to overcome their limitations, which is called Double Optical Gating (DOG) [125]. Thanks to the second harmonic that breaks the symmetry of the medium, the effective gating width can be increased by a factor of 2 as compared to the original PG, which loses the requirement on the driving pulse duration by a factor of  $\sim 2$  [125]. Later, Feng from Chang’s group pushed this idea further by controlling the ellipticity of the polarized field and experimentally generated single at-

tosecond pulses by using driving pulse durations as long as  $20 - 28fs$  [126], a method called Generalized Double Optical Gating (GDOG). Another technique called Interferometric Polarization Gating (IPG) shares the same idea but has more freedom of loosening the limitation of the pulse duration by flexibly controlling the ellipticity since the usage of the interferometer [127]. However, it has two shortcomings: i) it is delicate to stabilize the interferometer and ii) half of the energy is lost in the setup so that very energetic pulses are needed to generate intense attosecond pulses. Therefore, it turns out that Generalized Double Optical Gating is the most realistic way for us in the current setup since it is successfully working for “long” pulses. Furthermore, it uses a collinear alignment that has many advantages, i.e. easy to implement, less expensive and more energy efficient.

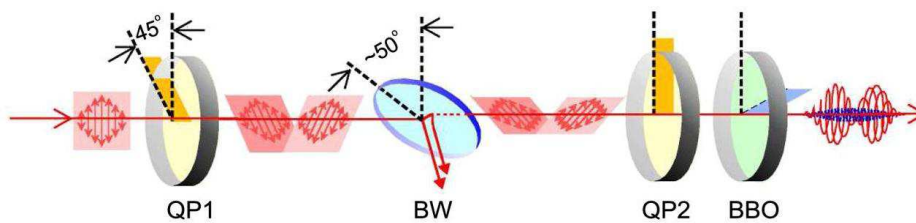


Figure 1.13: The GDOG setup (taken from [126]).

The setup is given in Figure 1.13, and only consists in 4 optics. The first quartz plate must be a full order multi-order waveplate (QP1) to ensure the driving field of DOG is parallel to the input polarization. Its optical axis oriented at 45 degrees with respect to the input polarization, which introduces a delay between the pulses propagating along the ordinary and extra-ordinary axis of the crystal. Then a Brewster Window (BW) reflects part of the polarization component parallel to the input laser polarization away in order to decrease the ellipticity ( $\epsilon$ ). A second quartz plate (QP2) combined with a BBO crystal together act as a zero-order quarter wave plate in order to form the circular-linear-circular polarization gate. Moreover, the BBO crystal generates the second harmonic field.

The total field after the four optics can be decomposed into orthogonal components as showed in Figure 1.14, the one parallel to the initial polarization direction (the driving field c)) and the one perpendicular to the polarization (the gating field d)). The symmetry of the total driving field is destroyed by adding a weak second harmonic (SH) field (a)) to the fundamental driving field (b)). To make a strong linear electric field in the gate, a big amplitude in the middle of the driving field is necessary, meanwhile keeping the field almost to zero in the middle of the gating field, which can be seen in c) and d). The total field is shown in e).

The physical origin of GDOG working with long pulses is because it shortens the delay between the two pulses, so that the ionization in the leading and trailing edge of the electric

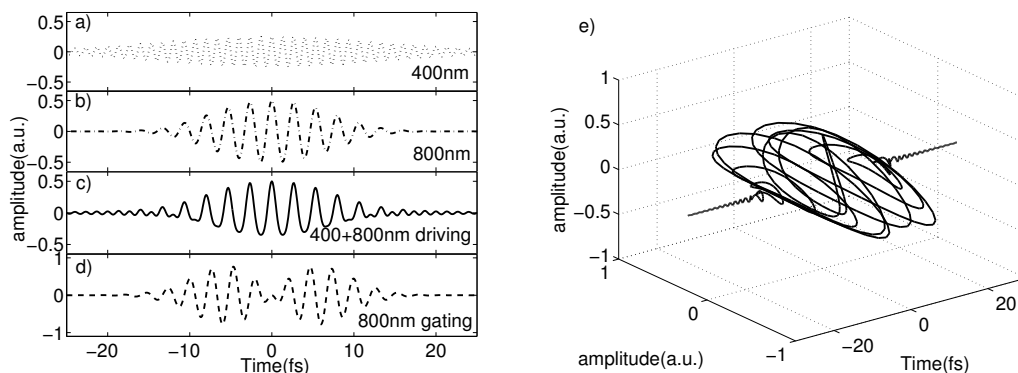


Figure 1.14: Simulation of GDOG field with ellipticity  $\varepsilon = 0.5$ . a) Second Harmonic field, b) Fundamental driving field, c) Driving field with second color, and d) Gating field. e) Total electric field of GDOG.

field is decreased. The gate width  $\delta t_G$  for GDOG is given by the equation:

$$\delta t_G \approx \varepsilon \frac{\tilde{\zeta}_{th} \cdot \tau_p^2}{\ln 2 \cdot T_d} \quad (1.55)$$

where  $\tilde{\zeta}_{th}$  is the threshold ellipticity for harmonic generation,  $\varepsilon$  is the intensity ratio between the driving field (component parallel to the input laser polarization) and gating field (component perpendicular to the input laser polarization),  $\tau_p$  is the pulse duration and  $T_d$  is the time delay between the two pulses. It is obvious that a long pulse duration needs a big time delay between the left and right circularly polarized pulses in order to get a small gate width. That means that the leading and trailing edges are large whereas they do not contribute to the attosecond emission but just deplete the ground state due to ionization. Thus, the idea for generating isolated attosecond pulses by using long pulses is to shorten the time delay between the two pulses. In GDOG, a second color field is used for breaking the symmetry of the laser field. As a result, the gate width for single attosecond pulses can be increased to one optical cycle instead of a half cycle in PG. Moreover, it is possible to decrease the ratio between driving and gating field ( $\varepsilon$ ). All these result in a decreased time delay ( $T_d$ ).

Figure 1.15 shows the ionization probability as a function of the input laser pulse duration for different gating techniques. The calculation uses the Ammosov, Delone, and Krainov (ADK) theory for the ionization of argon atoms [73]. The calculation was done assuming the peak intensity at the center of the gate width was  $2.2 \times 10^{14} \text{ W/cm}^2$ . From the figure, the depletion when using GDOG pulses is greatly reduced even for pulses nearly 25 fs in duration as compared to polarization gating and DOG techniques. Therefore, GDOG can be used even with long pulses. Once the reliable post-compression scheme is achieved, this technique can be used for generating isolated attosecond pulse in PLFA laser system.

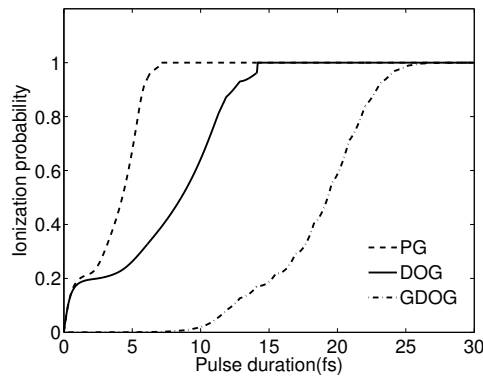


Figure 1.15: Ionization probability as a function of input pulse duration for different gating methods (ADK calculation). The peak intensity at the center of the gate was held constant at  $2.2 \times 10^{14} \text{W/cm}^2$  for all cases. The gate width was half an optical cycle for PG and one full cycle for both DOG and GDOG.

## 1.7 High-order Harmonic Generation from molecules

Molecules have a more complicated electronic structure and the additional degrees of freedom of rotation and vibration as compared to atoms. A basic molecular orbital theory mathematically describes the electronic wave function of a molecule by a linear combination of atomic orbitals (LCAO). Let us first recall how atomic orbitals can be constructed. A simple technique is the Hartree-Fock method, sometimes also called self-consistent-field method. The main assumption behind Hartree-Fock is that each electron moves in an average potential created by the other electrons and the nucleus and that can be expressed as a single charge centered on the nucleus. Then, the  $n$ -electron wavefunction,  $\phi(\mathbf{r}_1, \dots, \mathbf{r}_n)$ , of the atom can be approximated by an antisymmetrized product of one-electron wavefunctions,  $\phi(\mathbf{r}_i)$ , referred to as atomic orbitals. Starting from a basis of one-electron wavefunctions, linear combinations of the basis elements for each one-electron wavefunction are varied and at each step the orbital energy, i.e. expectation value of the single-electron Hamiltonian, is determined. The variation is then continued until the energy is minimal [71]. For molecules, if we take the Born-Oppenheimer approximation [128], the total wavefunction of the molecule can then be factorized into a nuclear and an electronic part. Having split off the nuclear degrees of freedom, one is still concerned with a multi-electronic wavefunction. The next level of approximation is thus again the Hartree-Fock approximation, which allows factorization of the multi-electron wavefunction into single-electronic orbitals. The Hartree-Fock method can then be applied to find molecular orbitals. Computing first the atomic orbitals and then combining these, each centered on their respective nucleus, the energy is minimized for various combinations of atomic orbitals [129]. This is the method we applied Chapter 4 and 5 for the molecular orbitals. The lowest energy level state occupied by electrons, is called highest occupied molecular orbital (HOMO). Counting down

towards occupied orbitals with higher energies, one speaks of (HOMO-1), (HOMO-2), and so forth. The energetically lowest unoccupied molecular orbital is abbreviated (LUMO).

In linear molecules, molecular alignment (controlling the angle between the molecular axis and the laser polarization, which will be detailed in Chapter 2) can alter both the ionization and recombination steps. Experiments have shown the ionization probability of  $N_2$  is  $\sim 4$  times greater for molecules aligned parallel rather than perpendicular to the laser polarization [130]. Additionally, molecules have anisotropic recombination cross-sections, which alters recombination probabilities [131]. Therefore, by using the Strong Field Approximation, the harmonic emission for single molecules can be written as a quantum version of the three-step model [132]:

$$\epsilon_{xuv}(\omega, \theta, I) = \eta \gamma(\omega, \theta, I) a(k, I) \langle \psi_0(\mathbf{r}) | \hat{\mathbf{d}} | \psi_c(\mathbf{r}) \rangle \quad (1.56)$$

where  $\eta$  is the pre-factor coming from the choice of the dipole operator.  $\gamma(\omega, \theta, I)$  is the square root of the tunnel ionization rate for molecules and  $\theta$  is the angle between the molecule and the polarization of the driving laser field.  $a(k, I)$  is a complex number including the gathered phase and the spreading during the excursion of the electron wave packet.  $\langle \psi_0(\mathbf{r}) | \hat{\mathbf{d}} | \psi_c(\mathbf{r}) \rangle$  is the recombination dipole matrix element between the initial bound state  $\psi_0$  and the continuum state  $\psi_c$ .  $\mathbf{k} = \mathbf{p} + \mathbf{A}(t_r)$  is the asymptotic wavenumber vector of the continuum electron and  $\mathbf{k} = (0, 0, k)$  is parallel to the driving laser polarization. The energy conservation at the recombination instant is given as:

$$q\omega_0 = \frac{k^2}{2} + I_p \quad (1.57)$$

where  $q$  is the harmonic order,  $\omega_0$  is the fundamental laser frequency.

The molecular tunnel ionization rate  $\gamma$  consists of two parts.

$$\gamma = w_m T(\theta) \quad (1.58)$$

The first term ( $w_m$ ) can be considered as the part that is not angle dependent, which can be calculated by Equation 1.32. The second term  $T(\theta)$  encodes the geometry of the molecular structure. The group of C.D.Lin extended the tunneling ionization model of Ammosov-Delone-Krainov (ADK) for atoms to molecules by considering the symmetry properties and the asymptotic behavior of the molecular electronic wave function [133][134]. This MO-ADK model aims to generalize the principles introduced in the atomic ADK model. MO-ADK has the same atomic tunneling rates  $w_m$  as the Equation 1.32. To include molecular characteristics, the molecular electronic wavefunctions in the asymptotic region are expressed in terms of summations of spherical harmonics expanded in one-center. The coefficients of the expansion are dependent on the angular momentum and magnetic quantum numbers implying alignment dependency  $T(\theta)$ , with respect to the laser field. Therefore, the orbital symmetry and geometry are inherently involved in  $T(\theta)$ . The limitation of this approach comes from the single-center expansion of the wavefunctions, that would be

problematic for complex, multi-center large molecules. There is another method, developed by R. Murray et al. ([135][136][137]), so called PYMOLION. In this method, the electronic wavefunction is described as the sum of basis functions expanded on multi-centers including the coulombic and higher order potential terms as well. Then the electron is propagated with the Wentzel-Kramers-Brillouin (WKB) method through the potential barrier. These considerations lead to a tunneling rate form as Equation 1.58, with  $w_m$  being the tunneling rate for an  $s$  atomic orbital obtained with ADK and  $T(\theta)$  containing both characteristics of molecular orbital symmetry and interference of the tunneling currents coming from the different lobes of the orbital. This model predicts a laser intensity dependent angular position of the tunnel ionization peak in  $CO_2$  that was confirmed by experiments [138]. Hence, PYMOLION is used throughout this thesis to describe the tunneling rates.

For the last step - recombination, we can rewrite the recombination dipole matrix in length form in order to generalize it to multi-electron systems and in particular to molecules:

$$\mathbf{d}_{rec}(\omega, \theta) = \mathbf{d}^*(\mathbf{p} + \mathbf{A}(t_r)) = \langle \psi_i(\mathbf{r}, \mathbf{R}_i) | \mathbf{r} | \psi_f(\mathbf{r}, \mathbf{R}_f) \rangle, \quad (1.59)$$

where  $\psi_i(\mathbf{r}, \mathbf{R}_i) = \chi_i(\mathbf{R})\phi(\mathbf{r}_1, \dots, \mathbf{r}_j, \dots, \mathbf{r}_N)$  and  $\psi_f(\mathbf{r}, \mathbf{R}) = \chi_f(\mathbf{R})\phi^+(\mathbf{r}_1, \dots, \mathbf{r}_{j-1}, \mathbf{r}_{j+1}, \dots, \mathbf{r}_N)\psi_c(\mathbf{r}_j)$  are the multi-electron wavefunctions for the neutral and the ionized system. The initial state is the product of the nuclear wavefunction  $\chi_i(\mathbf{R})$  and of the  $N$  electron orbital wavefunction  $\phi(\mathbf{r}_1, \dots, \mathbf{r}_j, \dots, \mathbf{r}_N)$ . The final state is also decomposed into a nuclear part  $\chi_f(\mathbf{R})$ , a one electron continuum part  $\psi_c(\mathbf{r}_j)$  and the wavefunction of the  $N - 1$  electron ionic core  $\phi^+(\mathbf{r}_1, \dots, \mathbf{r}_{j-1}, \mathbf{r}_{j+1}, \dots, \mathbf{r}_N)$ . In the case of atoms the above description is valid without the nuclear parts and the angular dependence. The dipole operator does not affect the nuclear wave function, hence their product can be factorized out  $\langle \chi_i(\mathbf{R}) | \chi_f(\mathbf{R}) \rangle$ , which is called the nuclear autocorrelation function.  $\chi_f(\mathbf{R})$  is the result of the projection of the initial  $\chi_i(\mathbf{R})$  nuclear wavefunction on the ionic state using the Franck-Condon principle, that is then propagated during the electron excursion in the continuum. Patchkovskii performed simulations to investigate the influence of the autocorrelation function on HHG in various molecules [139]. Surprisingly, he found a significant influence in many molecules such as  $O_2$ ,  $NO$ ,  $NO_2$  even using an 800nm laser. But in  $N_2$  and  $CO_2$ , the molecules that will be studied in this thesis, the effect is found to be negligible. Thus for the moment we assume that the initial and final nuclear wavefunctions are the same,  $\langle \chi_i(\mathbf{R}) | \chi_f(\mathbf{R}) \rangle = 1$ .

For a correct treatment of the recombination dipole multi-electron effects should be taken into account (Patchkovskii et al. [58][140], Santra and Gordon[60]), but a single active electron is assumed in the SFA upon which all our data analysis is based, hence we assume that from the  $N$  electrons, only the  $j$ th one is affected by the laser:

$$\mathbf{d}_{rec}(\omega, \theta) = \langle \phi(\mathbf{r}_1, \dots, \mathbf{r}_j, \dots, \mathbf{r}_N) | \mathbf{r}_j | \phi^+(\mathbf{r}_1, \dots, \mathbf{r}_{j-1}, \mathbf{r}_{j+1}, \dots, \mathbf{r}_N)\psi_c(\mathbf{r}_j) \rangle. \quad (1.60)$$

The  $\mathbf{r}_j$  dipole operator acts only on the continuum electron, hence the ionic core can be projected on the neutral molecule, resulting in the so called *Dyson-orbital*:  $\psi^D(\mathbf{r}_j) \propto$

$\langle \phi(r_1, \dots, r_j, \dots, r_N) | \phi^+(r_1, \dots, r_{j-1}, r_{j+1}, \dots, r_N) \rangle$ . Calculating the Dyson orbital can be interpreted as projecting out the difference between the neutral and the ionic core, which could be seen as a hole in the molecular cloud [48].

More visual picture can be retrieved by further assuming that (i) the multi-electronic states are constructed from Hartree-Fock orbitals, meaning that  $\phi(r_1, \dots, r_j, \dots, r_N)$  and  $\phi^+(r_1, \dots, r_{j-1}, r_{j+1}, \dots, r_N)$  are anti-symmetrized products of single-electron orbitals; (ii) there is no electronic relaxation in the ion after the tunnel ionization, so the remaining occupied electronic states in the ion are identical to the corresponding neutral electronic states, this is the Koopmans approximation. These assumptions result in the fact that the Dyson-orbital simplifies into the orbital from which the electron was removed. That is usually the HOMO orbital. Now, the recombination dipole takes the following simple form:

$$\mathbf{d}_{rec}(\omega, \theta) = \langle \psi^D(\mathbf{r}_j) | \mathbf{r}_j | \psi_c(\mathbf{r}_j) \rangle = \langle \phi_0(\mathbf{r}) | \mathbf{r} | \psi_c(\mathbf{r}) \rangle, \quad (1.61)$$

where we exchanged  $\mathbf{r}_j$  into  $\mathbf{r}$  and denote the active orbital as  $\phi_0(\mathbf{r})$ .

In this thesis, the atomic/molecular orbitals will be calculated with the Hartree-Fock method, giving real orbital functions, while for the continuum states of the electron we will use two approaches: plane wave approximation and scattering states. Plane wave approximation neglects the effect of the atomic/molecular potential on the continuum states exploiting the strong field approximation. The scattering continuum states calculations provide more precise dipole since they include the influence of the atomic/molecular potential on the continuum states. The scattering wave dipoles in the thesis are provided by Robert Lucchese (Department of Chemistry Texas A&M University) [141]. In fact, the calculations provide the photoionization transition dipoles. But the detailed balance principle states that radiative photorecombination is just the inverse process of single-photon ionization (note that the three-step model as well as the SFA and QRS theories assume a field-free recombination dipole moment). A comparison of the results from these two approaches will be given in Chapter 4.

Another thing has to be realized is that strong-field ionization is exponentially sensitive to the ionization potential  $I_p$  [142]. Unlike atoms, the bonding energy of lower lying orbitals in molecules are often only a few electron volts from HOMO, which means that ionization from them cannot be neglected even for exponential scaling of ionization rates. Moreover, the differential ionization cross sections for different orbitals in molecule have different angle dependences because of their geometries. Thanks to the molecular alignment technique, it is possible to reach the angle at which the ionization for HOMO is suppressed while that for the lower lying orbitals are enhanced. Therefore one can further increase relative populations of the excited electronic states of the ion, the ionization from different molecular orbitals creating different ionization channels. In this case, the HHG is thus a coherent superposition of all the contributing channels, which is called multi-orbital contributions to HHG [49]. A more detailed discussion of this effect will be found in Chapter 4.

---

# EXPERIMENTAL TOOLS FOR ATTOSECOND PHYSICS

---

Attosecond physics is based on a nonlinear process called High-order Harmonic Generation (HHG). HHG is produced by the interaction between an ultra-short laser field at high intensity ( $I \sim 10^{14} \text{W/cm}^2$ ) and the nonlinear medium which may be either atoms and molecules in the gas phase, nanoparticles, or free electrons in solid and plasma. This thesis concentrates on the applications of HHG produced in the gas phase. There are two main types of applications:

On the one hand, high-order harmonics have a great potential as a source of intense attosecond pulses in the extreme ultraviolet region, i.e., the spectral range 1 – 100nm (12 – 1200eV) referred to as the XUV range. With already characterized and controllable XUV pulses, we can perform time-resolved studies of the pump-probe type, e.g., studies of coherent photoionization in atoms/molecules combining XUV and laser pulses.

On the other hand, HHG is a very sensitive probe of the structural properties of the generating system, as well as of its dynamical properties, in particular in the presence of a strong field. The inelastic scattering of the recolliding electronic wave packet acts as an instantaneous “in situ” probe, combining attosecond temporal resolution and Ångström spatial resolution. This constitutes the new domain of “High Harmonic Spectroscopy” (named after an initial proposal of the CELIA–Bordeaux group and now worldwide adopted). Both schemes of experiments are investigated in the thesis. In this chapter, we introduce the different setups and the principal components.

All the experiments in Chapter 4, 5 and 6 have been performed at the Plateforme Laser Femtoseconde Accordable (PLFA) system at Saclay Laser-matter Interaction Center (SLIC), which is a partner lab of the LASERLAB-EUROPE network for transnational access to large scale Laser Infrastructures, in the 7<sup>th</sup> Framework Programme of the European Union. The PLFA system is entirely operated by high quality experts in the SLIC group. It delivers laser pulses centered at  $\sim 800\text{nm}$  with pulse duration of  $\sim 45\text{fs}$  and pulse energy of  $\sim 9\text{mJ}$  at  $1\text{kHz}$



---

repetition rate.

The generation stage corresponding to the attosecond pulse source will be detailed in section 2.1. The molecular alignment technique used in Chapter 4 and 5 will be presented in the next section 2.2. Then we will introduce two different schemes for the advanced characterization of the attosecond pulses, in both *amplitude* and *phase*. Finally, the experimental setups which are utilized in Chapter 4, 5 and 6 will be briefly described.

## RÉSUMÉ DU CHAPITRE

*La physique attoseconde est basée sur le processus non linéaire de Génération d'harmoniques d'ordre élevé (HHG pour High Harmonic generation). La HHG est produite par l'interaction entre un champ laser ultra-courte à haute intensité ( $I \sim 10^{14} \text{W/cm}^2$ ) et le milieu non linéaire, qui peut être soit composé d'atomes ou de molécules en phase gazeuse, de nanoparticules, ou d'électrons libres dans les solides et les plasmas. Cette thèse se concentre sur les applications de la HHG produite en phase gazeuse. Il existe deux principaux types d'applications:*

*D'une part, les harmoniques d'ordre élevé ont un grand potentiel en tant que source d'impulsions attosecondes intenses dans la région de l'ultraviolet extrême (ou XUV), i.e., la gamme spectrale 1 - 100 nm ( 12 - 1200eV ). Avec des impulsions XUV déjà caractérisées et contrôlables, nous pouvons réaliser des études résolues en temps de type pompe - sonde, par exemple, des études de photo-ionisation cohérente dans des atomes/molécules combinant source XUV et impulsions laser.*

*D'autre part, la HHG est une sonde très sensible des propriétés structurales du système de production, ainsi que de ses propriétés dynamiques, en particulier en présence d'un champ fort. La diffusion inélastique du paquet d'onde électronique de recollision agit comme une sonde "in situ" instantané, combinant résolution temporelle attoseconde et résolution spatiale à l'échelle de l'Ångström. Ceci constitue le nouveau domaine de «la spectroscopie harmonique d'ordre élevé» (nommée d'après une proposition initiale du groupe CELIA - Bordeaux).*

*Les deux types d'expériences sont étudiés dans la thèse. Dans ce chapitre, nous présentons les différentes configurations et les composantes principales.*

*Toutes les expériences dans les chapitres 4, 5 et 6 ont été effectuées sur la Plateforme Laser Femtoseconde Accordable (PLFA) au centre d'interaction laser-matière de Saclay (SLIC), qui est un laboratoire partenaire du réseau LASERLAB-EUROPE pour l'accès transnational aux infrastructures lasers à grande échelle, dans le 7e programme-cadre de l'Union européenne. Le système PLFA est entièrement géré par des experts de grande qualité appartenant au groupe SLIC. Il délivre des impulsions laser centrées à  $\sim 800$  nm avec une durée d'impulsion de 45 fs  $\sim$  et à une énergie pouvant aller jusqu'à 13 mJ avec un taux de répétition de 1 kHz.*

*L'étape de génération correspondant à la source d'impulsions attosecondes sera détaillée à la Section 2.1. La technique d'alignement moléculaire utilisé dans les Chapitres 4 et 5 sera présentée dans la Section 2.2. Ensuite, nous allons introduire dans la Section 2.3 deux schémas différents pour la caractérisation avancée des impulsions attosecondes, à la fois en amplitude et en phase. Enfin, les configurations expérimentales qui sont utilisés dans les Chapitres 4, 5 et 6 seront brièvement décrites dans la section 2.4.*

## 2.1 Attosecond pulse generation

In High-order Harmonic Generation in the gas phase, the interaction of atoms/molecules with the strong field of central frequency  $\omega_0$  leads to the generation of high odd harmonics  $q\omega_0$ . The harmonic field is radiated by a nonlinear dipole at the microscopic level; it then builds up coherently in the "forward" direction, i.e., along the propagation axis under the condition of phase-matching. Here we will discuss the experimental conditions necessary to generate high-order harmonics.

### Laser pulses

As already discussed in Chapter 1.1.1, HHG starts with tunnel ionization. Therefore, the laser intensity should be in the range  $10^{14} - 10^{15} \text{W/cm}^2$ , depending on the ionization potential of the medium. In this intensity range, the Coulomb potential barrier "viewed" by the ground state electron becomes finite so that the electron wave packet can tunnel out. At higher intensity, the medium is rapidly ionized through possible multiple ionization and HHG is canceled.

In this thesis, the major works are done by using the pulses delivered directly from PLFA system without post compression, which duration is around  $45 \text{fs}$ . Although the shorter pulses the better, in particular to extend the cutoff in HHG, one advantage of the relatively long pulses is that they provide "adiabatic" conditions for exploring strong field dynamics, such as multi-orbital effects in ionization at the optical cycle scale. Multi-orbital effects are highly dependent on the intensity. In the case of long pulses, the effects are coherently summed over many half optical cycles where the intensity keeps constant. In contrast in the case of ultra-short few-cycle driving pulses, the multi-orbital effects may be washed out due to the rapidly varying intensity.

The PLFA system has  $1 \text{kHz}$  repetition rate. Compared to the systems operating at a few tens Hz, the data acquisition is much faster. This is very convenient for experiments that need long averaging time such as those using the Magnetic Bottle Electron Spectrometer (MBES) and the COLd Target Recoil Ion Momentum Spectroscopy (COLTRIMS) apparatus in Chapter 4, 5 and 6. For the latter applications, the repetition rate might ideally be even higher (10 to  $100 \text{kHz}$ !).

### Gas medium

The gas medium for HHG can be prepared in a gas cell, a continuous or a pulse jet. In this thesis, we used a pulse jet for all the experiments, which has the advantage of keeping a relative high density (pressure  $\sim 1 - 10\text{mbar}$ ) in the gas medium for a low amount of injected gas. The supersonic "Attotech" pulsed valve (designed by Thierry Ruchon) is driven by a piezo-electric actuator. The actuator is mounted on the top of a mushroom-shaped valve with a flat end piece that is lifted in and out of an opening by an axial rod. It periodically opens and closes a 1 mm diameter pipe where the gas flows. The piezo controller synchronized with the driving laser operates at  $1\text{kHz}$  and has the shortest opening time of 100 microseconds.

In Chapter 4 and 5, High Harmonic Spectroscopy in aligned molecules requires high quality of molecular alignment, so that the rotational temperature of the molecular gas has to be low. By strongly pushing the gas with high backing pressure to a small nozzle this condition can be reached, as a result the molecules have a propagation velocity even larger than the speed of sound. The major source of heat in the molecular degrees of freedom – translation, rotation and vibration – in the gas medium comes from the collisions. The molecules are accelerated to become faster than the local speed of sound, which in turn decreases rapidly as the gas density drops during the expansion. In this adiabatic process, the heat energy of the gas (i.e. random translation, vibration, rotation) is converted into directed translational energy through numerous collisions. Very rapidly, the gas plume has expanded so far that the individual particles do no longer collide. Thus, low rotational temperature can be achieved. To further optimize the degree of molecular alignment by reducing the rotational temperature, we can increase the backing pressure of the gas, reduce the nozzle diameter or/and increase the relative distance between the laser focus and the nozzle. The experimental parameters used are  $200\mu\text{m}$  nozzle diameter,  $1.5 - 5$  bars backing pressure and  $\sim 300\mu\text{m}$  distance between the nozzle and the laser beam. This corresponds to a trade-off between the harmonic signal and the rotational temperature.

### Phase matching

To achieve good phase matching is crucial to optimize HHG. Good phase matching also assures that, to a first approximation, the microscopic single-atom/molecule response to the strong field predicts the shape of the harmonic spectrum as discussed in section 1.3. We use relatively long focusing lens of  $75\text{cm}$  to make a long Rayleigh length, i.e., a slowly varying intensity along the short generating medium. This slows down the geometrical mismatch (e.g. Gouy phase) and minimizes the intensity-dependent dipole phase mismatch. Moreover, we can compensate the Gouy phase shift after the focus by the intensity-dependent dipole phase. Finally, high ionization causes plasma dispersion that may immediately destroy the good phase matching condition. Therefore, we keep ionization at a low level in

the experiments.

By placing the laser focus a few mm before the gas jet, we optimize the contribution of the short trajectories to HHG, rather than of the long trajectories. Also, the dipole phase associated to the long trajectories varies much faster with intensity than that of the short ones, which leads to different divergences for the two trajectories. This results in their separation in space: long trajectories radiate off-axis whereas short trajectories radiate on-axis. We only select the on-axis emission. In this case, to a good approximation, the macroscopic HHG signal reflects the single atom or molecule response.

## 2.2 Molecular alignment

Thanks to the development of the molecular alignment techniques, the researchers investigating HHG have recently shifted their focus from rare gases to either unaligned or especially aligned linear molecules. Indeed, the alignment of the molecules not only provides a novel way of controlling the harmonic emission but also a novel important parameter for studying the molecular structure and alignment-dependent multi-orbital dynamics.

The alignment of small linear molecules is achieved by using an optical field. There are two schemes for aligning molecules: adiabatic alignment and non-adiabatic or field-free alignment. In adiabatic alignment, the pulse duration is much longer than the rotational period of the molecule. The molecule aligns along the field polarization, this minimizing the potential energy of the system. The alignment then vanishes after the laser pulse. In the adiabatic alignment, the atom-aligning field interaction adds to and significantly affects the HHG process [37]. In non-adiabatic alignment [35][34], the relatively strong laser pulse excite a wave-packet of rotational states through Raman scattering, which evolves freely after the pulse has passed. It regularly rephases and leads to an effectively aligned angular distribution of the molecular axis in field-free conditions. When the molecular axis is parallel to the laser polarization we call it alignment of the molecule, when the axis is perpendicular to the laser polarization we call it anti-alignment. This field-free scheme is very well adapted to the studies of HHG in aligned molecules.

In the two cases, in a linear molecule with no permanent dipole, the field induces a dipole, i.e., a polarization of the electronic cloud which in turn forces the nuclear rotation. It is worth to briefly recall the theoretical description of laser-induced alignment.

The molecules in the supersonic jet enter the interaction region in the HHG vacuum chamber with random alignment, i.e., with the molecular axes pointing in all the directions. In order to align all the molecules along one direction, a torque has to be applied to the system. If we shoot an intense short laser pulse on the molecules, the laser field  $\mathbf{E}(t)$  induces a dipole moment  $\mathbf{d} = \alpha \cdot \mathbf{E}(t)$ , where  $\alpha \equiv (\alpha_{\parallel}, \alpha_{\perp})$  is the polarizability tensor, with  $\alpha_{\parallel}$  and  $\alpha_{\perp}$  being the polarizabilities parallel and perpendicular to the molecular axis, respectively. The torque exerted on the dipole expresses as  $\mathbf{M} = \mathbf{d} \times \mathbf{E}$ . The potential energy of the induced

dipole in field writes as  $U = -\mathbf{d} \cdot \mathbf{E}(t) = -(\alpha \cdot \mathbf{E}(t)) \cdot \mathbf{E}(t)$ . The potential switches on and off rapidly during each laser field cycle so that the heavy nuclei cannot follow. As a result, the molecules feel a time-average potential over one laser cycle, which can be written as [143]:

$$U(\theta, t) = -(\Delta\alpha \cos^2(\theta) + \alpha_{\perp})E_0^2 f(t) = -U_0(t) \cos^2(\theta) - \alpha_{\perp} E_0^2 f(t) \quad (2.1)$$

where  $f(t)$  is the temporal envelope of the laser field of  $E_0$  amplitude,  $\theta$  is the angle between the laser field and the molecular axis. The last term is a constant energy which is not angle-dependent, hence it does not affect the angular distribution. As we can see, the molecules can be rotated, i.e., the field acts on the  $\theta$  angle, only when the polarizability is anisotropic, that is the polarizability difference  $\Delta\alpha = \alpha_{\parallel} - \alpha_{\perp} > 0$ . This is always true in diatomic molecule which have the maximal polarizability  $\alpha_{\parallel}$  along the internuclear axis. We neglect vibrational excitation because the spectral bandwidth of a 120fs aligning pulse ( $\Delta E \approx 14meV$ ) is much smaller than the energy to excite the vibrational states ( $\Delta E \approx 100meV$ ). Thus, the molecule aligns parallel to the laser field ( $\theta = 0$  in Eq.2.1), where the potential energy  $U(\theta, t)$  of the system is minimum.

In quantum mechanical terms, the "kick" creates a coherent rotational wavepacket in the molecules which are initially in a (incoherent) small set of rotational or angular momentum eigenstates. The angular part,  $\psi(\theta, \phi, t)$ , of the nuclear wavefunction of molecules is conveniently expressed as a sum of spherical harmonics  $\psi(\theta, \phi, t) = \sum_{J,M} c_J(t) |J, M\rangle e^{-iE_J t}$ , where  $J = 0, 1, 2, \dots$  is the angular momentum quantum number and  $M = -J, -(J-1), \dots, J-1, J$  is the projection of  $J$  onto the direction of the laser polarization,  $E_J = B_0 J(J+1)$  is the rotational energy,  $B_0$  has the dimension of a frequency and is referred to as the rotation constant, the coefficients  $c_J$  are determined by the interaction potential. The field-free Hamiltonian is  $B_0 \mathbf{J}^2$ , thus the total Hamiltonian can be written as  $H(t) = H_0 + H_L = B_0 \mathbf{J}^2 - U_0(t) \cos^2(\theta)$ . The TDSE for the rotational states in the presence of the laser pulse is written as:

$$i \frac{d}{dt} \psi(\theta, \phi, t) = [B_0 \mathbf{J}^2 - U_0(t) \cos^2(\theta)] \psi(\theta, \phi, t) \quad (2.2)$$

The Eq.2.2 is transformed into a series of differential equations, each equation corresponding to a specific  $|J, M\rangle$  state:

$$i \dot{c}_J = -U_0(t) \sum_{J', M'} c_{J'}(t) \langle J, M | \cos^2(\theta) | J', M' \rangle e^{-i(E_{J'} - E_J)t} \quad (2.3)$$

In Eq. 2.3, the transition matrix elements between two rotational states are mostly zero according to the selection rules, except for  $\Delta J = \pm 2$  and  $\Delta M = 0$ . Hence, Eq.2.3 can be greatly simplified including only two terms in the right hand side. Since molecules are not rigid rotors, their chemical bonds slightly stretch during the rotation. Thus, a correction of the rotation energy has to be applied:  $E_J = B_0 J(J+1) - D_0 [J(J+1)]^2$  [144]. Because  $D_0$  has a small value typically about  $10^{-6} B_0$ , it plays a role only for high  $J$  state. The initial conditions for Eqs 2.2 and 2.3 are associated by the molecules injected in the chamber from the gas jet. Because the energy interval between rotational states is as small as few  $meV$ , the

thermal ensemble is just an incoherent superposition of the rotational states  $|J, M\rangle$  even at low temperature in the supersonic jet.

The evolution of the rotational state is therefore better described using the density operator  $\hat{D}(t)$ , which satisfies to the evolution equation  $i\frac{d\hat{D}}{dt} = [H, \hat{D}]$ , and which is defined at zero time as a statistical sum over the  $|J, M\rangle$  states,  $\hat{D}(t=0) = \sum_{J,M} p_J |J, M\rangle\langle J, M|$ . If we note  $T_{rot}$  the rotational temperature in the interaction region, we can calculate the weight  $p_J$  of each rotational states by the Boltzmann distribution:

$$P_J = \frac{1}{Z} g_J (2J+1) e^{-E_J/k_B T_{rot}} \quad (2.4)$$

with  $k_B$  the Boltzmann constant, and  $g_J$  the factor controlling the relative weight between even and odd  $J$  states, due to nuclear spin effects. The Figure 2.1 shows a comparison of Boltzmann distributions of rotational levels  $J$  for  $N_2O$  and  $CO_2$  at different rotational temperatures  $T_{rot}$ , which are typical in the experiments. As expected in 2.1, the number of  $J$  states involved increases with temperature. An interesting point is that the involved  $J$  states are very similar for both  $N_2O$  and  $CO_2$  at the same temperature  $T_{rot}$ , which means that similar molecular alignment can be reached if we keep the same alignment intensity and backing pressure for both measurements in  $N_2O$  and  $CO_2$ .

Table 2.1: Properties of some common molecules.

Molecule	$B_0(\text{cm}^{-1})$	$D_0(\text{cm}^{-1})$	$\Delta\alpha(\text{\AA}^3)$	$g_{even}$	$g_{odd}$	$T(\text{ps})$
$H_2$	59.322	0.0471	0.2	1	3	0.28
$D_2$	29.90	0.01141	0.2	2	1	0.56
$O_2$	1.4376766	$4.84 \times 10^{-06}$	1.14	0	1	11.59
$N_2$	1.9896	$5.67 \times 10^{-06}$	1.0	2	1	8.38
$CO_2$	0.3902	$1.35 \times 10^{-7}$	2.0	1	0	42.71
$N_2O$	0.4190	$0.176 \times 10^{-7}$	3.22	2	1	39.78

Then the Equation 2.2 can be solved for the rotational states with large weights. We use a program developed by Sébastien Weber (Master2 report, 2008), which numerically solves the equation 2.2 over the duration of the laser pulse  $\tau_p$ , with a fourth-order Runge-Kutta method. The parameters of some common molecules needed in the calculation are given in Table 2.1.

Right after the laser alignment pulse, the molecule ensemble is aligned along the polarization. Subsequently, the rotational wave packet evolves in time and re-phases periodically. The time  $T = \frac{1}{2cB_0}$  is called the full revival time, equivalent to the rotational period. There are fractional revivals at fractions of the revival time  $T$  (i.e.  $1/2, 1/4, \dots$ ), during which only a portion of the states are in phase.

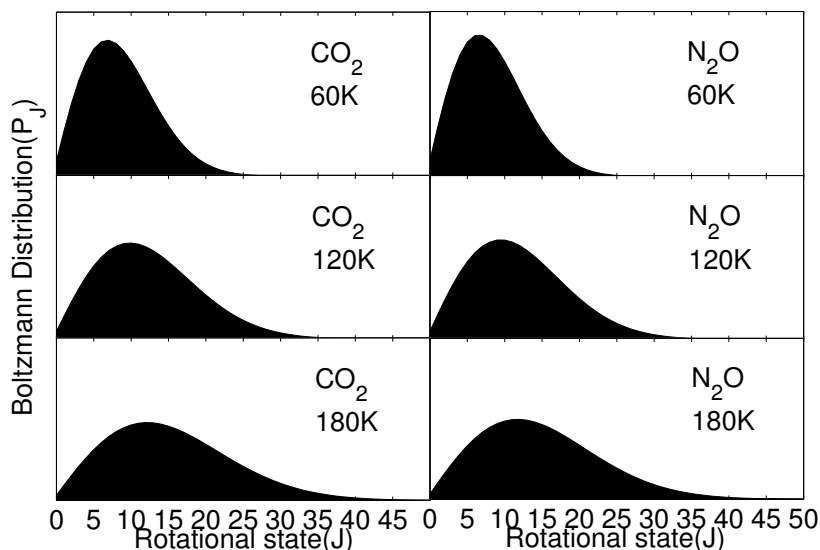


Figure 2.1: The comparison of Boltzmann distributions of rotational levels  $J$  for  $\text{N}_2\text{O}$  and  $\text{CO}_2$  at different rotational temperatures  $T_{rot}$ .

### Angular distribution

The angular distribution of the molecules in a given state  $\psi(\theta, \phi, t)$  at a given instant can be calculated as an incoherent sum over the rotational states with the relative weights obtained from the Boltzmann distribution, or equivalently using the density operator:

$$P(\theta, \phi, t) = \sum_{J,M} p_J c_J(t) c_J^*(t) |\langle \theta, \phi | J, M \rangle|^2 = \langle \theta, \phi | \hat{D}(t) | \theta, \phi \rangle. \quad (2.5)$$

The integration of the angular distribution should be equal to 1.

$$\int_0^\pi d\theta \int_0^{2\pi} P(\theta, \phi, t) \sin\theta d\phi = 1 \quad (2.6)$$

It worth noting that the angular distribution is not depending on the azimuth angle  $\phi$  because the initial molecular angular distribution is isotropic and the Hamiltonian in Eq. 2.2 is also  $\phi$ -independent. Therefore,  $P(\theta, t) = P(\theta, \phi, t)$ . Figure 2.2 shows the calculated angular distribution of  $\text{N}_2\text{O}$  at alignment and anti-alignment during the half revival, respectively. By integrating over the azimuthal angle  $\phi$ , the probability  $\sigma(\theta, t)d\theta = 2\pi \sin\theta \int_0^\pi d\theta \int_0^{2\pi} P(\theta, \phi, t)d\phi$  of finding the molecule between angle  $\theta$  and  $\theta + d\theta$  can be obtained. Figure 2.2 b) then presents the angular distribution  $\sigma(\theta, t)$  of  $\text{N}_2\text{O}$  when the molecules are aligned and anti-aligned, for a rotational temperature  $T_{rot} = 100\text{K}$ ,  $\tau_p = 120\text{fs}$  and alignment intensity  $I_{align} = 3 \times 10^{13}\text{W/cm}^2$ .

### Optimizing the alignment quality

The molecular alignment quality can be estimated from the statistical average of  $\cos^2\theta$ , given by  $\langle \cos^2\theta \rangle = \langle \psi(\theta, \phi, t) | \cos^2\theta | \psi(\theta, \phi, t) \rangle$ . This quantity has a maximum value of 1 when the molecules are perfectly aligned, that are all parallel to the laser polarization.

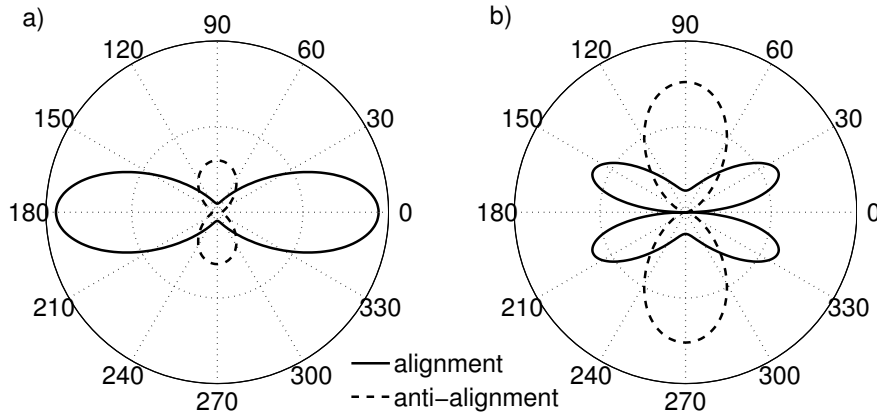


Figure 2.2: Angular distribution  $P(\theta)$  a) and Intergrated angular distribution  $\sigma(\theta)$  b) of  $\text{N}_2\text{O}$  at alignment and anti-alignment during the half revival. These calculations are done at  $T_{rot} = 100\text{K}$ ,  $\tau_p = 120\text{fs}$  and  $I_{align} = 3 \times 10^{13}\text{W}/\text{cm}^2$ .

Conversely,  $\langle \cos^2 \theta \rangle = 0$  at perfect anti-alignment, when all the molecules are perpendicular to the laser polarization. For an isotropic distribution,  $\langle \cos^2 \theta \rangle = \frac{1}{3}$ . A typical  $\langle \cos^2 \theta \rangle$  evolution as a function of time – over one rotational period – is showed in Figure 2.3 for the  $\text{N}_2\text{O}$  molecules. The molecules are immediately aligned after the laser pulse passes away, which is called prompt alignment. During the half revival around 20 ps, there is a peak at  $\langle \cos^2 \theta \rangle = 0.7$ . Most of the molecules are then aligned parallel to the laser polarization. Right after that we can see an anti-alignment, where  $\langle \cos^2 \theta \rangle = 0.2$ . The full revival is at  $t = 39.78\text{ps}$ .

Sébastien Weber’s code allows us to investigate the optimal theoretical conditions for molecular alignment. Figure 2.4 shows the evolution of  $\langle \cos^2 \theta \rangle$  as a function of different pulse durations and rotational temperatures, respectively. As we can see in a), the best alignment is achieved with  $\tau \approx 120\text{fs}$ . Therefore, we adjust the pulse duration to be close to this value by stretching the pulse from PLFA system, adding a glass block. For the dependence of the alignment quality on the rotational temperature in b), it gets better and better, as expected, as the temperature decreases. As mentioned in the last section, the cooling of the molecules is efficient by using a supersonic gas jet with high backing pressure and small nozzle diameter. The laser intensity affects the molecular alignment too: high intensity field excites a broader rotational wavepacket which produces a sharper revival. Previous experiments in Saclay rely on a collinear scheme of molecular alignment, i.e., the alignment beam is collinear to the generating laser beam. The alignment pulse should not drive high harmonic generation and, therefore, its intensity is limited to  $\approx 10^{13}\text{W}/\text{cm}^2$ . We developed a nonlinear setup in PLFA to overcome this limitation. Using a small angle between alignment and HHG beam allows higher intensities to be used. In our experiments, we use the alignment pulse at intensity of  $3 - 7 \times 10^{13}\text{W}/\text{cm}^2$ .



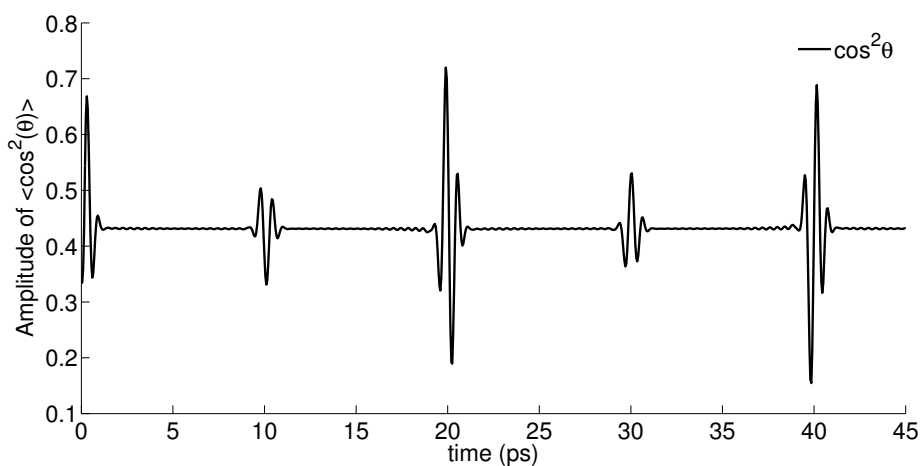


Figure 2.3: The evolution of the  $\cos^2\theta$  over more than one rotational period of  $\text{N}_2\text{O}$ . The first recurrence of alignment at the so-called half-revival at  $t = 19.9\text{ps}$  as well as the immediately following anti-alignment at  $t = 20.3\text{ps}$ . The full revival is at  $t = 39.78\text{ps}$ . The parameters used for the calculation is the same as Figure 2.2.

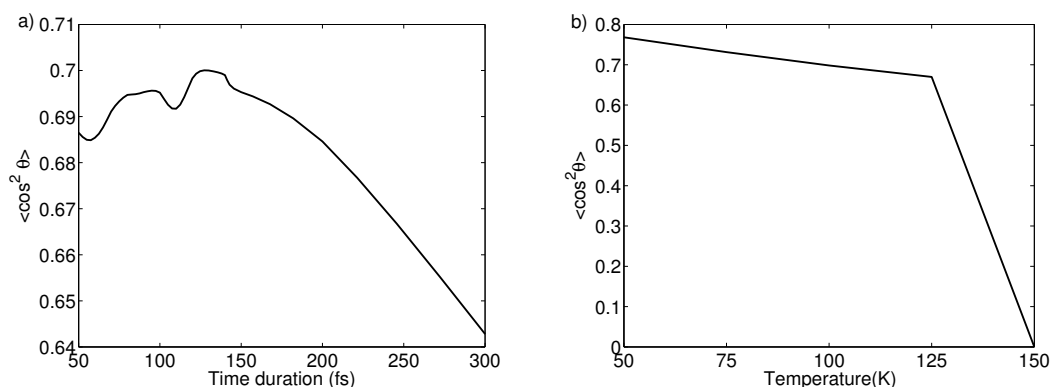


Figure 2.4: Dependence of the degree of alignment of  $\text{N}_2\text{O}$  on the pulse duration when the temperature is 50K a) and the rotational temperature when the pulse duration is 120fs b).

### Molecular frame and laboratory frame

Molecular alignment is performed in the molecular frame, which coordinates can be defined as the following:  $x$  axis is along the molecular axis,  $y$  axis is the direction perpendicular to the molecular axis and  $z$  axis is the same as the laser propagation direction. Note that the experimental results are usually measured in the laboratory frame. Therefore, it is required to convert the coordinates from the molecular frame to the laboratory frame in order to simulate the experimental results. For the laboratory frame, the  $\parallel$  axis is parallel to the generating laser polarization and the  $\perp$  is the axis perpendicular to both the  $\parallel$  axis and the laser propagation direction. The coordinates transformation can be done by:

$$\parallel = x \sin \theta + y \cos \theta \quad (2.7)$$

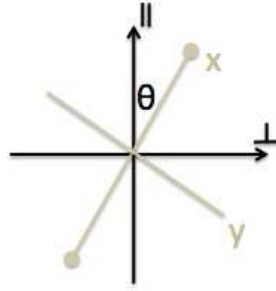


Figure 2.5: A schematic diagram of the laboratory frame (black) and the molecular scheme (gray).

$$\perp = x \cos \theta - y \sin \theta \quad (2.8)$$

### 2.3 Characterization of High-order Harmonic Generation

In the high harmonic spectroscopy, high harmonic or attosecond emission has to be completely characterized, i.e., by measuring *amplitude* and the *phase* of the field. This is also true for the applications of ultrashort harmonic/attosecond pulses in time-resolved studies. Due to the extremely short duration, measurement in the temporal domain is difficult. As already the case in the IR-visible-UV range, the idea is to characterize the attosecond pulse in the spectral domain, which allows reconstruction of the pulse profile in the time domain by Fourier transform. However, none of the optical techniques used in the IR-visible-UV range, such as SPIDER or optical FROG, can directly apply in the XUV, where manipulation of the pulse with XUV optics is limited, delicate and expensive. If the amplitude measurements are relatively simple, the phases are very difficult to obtain. In this section, we will describe the advanced experimental methods used for characterizing both amplitude and phase of the harmonic emission. To be definite, let us express the total harmonic field  $E_{XUV}(t)$ :

$$E_{XUV}(t, \theta, I) = \sum_q A_q(\theta, I) e^{-iq\omega_0 t + i\varphi_q(\theta, I)} \quad (2.9)$$

Fully characterizing the  $E_{XUV}(t, \theta, I)$  field means that both the spectral amplitude  $A_q$  and phase  $\varphi_q$  are measured over a broad spectral  $q\omega_0$  range, centered on  $\bar{q}\omega_0$ . In addition, it is crucial to study the variation of the amplitude  $A_q$  and phase  $\varphi_q$  as a function of structural parameters of the molecule, such as the alignment angle  $\theta$ , and dynamical parameters determining the interaction with the strong field, such as the alignment angle (again) and the laser intensity  $I$ . Note that, in Eq.2.9, the amplitude and phase may slowly depend on time  $t$ , e.g., through their dependence on the time-dependent intensity  $I(t)$ . As we will see, the “full mapping” of amplitude and phase as a function of photon energy, alignment, intensity,... requires to combine several techniques. To that purpose, we will introduce the two techniques that we have used, successively the *RABBIT* quantum interference technique

and the 2–source optical interference technique. For further discussion, it is convenient to split the variation of the phase into two terms:

$$\varphi(q, \theta, I) = \varphi_0(q_0, \theta_0, I_0) + \Delta\varphi_{\theta_0, I_0}(q) + \Delta\varphi_q(\theta, I), \quad (2.10)$$

where  $\varphi(q, \theta, I) \equiv \varphi_q(\theta, I)$ ,  $\Delta\varphi_{\theta_0, I_0}(q)$  is the phase variation over the  $[q_0, q]$  range, at fixed alignment angle and intensity,  $\Delta\varphi_q(\theta, I)$  is the phase variation over the  $[\theta_0 - \theta, I_0 - I]$  ranges, at fixed photon energy, and  $\varphi_0(q_0, \theta_0, I_0)$  is an arbitrary reference phase.

From Eq.2.9, the delay between the IR driving field and the XUV attosecond train is defined as the group delay  $\bar{t}_e = \frac{\partial\varphi}{\partial q\omega} |_{\bar{q}\omega_0}$  (instant of the maximum of the attosecond pulse envelope with respect to the maximum of the field amplitude).

### 2.3.1 Reconstruction of Attosecond Burst By Interference of Two-photon transition (RABBIT)

A successful way to characterize attosecond pulse train in Eq. 2.9 is the quantum interferometry RABBIT technique [145][23]. The RABBIT technique is particularly adapted to investigating the variation of the amplitude and phase as a function of the photon energy, or q–harmonic order.

#### RABBIT principle

The RABBIT technique is based on the *two–photon, multi–color* (XUV+IR) ionization of a target gas, usually an atomic rare gas. The broadband XUV beam – including all the harmonic components, i.e., forming a train of attosecond pulses, is generated on the one side, using a IR multi–cycle driving pulse. The (XUV+IR) photoionization (PI) is subsequently produced in the target gas, in the source volume of an electron spectrometer, on the other side. In RABBIT, we measure the (XUV+IR) photoelectron spectrum as a function of the delay between the XUV – the attosecond pulse train – and IR field. If there is only the XUV pulses that produce PI, the photoelectron spectrum is directly related to the XUV spectrum. We measure main lines in the photoelectron spectrum corresponding to odd–order harmonics, as showed by the violet peaks in Figure 2.6. When the XUV pulses are superimposed to the IR beam, new transitions become possible: the target atom can simultaneously, either absorb an XUV photon and an infrared photon, or absorb an XUV photon and emit an infrared photon, as presented by the violet solid lines and the red dash lines in the Figure. The intensity of the infrared beam has to be adjusted in order to produce sidebands but to prevent the absorption or emission of more than one photon, a condition which is typically achieved at  $10^{11} \text{ W/cm}^2$  (the case where higher order transition take place will be considered in Chapter 6). The two-photon PI therefore produces satellite lines or *sidebands* – see the blue peaks in Fig 2.6 – between the adjacent main lines, by *two photoionization channels which interfere*. As a result, the sideband amplitude oscillates with the XUV/IR delay which controls the

relative quantum phase between the interfering channels. Note that, experimentally, the IR “dressing” beam is usually derived from and therefore perfectly synchronized with the IR driving field.

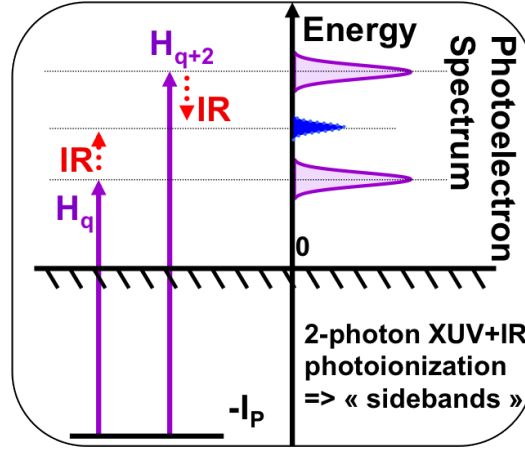


Figure 2.6: Principle of RABBIT.

The initial theoretical proposal of RABBIT [146] has shown that the sideband oscillation takes the form:

$$S_{q+1}(\tau) \propto S_0 + S_1 \cos(2\omega_0\tau + \varphi_{q+2} - \varphi_q + \Delta\phi_{q+1}^{atom}), \quad (2.11)$$

where  $\tau$  is the time delay between the XUV attosecond train (maximum of the attosecond pulse envelope) and the dressing IR field (maximum of the field amplitude) in the target gas, varying at the optical cycle scale. Note that the two-photon excited population at energy  $q\omega_0 + \omega_0 \equiv (q+2)\omega_0 - \omega_0$  in the continuum is produced out of the two one-photon excited populations at energy  $q\omega_0$  and  $(q+2)\omega_0$ , respectively. As a result, the sideband oscillation is concomitant with an out-of-phase oscillation of the main lines, the total population in the continuum being in principle constant for a constant harmonic yield.

The experimental setup that we have developed for RABBIT spectroscopy is described in the next section. The sidebands oscillation is already illustrated in Fig.2.7, where the XUV beam is generated in nitrogen, and the two-color PI produced in argon. The RABBIT technique is a variant of the general Frequency Resolved Optical Gating (FROG) [147]; the (*time, energy*) RABBIT spectrum is also called a spectrogram.

In Eq.2.11, the  $\Delta\phi_q^{atom}$  is the atomic phase of the target/detection gas, i.e., the phase of the two-photon transition dipole which depends on the initial and continuum final states of the target atom. The atomic phase can be obtained by either calculation [148] or measurement [149]. Theoretical calculations by Richard Taïeb at LCPMR show that, for atoms like argon and neon, the atomic phase is small, therefore we usually neglect it in our RABBIT analysis. If the atomic phase is known (or negligible), the spectral phase difference  $\varphi_{q+2} - \varphi_q$  of the consecutive harmonics can be extracted from the sideband oscillation in Eq.2.11.

The spectral phase difference is related to the *group delay* in the attosecond emission, also referred to as the *emission time*. The group delay is given by:

$$t_e(q\omega_0) = \frac{\partial \varphi}{\partial \omega} |_{q\omega_0} \approx \frac{\varphi_{q+2} - \varphi_q}{2\omega_0} \quad (2.12)$$

Note that in Eq.2.12, the  $t_e(q\omega_0)$  group delay is referred to the IR dressing field. To determine the absolute timing of the attosecond emission with respect to the IR driving field, we should correct  $t_e(q\omega_0)$  by the delay between the dressing and driving IR fields, writing:

$$\tau = \tau_{dress-drive} - \bar{t}_e, \quad (2.13)$$

where  $\tau_{dress-drive}$  is the delay between the dressing and driving fields. We should subsequently analyze the sidebands oscillation as a function of  $\tau_{dress-drive}$ , which directly provides the phase  $\Delta\varphi_{q+1} \equiv -2\omega_0\bar{t}_e + (\varphi_{q+2} - \varphi_q + \Delta\varphi_{q+1}^{atom})$ , i.e., the group delay  $t_e(q\omega_0)$  with respect to the driving field (same notation), also called the *absolute timing* of the attosecond emission. In High Harmonic Spectroscopy, it is important that the absolute timing or phase of the attosecond emission is determined, in particular for determining the influence of molecular alignment for each harmonic order. In a following section, we will describe how the absolute timing is measured in our experimental setup.

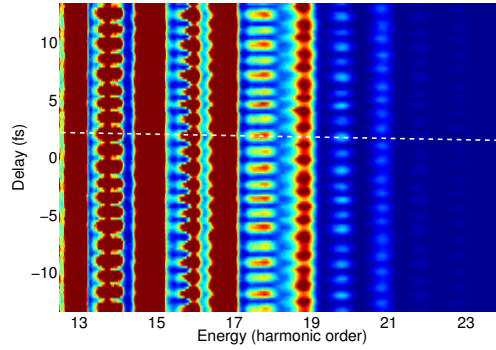


Figure 2.7: RABBIT scan taken with an HHG intensity of  $I = 1.4 \times 10^{14} \text{ W/cm}^2$  in nitrogen aligned at 0 degree and detecting in argon. The piezo step is 30 nm and 1000 laser shots are averaged per spectrum with the active stabilization system running. The total scan range is about  $4\mu\text{m}$ . The acquisition of this scan took about 5 minutes. The scan is calibrated to the energy domain.

### RABBIT spectroscopy : the Magnetic Bottle Electron Spectrometer

The RABBIT technique requires that photoelectron spectroscopy is performed with, i) a high enough two-color PI signal, i.e., collection efficiency of the electron spectrometer, and ii) a high enough energy resolution, typically better than  $100\text{meV}$  between 0 and  $30\text{eV}$ . To that purpose we have used a time-of-flight (TOF) of the Magnetic Bottle type, referred to as

Magnetic Bottle Electron Spectrometer (MBES), which principle has been originally developed by Kruit and Read [150]. In the MBES, the target gas is injected into the interaction volume by a needle with a diameter of  $500\mu m$ . A strong static magnetic field  $B \approx 1T$  is produced in the interaction region between the two polar pieces, by mean of a solenoid coil. The  $B$  field confines the photoelectrons ejected over  $2\pi$  steradian into a much collimated beam of half angle  $2^\circ$  which can enter the  $0.5m$  time-of-flight tube. The magnetic field is parallel to the flight tube and gradually reduces to  $\sim 10^{-3}T$ , a value which is kept constant. In this way, the electrons are traveling spirally around the magnetic field lines and the transverse component of their velocity is transferred to the longitudinal component. However, the kinetic energy of the electrons stay constant. Therefore, all the electrons that have the same kinetic energy eventually get the same speed and reach the detector at the same time. A stack of 3 micro-channel plates (MCP) is used for collecting the electrons. The choice of the detection gas depends on the spectral range we are interested in. As we can see from Figure 2.8, argon has a large cross section for low harmonic orders; neon has a flat cross section and is more sensitive for the high photon energies. The pressure in the source region is  $\sim 0.6 - 1 \times 10^{-3}mbar$  and  $1 \times 10^{-5}$  at the end of the tube, which is safe for the MCP.

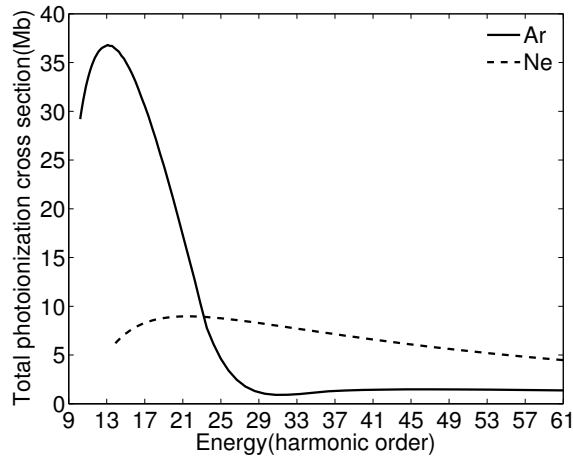


Figure 2.8: Total photoionization cross-section of argon (full curve) and neon (dashed curve) expressed in Mb as a function of the harmonic order of an 800 nm laser.

### Time-Energy calibration

The photoelectron signal is measured in the MBES as a function of the time-of-flight. In order to transform time-of-flight into kinetic energy, we use the dynamical law:

$$E_{kin} = \hbar\omega - I_p = \frac{m_e}{2} \left( \frac{L}{t_{TOF} - t_0} \right)^2 + E_a \quad (2.14)$$

where  $E_{kin}$  is the electron kinetic energy,  $m_e$  the electron mass;  $L = 0.5$  accounts for the length of the tube,  $t_0$  the delay for the electronics and light propagation since the trigger is from

the laser instead of the photoionization instant, and  $E_a$  takes into account the acceleration or deceleration due to the charge accumulation of the TOF during the electron traveling. Here, SI units are used.

The differential spectral intensity  $I(E)dE$  in the energy domain is equal to the  $I(t)dt$  differential element in the time domain ( $E \equiv E_{kin}, t \equiv t_{TOF}$ ). According to Eq.2.14, the jacobian of the transformation writes as :  $dt = -\frac{L\sqrt{m_e}dE}{[2(E-E_a)]^{3/2}}$ , and  $I(E) = -\frac{L\sqrt{m_e}I(t(E))}{[2(E-E_a)]^{3/2}}$ .

The energy resolution  $\Delta E$  is related to the time resolution  $\Delta t$  by  $\Delta E/(E - E_a) = 2\Delta t/(t - t_0) = -\frac{2\sqrt{2(E-E_a)}\Delta t}{L\sqrt{m_e}}$ . For constant resolution  $\Delta t$  in the time domain given by the MBS characteristics and the acquisition electronics, the energy resolution is degraded as the energy increases. In this thesis, for a length of the time-of-flight tube of  $0.5m$ , the time resolution is  $\Delta t \approx 1ns$ , so that the  $\Delta E$  energy resolution is  $\approx 150meV$  at electron energy of  $10eV$ . As already mentioned, the typical RABBIT spectrogram in Fig.2.7 has been measured in argon target gas, with the XUV field generated in aligned nitrogen (0 degree), for a dressing intensity of  $I = 3 \times 10^{11}W/cm^2$ . The attochirp, that is the variation of the  $\varphi_{q+2} - \varphi_q$  phase difference or  $t_e((q+1)\omega)$  group delay in Eq.2.11, is visible on the spectrogram where it is marked by the white dash line.

### Determination of the absolute timing in RABBIT

In Eq. 2.11, the delay between the dressing and XUV fields is varied by means of a high precision delay line using a piezo-crystal, which introduces a variable delay between the dressing and driving fields. Moreover, we designed both passive and active stabilization schemes to control the piezo position. As a result, the delay between the dressing and driving (XUV) fields is controlled with a  $\sim 100as$  accuracy.

As above mentioned, to determine the absolute timing of the attosecond emission, i.e., with respect to the IR driving field, it is necessary to measure the  $\tau_{dress-drive}$  delay. This is conveniently performed by having the two beams collinear. In the collinear geometry, the dressing beam crosses the generating medium. Its intensity is too weak to directly generate harmonics. However, it can modulate the intensity of the driving beam, inducing an overall modulation of the harmonic yield at frequency  $\omega_0$ . This results into the overall modulation at frequency  $\omega_0$  of the RABBIT spectrum, i.e., of the main and the sideband lines, in addition to the  $2\omega_0$  RABBIT oscillation. After integrating the spectrogram over electron energy at fixed delay and canceling the  $2\omega_0$  oscillation, one clearly monitor the  $\omega_0$  oscillation and determine  $\tau_{dress-drive} = \tau_{delay-line} + \tau_0$ , where  $\tau_{delay-line}$  is the delay controlled by the piezo-crystal delay line, and  $\tau_0$  is the offset delay which is required for absolute timing calibration. Experimentally, we measure the sideband oscillations in Eq.2.11 as a function of the  $\tau_{delay-line}$  parameter, in the form  $\cos(2\omega_0\tau_{delay-line} + 2\omega_0\tau_0 + (2\omega_0\bar{t}_e + \varphi_{q+2} - \varphi_q) + \Delta\phi_{q+1}^{atom})$ , and extract the phase. We directly obtain the  $2\omega_0\bar{t}_e + \varphi_{q+2} - \varphi_q$  absolute phase, or the absolute group delay, by subtracting the  $2\omega_0\tau_0$  and the  $\Delta\phi_{q+1}^{atom}$  atomic phase.

## Data analysis procedure

From the previous Sections, we summarize the successive steps in the analysis of the RABBIT spectrograms in Fig.2.7. Firstly, we integrate the signal spectrally to display the  $\omega_0$  oscillations due to the superposition of the driving and dressing fields, as shown in Figure a). From this weak modulation of the signal, we extract the  $\omega_0 \tau_0$  phase through a Fourier transform (see Figure b)), by averaging the phase over the full width at half maximum (FWHM) of the  $\omega_0$  peak. In order to get rid of the  $\omega_0$  oscillation in the sidebands, we normalize each sideband by the total signal modulation in a). Figure b) is an example of the normalized signal for the sideband 18, where we see clear  $2\omega_0$  oscillation with a very good contrast. The Fourier transform of c) is presented in d). There is a big peak at  $2\omega_0$  and the phase is averaged over the FWHM of the peak again, which gives the value of the experimental  $2\omega_0 \tau_0 + 2\omega_0 \bar{t}_e + \varphi_{19} - \varphi_{17} + \Delta\phi_{18}^{atom}$  phase. Then the relative phase between the neighboring harmonic can be extracted by subtracting the  $2\omega_0 \tau_0$  and the atomic phase  $\Delta\phi_{18}^{atom}$ .

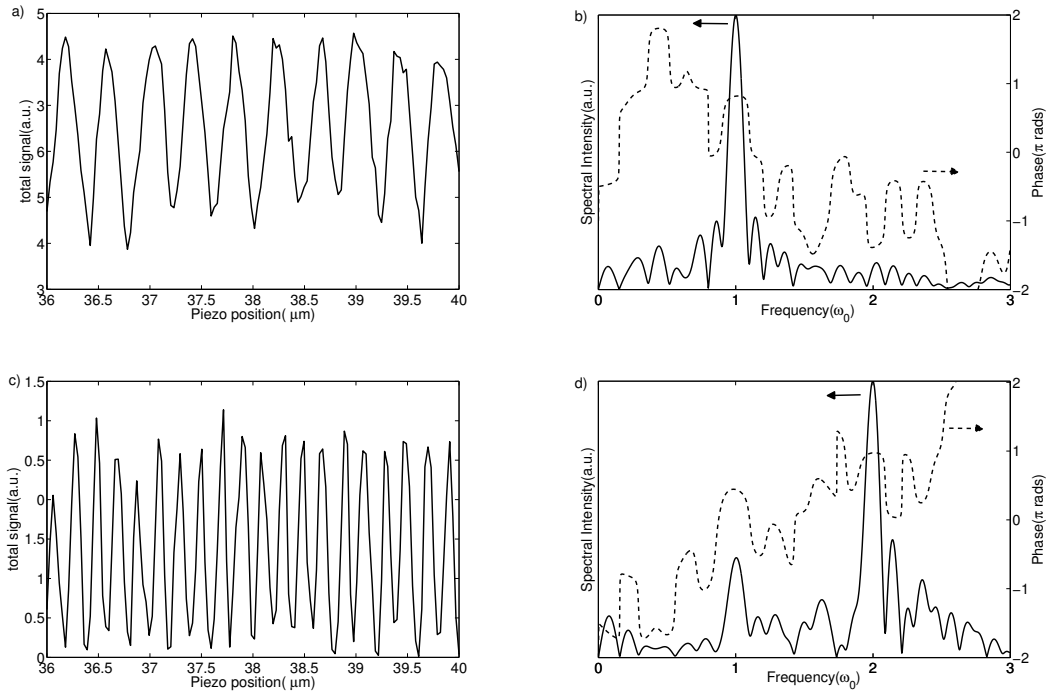


Figure 2.9: The data analysis of Figure 2.7. a) The evolution of the total signal in a function of the piezo position. b) The intensity and phase from the FFT of a). c) The oscillation of sideband 18 normalized by the total signal in a). d) The intensity and phase from the FFT of c)

The error bar is defined as the standard deviation of the sideband FFT phase within the FWHM of the  $2\omega_0$  peak plus twice the standard deviation of the FFT phase of the total signal, within the FWHM of the  $\omega_0$  peak.

In conclusion of this section, we have shown that the RABBIT technique was well



adapted to measuring the variation of the amplitude  $A_q(\theta, I)$  and phase  $\varphi_q(\theta, I)$  – or the variation we have noted  $\Delta\varphi_{\theta, I}(q)$  in Eq.2.15 – as a function of the photon energy or  $q$ -order, for the other parameters  $\theta$  and  $I$  fixed. However, the variation of the phase as a function of  $\theta$  and  $I$  for fixed photon energy, – or the variation we have noted  $\Delta\varphi_q(\theta, I)$  in Eq.2.15 – is not measured and should be set arbitrarily. To complete the phase determination, we now use an optical interferometry technique.

### 2.3.2 Two Source Interferometry (TSI)

As just mentioned, the RABBIT technique is very successful on measuring the phase difference between adjacent harmonic orders, but there is no relation between RABBIT spectrograms for different molecular alignment angles, or different laser intensities. This continuous variation of the phase, however, may give fruitful information in High Harmonic Spectroscopy. In order to access this quantity, i.e., the variation we have noted  $\Delta\varphi_q(\theta, I)$  in Eq.2.15, researchers developed another technique based on optical interferometry, that is effective only at fixed XUV wavelength or  $q$  harmonic order. The *2-source* technique reproduces the basic scheme of the Young's double slits. If, by manipulating the driving field, one creates two foci and therefore two mutually harmonic sources, in the dimension (vertical) perpendicular to the propagation axis, the two harmonic beams respectively originated from the two sources might interfere in the far field [151], [152]. By dispersing spectrally, using a grating, the different harmonic orders in the dimension (horizontal) perpendicular to the two previous ones, one obtains a fringe pattern in the far-field for each harmonic order. The fringe pattern contains the information on the relative phase between the two sources. Now, one of the two source may be viewed as a reference. When changing the generation conditions in the other source, for example the molecular alignment or the driving intensity, one can measure the relative variation of the phase in the perturbed source by monitoring the phase shift of the fringes in the interference pattern. In the thesis work, we have used the *2-source* technique to study the variation of the harmonic phase as a function of the molecular alignment. We induce variable non-adiabatic alignment in the second source whereas the molecules remain unaligned in the first reference source.

Compare to the photoelectron measurement in the RABBIT technique, the *2-source* technique is more straightforward since it is direct optical interferometry. It was used to characterize the intrinsic and the mutual spatial coherence of the harmonic emission, as well as the atomic dipole phase [153][154]. It has also served in application to plasmas diagnostic [155], or Fourier Transform Spectroscopy [152]. Later this idea has been adapted by the JILA group at Colorado University for investigating molecules in a relative simple regime [156][157], where two foci are made using two thin glass plates. The plates introduce a phase difference between the two parts (halves) of the beam when it is tilted in different angles. If the two parts of the beam have a  $\pi$  phase difference, the destructive interference

in the middle makes a dark fringe while the constructive interference produces two lateral focal spots.

Because the beam diameter of our beamline is  $\sim 35\text{mm}$ , it is very difficult to keep the wavefront homogeneous after propagation through the tilted plates. Antoine Camper, an other PhD student in the Attophysics group, has recently developed a new scheme to produce two focal spots. The idea is to produce the  $\pi$  phase difference in the beam by using a phase mask, which has different thickness for the two parts as showed in Figure 2.10. After focusing the transmitted beam, two spots are created. The transverse cut of the focal region simulated with Zemax ray-tracing code is presented in the color plot, while the real focal region imaged by a CCD camera in the experiment is showed in gray picture (two pictures are not in the same scale). Both of them have very regular profiles. To spectrally analyze the harmonics, we use an XUV spectrometer which consists of a flat field grating and a multi-channel plate detector backed with a phosphor screen. The images are taken by a CCD camera. A typical image is displayed in Figure 2.10 as well, where we see clearly contrasted fringes for several harmonic orders. The 2-source technique requires high relative stability of the beams over time, in order not to blur the fringes pattern. Since the  $\pi$  phase-shift introduced by the phase mask is fixed, the two halves of the beam are automatically phase-locked. If we only align the molecules at one source, the fringes will shift up and down when changing the alignment angle or the relative delay between alignment and generation beam. From this variation, the  $\Delta\varphi_q(\theta, I)$  phase variation in Eq.2.15 is directly obtained as a function of the alignment angle, for each harmonic order and at a given laser intensity.

The two-source interferometry in aligned molecules gives access to the  $\Delta\varphi_q(\theta, I)$  phase variation with the alignment angle. However, it does not connect the different spectral components : the  $\Delta\varphi_{\theta, I}(q)$  phase variation with the photon energy is undefined and should be set arbitrarily. Conversely, as we have seen above, the RABBIT gives access to the  $\Delta\varphi_{\theta, I}(q)$  variation with photon energy but it lets the other term undefined. The RABBIT and TSI techniques are measuring the phase in two different dimensions. To perform the two types of measurement in the same molecular system under the same experimental condition can test their validity. More importantly, by combining the two techniques, it is possible to completely determine the phase variation in Eq.2.15, that is to provide a full mapping of the harmonic phase:

$$\varphi(q, \theta, I) = \varphi_0(q_0, \text{unalign}, I) + \Delta\varphi_{\text{unalign}}(q, I) + \Delta\varphi_q(\theta, I) \quad (2.15)$$

The NRC group at Ottawa in Canada has performed a similar approach of the “full mapping” issue, by combining the gas mixing technique [158][159][160] and TSI. However, they have to assume the phase for the reference atom [161]. From our experience, even the phase for atom gas can be complicated under some conditions. Thus the present combination of RABBIT and TSI may be more straightforward and reliable. In Chapter 4, we present

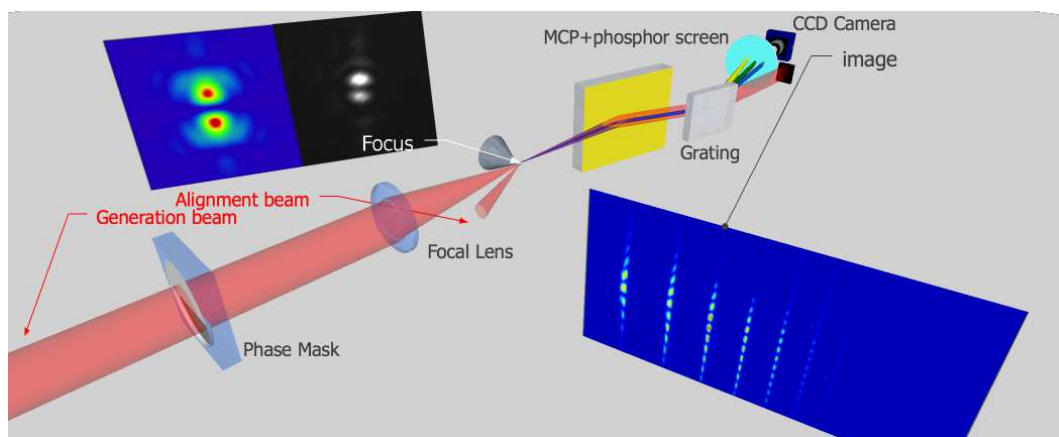


Figure 2.10: Sketch of the principle of Two Source Interferometry. The two focus are produced by using a phase mask with different thickness for the two parts. The simulated and experimental focus are showed on the left and right in the small graph, respectively. The harmonic signal is dispersed by a flat field grating. Then the signal is collected by a multi-channel plate and projected to the phosphor screen. The images are taken by a CCD camera at the end.

the TSI and RABBIT measurements in different molecules, as well as their combination for a full mapping of the phase.

## 2.4 The experimental setups : optical lines

### 2.4.1 The RABBIT and Two-color photoionization optical line

The experimental setup of RABBIT and Two-color photoionization experiments is showed in Figure 2.11. The PLFA system provides intense femtosecond pulses with s-polarization (vertical) and a maximal energy of  $9mJ$  at a repetition rate of  $1kHz$ . The pulse length is usually  $45fs$  and the central wavelength is  $800nm$  with  $25nm$  bandwidth at full width at half-maximum (FWHM). The incoming beam is splitting into two sub-beams. The first sub-beam with an energy of  $0.5 - 1.0mJ$  is used for transient molecular alignment, which is arranged in a non-collinear configuration to prevent propagation into the detection chambers. The beam size is controlled by a telescope in order to fully align the molecular ensemble. A glass block of  $\sim 5mm$  is inserted in the beam to stretch the pulse duration and optimize the alignment efficiency, as well as a half-wave plate for varying the polarization. The beam is focused by means of spherical mirror of  $1m$  focal length. The second sub-beam is further divided into two arms by a Mach-Zehnder interferometer which consists of two drilled mirrors with hole diameter of  $(4, 8, 10mm)$  depending on the incoming energy. The outer annular beam of maximum energy ( $0.7 - 1.5mJ$ ) is used for driving high harmonic generation, while the inner small beam ( $50 - 100\mu J$ ) is for two-color PI or dress-

ing in the RABBIT technique. The two driving and dressing beams are focused by a  $0.75\text{m}$  lens. The relative delays between the dressing and the alignment beams (pulses) with respect to the generation one are respectively controlled by two delay stages. To compensate for the temperature drift in the lab we developed an active stabilization of the delay with a helium:neon (He:Ne) laser at a wavelength of  $543.5\text{ nm}$ . Apart from the optical table, all the optical elements are in vacuum chambers for reducing the absorption of the XUV radiation. The annular generation beam is blocked by an iris after the harmonic generation, whereas the on-axis XUV and the dressing beams which have small divergence can go through. The two beams are transported by gold-coated plane mirror and refocused by a gold-coated toroidal mirror into the interaction volume of the time-of-flight MBES.

For the two-color XUV+IR photoionization studies in Chapter 6 performed in collaboration with the group of Institut des Sciences Moléculaires d'Orsay (ISMO), we have implemented the COLd Target Recoil Ion Momentum Spectroscopy (COLTRIMS CIEL) of the ISMO group downstream. Another toroidal mirror is used for focusing the beam in the supersonic target gas jet. All the mirrors are used at grazing-incidence ( $11.5^\circ$ ). They preferentially transmit the s-polarized component with a 2:1 contrast.

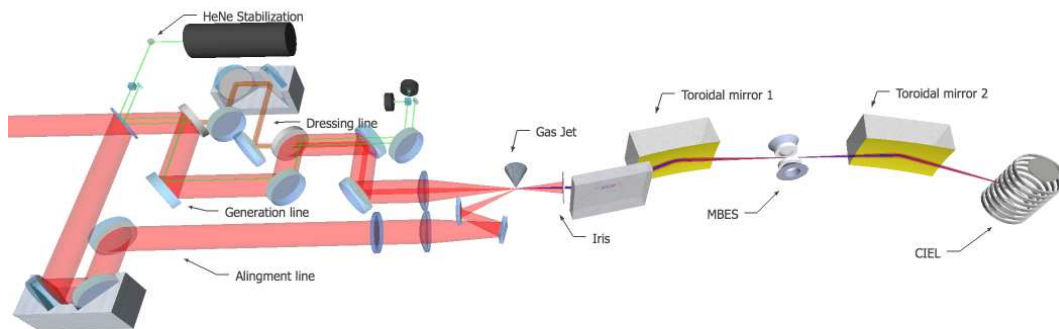


Figure 2.11: Experimental setup for RABBIT and photoionization.

## 2.4.2 The 2-source optical line

The setup for the Two-Source Interferometry is presented in Figure 2.12, which is adapted from the setup in Figure 2.11. The alignment arm is kept but the dressing arm is removed. The phase mask in the driving beam prepares two focal spots for harmonic generation by two mutually coherent sources spaced by  $50 - 200\mu\text{m}$  in the vertical dimension. The XUV spectrometer and the detection system are described in Section 2.3.2.

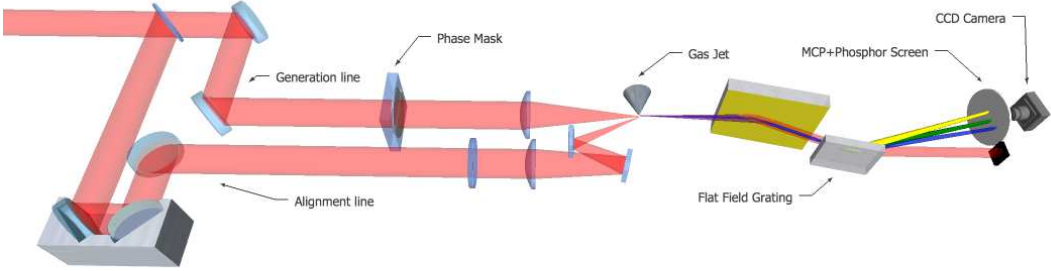


Figure 2.12: Experimental setup for TSI.

---

# THE FUNDAMENTALS OF HIGH-ORDER HARMONIC SPECTROSCOPY

---

High-order Harmonic Generation is a way towards a tunable ultrashort tabletop source of eXtreme UltraViolet/Soft X-rays radiation. But it also encodes coherently in the XUV radiation the structure and dynamical charge rearrangement of the radiating atoms/molecules. By advanced characterizing the radiation, we are able to extract the properties of the generation medium interacting with the strong driving field. This process of high harmonic generation where an atom/molecule is probed by its own electrons is called self-probing scheme. The power of HHG for probing dynamical processes relies on its inherent pump-probe scheme: tunnel ionization of an electronic wave packet (EWP) originally bound to the molecule (pump), acceleration of the released EWP by the strong laser field (time-frequency mapping allowing access to attosecond dynamical processes) and recombination (probe) to the core with emission of a burst of XUV coherent light. This self-probing technique or high harmonic spectroscopy opens up the perspective of investigating the molecular structures and dynamics in a combination of attosecond temporal resolution and nanometer spatial resolution.

In this chapter, the principles of this technique will be presented. We will start with the advantages of this technique in Section 3.1. The access to the recombination dipole moment, which is a very interesting and fruitful quantity that contains lots of information on the molecules, will be discussed in Section 3.2. It relies on the calibration of the harmonic signal from the studied molecule with that from a reference atom of same ionization potential and in the same generation conditions. Then we will study in Section 3.3 how this dipole allows a tomographic reconstruction of the molecular orbital using a plane-wave approximation for the continuum states. Next, we will illustrate the structural interference present in the recombination dipole using the two-center interference model in Section 3.4. The latter is a simple example showing how the structure of the molecular orbital is directly encoded in the recombination dipole and thus can be retrieved from it. Finally, the dynam-

---

ical interference resulting from multi-channel HHG is detailed in Section 3.5. By measuring it, we get access to the dynamics of the hole created in the molecular electronic cloud by coherent tunnel ionization from multiple orbitals (or to multiple ionic states).

## RÉSUMÉ DU CHAPITRE

La génération d'harmoniques d'ordre élevé est une voie vers une source ultra-courte de rayonnement XUV/Rayons X mous. Ce rayonnement encode de manière cohérente la structure et le réarrangement dynamique des charges intervenant dans les atomes/molécules du gaz de génération. En caractérisant de manière avancée cette radiation, nous sommes capables d'extraire les propriétés du milieu de génération interagissant avec le laser en champ fort. Ce processus de génération d'harmoniques d'ordre élevé où un atome/molécule est sondé par ses propres électrons est appelé le schéma d'auto-sonde. La puissance de la HHG pour sonder les processus dynamiques repose sur un schéma inhérent de pompe-sonde: l'ionisation tunnel d'un paquet d'onde électronique (EWP) originalement attaché à la molécule (pompe), l'accélération de l'EWP relâché par le champ laser (cartographie temps-fréquence permettant l'accès aux processus dynamiques attosecondes) et la recombinaison (sonde) vers le cœur avec émission d'un «flash» XUV de lumière cohérente. Cette technique d'auto-sonde ou de spectroscopie harmonique ouvre la perspective d'étudier les structures et la dynamique dans les molécule, le tout avec une résolution temporelle attoseconde et spatiale de l'ordre de l'Ångström. Dans ce chapitre, le principe de cette technique sera présenté. Nous commencerons avec les avantages de cette technique dans la section 3.1. L'accès au moment dipolaire de recombinaison, qui est une quantité très intéressante et fructueuse, qui contient l'information sur les molécules, sera discuté à la section 3.2. Cela repose sur la calibration du signal harmonique provenant de la molécule étudiée par celui provenant d'un atome de référence avec le même potentiel d'ionisation et dans les mêmes conditions de génération. Ensuite nous étudierons dans la Section 3.3 comment ce dipôle permet une reconstruction tomographique de l'orbitale moléculaire en utilisant l'approximation de l'onde plane pour les états du continuum. Ensuite, nous illustrerons les interférences structurelles présentes dans le dipôle de recombinaison en utilisant le modèle d'interférence à deux centres dans la Section 3.4. Ce modèle est un exemple simple montrant comment la structure de l'orbitale moléculaire est directement encodé dans le dipôle de recombinaison and peut donc être retrouvé à partir de ce dernier. Finalement, les interférences dynamiques résultant de la HHG provenant de plusieurs canaux sont détaillées dans la Section 3.5. En mesurant ces interférences, nous avons accès à la dynamique du trou créée dans le nuage électronique moléculaire, obtenu par ionisation tunnel cohérente à partir de plusieurs orbitales (ou vers plusieurs états ioniques).

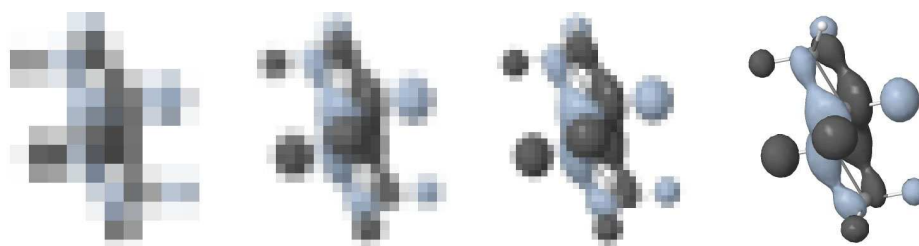


Figure 3.1: The illustration of how the spatial resolution affects the image quality.

### 3.1 Combining attosecond and Ångström resolutions

The spatial resolution is obviously a very important parameter of a camera that partly determines the quality of the image. We all prefer to use a camera which has a high resolution, because the image becomes sharper, more clear and more defined. Figure 3.1 shows how the resolution affects the quality of the image of a butane molecule orbital. As the resolution increases from the left to the right, we gradually gain more information on the molecular structure. For decades, people have been trying to always improve the resolution in order to image objects of even smaller scale. At the same time, a good temporal resolution is another crucial parameter for a camera when people want to capture the object in motion. This means that the camera shutter speed has to be faster than this motion. Therefore, we also would like to improve the shutter as much as possible.

The measurement of structural changes of matter as it undergoes processes important to physics, chemistry and biology has always been one of the prime goals of experimentalists. Therefore, the demand for combining both high spatial and temporal resolutions is much higher in scientific research than in photography. At the frontier of ultrafast dynamical studies, the time dependent investigation of electronic dynamics in atomic and molecular systems requires very precise probes with a space-resolution on the atomic scale (Ångström) and a few attosecond time resolution on the scale of the atomic unit of time (24as). As for spatial resolution, the requirement turns into a probe wavelength of the order of 1 Ångström; as for temporal resolution, it requires attosecond bursts. Atomic and molecular physics have developed tools which achieve either high spatial resolution (synchrotron radiation for crystallography or coherent diffraction imaging, electron scattering, electron guns for scanning tunneling microscope...) or high time resolution (accelerated ion collision). But to combine these two requirements into one tool has been impossible until the discovery of High Harmonic Generation. During this fundamental process of attosecond science, an intermediate step is the formation of an electronic wave packet in the continuum, whose central wavelength and duration perfectly match the spatial and temporal resolutions required. Eventually, the recolliding EWP takes the role of a probe pulse and the emitted photons that of the signal carrying information on the molecule to the detector. The use of electrons instead of photons bring many attractive properties [162].



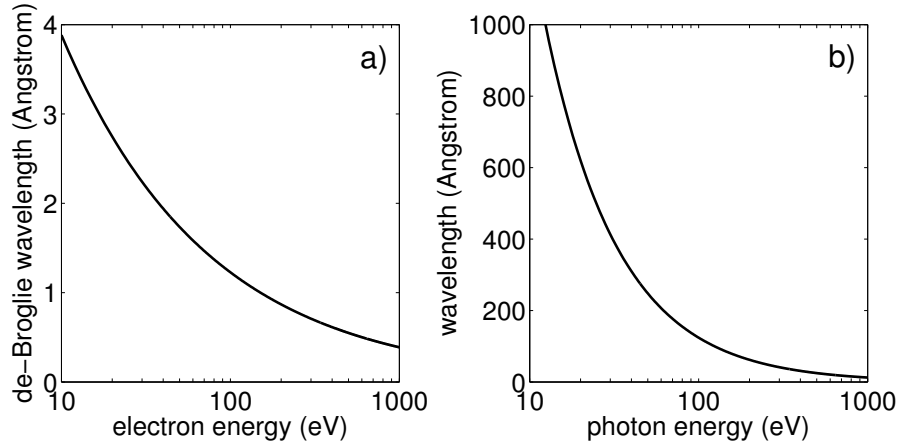


Figure 3.2: Wavelength associated with (a) an electron and (b) a photon as a function of the energy. Replotted from [162].

First of all, electrons reach Ångström scale much easier than photons due to different dispersion conditions. The de Broglie wavelength of the electron is given as (a.u.):

$$\lambda_e = \frac{2\pi}{\sqrt{2E_e}} \quad (3.1)$$

where  $E_e$  is the electron energy. But for photons, the wavelength is given by

$$\lambda_p = \frac{2\pi c}{E_p} \quad (3.2)$$

where  $c$  is the speed of light in vacuum and  $E_p$  is the photon energy. Figure 3.2 shows the energy and wavelength relations for electrons and photons, respectively. The photon energy has to exceed 10 keV for reaching 1 Ångström spatial resolution. But for electrons, it only needs 150 eV for 1 Å wavelength and 38 eV for 2 Å wavelength. These are energies easily achieved in the HHG process.

As for the temporal resolution, the EWP duration is determined by the driving laser optical cycle. For 800 nm wavelength laser, the period is 2.7 fs and the EWP in the continuum is of  $\sim 1$  fs duration. Moreover, the harmonic generation process has an intrinsic time delay between the different emitted harmonics that is usually called atto-chirp (see section 1.3). Each harmonic is produced by a specific part of the EWP with the corresponding kinetic energy at the recollision with the ion. This recollision time depends for a broad range of different harmonics almost perfectly linearly with the energy of the harmonic. So a direct mapping of the energy of the harmonic to the recollision time is possible. The time scale of this delay is on the order of a few ten attoseconds. Therefore, we can make use of the electrons in different spectral regions in order to reach attosecond time resolution. This is the principle of the PACER technique that has revealed nuclear movements on the as timescale in  $H_2/D_2$  and  $CH_4/CD_4$  [51].

In recent years, High Harmonic Spectroscopy has attracted tremendous attention due to the combination of these extreme spatial and temporal resolutions. In the following

sections, we will study how the information is encoded in the harmonic emission and how we can access it.

### 3.2 Accessing the recombination dipole moment

The photoionization (PI) spectroscopy [163][164] and scanning tunneling microscopy (STM) [165][166] have been proven their ability to measure the electronic structure of molecules. However, the important information on the spectral phase is usually lost and they give access to the electron densities only. The great potential of High Harmonic Spectroscopy (HHS) arises from the coherence of the process. More precisely the coherence of the EWP formed by a combination of scattering states and the initial bound state provides the possibility to measure not only the intensity of the radiating dipole but also its phase [162][25]. The observable of interest in HHS is the recombination dipole matrix element (DME)  $\mathbf{d}_{rec}$ , which is not directly measured but extracted from a more readily accessible quantity. In this section, we will concentrate on the extraction of the DME  $\mathbf{d}_{rec}$  from the experimental observation.

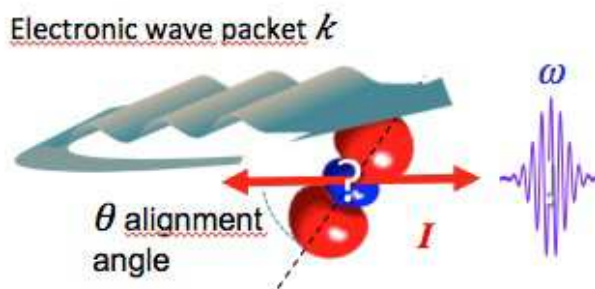


Figure 3.3: The illustration of molecular self probing scheme: A molecule aligned at  $\theta$  respect to the driving laser polarization. The electron wave packet  $k$  upon photoionization is driven by the laser field, which recollides to the parent ion eventually and encodes the molecular properties into the XUV radiation.

As discussion already in section 1.7, if only the contribution of the short trajectories to HHG is selected through phase matching restricted to those trajectories, the macroscopic emission is a replica of the single atom/molecule response. In this case, using an ansatz based on the strong-field approximation (SFA), the quantum version of the three-step model results in a factorized expression for the complex-valued dipole as showed by Equation 1.56 [132]. For accessing the recombination dipole moment  $\mathbf{d}_{rec} = \langle \psi_0(\mathbf{r}) | \hat{\mathbf{d}} | \psi_c(\mathbf{r}) \rangle$ , we have to get rid of the components of tunnel ionization  $\gamma$  and acceleration  $a(k)$ . This problem can be overcome as suggested by Itatani et al. [41] by calibrating the harmonic emission of the wanted molecule with a reference atom, whose DME can be calculated precisely (typically

a rare gas atom). If the experimental conditions are kept unchanged during the measurements and the reference atom has the same ionization potential, then the pre-factor  $\eta$ , the continuum factor  $a(k)$  and a part of the tunnel ionization independent on the recolliding angle can be cancelled out when dividing the two measurements:

$$\frac{\epsilon_{xuv}^{mol}(\omega, \theta)}{\epsilon_{xuv}^{atom}(\omega)} = \frac{T(\theta) \langle \psi_0^{mol}(\mathbf{r}) | \hat{\mathbf{d}} | \psi_c^{mol}(\mathbf{r}) \rangle}{\langle \psi_0^{atom}(\mathbf{r}) | \hat{\mathbf{d}}_{\parallel k} | \psi_c^{atom}(\mathbf{r}) \rangle} \quad (3.3)$$

the angle independent main factor of tunnel ionization (Keldysh tunneling rate  $w_m$  in Eq. 1.58) is removed after the calibration with the reference atom so that only the factor encoding the structure ( $T_\theta$ ) of the molecule remains. For the complex continuum amplitude ( $a$  in Eq. 1.56), Le et al. [167][168] found that  $a(k)$  is only dependent on the laser intensity and the ionization potential, which implies that the  $k$ -dependence of  $a(k)$  is approximately the same for the reference atom and the molecule for all the recolliding angles. Jin et al. [169][170][171][172] also studied the macroscopic phase matching effect. They concluded that even in the macroscopic case, the calibration can still be performed if the free electron density and the absorption are similar in the molecular/atomic gases. Note that the harmonic dipole  $\epsilon_{xuv}^{atom}$  and the recombination dipole  $\langle \psi_0^{atom}(\mathbf{r}) | \hat{\mathbf{d}}_{\parallel k} | \psi_c^{atom}(\mathbf{r}) \rangle$  for the reference atom are scalar quantities. This is because both the recombination dipole and harmonic dipole for an atom always have a polarization direction parallel to the electron recollision direction. In Equation 3.3, we divide by this component parallel to  $\mathbf{k}$ .

Therefore, if the polarization state  $\hat{n}$ , the amplitude  $A$  and the phase  $\varphi$  of the harmonic emission is characterized both for the aligned molecule and the reference atom, we are able to get access to the recombination dipole moment of the studied molecule:

$$\begin{aligned} \frac{\hat{n}^{mol}(\omega, \theta) A^{mol}(\omega, \theta) e^{i\varphi^{mol}(\omega, \theta)}}{A^{atom}(\omega) e^{i\varphi^{atom}(\omega)}} &= \frac{T(\theta) \langle \psi_0^{mol}(\mathbf{r}) | \hat{\mathbf{d}} | \psi_c^{mol}(\mathbf{r}) \rangle}{\langle \psi_0^{atom}(\mathbf{r}) | \hat{\mathbf{d}}_{\parallel k} | \psi_c^{atom}(\mathbf{r}) \rangle} \quad (3.4) \\ \implies \langle \psi_0^{mol}(\mathbf{r}) | \hat{\mathbf{d}} | \psi_c^{mol}(\mathbf{r}) \rangle &= \frac{\langle \psi_0^{atom}(\mathbf{r}) | \hat{\mathbf{d}}_{\parallel k} | \psi_c^{atom}(\mathbf{r}) \rangle}{T(\theta)} \frac{\hat{n}^{mol}(\omega, \theta) A^{mol}(\omega, \theta)}{A^{atom}(\omega)} e^{i[\varphi^{mol}(\omega, \theta) - \varphi^{atom}(\omega)]} \end{aligned}$$

This requires in particular a complete characterizing of  $\varphi^{mol}(\omega, \theta) - \varphi^{atom}(\omega)$ . The spectral phase (i.e. the  $\omega$  dependence) can be measured by RABBIT in separate scans for the molecule aligned at different angle and the reference atom, respectively. However, the polarization measurement needs a separate experiment. Another phase characterization technique is also used in this thesis, which is Two Source Interferometry. It investigates the phase as a function of molecular alignment angle for a given harmonic order. In TSI measurements, the molecules at only one of the two sources is aligned. The other non-aligned molecules therefore can be treated as a reference instead of a rare gas. More details can be found in section 2.3.2

### 3.3 Molecular orbital tomography

Once the dipole of the aligned molecule has been extracted, one can go one step further in the molecular structure analysis. Using the plane wave approximation (PWA), the continuum state  $\psi_c$  is given as  $e^{i\mathbf{k}\cdot\mathbf{r}}$ . Thus the description of the recombination dipole moment  $\langle\psi_0(\mathbf{r})|\hat{\mathbf{d}}|\psi_c(\mathbf{r})\rangle$  can be simplified to  $\langle\psi_0(\mathbf{r})|\hat{\mathbf{d}}|e^{i\mathbf{k}\cdot\mathbf{r}}\rangle$ . The advantage of using PWA is that the recombination dipole moment is taking the form of a Fourier transform. In the experiment, the laser polarization is always in  $xy$  plane, therefore we only consider the  $x$  and  $y$  component of the dipole. Depending on the choice of the dipole operator (length/velocity), the  $u$ -component ( $u = x, y$ ) of the dipole matrix element can be written as:

$$d_u(\mathbf{k}) = \langle\psi_0(\mathbf{r})|u|e^{i\mathbf{k}\cdot\mathbf{r}}\rangle = \iint u\psi_0(x, y)e^{i(k_x x + k_y y)} dx dy \quad (3.5)$$

$$d_u(\mathbf{k}) = -i\langle\psi_0(\mathbf{r})|\frac{\partial}{\partial u}|e^{i\mathbf{k}\cdot\mathbf{r}}\rangle = k_u \iint \psi_0(x, y)e^{i(k_x x + k_y y)} dx dy \quad (3.6)$$

Note that the experimental results of  $d_u(\mathbf{k})$  are usually measured in the laboratory frame, which prevents from applying the inverse Fourier transform directly. Thus we have to convert the data from the laboratory frame to the molecular frame:

$$d_x = d_{\parallel} \sin \theta + d_{\perp} \cos \theta \quad (3.7)$$

$$d_y = d_{\parallel} \cos \theta - d_{\perp} \sin \theta \quad (3.8)$$

Le et al. [173] found that the perpendicular  $d_{\perp}$  component of DME is usually much smaller than the parallel component in the length form. Moreover, the transmission of our setup used for RABBIT measurement favors the parallel component. Thus for the first step it is reasonable to assume  $d_{\perp} = 0$ . If the velocity gauge is chosen, there is no perpendicular component since the DME vector is parallel to  $\mathbf{k}$  (the generating laser polarization). As a result, the rotation procedure can be simplified for both gauges as:

$$d_x = d_{\parallel} \sin \theta \quad (3.9)$$

$$d_y = d_{\parallel} \cos \theta \quad (3.10)$$

Therefore, the molecular orbital can be reconstructed by inverse Fourier transform of the rotated experimental data  $d_u(\mathbf{k})$ :

$$\psi_0^u(x, y) = \frac{\mathcal{F}_{\mathbf{k}\rightarrow\mathbf{r}}[d_u(k_x, k_y)]}{u} \quad (3.11)$$

$$\psi_0^u(x, y) = \frac{\mathcal{F}_{\mathbf{k}\rightarrow\mathbf{r}}[d_u(k_x, k_y)]}{k_u} \quad (3.12)$$

Equation 3.11 is in length form and 3.12 in velocity form. Whatever the form chosen, the molecular orbital can be obtained from both the  $x$  and  $y$  component of the dipole. In principle, they should be equal, but it is not the case generally due to the discrete sampling in

the Fourier space and to the errors imported by the assumptions. Therefore, the average of both components is taken as the definition of the reconstructed molecular orbital:

$$\psi_0(x, y) = \frac{\psi_0^x(x, y) + \psi_0^y(x, y)}{2} \quad (3.13)$$

The molecular orbital is thus encoded in the spectral and angular dependence of the recombination dipole. In order to illustrate this, let us now detail the two-center interference model proposed by Manfred Lein [39][40].

### 3.4 Two-center interference model

In the simplest case, the HOMO of a diatomic molecule can be treated as a combination of two atomic orbitals:  $\psi_{mol} = \psi_0(\mathbf{r} - \mathbf{R}/2) \pm \psi_0(\mathbf{r} + \mathbf{R}/2)$ , with  $\mathbf{R}$  being the internuclear distance vector that makes an angle  $\theta$  with the polarization of the driving laser. '+/-' depends on the symmetric/antisymmetric combination of atomic orbitals. The recombination dipole moment in the velocity form therefore can be written as:

$$\begin{aligned} \langle \psi_{mol}(\theta) | \hat{\mathbf{d}} | e^{i\mathbf{k}\cdot\mathbf{r}} \rangle &= \langle \psi_0(\mathbf{r} - \mathbf{R}/2) | \hat{\mathbf{d}} | e^{i\mathbf{k}\cdot\mathbf{r}} \rangle \pm \langle \psi_0(\mathbf{r} + \mathbf{R}/2) | \hat{\mathbf{d}} | e^{i\mathbf{k}\cdot\mathbf{r}} \rangle \\ &= \mathbf{k} \left( e^{-i\frac{\mathbf{k}\cdot\mathbf{R}}{2}} \pm e^{i\frac{\mathbf{k}\cdot\mathbf{R}}{2}} \right) \langle \psi_0(\mathbf{r}) | e^{i\mathbf{k}\cdot\mathbf{r}} \rangle \end{aligned} \quad (3.14)$$

For '+' sign:

$$\langle \psi_{mol}(\theta) | \hat{\mathbf{d}} | e^{i\mathbf{k}\cdot\mathbf{r}} \rangle = 2\mathbf{k} \cos\left(\frac{\mathbf{k}\cdot\mathbf{R}}{2}\right) \langle \psi_0(\mathbf{r}) | e^{i\mathbf{k}\cdot\mathbf{r}} \rangle \quad (3.15)$$

For '-' sign:

$$\langle \psi_{mol}(\theta) | \hat{\mathbf{d}} | e^{i\mathbf{k}\cdot\mathbf{r}} \rangle = 2\mathbf{k}i \sin\left(\frac{\mathbf{k}\cdot\mathbf{R}}{2}\right) \langle \psi_0(\mathbf{r}) | e^{i\mathbf{k}\cdot\mathbf{r}} \rangle \quad (3.16)$$

This model thus predicts a minimum and a corresponding  $\pi$  phase jump in the recombination dipole moment, when the pre-factors before  $\langle \psi_0(\mathbf{r}) | e^{i\mathbf{k}\cdot\mathbf{r}} \rangle$  in Equation 3.15 and 3.16 reach 0. Therefore for '+' sign the minimum occurs at:

$$R \cos \theta = \left(n - \frac{1}{2}\right) \lambda_e \quad (3.17)$$

For '-' sign:

$$R \cos \theta = n \lambda_e \quad (3.18)$$

where  $n$  is an integer and  $\lambda_e = 2\pi/k$  is the de Broglie wavelength of the electron. The minimum happens if the internuclear distance projected on the driving laser polarization is equal to an odd multiple of half the electron wavelength for '+' sign. The physical origin of this minimum is related to the additional path length that the electron wave packet has to travel between the two lobes of the orbital. When it is equal to  $\lambda_e/2$ , it induces a  $\pi$  phase difference in the emission from the 2 lobes that interference destructively. For '-' sign, the additional  $\pi$  shifts the destructive interference to a path length difference of  $\lambda_e/2$ . For a given sign of the atomic orbital superposition, the minimum position is depending on

the projected internuclear distance, meaning it is angle dependent. The minimum and the phase jump shift to higher photon energy as  $\theta$  increases. This position is determined only by the structure of the orbital and is not influenced by the laser parameters (intensity and wavelength). This phenomenon is thus called structural interference. This interference in the dipole will induce a corresponding minimum and phase jump in the harmonic spectrum at a position given in principle by the dispersion relation  $E_k = nh\nu$ . The predicted minimum position in  $H_2^+$  agrees well with the TDSE simulations [174][175]. In the next chapter, a comparison between the dipole simulated using this two-center interference model and the quantitative rescattering theory calculated dipoles will be presented for  $N_2O$  and  $CO_2$ . The major properties of the scattering dipole such as the minimum positions for different angles are successfully predicted by the simple model. The latter thus provides useful physical insight into HHG from single molecular orbitals.

### 3.5 Multi-channel harmonic generation

All the descriptions above are based on a single channel picture of HHG, i.e. the harmonic generation is only produced by the EWP ionized from the HOMO and recombining to the same orbital. However, this is not a general case in molecules. As mentioned in section 1.7, sometimes the contribution of harmonic emission from the lower lying orbitals cannot be ignored anymore for two reasons: i) In molecules, the separation in energy of the different valence states reduces to few eV. ii) The structures of the molecular orbitals influence the ionization as well, and may induce for some alignment angles an enhancement for the lower lying orbital and a suppression for HOMO (e.g. at a nodal plane). When such a molecule is exposed to a strong laser field, the electron may tunnel out from different orbitals creating different ionization channels. The channel X refers to the ionization of an electron from HOMO (leading to an ion in its ground state), while channels A and B refer to an electron ionized from HOMO-1 (ion in its first excited state) and HOMO-2 (ion in its second excited state). Therefore the harmonic emission is a coherent summation of all the contributing channels (length form):

$$\epsilon_{xuv}(\omega, \theta, I) = \sum_i \gamma_i(\omega, \theta, I) a_i(k, I) \mathbf{d}_{rec,i}(\omega, \theta) \quad (3.19)$$

where  $i = X, A, B, \dots$ . The first evidence of multiple ionization channels have been found in  $N_2$  by McFarland et al. [176]. Later Smirnova investigated  $CO_2$  and successfully linked the various minimum positions obtained by many groups to the multi-channel effects [47]. Since then many studies have investigated there dynamical interference[177][178][179][180].

Note that we have considered that the different channels are independent. But it is not necessary that the ionized electron from an orbital recombines to the same orbital. Mairese et al. [181] found that an electron may ionize from the HOMO, leaving the ion in the X state,

but this ion is then excited from the X state to the A state between ionization and recombination so that the recombination occurs in the A state. This coupled channel connecting the X and A channels is called channel XA. It results from the strong coupling between the X and A states induced by the intense laser field which is almost resonant ( $1.55eV$  photon energy for  $\Delta\epsilon \sim 1.4eV$ ).

The relative phase of the different channels includes a phase difference accumulated during the electron excursion in the continuum: it thus depends on the laser parameters (intensity and wavelength). In some conditions, it leads to a destructive interference between the contributing channels at some position in the harmonic spectrum, position that can be varied by tuning the laser parameters. This process is called dynamical interference.

The first step in resolving multi-electron dynamics is to identify the multiple orbitals (ionic states) participating in the process. Next, we can observe their interference to see how these channels affect the harmonic radiation. In the next chapter, we will present the studies of multi-channel effects in  $CO_2$  and  $N_2O$ .

### Hole dynamics

A direct application of the multi-electron dynamical study is to image how the electrons ionized from the molecule, which is a great step towards attosecond time resolved high harmonic spectroscopy for molecules in strong field. The hole left in the molecule by ionization is the coherent superposition of the ionizing channels. Assuming there are two channels X and A, the electronic hole evolution in time can be written as:

$$\psi_{hole}(\mathbf{r}, t) = \psi_X(\mathbf{r}) + \alpha_{A/X} e^{i(\Delta\varphi + \Delta I_p t)} \psi_A(\mathbf{r}) \quad (3.20)$$

where  $\alpha_{A/X}$  is the ratio of the ionization rate between channels A and X,  $\Delta\varphi$  is the phase difference between the two channels in the ionization. When the electron comes back to the ion, it probes the ion at the instant of recombination. Therefore, the evolved electronic hole is probed about  $t = 1.5fs$  after its creation. The emitted harmonics thus encode a snapshot of the hole averaged over  $\tau \approx 600as$ , given by the attochirp in the spectral range of our experiment. Theoretically, we can set  $t$  to zero and calculate the position of the electronic hole at the ionization instant. Haessler et al [42] reconstructed the probability density of the electronic hole flipped from one side of the molecule to the other as the time passed.

---

# HIGH-HARMONIC SPECTROSCOPY OF N<sub>2</sub>O AND CO<sub>2</sub>

---

As discussed in the preceding chapter, many important features appearing in the harmonic spectra are associated to destructive interferences: the latter induce a minimum in the intensity spectrum and a corresponding big jump in the spectral phase. Such an interference can be found when the recolliding electron recombines with different sites of the highest occupied molecular orbital (HOMO) and the corresponding emissions interfere destructively. This -so-called- *structural* interference has a spectral position defined by the internuclear distance of the molecule projected on the recollision direction (given by the driving laser polarization) [39]. However, an interference can also be expected if different ionization channels give comparable contributions to HHG. This *dynamical* interference is determined by the relative phase of the different channels, that depends in particular on the action accumulated along the corresponding electron trajectories. For some laser parameters (intensity, wavelength), this phase difference between the contributing channels may reach  $\pi$  leading to a destructive interference. Therefore, an observed minimum may be caused by very different processes related to the molecular structure or dynamics, and is very often a subject of hot debate. Understanding the physics behind it is important for molecular orbital imaging and the study of multiple channel dynamics.

In this chapter, we will carefully characterize the HHG from two iso-electronic molecules, N<sub>2</sub>O and CO<sub>2</sub> that have very similar properties. The comparison of the electronic structure and valence orbitals of these molecules will be given in Section 4.1. By implementing two different characterization methods (RABBIT and TSI), we observed that the position of the destructive interference in N<sub>2</sub>O and CO<sub>2</sub> shifts when changing the generation intensity as shown in Section 4.2. Therefore, our results reveal multi-orbital contributions to HHG in both molecules. The characterization of the harmonic emission in two different dimensions (spectrally in RABBIT and angularly in TSI) can test the approxima-



---

tions made for each method. More importantly, the combination of the two measurements leads to a full mapping of the harmonic phase, which can be found in Section 4.3. In addition, we performed a detailed investigation for aligned  $\text{N}_2\text{O}$  and  $\text{CO}_2$  under the same generation conditions. Striking differences between the two measurements were observed by using both methods even though they have similar molecular structures. The results will be presented in Section 4.4. Later on, a simple model is developed in Section 4.5 to understand the underlying physics. It provides excellent agreement with our experimental results as well as explains that the differences between  $\text{N}_2\text{O}$  and  $\text{CO}_2$  in terms of the different contribution ratios to the harmonic emission from the lower lying orbitals. Interestingly, we are able to observe more intense harmonic emission from HOMO-1 than from HOMO. We also improved the theoretical model in Section 4.6 by using more advanced recombination dipole moments where the continuum states are calculated by taking into account the effect of the molecular potential. Next, we give in Section 4.7 an application of our advanced harmonic emission characterization, where we shape the attosecond pulses from aligned molecules with attosecond precision. Finally, the conclusions are given in Section 4.8.

## RÉSUMÉ DU CHAPITRE

*Comme nous en avons discuté dans le chapitre précédent, plusieurs caractéristiques importantes apparaissant dans le spectre harmonique sont associées aux interférences destructives: ces dernières induisent un minimum d'intensité dans le spectre et un saut de phase spectrale correspondant. De telles interférences peuvent être trouvées quand l'électron de recollision se recombine avec différents sites de l'orbitale moléculaire occupée la plus haute (HOMO) et les émissions correspondantes interfèrent destructivement. Cette interférence structurale a une position spectrale définie par la distance internucléaire de la molécule projetée dans la direction de recollision (donnée par la polarisation du champ laser) [39]. Cependant, des interférences peuvent être également observées quand différents canaux d'ionisation apportent une contribution comparable au signal harmonique. Cette interférence dynamique est déterminée par la phase relative des différents canaux qui dépend en particulier de l'action accumulée le long des trajectoires électroniques. Pour certains paramètres lasers (intensité, longueur d'onde), la différence de phase entre les canaux contribuant au phénomène peut atteindre  $\pi$ , conduisant à des interférences destructives. Donc, une interférence observée dans l'émission harmonique peut être causée par des processus très différents associés à la structure ou à la dynamique moléculaire et est très souvent sujet à débat. La compréhension de cette physique est importante pour l'imagerie d'orbitale moléculaire et l'étude de la dynamique à plusieurs canaux.*

*Dans ce chapitre, nous caractériserons le signal harmonique provenant de deux molécules iso-électroniques qui possèdent des propriétés très similaires,  $\text{N}_2\text{O}$  et  $\text{CO}_2$ . La*

comparaison des structures électroniques et des orbitales de valence de ces molécules sera présentée en Section 4.1. En implémentant deux méthodes de caractérisation différentes (RABBIT and TSI), nous avons observé que la position des interférences destructives dans  $N_2O$  et  $CO_2$  se décale lorsqu'on change l'intensité de génération, comme nous le montrerons dans la Section 4.2. Ainsi, nos résultats révèlent une contribution multiorbitaire au signal harmonique dans les deux molécules. La caractérisation de l'émission harmonique dans deux dimensions différentes (spectralement via RABBIT et angulairement via TSI) peut tester les approximations faites pour chaque méthode. De plus, la combinaison de ces deux mesures amène à une carte complète de la phase harmonique, qui peut être trouvée dans la Section 4.3. De plus, nous avons effectué une étude détaillée des molécules  $N_2O$  and  $CO_2$  alignées, dans les mêmes conditions de génération. Des différences frappantes entre les deux mesures ont été observées en utilisant les deux méthodes même si les structures moléculaires sont similaires. Les résultats associés sont présentés dans la Section 4.4. Ensuite, un modèle simple est développé dans la Section 4.5 pour comprendre la physique sous-jacente. Ce modèle apporte un très bon accord avec nos résultats expérimentaux ainsi qu'il explique les différences entre  $N_2O$  et  $CO_2$  par les différentes contributions des orbitales plus basses. Nous sommes ainsi capables d'observer le résultat contre-intuitif d'une émission harmonique plus intense provenant de HOMO-1 que de HOMO. Nous avons aussi amélioré le modèle théorique dans la Section 4.6 en utilisant des moments dipolaires de recombinaison plus avancés où les états du continuum sont calculés en prenant en compte l'effet du potentiel moléculaire. Ensuite, nous donnons dans la Section 4.7 une application de notre caractérisation avancée de l'émission harmonique où nous façonnons des impulsions attosecondes provenant de molécules alignées avec une précision attoseconde. Finalement, nous concluons ce chapitre dans la Section 4.8.

---

Structural minima in photo-recombination dipole were first predicted numerically in aligned  $\text{H}_2^+$  by a two center model [39]. Later on, many groups experimentally found minima in the harmonic spectra of aligned  $\text{CO}_2$ , but they were surprisingly at different positions [44][45][46][156]. Then Smirnova et al. attributed that to the dynamical interference by taking into account the contribution to HHG from the lower lying orbitals in  $\text{CO}_2$  [47], which could explain the different minimum positions due to the different generation conditions and in particular, laser intensity. This study was extended to broad harmonic spectra by using mid-infrared laser sources: Torres et al. [177] showed that the minima were the result of the interplay of both structural and dynamical interferences, whereas Vozzi et al. observed only structural interferences [43]. These different observations were attributed to the different pulse durations used in two experiments. The former used  $40\text{fs}$  pulses at  $1300\text{nm}$  wavelength, while the latter had only  $18\text{fs}$  pulses at  $1450\text{nm}$ , which corresponds to only 3 – 4 optical cycles. It was thus argued that dynamical interferences require a quasi-adiabatic generation condition (namely the exploitation of multicycle driving pulses), otherwise the intensity-dependent destructive interference of different harmonic generation pathways would be washed out along the driving pulses. The generation conditions thus appear to be critical for the observation of structural/dynamical interferences. In the case of  $\text{N}_2\text{O}$ , a molecule similar to  $\text{CO}_2$ , only evidence of structural interferences [157] [182] had been reported at the beginning of my thesis. Later, in parallel to our studies, Wörner et al. performed a study of the driving wavelength dependence of the intensity minimum in both molecules, published recently [179][180].

Understanding the relations and differences between  $\text{CO}_2$  and  $\text{N}_2\text{O}$  was thus a strong motivation of my studies, in order to answer the important question: can HHG spectroscopy differentiate between two very-close species. Moreover, in the case of dynamical interferences, can we get more quantitative information on the contributions of lower lying orbitals? This would provide us with useful information for a better understanding of the multi-channel processes, which has not been accessed by previous studies. In this chapter, we will first discuss the similarities and differences of the electronic structures of the two molecules in Section 4.1, then present an experimental investigation of the origin of the observed interferences in Section 4.2, providing a complete description of the interferences in Section 4.3. A comparison of HHG from the two species in exactly the same conditions is presented in Section 4.4, followed by the description of a model that I developed to explain the differences in HHG from  $\text{CO}_2$  and  $\text{N}_2\text{O}$  in Section 4.5. Next, an improved model is presented in Section 4.6. The application of attosecond pulse shaping by using aligned molecules is introduced in Section 4.7. Finally, the conclusion of this Chapter is given.

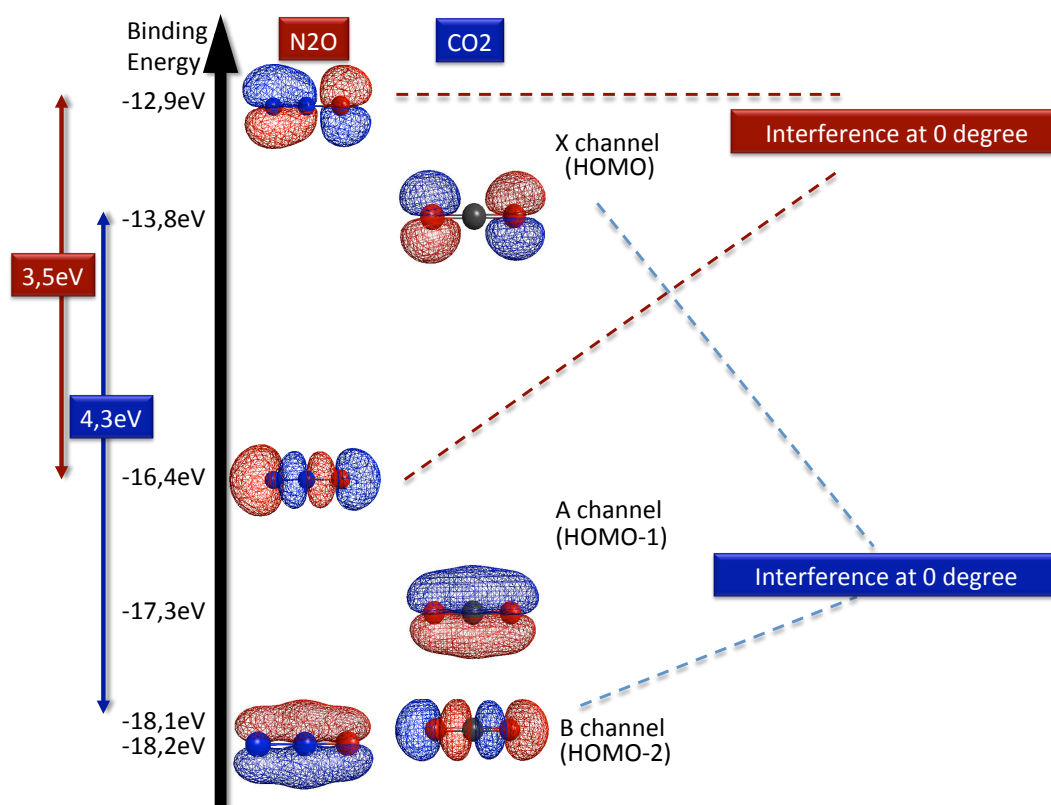
4.1 Comparison of  $N_2O$  and  $CO_2$ 

Figure 4.1: Comparison of the electronic structure and valence orbitals of  $N_2O$  and  $CO_2$  (calculated by GAMESS).

The electronic structure and valence orbitals of the two species are compared in Figure 4.1.  $N_2O$  and  $CO_2$ , being isoelectronic molecules, have many common features. First, they have the same internuclear distance (the distance between the two outer nucleus), which is 2.3 Ångström. Second, the ionization energy of HOMO in  $N_2O$  and  $CO_2$  is close ( $\sim 0.9eV$  difference). Third, their HOMO structures are similar. Even though there is a bit of asymmetry for the  $N_2O$  HOMO, it is dominated by its antisymmetry with the two nodal planes. A plane wave calculation was performed to check this as shown in Figure 4.2. The asymmetry makes the recombination dipole complex instead of purely real or imaginary. It turns out that the imaginary part is 10 times bigger than the real part, showing that the orbital is dominantly antisymmetric. This becomes a factor 100 in the harmonic spectrum, since the dipole is squared. More detail can be found in APPENDIX B.1. Finally, the HOMO-1 and HOMO-2 are very similar in the two molecules, but inverted.

Let us first discuss, in the case of  $CO_2$ , the expected contributions to HHG of the different orbitals. The  $CO_2$  HOMO structure suppresses the strong-field ionization when the molecule is aligned parallel to the driving laser polarization due to the nodal plane [133] [137][183]. The two parts of the electron wavefunction that tunnel out from the two lobes of the HOMO have opposite sign, therefore they interference destructively so that the ion-

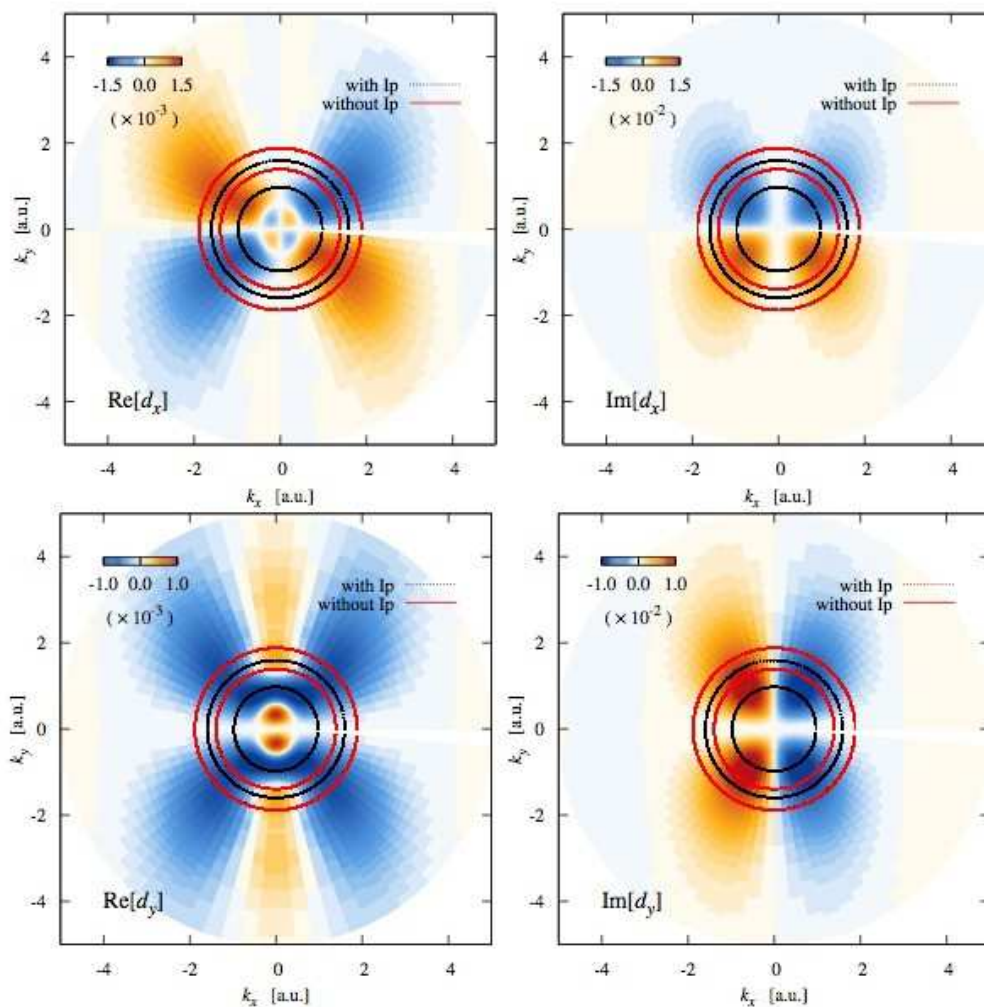


Figure 4.2:  $N_2O$  HOMO- Plane Wave dipole. Left: real part; Right: imaginary part; Top: x-component; Bottom: y-component. The circles indicate the range covered by harmonics 17 to 31 when including Ip (black) or not (red) in the dispersion relationship.

ization from this orbital is inhibited. For the same reason, the ionization from HOMO-1 of  $CO_2$  is suppressed. Moreover, since strong field ionization is exponentially sensitive to the ionization potential, the 3.5 eV energy difference between the HOMO-1 and HOMO results in a negligible contribution of HOMO-1 to HHG at 0 degree alignment. However, the ionization from HOMO-2 of  $CO_2$  aligned at 0 degree is strongly enhanced by the elongated structure that will favor tunnel ionization from the outer lobe. This may compensate for the decreased rate due to the 4.3 eV binding energy difference, so that the HOMO-2 and HOMO may give comparable contributions to HHG, making them interfere at 0 degree (Smirnova et al. [47]). If we compare the structures, a similar behavior can be expected in  $N_2O$  but between HOMO and HOMO-1. The smaller 3.5 eV binding energy difference for  $N_2O$  than for  $CO_2$  may lead to even bigger contribution to HHG from the lower lying orbital, and thus to stronger dynamical interferences. However, as mentioned above, only structural

interferences had been reported for the case of  $N_2O$  at the start of my studies.

## 4.2 Structural or dynamical interferences?

The important criteria to disentangle these two effects are the laser intensity and wavelength dependences, since they both shift the position of a dynamical interference but do not affect a structural interference. However, the laser intensity/wavelength also influences the harmonic emission in a general way: cutoff extension, atto-chirp, etc... The latter influence can be removed by calibrating the harmonic signal obtained in the molecule by that of a reference atom with same ionization potential and in the same generation conditions. This will allow unraveling the molecular interference and its possible variation with intensity/wavelength.

The characterization of high harmonic emission by using RABBIT technique is based on the conversion of photon energy to electron energy through photoionizing rare gas atoms. In this Chapter, the rare gas we used in MBES is neon, who has an  $I_p$  of  $21.6eV$ . Therefore, the harmonic emission with photon energies larger than that could be observed. If a weak infrared beam is superposed to the harmonic signal in the detection volume, they can create the photoelectron spectrum by absorption of one harmonic photon and simultaneous absorption or stimulated emission of one infrared (IR) photon. This multi-color two-photon process produces sideband between the odd order harmonic. And its oscillation when varying the time delay between XUV and IR encodes the relative phase of the neighboring harmonics. As discussed in Chapter 2, from the Fourier transform of the sideband oscillation, we could extract the relative phase, and thus the group delay or emission time. An example the the measured emission time for  $CO_2$  parallel aligned (red) and krypton (black) is shown in Figure 4.3 a). RABBIT detects only the spectral phase but it is not able to measure the phase variation with alignment angle at a fixed harmonic order nor the absolute phase difference with krypton. But our two source interferometry measurement could get access to that. The phase is almost flat as a function of the alignment angle for HH15 and HH17 (presented later in Figure 4.5). Our calibration procedure imposes that the emission time of sideband 16 is the same as in Kr for  $CO_2$  parallel aligned. Figure 4.3 b) shows the normalization at sideband 16 for both measurements. The ionization potentials for both are very close:  $13.8eV$  for  $CO_2$ , while  $13.9eV$  for krypton. However, we could see a clear deviation in  $CO_2$  for the side band 24 and 26, which may be a signature of the destructive interference from the HOMO structure or multi-orbital contribution to HHG. Then the spectral phase of  $CO_2$  and krypton can be obtained by the integration of the emission times as shown in 4.3 b), respectively. Due to their close  $I_p$ s, the attochirp of  $CO_2$  could be removed by calibrating the harmonic signal from molecules by that of krypton while keeping the same experimental conditions, as shown in d). As a consequence of normalizing to sideband 16, we add an  $\omega$ -independent phase term. Hence it does not change the spectral

characteristics of the dipole. In addition, we impose the same phase for HH15 and HH17.

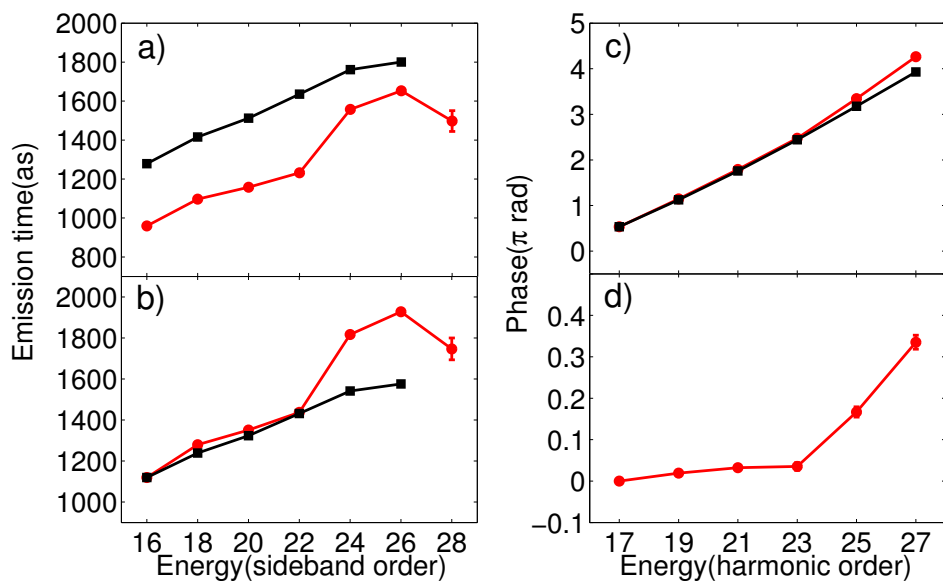


Figure 4.3: An example of RABBIT analysis ( $\theta = 0^\circ$ ): from the measured emission times to the calibrated phase. Emission times as measured a), Emission times with normalized absolute timing b), phase obtained by integrating the emission times c), CO<sub>2</sub> phases normalized by the krypton phase d). Red lines stand for the measurement of CO<sub>2</sub>, while the black lines are for krypton. The measurement was performed at  $1.6 \times 10^{14} \text{W/cm}^2$ .

In order to disentangle structural or dynamical interference, we performed a systematic experimental study of the harmonic emission as a function of the generating intensity for CO<sub>2</sub> and N<sub>2</sub>O aligned parallel to the laser polarization by using the RABBIT technique. The measured spectral intensity and phase for both CO<sub>2</sub> and N<sub>2</sub>O calibrated by the reference atom krypton are presented in Figure 4.4. The upper graphs are for the intensities of CO<sub>2</sub> and N<sub>2</sub>O, respectively. And the bottom ones are for the phases in the two molecules. The same phase analysis procedure is performed as Figure 4.3.

We observe clear signatures of molecular interferences: spectral minima and corresponding phase deviations for both systems, which are marked by the dashed lines. By increasing the intensity, the intensity minimum and phase jump are shifting to higher harmonic orders. Therefore, we confirm that the measured minima and the phase jump are related to the dynamical interference under our experimental conditions. From 1.0 to  $1.6 \times 10^{14} \text{W/cm}^2$ , the minimum shifts by 6 harmonic orders in N<sub>2</sub>O. But the minimum is less intensity dependent in CO<sub>2</sub>, which is shifted by two orders from 1.1 to  $1.4 \times 10^{14} \text{W/cm}^2$ . A possible reason that we see less dynamical behavior in CO<sub>2</sub> may be that we are just at the limit to observe dynamical interference because it only appears in the spectral region where both contributing channels have similar weight.  $\Delta I_p$  between the two channels in CO<sub>2</sub> being larger than in N<sub>2</sub>O, the lower lying orbital is expected to contribute less to HHG. And

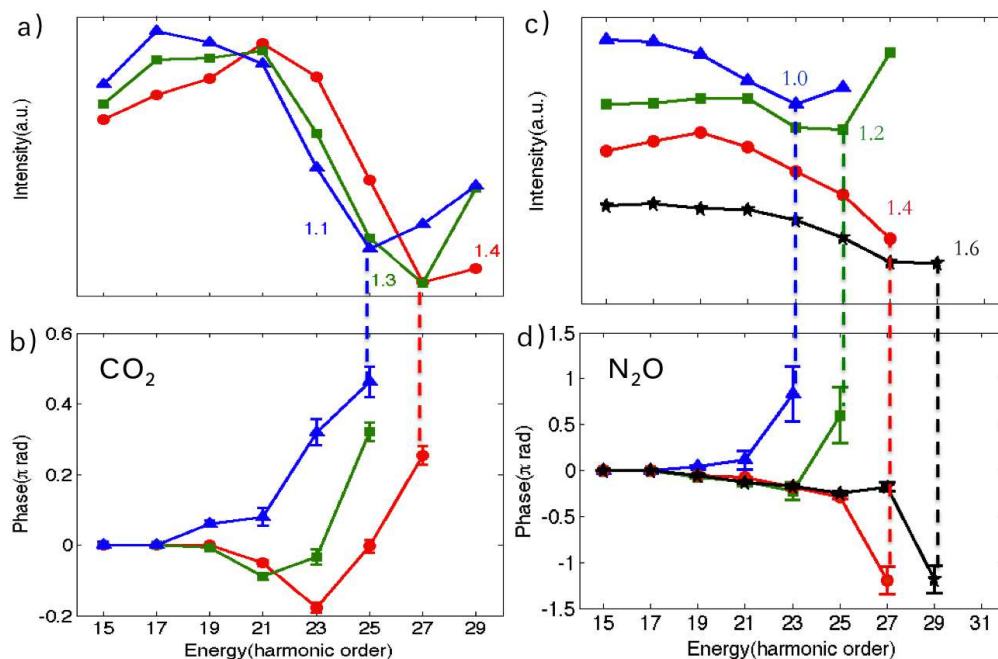


Figure 4.4: Spectral intensity for a)  $CO_2$  and c)  $N_2O$ , and phase for b)  $CO_2$  and d)  $N_2O$  measured by the RABBIT technique for different intensities when the molecular axis is aligned parallel to the laser polarization. Different colors correspond to different laser intensities, whose units are given in units of  $10^{14}W/cm^2$ . The related intensity minima and phase deviations are marked by colorful dashed lines.

the relative weight is changed by changing the intensity so that the evolution of the interference with intensity may be obscured. This may also explain why the amplitude of the phase jump measured in  $CO_2$  is only of  $\sim \pi/2$  (close to the previous measurements reported in Boutu et al. [46]), instead of  $\sim \pi$  in  $N_2O$ . This will be further studied in Section 4.5.

Another type of method for characterizing the harmonic intensity and phase has also been developed, which is two source interferometry (see section 2.3.2). Different from RABBIT, TSI is measuring the angular phase or in other words, the phase variation with molecular alignment angle for each harmonic order. Because TSI has no access to the harmonic spectral phase, we have to normalize to one molecular alignment angle to compare the variations of the different harmonic orders. From RABBIT measurements that will be detailed in Section 4.4, we know that the calibrated spectral phase is almost flat for  $CO_2$  perpendicularly aligned, so all the TSI measurements for different harmonic orders are normalized to 90 degrees. As for the harmonic intensities, they are normalized to 1 at 0 degree.

The results for  $CO_2$  are shown in Figure 4.5. The upper and lower panels correspond to two different laser intensities. At  $1.4 \times 10^{14}W/cm^2$ , the phase is flat for the first orders and starts to deviate for small angles at harmonic orders 21 and 23 with a negative shift of  $\sim -0.2\pi$ . Order 25 shows an intermediate behavior while orders 27 to 33 show a positive phase shift that reaches  $\sim \pi/2$ . At  $1.6 \times 10^{14}W/cm^2$ , the phase shows a smooth and relatively



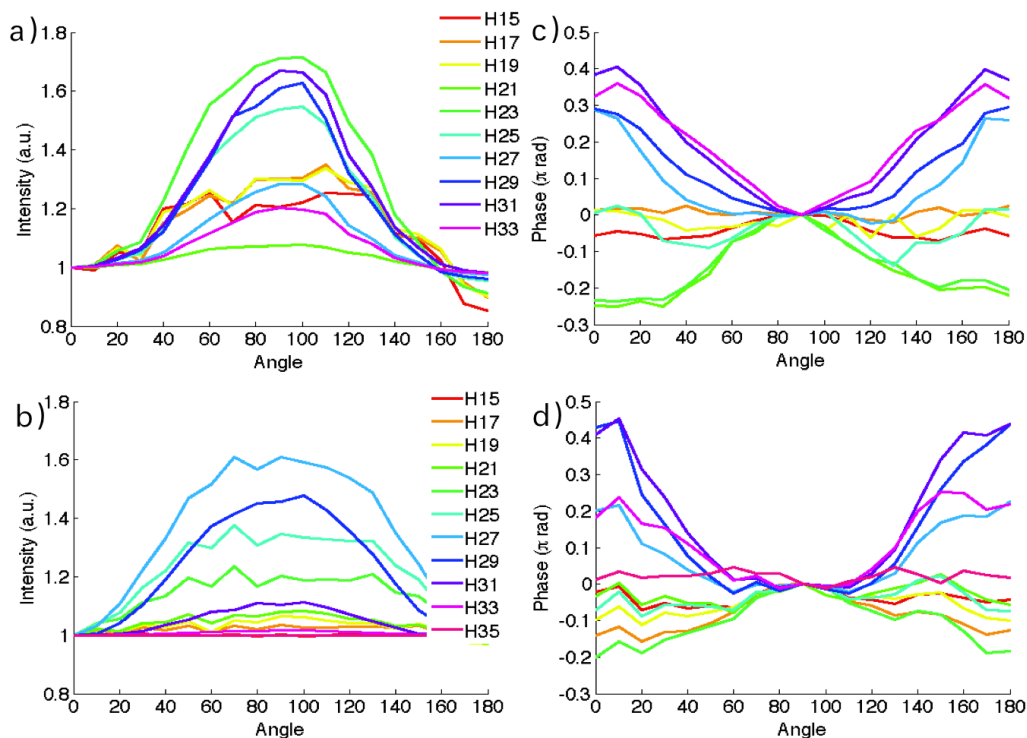


Figure 4.5: Intensity a),b) and phase c),d) for different harmonic orders generated from CO<sub>2</sub> measured by TSI for two laser intensities: a),c)  $1.4 \times 10^{14} \text{W/cm}^2$ , and b),d)  $1.6 \times 10^{14} \text{W/cm}^2$ . Different colors correspond to different harmonic orders indicated in the figure.

flat evolution until order 27 where it starts to deviate positively. But it is at H29 and H31 that the maximum deviation of  $\sim \pi/2$  is obtained. As compared to the lower intensity, the phase curves are flatter around 90 degrees and rise quite steeply at intermediate angles of 20-40 degrees. Concerning the harmonic intensities, they are all maximum at 90° with a contrast (ratio 90° over 0°) that in general increases with the order, despite some scattering of the data. The evolution of the highest orders may not be relevant since they suffer from low signal to noise ratio. In conclusion, like for the RABBIT measurements, we observe in CO<sub>2</sub> by using TSI some evolution with the laser intensity indicating dynamical interferences, even though the evolution is not very marked.

The results for N<sub>2</sub>O are shown in Figure 4.6. The measured intensities are plotted on the left and the phases, on the right. From top to bottom, the measurements are performed at laser intensities in the range  $1.2 - 1.8 \times 10^{14} \text{W/cm}^2$  by decreasing steps of  $0.2 \times 10^{14} \text{W/cm}^2$ . The phases are all normalized to 90°, and the amplitudes to 0°. At the highest intensity ( $1.8 \times 10^{14} \text{W/cm}^2$ ) in e), the phase curves for the low orders are very flat and start to deviate from this behavior at H29. Then, there is a sudden phase jump of  $\pi$  radians close to 40 degrees for harmonic order 31 and close to 50° for harmonic 33. At  $1.6 \times 10^{14} \text{W/cm}^2$  in d), the big phase evolution shifts to H29 and H31. Decreasing the intensity to  $1.4 \times 10^{14} \text{W/cm}^2$  in g), the harmonic order where the phase jump occurs is H27. Decreasing further the

intensity to  $1.2 \times 10^{14} W/cm^2$  in h), the phase jump then shifts to H25. Therefore, the shift of the phase jump with intensity in  $N_2O$  is also observed as a function of the alignment angle using TSI. These results are very consistent with that of the RABBIT measurements presented in Fig. 4.4: if we only look at 0 degree (and assume that the spectral calibration of the phase at  $90^\circ$  is correct), then we find a  $\pi$  phase jump between H23 and H25 at the lowest intensity that shifts to higher orders with increasing intensity.

Next, let us consider the harmonic intensities as a function of molecular alignment angle. For a) and b), the intensities for all harmonic orders are going up when rotating the molecules from parallel to perpendicular alignment, with a contrast depending on the order. And they are decreasing again from 90 to 0 degree by symmetry due to alignment and not orientation of the molecules. For c), this is also the case for the highest three orders (H27, H25 and H23) with an increasing broadening of the distribution. And for the lower harmonic orders, there appears a clear “double peak” structure, corresponding to a maximum emission not any more at  $90^\circ$ , but at an intermediate angle between  $50^\circ$  and  $60^\circ$ . At the lowest intensity shown in d), these “double peaks” are more obvious and even H23 starts to be like that. The reason for such “double peaks” may be related to the HOMO structure. The two dips at  $0^\circ$  and  $90^\circ$  could be a trace of the orbital nodal planes that suppress the ionization. The orbital lobe in between may create the double peaks due to the fact that the ionization will favor the intermediate alignment angles. The contribution of the HOMO-1 may be the reason why these “double peaks” do not appear for high orders (cutoff region) and high intensities. Indeed, these are the conditions where one expects a strong contribution from the HOMO-1 that may blur the clear behavior observed at low intensity and harmonic orders, where the HOMO dominates.

As a summary, two different characterization methods have been used in this section in order to study the structural or dynamical origin of the interferences observed in the harmonic emission. These two methods, while probing two different dimensions (photon energy and alignment angle) give consistent results. And they both confirm the observation of dynamical interferences under our experimental conditions.

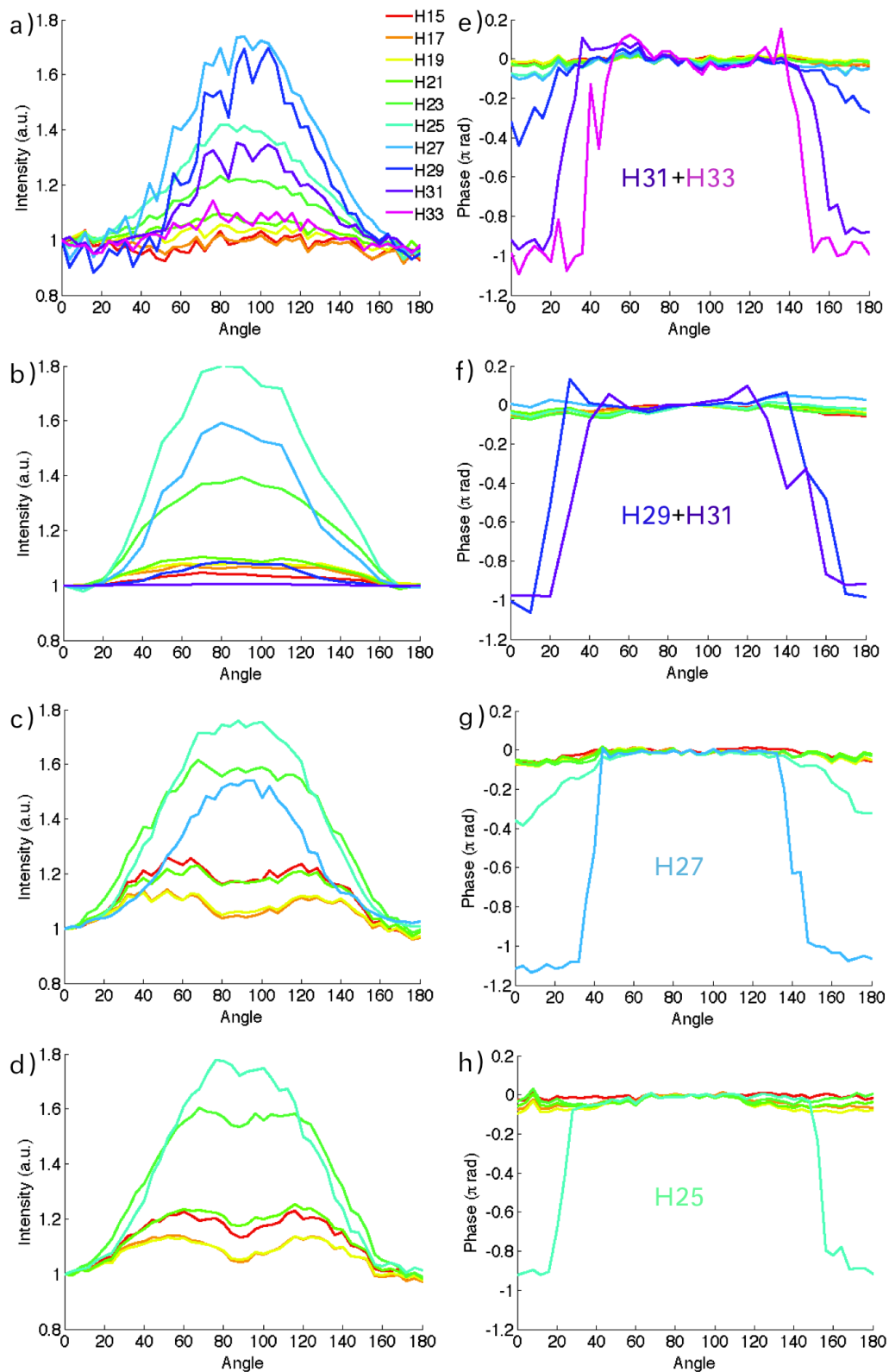


Figure 4.6: Intensity a),b),c),d) and phase e),f),g),h) for different harmonic orders generated from  $N_2O$  for different driving intensities measured by TSI. From top to bottom, the measurements are performed at laser intensities from  $1.8 \times 10^{14} W/cm^2$  to  $1.2 \times 10^{14} W/cm^2$  with a step of  $0.2 \times 10^{14} W/cm^2$ . Different colors correspond to different harmonic orders.

### 4.3 Combining TSI with RABBIT

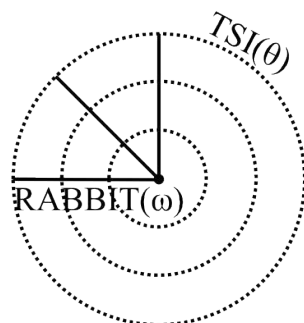


Figure 4.7: Harmonic phase plot in polar coordinates. The radial coordinate represents the energy (harmonic order) and the angular coordinate indicates the molecular alignment angle.

TSI and RABBIT are measuring the harmonic phase in two different dimensions: TSI measures the phase as a function of the molecular alignment angle for each harmonic order, but it does not access the relations between harmonic orders as shown by the dotted circles in Figure 4.7. RABBIT characterizes the spectral phase, i.e. the phase as a function of harmonic order as given by the solid lines in Figure 4.7, but without any reference between different alignment angles. So in each technique, we have to make assumptions in order to access the full phase variation. For example, we had to normalize at  $90^\circ$  the phases measured for the different harmonic orders by TSI in order to access the spectral variation. Similarly, we always assume that the spectral phase is less angular dependent for the lowest harmonic order, and so we normalize the spectral phase at H15 for all alignment angles in order to get the angular phase. We would not need that anymore if we could combine the two measurements. As a matter of fact, to get a full phase mapping, only one measurement of the complementary technique is needed: a single RABBIT measurement for instance at  $90^\circ$  is enough to complete a set of TSI measurements and a single TSI measurement for instance at H15 is enough to complete a set of RABBIT measurements. By performing a full set of measurements for both techniques, one gets an oversampling of the phase space and one can check very stringently the consistency of the two techniques.

Such a combination has never been performed up to now because of the complexity of the two techniques that furthermore need to be implemented in exactly the same generation conditions. Indeed, the harmonic phase is very sensitive to the experimental conditions such as molecular alignment quality and laser intensity. Because the two measurements were done separately, it is important to make sure that they have comparable experimental conditions before comparing or combining them. In particular, the experimental determination of the laser intensity always involves quite large error bars. For this purpose, I compare the harmonic spectra in the two measurements. As an example, I plot in Figure

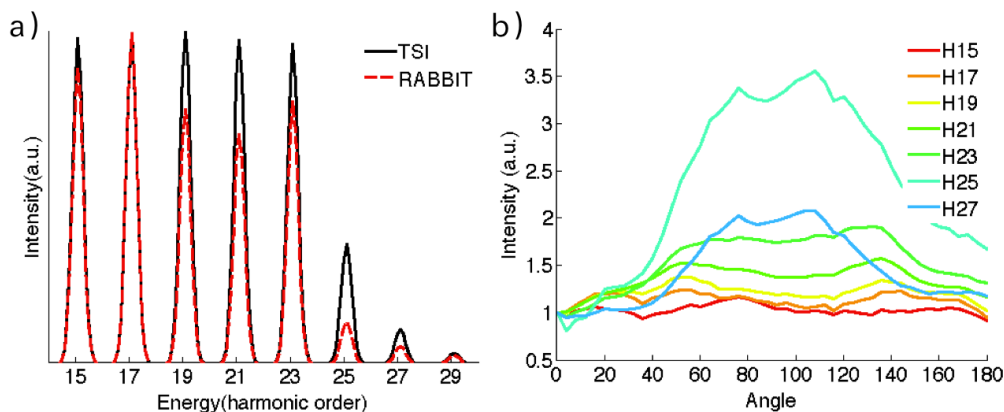


Figure 4.8: a) Harmonic spectra measured in  $N_2O$  with RABBIT (red dashed line) and TSI (black solid line) at  $0^\circ$ . The laser intensity is  $1.4 \times 10^{14} W/cm^2$ . b) Harmonic intensity as a function of the alignment angle for the same laser intensity as in a) obtained from RABBIT. The different colors correspond to the different harmonic orders, indicated in the figure.

4.8a) the two spectra obtained in  $N_2O$  from RABBIT and TSI at an estimated intensity of  $1.4 \times 10^{14} W/cm^2$ . The spectra are very similar with cut-off positions at H25. Then, I compared the angular variations of the harmonic intensities obtained from the two techniques in these conditions. The TSI and RABBIT results are shown in Figure 4.6c) and 4.8b), respectively. Note that the contrast of the variation is different because we align the molecules only at one of the two sources in TSI, while aligning the whole source in RABBIT, which explains the larger contrast. However, the general trend is very similar in both measurements. The angular variations in the RABBIT measurements have a single peak for high harmonic orders, a broadening with decreasing order and then double peaks for low harmonic orders in Figure 4.8 b), which is also the case for the TSI measurements in Figure 4.6 c). Finally, the phase analysis performed in the preceding Section revealed a phase jump at H27 for both measurements. Since this phase jump is the result of a dynamical interference, its position is closely related to the generation conditions. Therefore, all the three analysis above prove that we have comparable conditions.

To combine the two sets of data, we have to build a “bridge” to connect the 2 dimensions. There are many ways to do this. Since the angular variation of the phase is accurately measured using TSI, I chose one measurement from RABBIT at a given angle to perform the bridge to connect all the TSI measurements and get the full phase mapping. Then, in order to check the compatibility of the two measurements, I extracted a set of data in energy domain for another alignment angle from the obtained phase map. Eventually, I compared it with the RABBIT measurement for this alignment angle. Figure 4.9 a) shows a mapping of the harmonic phase obtained by using the RABBIT measurement at 90 degree as a bridge. Then I take a line out for  $0^\circ$  along the photon energy dimension (red solid line in Figure 4.9 b)) to compare with the RABBIT measurement for 0 degree (blue squares in Figure 4.9 b)).

The extracted data is in very good agreement with the RABBIT measurement. Therefore, these two sets of data are indeed consistent and give a full mapping of the harmonic phase. The phase map in Figure 4.9 a) contains both the TSI information, like the phase deviation of  $\sim \pi$  for H27 around  $40^\circ$  degrees, and the RABBIT information, like the phase jump of  $\sim \pi$  for  $0^\circ$  at H27. But in addition, it gives the full variation of the phase jump in the (energy, angle) space. The phase variation with angle for the lowest harmonic order (H15) is indeed quite flat, which proves our previous assumption for the normalization of the RABBIT measurements. Similarly, the spectral phase is very flat at  $90^\circ$ , providing a reference for the TSI measurements. Figure 4.10 shows the maps for  $N_2O$  at two other intensities. They both give good results, and show that the phase jump position is shifting with intensity.

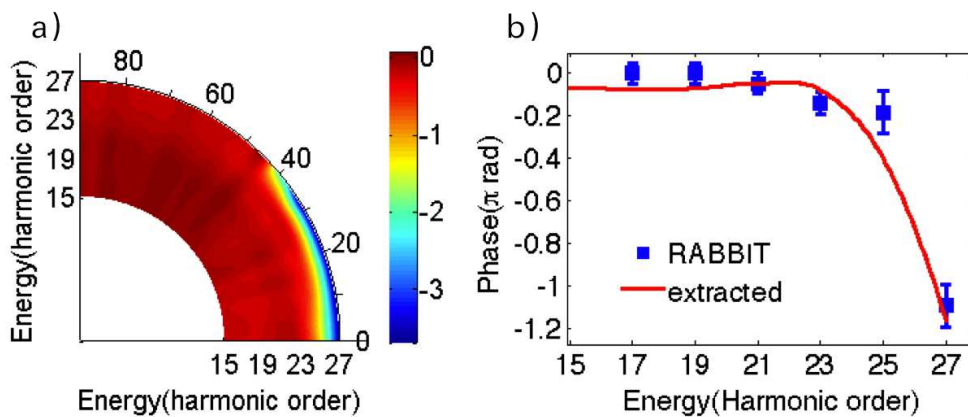


Figure 4.9: a) Full harmonic phase map for  $N_2O$  at  $1.4 \times 10^{14} W/cm^2$ . b) Comparison of the data extracted from the map at  $0^\circ$  with the RABBIT measurement at this angle.

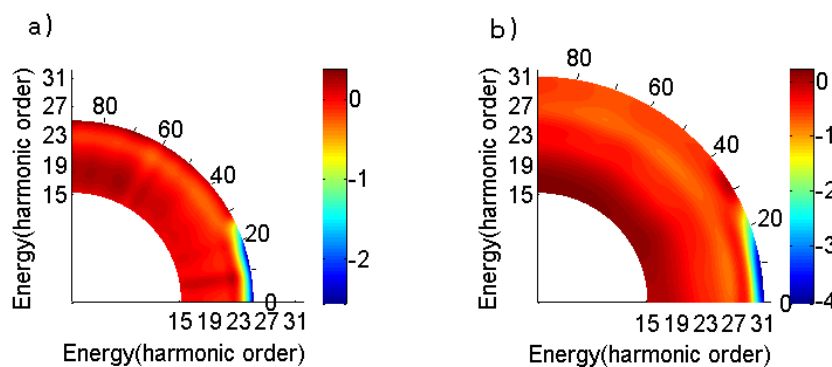


Figure 4.10: Full harmonic phase map for  $N_2O$  at  $1.2 \times 10^{14} W/cm^2$  a) and  $1.6 \times 10^{14} W/cm^2$  b).

#### 4.4 Experimental comparison of the harmonic emission from N<sub>2</sub>O and CO<sub>2</sub>

We have already compared the properties of N<sub>2</sub>O and CO<sub>2</sub> molecules. The two orbitals contributing to HHG at 0 degree have similar structures (see Figure 4.1). From previous harmonic intensity measurements in these two molecules, people have not found big differences between them, except for a slight shift of the spectral minimum position [157, 177–180, 182]. Since the phase contains additional information as compared to the intensity, it is interesting to investigate if there is any difference in such two similar systems. It may provide us with the possibility to access more information on the underlying physics. Note that previous TSI measurements revealed  $\pi$  phase jumps in both molecules when scanning the delay between the alignment and generation laser pulses in the half or 3/4th revival [157]. These phase jumps were attributed to the change of the molecular distribution from alignment to anti-alignment (both laser pulses had parallel polarizations). By staying at the half revival and changing the alignment laser polarization, we may have a finer angular sampling of the harmonic phase and also narrower angular distributions. In this Section, I will discuss the experiments performed with the two phase characterization methods in the two gases in the same experimental conditions.

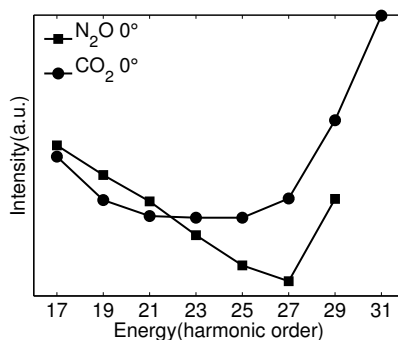


Figure 4.11: Harmonic spectra measured with RABBIT in CO<sub>2</sub> and N<sub>2</sub>O aligned at 0 degree at  $1.4 \times 10^{14} \text{ W/cm}^2$  and calibrated with the krypton spectrum.

Figure 4.11 shows the harmonic spectra measured by RABBIT for N<sub>2</sub>O and CO<sub>2</sub> aligned at 0 degree, after calibration by Krypton reference. The minimum for CO<sub>2</sub> is quite shallow and centered at H23 while for N<sub>2</sub>O, it is deeper and at H27. These minima disappear when the alignment angle is increased to 90° (not shown). This is all the information that we can get from the intensity measurements. So let us have a look at the phase measurements. Figure 4.12 presents the calibrated harmonic phase for CO<sub>2</sub> and N<sub>2</sub>O for different molecular alignment angles. The phases are all flat for both molecules at 90 degrees. But the phases start to deviate at low angles. Especially, there are clear deviations for 0 degree. The phase jump positions are the same as the minimum positions, i.e. about H23 for CO<sub>2</sub> and H27 for N<sub>2</sub>O. Moreover, phase measurements provide us more detailed information. First, the sign

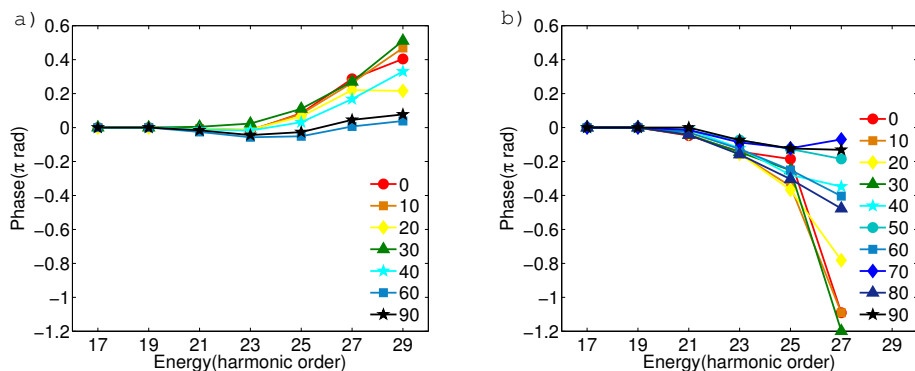


Figure 4.12: Harmonic phase measured with RABBIT in  $CO_2$  a) and  $N_2O$  b) at  $1.4 \times 10^{14} W/cm^2$  and calibrated by krypton, for different alignment angles indicated in the panels. The error bars, that are about of the size of the symbols, are removed for clarity.

of the phase jump is negative in the case of  $N_2O$  while being positive for  $CO_2$ . Second, the jump is very sudden in  $N_2O$ , which only happens at H27. And its amplitude is almost  $\pi$  radians. In contrast, the phase deviation is smooth in  $CO_2$ , starting at H23 and spreading over several harmonic orders. And its amplitude is only about  $\pi/2$  radians. Therefore, phase measurements are indeed sensitive enough to observe significant differences between the two gases that have never been reported up to now.

It is worth to note that the RABBIT, like all interferometric techniques, follows the trend of the phase deviation when the phase jump is small enough or spread over many orders as in the case of  $CO_2$ . But if the phase jump is sudden and close to  $\pi$  between adjacent harmonic orders, like in the measurement of  $N_2O$ , it cannot determine the sign since the interferometric measurement is done modulo  $2\pi$ . Fortunately, the phase variation with angle at H27 in Figure 4.12 shows a clear evolution towards negative values for intermediate angles. In order to check this more thoroughly, we implemented TSI for these two molecules in the same conditions. The results were presented in Figure 4.5 c) and 4.6 g), respectively. In this last Figure, it also appears clearly that the phase starts to shift negatively for H25 before reaching  $\sim \pi$  for H27. So we can now compare the evolution in the two gases for H27 as plotted in Figure 4.13. The phase jump is negative in  $N_2O$  while being positive in  $CO_2$ . Also, the phase varies smoothly and with less amplitude in  $CO_2$  than in  $N_2O$ . Therefore, we observe significant differences in the phase behavior for  $CO_2$  and  $N_2O$ , despite the similar structures of the contributing orbitals. What is the reason for that? And what kind of information can we extract from these data?

#### 4.5 Modeling harmonic generation from $N_2O$ and $CO_2$

In order to answer the questions raised in the previous sections, I developed a simple model to help us understand the underlying physics. As already discussed, tunnel ionization



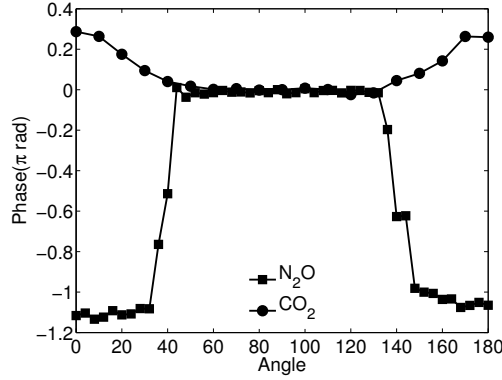


Figure 4.13: Harmonic phase for H27 measured by TSI in CO<sub>2</sub> and N<sub>2</sub>O at  $1.4 \times 10^{14} \text{ W/cm}^2$ .

may occur coherently from different orbitals simultaneously creating different ionization channels in molecules. In this case, the total harmonic dipole is a coherent superposition of the contributing channels. Since the  $\Delta I_p$ s in both molecules are big (3.5eV for CO<sub>2</sub> and 4.3eV for N<sub>2</sub>O), the channel coupling effects between channels are neglected. Therefore, the molecular dipole can be written as:

$$D(\omega, I_L, \theta) = \sum_i \gamma_{ion,i}(\omega, I_L, \theta) a_{con,i}(\omega, I_L) e^{i\varphi_{con,i}} d_{rec,i}(\omega, \theta) e^{i\varphi_{rec,i}} \quad (4.1)$$

where  $i = X, A, B, \dots$ . Each channel contains three steps: tunnel ionization ( $\gamma_{ion,i}$ ), acceleration ( $a_{con,i} e^{i\varphi_{con,i}}$ ) and recombination ( $d_{rec,i} e^{i\varphi_{rec,i}}$ ). Following [47], we here assume that the tunnel ionization phase of CO<sub>2</sub> is equal to 0 because the wave function after electron tunneling through the barrier is an extension of the real wave function that characterizes the bound state for each channel [47]. It is then reasonable to assume that the tunnel ionization phases of the different channels in N<sub>2</sub>O are also equal to 0 because of the similar electronic structure. As already discussed, we consider that for N<sub>2</sub>O aligned at 0 degree, there are mainly two (X and A) channels that contribute to HHG. Thus, the dipole is given by:

$$\begin{aligned} D_{N_2O} &= \sum_{i=X,A} \gamma_{ion,i}(\omega, I_L, \theta) a_{con,i}(\omega, I_L) e^{i\varphi_{con,i}} d_{rec,i}(\omega, \theta) e^{i\varphi_{rec,i}} \quad (4.2) \\ &= \gamma_{ion,X} a_{con,X} e^{i\varphi_{con,X}} d_{rec,X} e^{i\varphi_{rec,X}} \left( 1 + \frac{\gamma_{ion,A} a_{con,A} d_{rec,A}}{\gamma_{ion,X} a_{con,X} d_{rec,X}} e^{i(\varphi_{con,A} - \varphi_{con,X}) + i(\varphi_{rec,A} - \varphi_{rec,X})} \right) \end{aligned}$$

The first two factors ( $\gamma_{ion,X} a_{con,X}$ ) are mainly dependent on the driving laser intensity and the ionization potential of the medium, so they can be partly removed by calibrating with the reference atom (Krypton). The recombination dipole of HOMO ( $d_{rec,X} e^{i\varphi_{rec,X}}$ ) divided by that of Krypton remains in the factorized factor. This may induce important amplitude and phase variations close to, e.g., structural interferences. However, far from them, it will have a smooth behavior over the narrow range where the dynamical interference will occur. Therefore, we write the N<sub>2</sub>O dipole for 0 degree after calibration as:

$$D_{cal} = \frac{D_{N_2O}}{D_{Kr}} \approx 1 + \alpha e^{i(\Delta\varphi_{con} + \Delta\varphi_{rec})} \quad (4.3)$$

where  $\alpha$  is the relative weight between channels A and X. This simple model tells us that the dynamical destructive interference will occur when the total phase difference is equal to an odd multiple of  $\pi$ :

$$\Delta\varphi_{tot} = \Delta\varphi_{con} + \Delta\varphi_{rec} = \pm n\pi (n = 1, 3, 5\dots) \quad (4.4)$$

where  $\Delta\varphi_{con}$  is the phase difference in the continuum and  $\Delta\varphi_{rec}$  is the phase difference in the recombination between channels A and X. Similarly, a constructive interference happens when the phase difference equals to an even multiple of  $\pi$ , but it is more difficult to identify precisely in the spectrum because the dipole varies slowly through the maximum.

The continuum phase difference can be calculated by the strong field approximation, and is close to  $-\Delta I_p \tau_\omega$  [184]. Here,  $\Delta I_p$  is the ionization energy difference between the two contributing ionization channels and  $\tau_\omega$  is the average excursion time of the trajectory corresponding to the emission of harmonic  $\omega$ . We consider here only the short trajectories since their contributions are selected in our experimental conditions by phase matching and on-axis spatial filtering. The recombination dipole phase difference is strongly influenced by the symmetry of the molecular orbitals. Because we implement molecular alignment instead of orientation, the originally asymmetric orbitals of N<sub>2</sub>O are artificially symmetrized. As a result, the HOMO and HOMO-1 orbitals of N<sub>2</sub>O can be considered to have  $\pi_g$  and  $\sigma_u$  symmetry, respectively, the same as for HOMO and HOMO-2 of CO<sub>2</sub>. If we model the continuum states by plane waves, we get a phase difference of  $\pm\pi/2$  for these plane wave dipoles. There is an uncertainty on the sign. The calculated total phase difference for an intensity of  $1.4 \times 10^{14} \text{ W/cm}^2$  is shown in Fig. 4.14 a) for N<sub>2</sub>O and b) for CO<sub>2</sub>. If the recombination phase difference is positive as shown by the dashed lines, there is a destructive interference close to H11 and a constructive interference at H27 in N<sub>2</sub>O, while there is a destructive interference close to H31 in CO<sub>2</sub>. None of these are observed in the experiments. If the recombination phase difference is negative as shown by the solid lines, there is a destructive interference close to H27 in N<sub>2</sub>O and also a destructive interference close at H23 in CO<sub>2</sub>, which are both fitting nicely the measured dynamical interference positions. Furthermore, the positions measured for the other intensities are also reproduced by recalculating the continuum phase difference for these intensity values. Therefore, the recombination phase difference in our case is close to  $-\pi/2$  for both CO<sub>2</sub> and N<sub>2</sub>O.

Now that we are able to reproduce the interference positions, we can compare the intensity and phase of the calibrated dipole (eq. 4.3) to the experimental results, and also evaluate the  $\alpha$  dependence of the results. Figure 4.15 shows the absolute amplitude and phase of the calibrated dipole of N<sub>2</sub>O. The different curves correspond to different relative weights ( $\alpha$ ) between channels A and X. In good agreement with the experimental results, we can see a clear minimum appearing at H27 in the amplitude as well as a corresponding phase jump at the same position in the phase simulation. Particularly interesting is the finding that in the simulated phase the contributing ratio  $\alpha$  plays an important role in de-

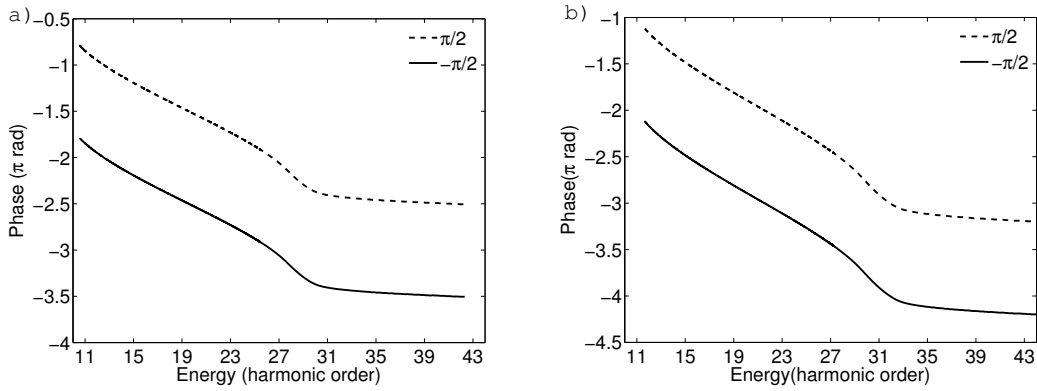


Figure 4.14: Total phase difference of the two channels involved in HHG for a) N<sub>2</sub>O and b) CO<sub>2</sub> for an intensity of  $1.4 \times 10^{14} \text{W/cm}^2$ . The dashed and solid lines are the results obtained by using  $\pi/2$  and  $-\pi/2$  for the recombination phase difference, respectively.

termining the phase jump. When  $\alpha$  is equal to 1, meaning that channels A and X contribute equally to HHG, there is a perfectly destructive interference. The amplitude minimum goes to 0 and the phase jump is exactly equal to  $\pi$ . When  $\alpha$  is smaller than 1, meaning that the HOMO contributes more to HHG, the phase jump is positive and small, which is very similar to the measurements in CO<sub>2</sub>. Conversely, if  $\alpha$  is bigger than 1, the phase jump is negative and big like in the measurements in N<sub>2</sub>O.

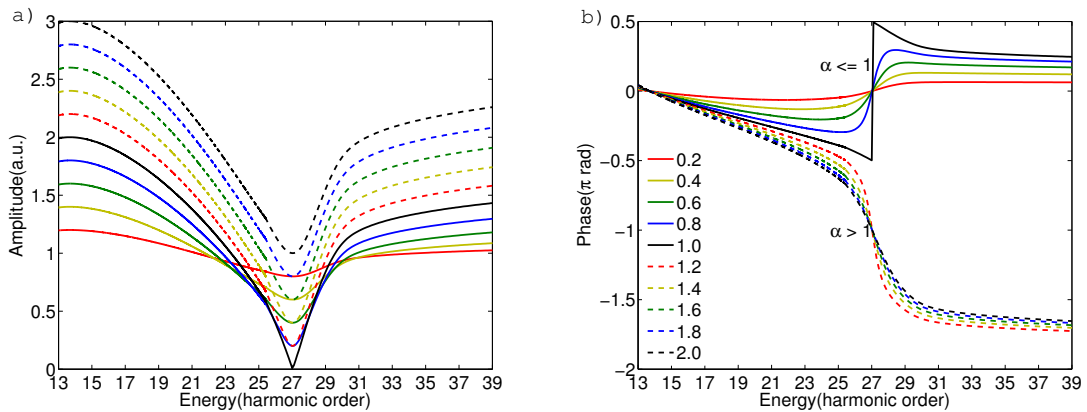


Figure 4.15: a) Amplitude and b) phase of the calibrated dipole of N<sub>2</sub>O. The different curves correspond to different relative weights ( $\alpha$ ) of channels A and X.

So, we are now able to understand the differences between the measurements in CO<sub>2</sub> and N<sub>2</sub>O: since  $\Delta I_p$  is smaller in N<sub>2</sub>O than in CO<sub>2</sub>, the contribution to HHG from HOMO-1 becomes larger than that of HOMO ( $\alpha > 1$ ), so that the sign of the phase jump is switched from positive to negative. From this model, we find that there are two requirements in order to observe dynamical interferences. First, the phase difference between two HHG channels must be an odd multiple of  $\pi$ . Second, the relative weight between these two channels

has to be close to 1. The contrast of the minimum and of the phase jump is reduced as long as the lower lying orbital does not contribute efficiently to HHG. As we can see from Figure 4.15, the minimum and phase jump are almost invisible when  $\alpha = 0.2$ . Therefore, even though we can get odd multiples of  $\pi$  somewhere in the spectrum, we still need close contributions to HHG for the two channels to observe that. Maybe this is the reason why not all measurements show evidence of multi-orbital contributions since people have to find the right conditions to satisfy both requirements.

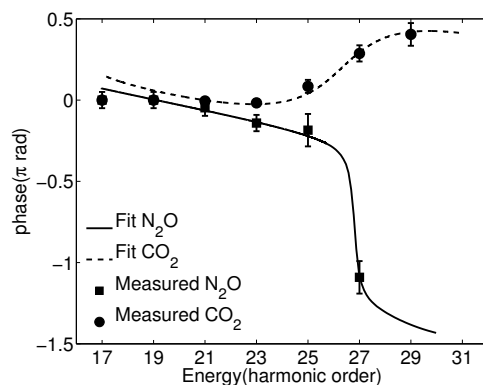


Figure 4.16: Theoretical fit of the spectral phase measured by RABBIT in  $CO_2$  (dashed line) and  $N_2O$  (solid line) when the molecules are aligned parallel to the laser polarization at  $1.4 \times 10^{14} W/cm^2$ . The measured data are shown by the symbols indicated in the figure.

The simple model also provides us with the possibility to extract the relative weight of the contributing channels. Figure 4.16 shows the theoretical fits from the model to the RABBIT measured phases. The circle points are the phases measured for  $CO_2$  aligned at 0 degree, and the dashed line is the fit from the model by using a ratio ( $\alpha$ ) between channel B and X of 0.65. The nice agreement means that the contribution to harmonic generation from channel B is 65% of that of channel X in amplitude, and 42% in intensity. The square symbols are the phases measured for  $N_2O$  and the solid line is the theoretical fitting with a ratio ( $\alpha$ ) of 1.05 between channel A and X. Thus, channels A and X have similar contributions to HHG when  $N_2O$  is aligned parallel to the laser polarization. The channel A can even contribute a bit more as compared to channel X, which is the first time people have evidence of higher contribution from a lower lying orbital than from HOMO. Moreover, the model gives good agreement to the other experimental results as well for both  $CO_2$  and  $N_2O$  at different driving intensities when the molecules are parallel aligned, as shown in Figure 4.17. It is worth noting that in principle, we extract the relative weight with good precision only in the region of destructive interference, where this weight determines stringently the shape of the interference. Now, obviously this weight is not constant over the whole spectrum: the lower-lying orbitals, because of their larger  $I_p$ s, have a slightly extended cutoff, which increases their weight relative to the HOMO in this region. In the plateau region, we

expect that the HOMO will contribute more to the emission, changing the relative weight in favor of the HOMO. It is thus amazing that our model can fit so nicely also the phase evolution in the plateau region.

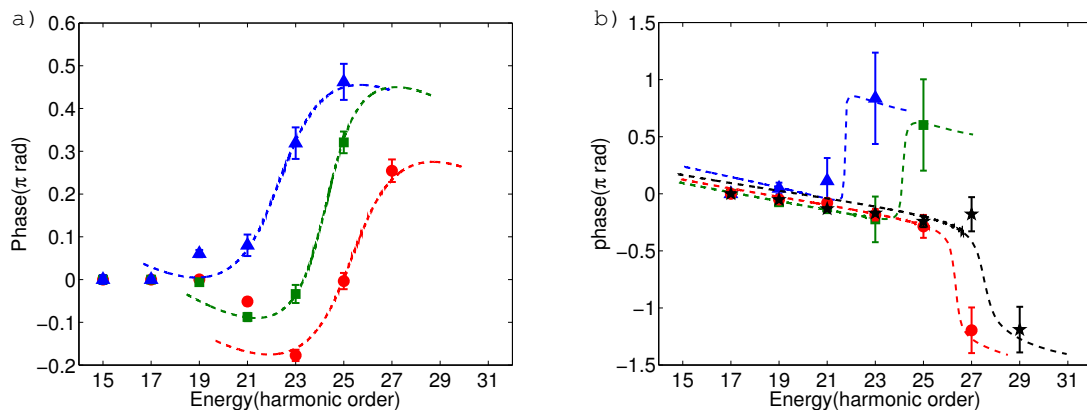


Figure 4.17: Theoretical fits (dashed lines) for the spectral phase measured in CO<sub>2</sub> a) and N<sub>2</sub>O at different laser intensities. The experimental data are shown with the same symbols as in Figure 4.4 with different colors corresponding to different generating intensities.

## 4.6 Improving the model

This simple model already provides us with a clear understanding of the underlying physics. Next, we can try to further improve it by lifting some of the assumptions made: instead of plane-wave dipoles, use scattering wave recombination dipoles; instead of single molecule response, consider the molecular alignment angular distribution.

### Recombination dipole moments of N<sub>2</sub>O and CO<sub>2</sub>

We collaborated with Prof. Robert Lucchese from Texas A&M University who developed codes of quantum chemistry performing *ab initio* quantum scattering calculations where the continuum states of the electron wavepacket are calculated by taking into account the effect of the molecular potential [179, 180]. The scattering-wave ionization dipole moments calculated for CO<sub>2</sub> and N<sub>2</sub>O as a function of molecular alignment and photon energy are shown in Figures 4.18 and 4.19, respectively. We are showing the parallel dipoles, i.e., the ones corresponding to an electron emission in the direction of the photon polarization, which are the ones mainly involved in HHG (of course, their complex conjugates describe the recombination). Each of the Figures contains the data relative to three molecular orbitals (HOMO, HOMO-1 and HOMO-2). The orbital symmetry appears clearly in the dipole phase. As shown in Figure 4.1, HOMO and HOMO-2 of CO<sub>2</sub> are antisymmetric with respect to the plane perpendicular to the molecular axis, so there is a  $\pi$  phase difference on either side of 90 degree (see Figure 4.18 b) and f)). In contrast, HOMO-1 of CO<sub>2</sub> is symmetric with respect

to 90 degree, and this appears in the dipole phase in Figure 4.18 d). For N<sub>2</sub>O, HOMO and HOMO-1 have similar structures as HOMO and HOMO-2 in CO<sub>2</sub>, so there is also a sign switch before and after ~ 90 degrees as shown in Figure 4.19 b) and d), that is absent for HOMO-2 as presented in Figure 4.19 f). However, the molecule (and thus its orbitals) being asymmetric, the dipoles do not present the mirror (anti-)symmetry any more. So the two parts with respect to 90 degree are not exactly the same, which means that the electron-ion recollisions on the Oxygen or Nitrogen side are different (0° corresponds to an electron recombining on the oxygen side). Note that the molecule being symmetric with respect to the plane containing the internuclear axis, the orbitals and corresponding dipoles will be symmetric or antisymmetric with respect to it.

In the experiment, the orbitals are artificially symmetrized by molecular alignment instead of orientation. Therefore, we have to coherently sum up the oriented orbital dipoles:

$$d_{aligned}(\theta) = d_{oriented}(\theta) + \alpha e^{i\Delta\varphi} d_{oriented}(\pi - \theta) \quad (4.5)$$

where  $\alpha$  is the relative weight of the electron wavepackets recolliding on the oxygen/nitrogen sides and  $\Delta\varphi$  is the phase difference involved in the symmetry around 180°. For the moment, we consider that the recolliding wavepackets are the same, so  $\alpha = 1$ .  $\Delta\varphi$  has to be  $\pi$  for HOMO and HOMO-1 but 0 for HOMO-2. The results of the coherent summation for N<sub>2</sub>O orbitals are shown in Figure 4.20, and will be discussed in the next section.

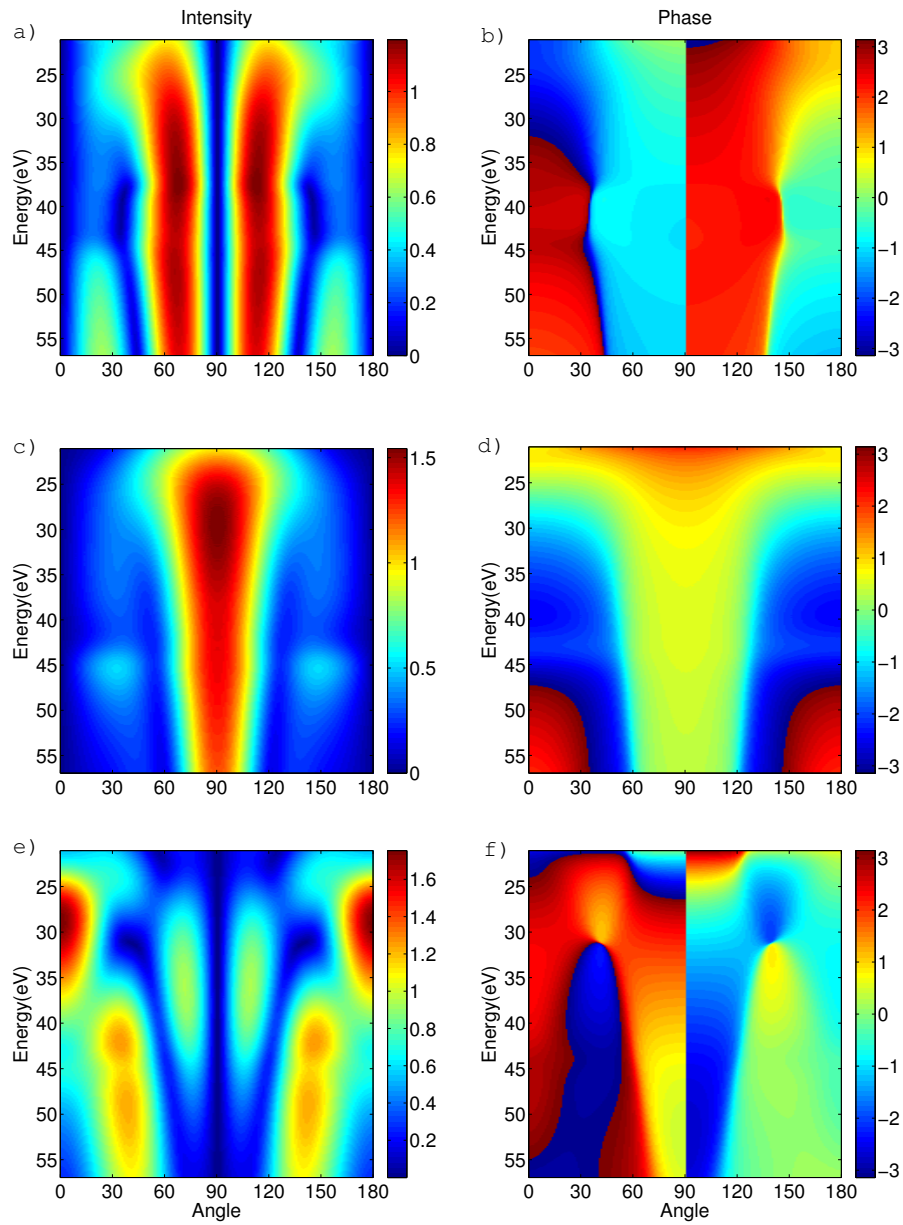


Figure 4.18: Ionization scattering wave dipoles of aligned CO<sub>2</sub> as a function of alignment angle and photon energy for different orbitals: HOMO dipole intensity (a) and phase (b), HOMO-1 intensity (c) and phase (d), HOMO-2 intensity (e) and phase (f).

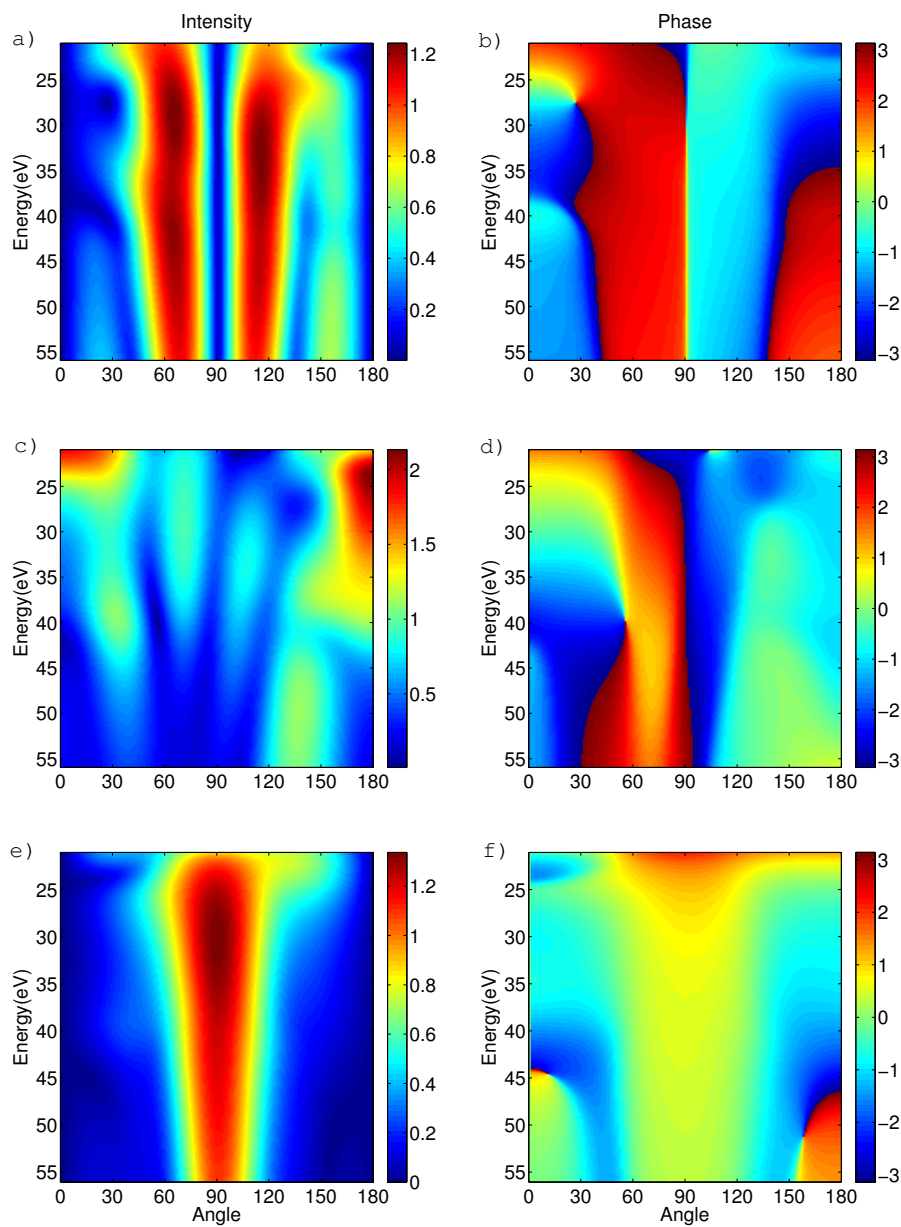


Figure 4.19: Ionization scattering wave dipoles of oriented  $N_2O$  as a function of alignment angle and photon energy for different orbitals: HOMO dipole intensity (a) and phase (b), HOMO-1 intensity (c) and phase (d), HOMO-2 intensity (e) and phase (f).



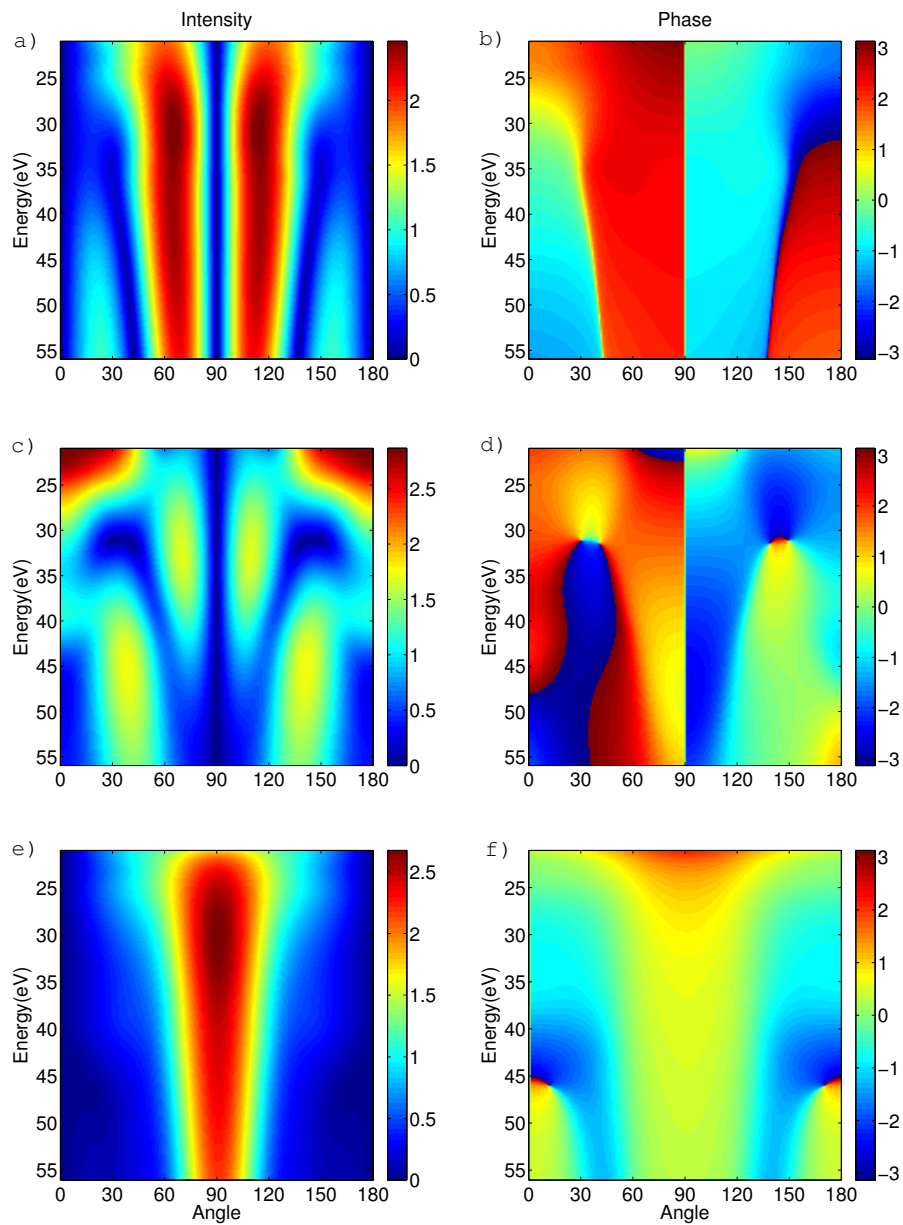


Figure 4.20: Ionization scattering wave dipoles of aligned  $N_2O$  as a function of alignment angle and photon energy for different orbitals: HOMO dipole intensity (a) and phase (b), HOMO-1 intensity (c) and phase (d), HOMO-2 intensity (e) and phase (f).

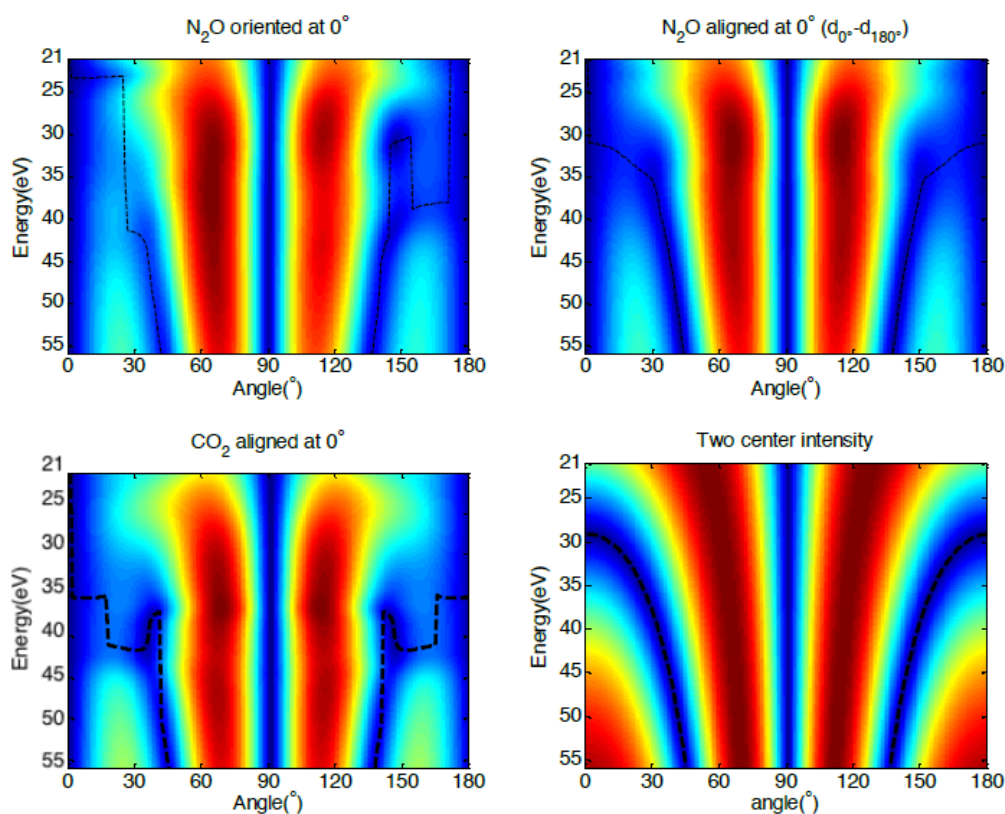


Figure 4.21: Comparison of the intensity of the HOMO dipoles for: (upper left) oriented N<sub>2</sub>O, (upper right) aligned N<sub>2</sub>O, (lower left) aligned CO<sub>2</sub>, (lower right) two center-interference model. The position of the spectral minimum for each angle is marked by dashed lines.

### Study of the structural interferences in the dipoles

As mentioned before, the HOMO structure may induce a structural interference in the recombination dipole, which position depends on the molecular alignment angle but does not depend on the laser intensity. A simple case for structural interference is given by the two-center interference model proposed by Manfred Lein [39, 40] (see Section 3.4). For an antisymmetric molecular orbital, the corresponding dipole may be written as [157]:

$$d_{TCM}(\omega, \theta) = A \sin\left(\frac{\pi R}{\lambda} \cos \theta\right) \quad (4.6)$$

where  $A$  is a constant,  $R$  is the internuclear distance, and  $\lambda = 2\pi/\sqrt{2\omega}$  is the De Broglie wavelength of the recolliding electron.

Figure 4.21 displays the comparison of the different HOMO dipoles. There is a striking similarity of these dipoles due to 2 features: i) the obvious zero at 90° coming from the common antisymmetry and ii) a minimum moving towards high energy with increasing angle (in the first quadrant). The position of this minimum is marked by a dashed line for comparison. The dipole from the two-center interference model (lower right panel) allows

to identify it as the signature of a structural interference that moves from 30 eV at  $0^\circ$  to 55 eV at  $45^\circ$ . When considering the dipole of oriented  $N_2O$  as shown by the upper left panel, the spectral minimum does not behave exactly the same on either side of 90 degree due to the difference in recollision on O or N sides. Moreover, it seems blurred due to the orbital asymmetry. After the symmetrization, the  $N_2O$  dipole presents very nice and clear minima, and is very similar to the  $CO_2$  dipole (compare the upper right and lower left panels). Note that there is a phase jump at the position of the observed minimum that is shifting correspondingly with energy (not shown). The two center model thus surprisingly predicts the major features of the scattering wave dipoles, with almost the same structural interference position.

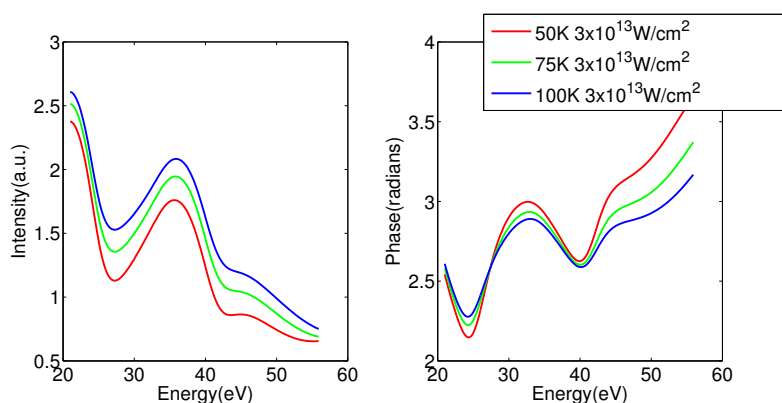


Figure 4.22: Scattering wave dipole of oriented  $N_2O$  HOMO ( $0^\circ$ ) integrated over the angular distribution. Different colors in the figure correspond to different temperatures of the medium indicated in the figure. The alignment intensity in all cases is  $3 \times 10^{13} W/cm^2$ . (left) Intensity, (right) Phase.

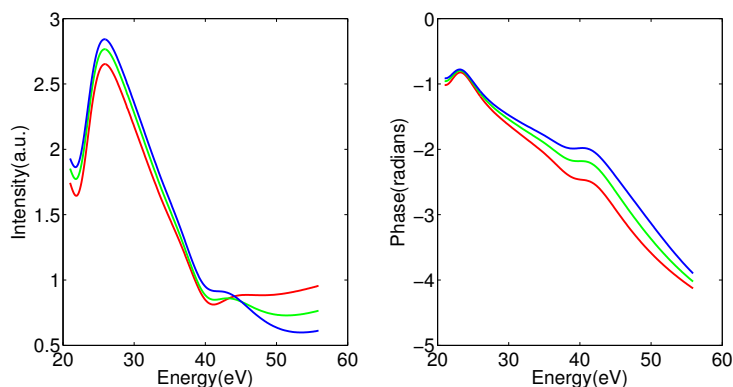


Figure 4.23: Scattering wave dipole of oriented  $N_2O$  HOMO ( $180^\circ$ ) integrated over the angular distribution. Different colors in the figure correspond to different temperatures of the medium. (left) Intensity, (right) Phase.

These results correspond to the case where all the molecules are perfectly aligned, i.e.

all the molecules are in one single direction, which is not the case in practice because the molecules are distributed with a probability distribution around the main alignment angle. We are particularly interested in what happens for the main angles of  $0^\circ$  and  $180^\circ$ . We can then integrate the dipoles over the alignment distributions calculated in Chapter 2:

$$d_{int,0^\circ} = \int_0^{\pi/2} d_{oriented}(\theta)P(\theta, t) \sin(\theta)d\theta \quad (4.7)$$

and

$$d_{int,180^\circ} = \int_0^{\pi/2} d_{oriented}(\pi - \theta)P(\theta, t) \sin(\theta)d\theta \quad (4.8)$$

where  $P(\theta, t)$  is the molecular angular distribution taken for  $t$  at the half revival of  $N_2O$ , in which case the molecular axis is mainly aligned parallel to the driving laser field. Figure 4.22 and 4.23 present these integrated scattering wave dipoles for the  $N_2O$  HOMO oriented at  $0$  and  $180$  degree. Since the alignment distribution is mainly peaked around  $30^\circ$ , we expect to observe the behavior of the single-molecule dipole around this angle for orientation at  $0$  degree (and  $150^\circ$  for orientation at  $180^\circ$ ). Indeed, we observe an asymmetric behavior, with blurred signatures of dynamical interferences around  $40$ - $45$  eV in both cases: local minimum and phase evolution much less than  $\pi$ .

Again, because we align the molecules instead of orienting them, we have to sum up the integrated dipole for both orientations in order to simulate the experimental results, while taking into account the dipole symmetry. As discussed in Equation 4.5, the effective total dipole after integration is:

$$d_{total} = d_{int,0^\circ} - d_{int,180^\circ} \quad (4.9)$$

The result is shown in Figure 4.24.

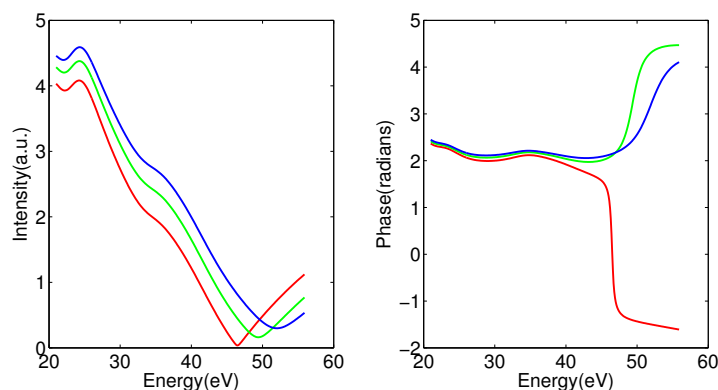


Figure 4.24: Symmetrized scattering wave dipole of aligned  $N_2O$  HOMO ( $0^\circ$ ). (left) Intensity, (right) Phase.

Comparing Figure 4.24 to 4.22 and 4.23, we find obvious differences. Indeed, after summation of both directions, a clear minimum appears in the energy spectrum and also a big phase deviation close to  $\pi$ . These results are very interesting: they reveal that the structural interference result from the destructive interference between the oppositely oriented

molecules. The weight between both interference components decides the deepness of the minimum as well as the phase jump. Moreover, the sign of the phase jump gives an indication on which side of recollision is dominating. When increasing the medium temperature, the averaging of the dipoles over a larger angular distribution tends to smooth out the structural interferences and to shift their position to higher energies. In any case, since our experimental temperature was larger than 50 K, it seems clear that such a structural interference above 47 eV was not observed in our data (harmonic order H29 corresponding to 45 eV).

### Single molecule response using Scattering Wave Dipole moments

The model discussed in Section 4.5 was able to reproduce the positions of the dynamical interferences for the different intensities in both  $\text{N}_2\text{O}$  and  $\text{CO}_2$ . It was based on the Plane Wave approximation for the scattering states, that resulted in a phase difference of the recombination dipoles of  $-\pi/2$ . Let us now use accurately calculated scattering wave dipoles and estimate their influence on the total phase difference. Figure 4.25 gives the phase differences in the scattering wave recombination and in the total process for the channels involved in the HHG from  $\text{N}_2\text{O}$  a) and  $\text{CO}_2$  b) aligned at 30 degree for intensities of  $1.3 \times 10^{14} \text{W/cm}^2$  and  $1.4 \times 10^{14} \text{W/cm}^2$ . As mentioned above, this angle is the one giving the maximum contribution to the emission averaged over the molecular angular distribution. The dipoles for  $\text{N}_2\text{O}$  are symmetrized. We can see that the values of the phase difference in the recombination are varying significantly around  $-\pi/2$  over the spectral range for both molecules as shown by the black solid lines, which is not the same as in the plane wave calculations. As a result, a destructive dynamical interference would be expected for the  $-\pi$  total phase difference at H29 for  $1.4 \times 10^{14} \text{W/cm}^2$  in  $\text{N}_2\text{O}$  (see Figure 4.25 a)). And a dynamical interferences would appear in  $\text{CO}_2$  at H24 for a  $-\pi$  total phase difference for  $1.4 \times 10^{14} \text{W/cm}^2$ , as shown in Figure 4.25 b). However, such interferences were not found in the experiments in neither molecules. We notice from Figure 4.25 that the observed interference position for  $\text{N}_2\text{O}$  at H27 corresponds to a  $\sim -0.75\pi$  phase difference and the interference for  $\text{CO}_2$  at H23, to a  $\sim -0.75\pi$  phase difference. It seems that the we have to shift the total phase difference by  $-\pi/4$  to achieve the measured results. However, the estimations of the intensities in the laser-matter interaction region for previous Sections are mainly done by using the simple model to fit the destructive interferences at the same positions as in the experiments. The accuracy of the estimations was influenced by the plane wave approximation we made for the scattering states. In order to fit the destructive interferences at the right positions by using the scattering wave calculations for both  $\text{N}_2\text{O}$  and  $\text{CO}_2$ , the intensity is at  $1.3 \times 10^{14} \text{W/cm}^2$ , which is 7% away from the previous estimation. As we can see in Figure 4.25 a) and b), the total phases for  $1.3 \times 10^{14} \text{W/cm}^2$  are given in red solid lines. The destructive interferences are at H27 for  $\text{N}_2\text{O}$  and at H23 for  $\text{CO}_2$ , which are

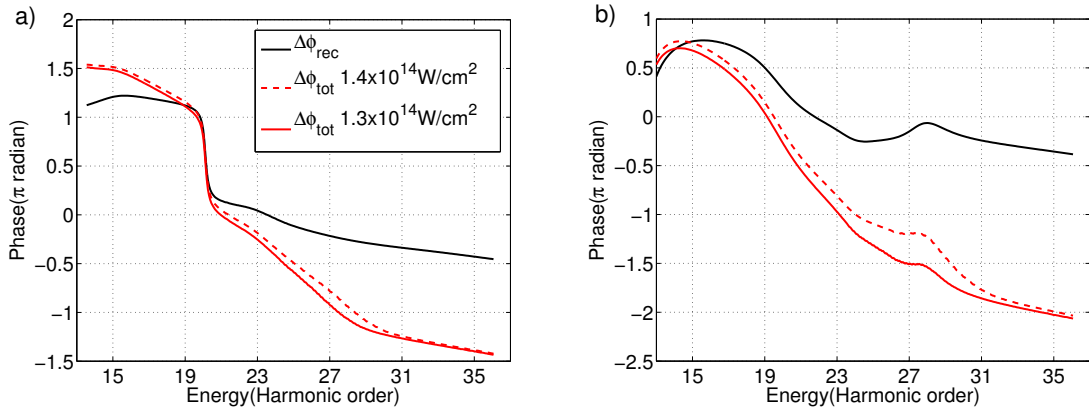


Figure 4.25: Recombination phase difference (black lines) and total phase difference (red lines) for the channels involved in HHG for N<sub>2</sub>O (a) and CO<sub>2</sub> (b) aligned at 30 degree for intensities of  $1.3 \times 10^{14} \text{W/cm}^2$  (red solid) or  $1.4 \times 10^{14} \text{W/cm}^2$  (red dashed).

the same as in the experiments.

### Harmonic emission integrated over the molecular angular distribution

In this section, the distribution of molecular alignment is taken into account. Equations 4.5, 4.7 and 4.8 are used for calculating the integration over the molecular angular distribution of the scattering recombination dipole moment for each channel involved at 0 degree for CO<sub>2</sub> and symmetrized N<sub>2</sub>O. The molecular angular distribution is simulated for  $3 \times 10^{13} \text{W/cm}^2$  alignment beam intensity and 125K temperature. Next, the phase differences for the integrated recombination dipoles of the different channels are extracted, as shown in Figure 4.26 b) for N<sub>2</sub>O and e) for CO<sub>2</sub>. These phase differences are flatter than in the single molecule response, and their value deviate around  $-\pi/4$  in the region where the destructive interferences take place.

The phase differences of the two contributing channels accumulated in the continuum for N<sub>2</sub>O and CO<sub>2</sub> are presented in Figure 4.26 a) and b), respectively. They were calculated for different laser intensities using SFA. Their values are approximately equal to  $-\Delta I_p \tau$  as mentioned before. This continuum phase difference is very sensitive to the intensity. This is the reason for the variation of the phase jump position when changing the intensity. Finally, the total phase differences for N<sub>2</sub>O and for CO<sub>2</sub> are indicated in c) and f), as obtained by summing up the phase differences in the continuum and in the recombination. Similarly as in the single molecule response, the  $\pi$  (modulo  $2\pi$ ) phase differences are at the interference positions measured in the experiment for  $1.3 \times 10^{14} \text{W/cm}^2$  for both molecules. Moreover, the minima and phase shifts at  $1.1 - 1.5 \times 10^{14} \text{W/cm}^2$  for N<sub>2</sub>O as well as that at  $1.3 - 1.5 \times 10^{14} \text{W/cm}^2$  for CO<sub>2</sub> in the experiments are well predicted.

Next we can calculate the calibrated dipole by Equation 4.3 for N<sub>2</sub>O as an example. Its

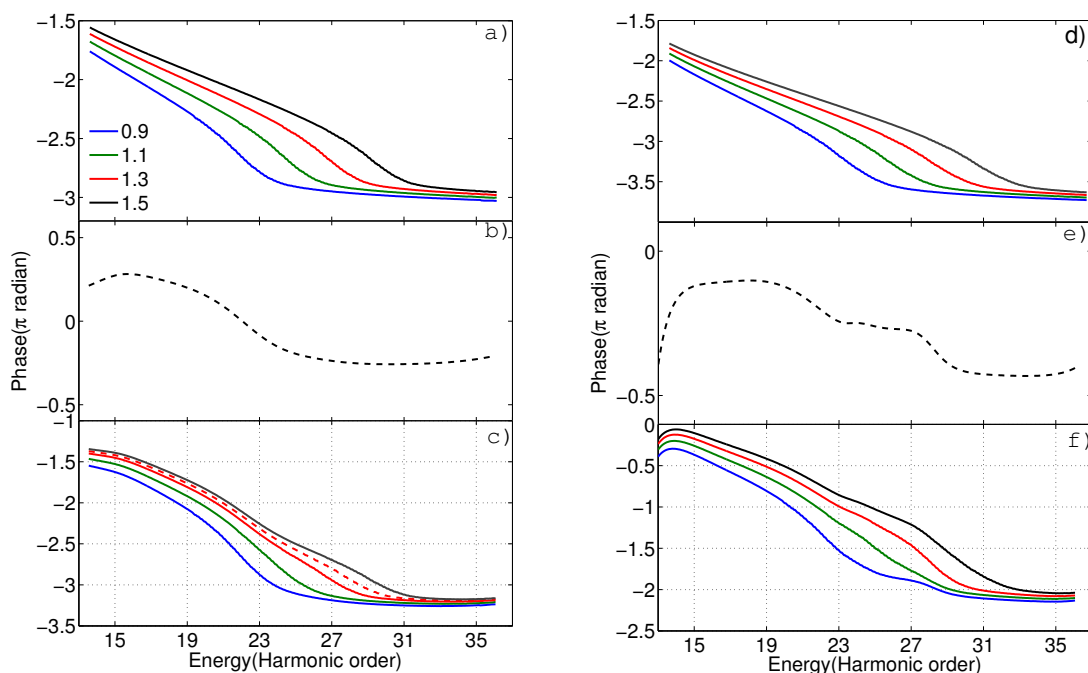


Figure 4.26: Phase differences of the contributing channels for  $\text{N}_2\text{O}$  (left) and  $\text{CO}_2$  (right) aligned at 0 degree when taking into account the molecular alignment distribution: continuum phase difference of  $\text{N}_2\text{O}$  a) and  $\text{CO}_2$  d) for different harmonic generating intensities indicated in the figure in units of  $10^{14}\text{W}/\text{cm}^2$ ; recombination phase differences of  $\text{N}_2\text{O}$  b) and  $\text{CO}_2$  e); total phase difference for  $\text{N}_2\text{O}$  c) and  $\text{CO}_2$  f). The red dashed line in c) is for  $1.4 \times 10^{14}\text{W}/\text{cm}^2$ .

intensity and phase are shown in Figure 4.27. As expected, we find a spectral minimum in the intensity at H27 and also a corresponding phase jump at the same harmonic order. By changing the contributing ratio ( $\alpha$ ), we can see that the phase deviation behaves like in the simple model.

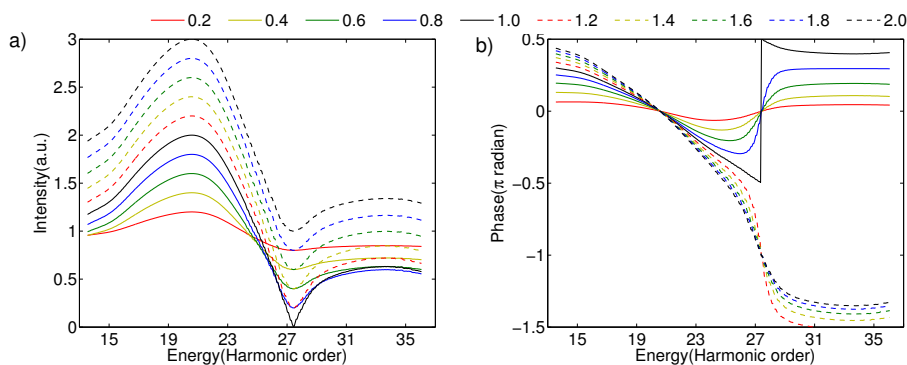


Figure 4.27: Intensity a) and phase b) of the calibrated dipole for  $\text{N}_2\text{O}$  at  $1.3 \times 10^{14}\text{W}/\text{cm}^2$ . Difference curves correspond to different contributing ratio ( $\alpha$ ) between channels A and X.

The comparison of the theoretical fit for N<sub>2</sub>O and the RABBIT measured spectral phase for 0 degree alignment at  $1.3 \times 10^{14} \text{W/cm}^2$  is presented in Figure 4.28. The fitting by using the advanced model with single  $\alpha$  value cannot reproduce all the measured points. This is reasonable because the dynamical interference only happens at the cutoff region, where the HHG from HOMO-1 contributes significantly. At low energy, the HHG is dominant by HOMO. Therefore, the  $\alpha$  value should not be constant. As we can see in the figure,  $\alpha = 1.1$  in the destructive interference region (H25-H27), which means that HOMO-1 contributes a bit more to HHG than HOMO. In the lower energy domain,  $\alpha = 0.4$ , indicating a much stronger contribution from HOMO than HOMO-1 to HHG. Thus, the fitting method is still working nicely. We can even extract the contribution ratio between channel A and X in different energy regions.

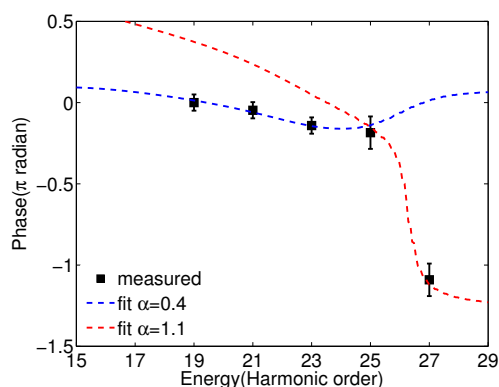


Figure 4.28: Comparison of the theoretical fit for N<sub>2</sub>O (dashed line) with different  $\alpha$  value and the RABBIT measured spectral phase (square points) for 0 degree alignment at  $1.3 \times 10^{14} \text{W/cm}^2$ .

#### 4.7 Coherent control of attosecond emission

We have shown that High-order Harmonic Generation is a great tool to investigate the multielectron dynamics in molecules. Since HHG leads to attosecond emission in extreme-ultraviolet region, it can also serve as an ideal light source with extremely good temporal resolution. However, it is always challenging to flexibly manipulate those pulses. Boutu et al. [46] presented a method of coherently control the attosecond emission in a linear molecule (CO<sub>2</sub>). Indeed, compared to atoms, HHG from molecules provides more possibilities for controlling the attosecond emission due to the angular dependence of the emission from molecules. As shown in Figure 4.12, the spectral phase changes by varying the molecular alignment angle in particular close to the destructive dynamical interference. In this section, we will investigate how this can be used to control the attosecond pulses emitted by linear molecules (N<sub>2</sub>O and CO<sub>2</sub>).



High-order Harmonic Generation by using a multicycle ( $\sim 50fs$ ) laser pulse leads to periodic emission of light bursts with a discrete spectrum containing only odd multiples of the laser frequency  $\omega_0$  in spectral domain (see section 1.6). We have already characterized the spectral amplitude ( $A_q$ ) and phase ( $\varphi(q\omega_0)$ ) for the harmonics ( $q$ ) by RABBIT. Consider  $N$  harmonics, the intensity profile  $I(t)$  emitted by these harmonics can be reconstructed by:

$$I(t) = \left| \sum_N A_q \exp[-iq\omega_0 t + i\varphi(q\omega_0)] \right|^2 \quad (4.10)$$

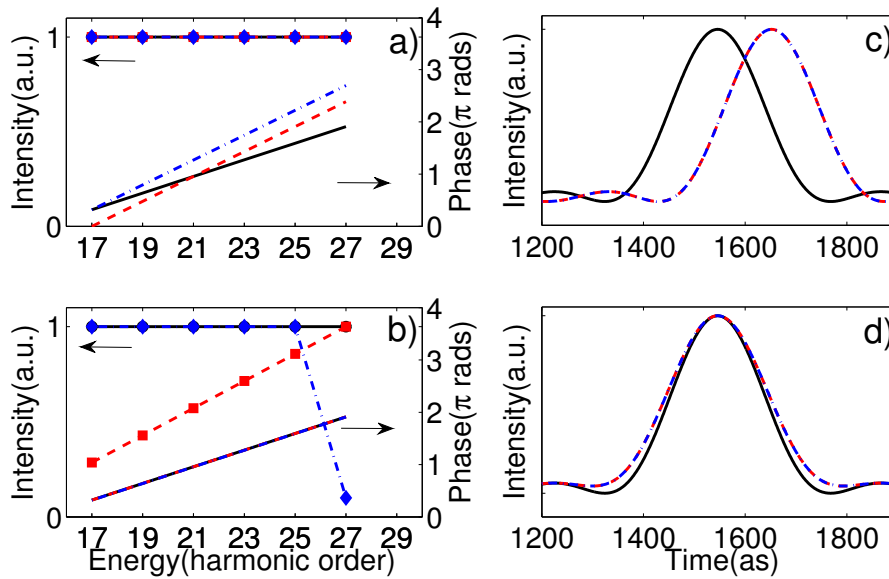


Figure 4.29: Simulation of the attosecond emission by assuming equal amplitude a) or linear phase b), respectively. The spectral intensity is indicated by color lines with symbols, and the phase is showed by different color lines. Their corresponding intensity profile in time domain is showed in c) and d). The lines with same color present for the same simulation.

In order to recall the relation between the spectral amplitude/phase and temporal profile, we performed some basic simulations:

i) by setting equal values for  $A_q$  (colorful lines with symbols) while varying the phase (the lines without symbols) as shown in Fig.4.29 a). The corresponding temporal profiles are presented in Fig. 4.29 c). The global shift for the phase (red dashed line and blue dash-dotted line in a)) does not affect the attosecond emission while the change of slope of the spectral phase (black solid line) shifts the attosecond emission in the time domain.

ii) by setting a linear spectral phase for all the three simulations in Fig. 4.29 b) (colorful lines without symbols) while changing the spectral intensity (colorful lines with symbols). The corresponding attosecond emissions are then shown in Fig. 4.29 d). The emission is broadened when the spectral intensity is not constant due to the reduction of the effective spectral bandwidth. However, its influence is quite limited in this case.

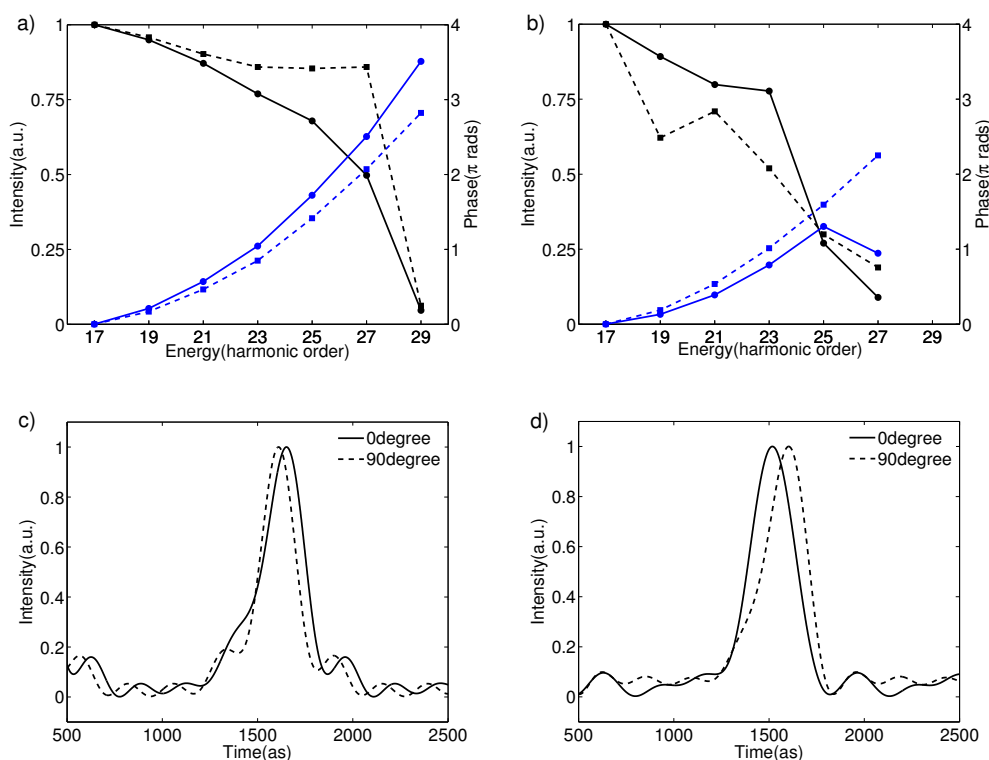


Figure 4.30: Spectral intensity (black) and phase (blue) characterized by RABBIT technique when the molecule is aligned parallel (solid) or perpendicular (dash) to the generating laser polarization for  $CO_2$  a) and  $N_2O$  b), for a generation intensity of  $1.3 \times 10^{14} W/cm^2$ . The reconstructed temporal intensity profile is showed in c) for  $CO_2$  and d) for  $N_2O$ .

Figure 4.30 a) and b) show the spectral intensity and phase characterized by RABBIT from  $CO_2$  and  $N_2O$  in the same experimental conditions. Note that, in contrast to the preceding sections, we are not calibrating the spectral phase with that of the reference gas: the atto-chirp due to the continuum dynamics result in a quadratic spectral phase of the emission. The solid lines correspond to molecules parallel aligned, while the dashed lines indicate molecules perpendicularly aligned. Figure 4.30 c) and d) then show the temporal profile  $I(t)$  of the intensity of the emitted pulses for  $CO_2$  corresponding to harmonics 17 to 29 and for  $N_2O$  corresponding to H17 to H27, respectively. The shortest pulse duration can be reached if the spectral amplitude for each peak is equal and the spectral phase is locked, i.e. the phase is linear with respect to the photon energy [185]. The Fourier transform limited pulse duration is given by [100]:  $\tau_{xuv} \simeq \frac{T_0}{2N}$ , with  $T_0$  being the optical cycle period, which is  $2.67 fs$  for  $800 nm$  laser wavelength. The pulse duration of the attosecond emission from  $CO_2$  at full width half maximum (FWHM) is  $220 as$  for 0 degree and  $200 as$  for 90 degree in a). Both of them are close to the Fourier transform limited duration, which is  $\sim 190 as$  for 7 harmonics. The duration is slightly longer due to the not exactly linear phase and the unequal amplitudes. The phase for  $CO_2$  at 0 and 90 degree have small difference of general

slope, resulting in a slight shift in time. Moreover, the biggest phase deviation between 0 and 90 degree in CO<sub>2</sub> is at the highest harmonic order, where the spectral intensity has a very small weight to the total emission. This is why the shapes of the emission for 0 and 90 degree are similar. For N<sub>2</sub>O perpendicularly aligned, when the phase is more linear (see b)), the pulse duration is  $\sim 250as$ , which is close to the Fourier transform limited duration ( $\sim 230as$ ) for 6 harmonics. When we turn the molecule parallel to the laser polarization, the phase is distorted by the dynamical interference at H27, resulting in a slight shape change in the temporal domain as shown in d). For the same reason, the weight to the emission is not enough significant so that the shape distortion is small.

In order to shape the attosecond emission, we need to increase the weight of the distorted harmonic in the total emission, which can be done by selecting less harmonics. Figure 4.31 shows an investigation of the selection of different numbers of harmonic orders in the spectrum for CO<sub>2</sub> (left) and N<sub>2</sub>O (right), respectively. From top to bottom, we select the last 6 harmonic orders (HH19-29 for CO<sub>2</sub> and HH17-27 for N<sub>2</sub>O) to the last 2 orders (HH27-29 for CO<sub>2</sub> and HH25-27 for N<sub>2</sub>O) in the spectrum for both CO<sub>2</sub> and N<sub>2</sub>O. By selecting less harmonics, the pulse duration is increased for both CO<sub>2</sub> and N<sub>2</sub>O due to the decreased spectral bandwidth. The phase difference between 0 and 90 degree in CO<sub>2</sub> is small, so we don't see big variation in the pulse shape for all the selections. However, the pulse delay between 0 and 90 degree is increased from a) to e) due to the bigger and bigger slope difference in different spectral region. It is more interesting to consider N<sub>2</sub>O. The pulse broadening at 0 degree compared to 90 degree is more and more clear when selecting fewer harmonics from f) to i), which is reasonable since we get rid of the big contribution from low harmonics, making the contribution from the last order more and more significant. The pulse duration is increased from 290as to 360as by turning the molecule from 90 degree to 0 degree in g), and 540as compared to 340as in h). In i), the pulse duration increases from 440 to 930 by a factor more than 2 just by turning the molecules by 90°. The oscillating emissions resulting from the beating of the two last orders are in opposite phase for 0 and 90 degree, due to the  $\pi$  phase difference of the spectral phase of these two harmonics at 0 degree and not at 90 degree, as shown in j).

The development of XUV multilayer mirrors makes the selection of different spectral regions possible, and it provides the great potential for flexibly controlling the intensity in different spectral ranges [186]. Therefore, we also study the attosecond emission for equal spectral intensity of all harmonic orders, assuming the feasibility of a spectral filter compensating for the harmonic cutoff (obviously at the expense of the total number of photons). The results are presented in Figure 4.32. From top to bottom, we select the last 6 harmonic orders (HH17-27) up to the last 2 orders (HH25-27) in the spectrum for N<sub>2</sub>O using equal spectral intensity for the harmonics but the measured phases. For a) and b), the attosecond pulse is not varying much from 0 to 90 degree except for a temporal shift. When using 4 harmonics (HH21-27), the attosecond emission is split into 3 pulses with  $\sim 500as$  interval by

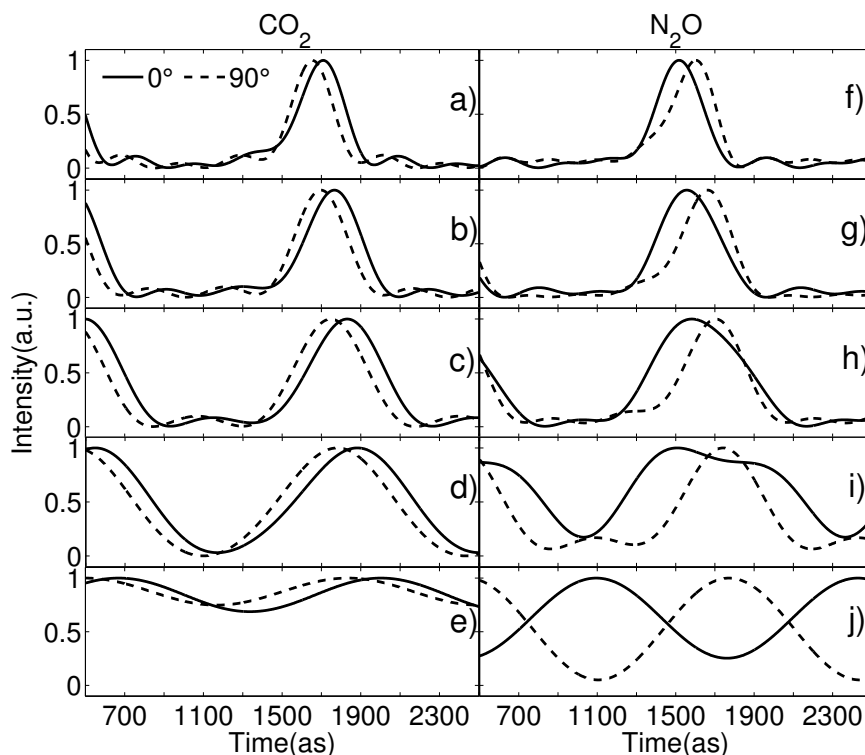


Figure 4.31: Attosecond emission resulting from the selection of different harmonic orders for  $CO_2$  (left) and  $N_2O$  (right), respectively. From a) to e), HH19-29, HH21-29, HH23-29, HH25-29 and HH27-29 are used. From f) to j), HH17-27, HH19-27, HH21-27, HH23-27 and HH25-27 are used.

turning the molecule from 90 to 0 degree as shown in c). When selecting the last 3 harmonics, the attosecond pulse is split into two pulses with a delay of 700as from 90 to 0 degree, as presented in d). The attosecond beating switches sign in e) by turning the angle in the case of only two harmonics.

Figure 4.33 shows the attosecond emission as a function of the molecular alignment angle for HH25-27 a), HH23-27 b) and HH21-27 c) assuming constant spectral intensity. By turning the angle, we can control finely the timing of the attosecond emission with respect to the driving field.

We have reconstructed the attosecond pulse emission from aligned  $CO_2$  and  $N_2O$  under the same experimental conditions. The angular dependence of the spectral phase close to the dynamical interference provides us with new possibilities for manipulating the attosecond pulses generated from molecules in a simple regime just by turning the molecular axis with respect to the driving laser polarization. The control of the attosecond emission is a further step towards the extreme-ultraviolet pulse shaping that will open a new class of experiments, such as extreme-ultraviolet coherent control of atomic and molecular systems.

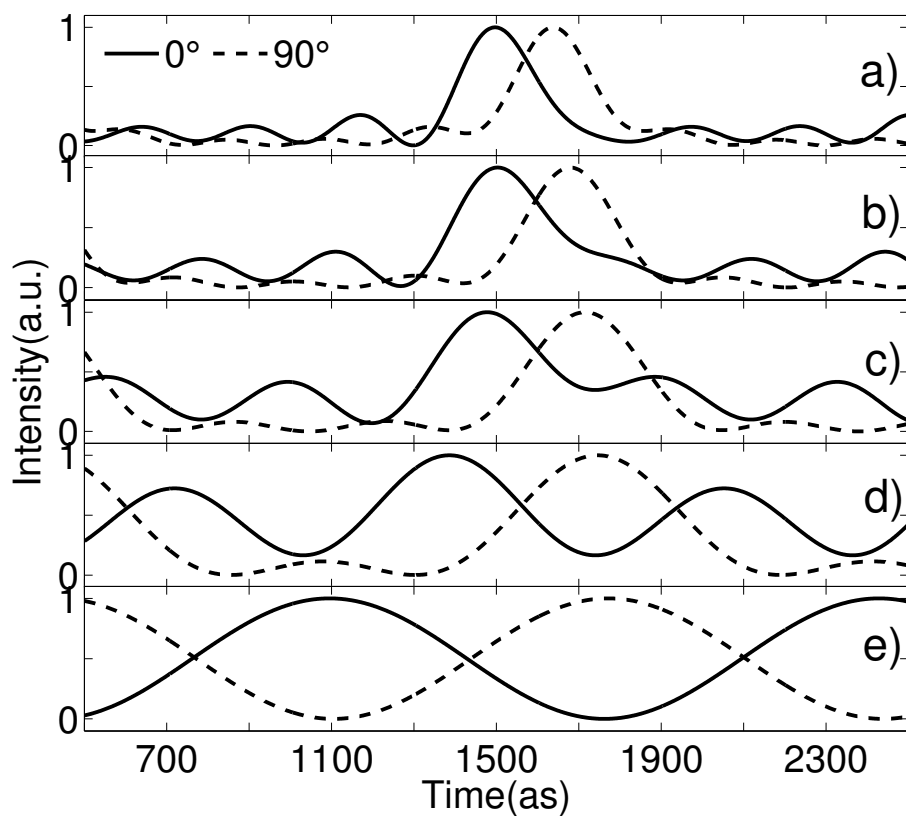


Figure 4.32: Attosecond emission obtained by selecting different spectral ranges for  $N_2O$  assuming a constant spectral intensity. From a) to e), HH17-27, HH19-27, HH21-27, HH23-27 and HH25-27 are used.

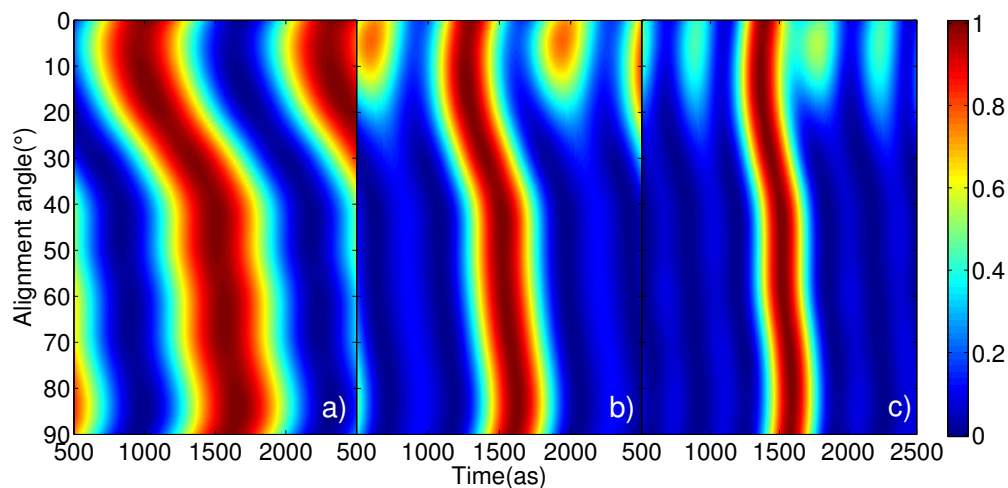


Figure 4.33: Temporal profile of a typical attosecond pulse in the generated train mapped as a function of the alignment angle, with  $t = 0$  at the maximum of the generating field. This dynamics is reconstructed by using equal spectral intensity and the spectral phase in 4.30 b) for HH25-27 a), HH23-27 b) and HH21-27 c).

## 4.8 Conclusions

We have implemented two methods in order to characterize the amplitude and phase of the harmonic emission from CO<sub>2</sub> and N<sub>2</sub>O molecules that are aligned with respect to the polarization of the driving laser. The two measurements give consistent results and directly lead to a full mapping of the phase as a function of both photon energy and alignment angle for the first time. We discovered new effects in the high harmonic generation which could not be explained by the structure of the highest occupied molecular orbital (HOMO). Instead we found that during the interaction with the laser field, two electronic states are coherently excited and form a hole wave packet moving on an attosecond timescale in the molecule after tunnel ionization. We focused on exploring this coherent electronic motion inside the molecule, and compared the measurements in N<sub>2</sub>O and CO<sub>2</sub>. The striking difference in the harmonic phase behavior led us to the development of a multi-channel model allowing the extraction of the relative weight and phase of the two channels involved in the emission. An unexpected  $\pi/2$  phase shift between the two channels is obtained. Finally, this allowed in turn reconstructing the image of the hole wavepacket evolving in the molecule on an attosecond timescale. Moreover, we studied the attosecond generation from these two molecules, and we showed a simple but flexible way for performing attosecond pulse shaping.



---

# HIGH HARMONIC SPECTROSCOPY IN $N_2$ , $SF_6$ AND HYDROCARBONS

---

In this chapter, we extend High Harmonic Spectroscopy to more complicated molecules based on our advanced characterization of HHG in intensity and phase.

First, we present in Section 5.1 the investigations of the low order harmonics generated in nitrogen ( $N_2$ ). We found that the harmonic intensity of HH11 in the rotational revival presents an opposite behavior compared to the other harmonic orders at high driving laser intensity. By decreasing the generation intensity, we could continuously change the harmonic intensity of HH11 from the opposite to the same as the other harmonic orders. However, we did not measure a big evolution of the phase spectrally or angularly from the measurements with RABBIT or TSI, respectively.

Next, we implement the first characterization of both intensity and phase of HHG for hydrocarbon molecules as reported in Section 5.2. Although we were limited by the narrow spectral range due to the small ionization potential of hydrocarbons, we could observe angular dependent behavior for both the harmonic intensity and phase of aligned ethylene and acetylene. Moreover, the comparison we made for  $CH_4$  and  $CD_4$  revealed signatures of the nuclear dynamics occurring during the electron excursion in the continuum. We measured for the first time the relative phase  $CD_4/CH_4$ , which revealed a slight spectral phase deviation.

Finally, we present in Section 5.3 our investigations of HHG in  $SF_6$ . In the emitted spectrum, a minimum is observed at the high harmonic order 17 of the 800 nm driving field with a corresponding distortion in the spectral phase. We performed an analysis based on the HOMO structure of  $SF_6$  molecules and on the multichannel contributions issuing from lower lying orbitals.

As mentioned in the conclusions of Section 5.4, all the measurements in this chapter prove that HHS can be applied to complex molecules and reveal many results which were



---

not reported by any other methods. Moreover, the fruitful information we obtained in this chapter can be used to test the existing theories as well as lead to a deeper understanding of many physical phenomena with attosecond resolution, i.e. resonance, nuclear motion, electronic structure and dynamics.

## RÉSUMÉ DU CHAPITRE

*Dans ce chapitre, nous étendons la spectroscopie harmonique à des molécules plus compliquées à l'aide de notre caractérisation avancée de l'émission harmonique en intensité et en phase.*

*Tout d'abord, nous présentons dans la Section 5.1 les études des ordres harmoniques faibles générés dans N<sub>2</sub>. Nous avons trouvé que l'intensité de l'harmonique 11 au «revival» rotationnel présente un comportement opposé comparé aux autres ordres harmoniques à des intensités lasers élevées. En diminuant l'intensité de génération, nous pouvons changer de manière continue l'intensité de l'harmonique 11 par rapport aux autres harmoniques, la faisant passer d'un comportement opposé à ces dernières à un même comportement. Cependant, nous n'avons pas mesuré une grande évolution de la phase, spectralement ou angulairement à partir de nos mesures RABBIT ou TSI, respectivement.*

*Ensuite, nous implémentons la première caractérisation de l'émission harmonique à la fois en intensité et en phase pour des molécules hydrocarbonées comme indiqué dans la Section 5.2. Bien que nous étions limités par la gamme spectrale étroite du fait du faible potentiel d'ionisation des hydrocarbures, nous avons été capables d'observer des comportements dépendant angulairement, à la fois de l'intensité et de la phase de l'émission harmonique pour les molécules alignées d'éthylène et d'acétylène. De plus, la comparaison que nous avons faite pour CH<sub>4</sub> et CD<sub>4</sub> a révélé les signatures de la dynamique nucléaire survenant pendant l'excursion de l'électron dans le continuum. Pour la première fois, nous avons mesuré la phase relative de CD<sub>4</sub>/CH<sub>4</sub>, révélant ainsi une légère déviation de la phase spectrale.*

*Finalement, nous présentons dans la Section 5.3 nos études de génération d'harmoniques dans SF<sub>6</sub>. Dans le spectre émis, un minimum est observé à l'ordre harmonique 17 du 800nm avec une distorsion dans la phase spectrale associée. Nous avons effectué une analyse basée sur la structure HOMO de SF<sub>6</sub> et sur la contribution multicanaux des orbitales plus faibles. Comme mentionné dans la conclusion de la Section 5.4, toutes les mesures de ce chapitre prouvent que la spectroscopie d'harmoniques d'ordre élevé peut être appliquée à des molécules complexes et révèle de nombreux résultats non accessibles par d'autres techniques. De plus, l'information obtenue dans ce chapitre peut être utilisée pour tester les théories existantes ainsi qu'amener à une compréhension plus profonde de nombreux phénomènes physiques, tels que les mouvements nucléaires, la structure et la dynamique électronique en particulier près des résonances, le tout avec une résolution*

attoseconde.

## 5.1 HHS in aligned $N_2$

Nitrogen molecule has been intensely investigated by HHS in order to reconstruct its molecular orbitals [41][42] and to study the multi-channel dynamics [187][188][189]. Although  $N_2$  is a very popular candidate in HHS, there are still some interesting properties that are not understood. For example, Soifer et al. [190] found that the harmonic emission of first harmonic order above the ionization potential (HH11 at  $800nm$  wavelength) has an inverse behavior compare to the other harmonic orders, but the physical reason is not clear. Indeed, Strong Field Approximation is not valid in that spectral range because the Coulomb potential of the ionic core is comparable to the electron kinetic energy, meaning it cannot be ignored anymore. Therefore, both theoretical and experimental elements are required to understand the physical process within this special region. In this section, we concentrate on investigating the harmonic emission close to the ionization potential ( $15.7eV$ ) by using our unique amplitude and phase characterization methods.

### Spectral amplitude and phase of HHG from $N_2$

First of all, we study the spectral amplitude and phase of the High-order Harmonic emission from aligned  $N_2$ . The HHG spectrum is taken by converting the photon energy to electron energy through photoionization (PI) in MBES with acetylene ( $C_2H_2$ ) as the detection gas. The use of acetylene as detection gas has the advantages: i) the ionization potential of acetylene is as low as  $11.4eV$  so that the first harmonic order appearing in the PI spectrum is HH9, which is below the ionization potential of  $N_2$  ( $15.7eV$ ). The spectral region near the ionization threshold is, in general, spectroscopically very rich [191]. We could thus get fruitful information on the HHG mechanism in this special range. ii) The difference in the binding energy between HOMO and HOMO-1 of acetylene is as big as  $\sim 5eV$ , i.e., 3.2 times the laser photon energy. The two ionization channels are thus clearly separated. Moreover, the ionization from HOMO-1 is negligible as we will see in the photoemission spectra below. Therefore, the spectrum is "clean" (only one channel appears in the spectrum).

The alignment beam comes first to "kick" the molecules to generate a rotational wave packet and the wave packet rephases periodically, resulting in most of the molecules being aligned in the same direction at a proper time (so called revival) after the beam passes (detailed in Chapter 2). A second beam comes after the alignment beam, which is used to generate harmonics. Then the harmonic signal is detected through PI in MBES. Keeping the polarization of the molecular alignment beam and generation beam parallel, we take the HHG spectrum as a function of the time delay between these two beams close to the half revival of  $N_2$ , which is shown in Figure 5.1.  $x$  axis indicates the time delay and  $y$  axis is for the photon energy. The full revival time of  $N_2$  is  $8.4ps$ [192]. The molecular

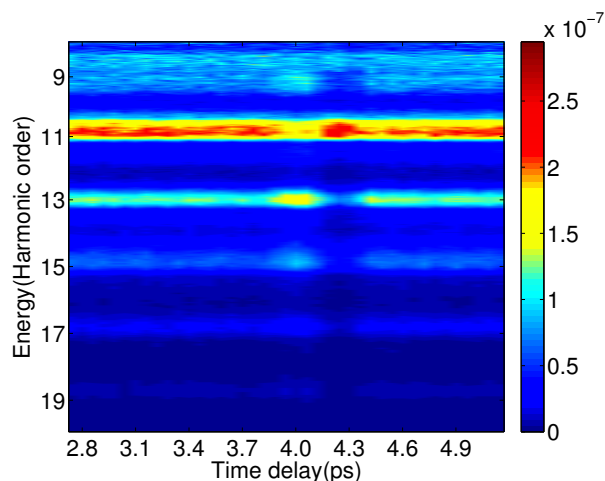


Figure 5.1: Harmonic intensity with respect to the photon energy and the time delay between the alignment and generation beams.

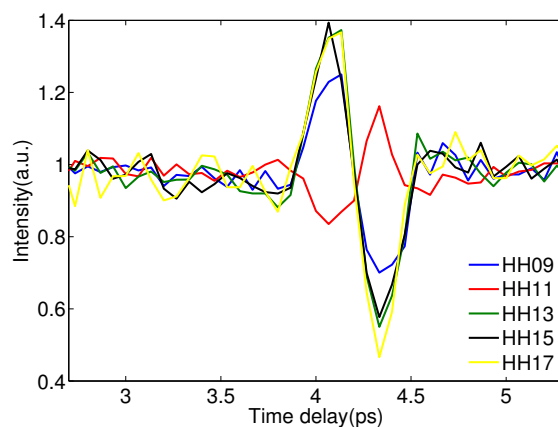


Figure 5.2: Harmonic intensity for each harmonic order as a function of the time delay between alignment and generation beams.

alignment (molecular axis parallel to the laser polarization) of  $N_2$  at half revival is at  $4ps$  and the molecular anti-alignment (molecular axis perpendicular to the laser polarization) of  $N_2$  is at  $4.2ps$ . For the instant of molecular alignment at  $4ps$ , we can see the harmonic intensity reaches the maximum for each harmonic order while that of HH11 reaches its minimum. For the anti-alignment at  $4.2ps$  the behavior of HH11 is again inverted compared to the others: HH11 reaches the maximum but the other orders get to the minimum. Figure 5.2 shows the lineout of each harmonic order. The revival scan is clearly inverted from HH11 to the others. Note that HH11 is the first order above the ionization potential of  $N_2$  and HH9 is below the  $I_p$ . In order to verify that this inversion of HH11 is specific for  $N_2$  instead of a general behavior in other molecules, we checked the revival scan for  $N_2O$  and  $CO_2$ . However, this inversion has not been found in these two molecules. We also would like to check if this inversion only happens at half molecular revival, so we implement a

longer revival scan which includes two cycles of revival, as shown in Figure 5.3. Not only the intensity for HH11 at half revival but also that at  $1/4(2ps)$ ,  $3/4(6ps)$  and full revival is opposite to that of HH09.

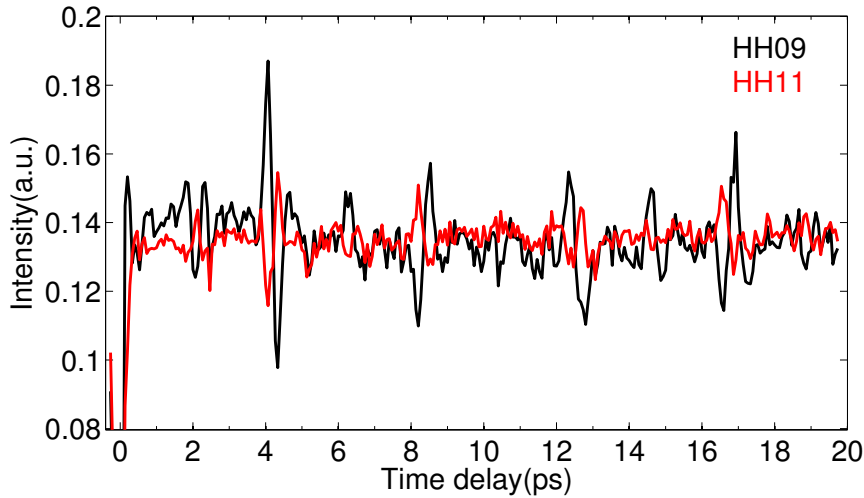


Figure 5.3: A long revival scan that includes two cycles of revival.

Then we make revival scans for different intensities in the generation region. In order to keep the focus size unchanged, we use an attenuator (a half wave plate + a polarizer) to control the intensity. The results are presented in Figure 5.4, where we find that the structure of the intensity variation with time delay of HH11 is highly depending on the driving laser intensity while that of the other orders is roughly constant. For the generation energy above 0.45mJ, the revival structure of HH11 is inverted (first a minimum then accompanied by a maximum). Between 0.4 to 0.3mJ, the intensity is flat as a function of the time delay. And for the low energy (0.25mJ), the intensity varies the same as the other harmonic orders.

Next we perform the RABBIT measurement for accessing the spectral phase. In order to avoid adding more complexity through the molecular phase  $\Delta\phi^{mol}$ , we change the detection gas to argon since its atomic phase is known. Note that the RABBIT technique is based on two photon transitions when the IR dressing beam can be seen as a perturbation. If the dressing intensity cannot be ignored, the RABBIT is not working due to the multiple photon transitions that may be produced. We performed the RABBIT for high generation energy (0.7mJ). And the inversion of HH11 is optimized at this energy (see Figure 5.4). The results and the analysis procedure are shown in Figure 5.5. We set the time delay between alignment and generation beam at 4ps and make RABBIT scan for the molecules aligned at  $0^\circ$  and  $90^\circ$ . In order to extract the recombination dipole element, a scan by using argon gas as a reference is performed. The  $I_p$  of argon (15.6eV) and  $N_2$  (15.7eV) are very close. From the RABBIT scans, the emission times (or the group delay  $\partial\phi/\partial\omega$ ) are extracted as shown in Figure 5.5 a). The fluctuation of the absolute timing is removed by normalizing the curves to one sideband (SB). We choose SB16 because the phase variation of the neighboring

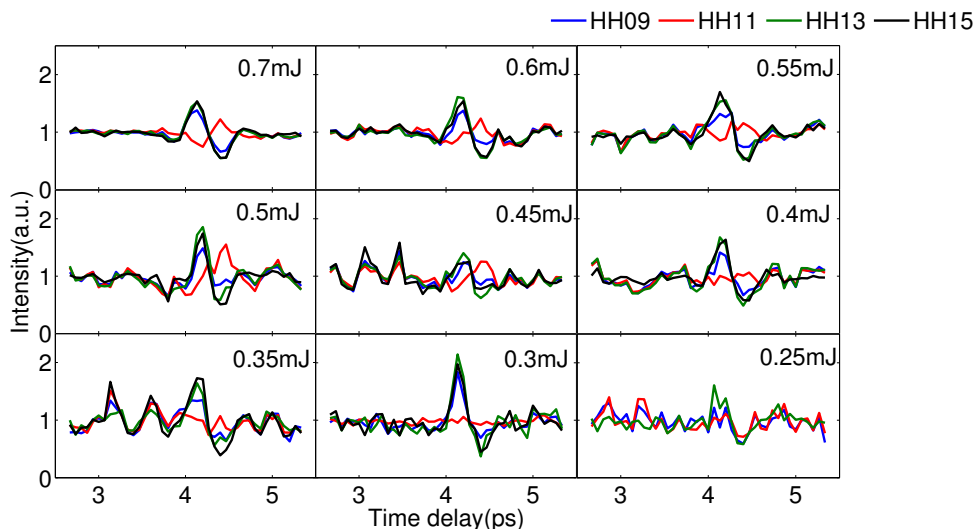


Figure 5.4: Harmonic intensity as a function of the time delay between alignment and generation beams for different generation energies.

harmonics when changing the alignment is very small in this generation energy, as we will see later using two-source interferometry. The emission time after normalization is in Figure 5.5 b). Then the spectral phase  $\varphi$  can be obtained by integrating the emission time  $\partial\varphi/\partial\omega$ . From the SB16, integrating on both sides, we get the phase in Figure 5.5 c). Eventually, we reach the DME phase by subtracting to the phase for  $N_2$  the argon reference phase, which is shown in Figure 5.5 d). Surprisingly, unlike the spectral intensity, there is no dramatic variation in the spectral phase between HH11 and HH13 for both  $0^\circ$  (red line) and  $90^\circ$  (black line). The very small variation is probably within the error bars and is not reproducibly measured in other measurements.

### Angular amplitude and phase of HHG from $N_2$

We also characterized the angular variation of the HHG amplitude and phase from  $N_2$  by TSI. This experiment was performed in CELIA bordeaux in a cooperation with Yann Mairesse and his PhD student Amélie Ferré.

First, let us have a look at the HHG intensity for different generation energies when the delay of alignment beam and generation beam is at  $4\text{ps}$ , which is presented in Figure 5.6. The curves with different colors in Figure 5.6 correspond to different harmonic orders. By changing the molecular alignment angle of one of the two sources, we measure the intensity as a function of angle. When the generation energy is high, e.g.  $0.59\text{mJ}$  and  $0.52\text{mJ}$ , we can see that the intensity of HH11 reaches the minimum at  $0^\circ$  and increases gradually to  $90^\circ$ , while the intensity of the other orders have inverse behavior (optimized at  $0^\circ$  but minimized at  $90^\circ$ ). By decreasing the generation energy to  $0.48\text{mJ}$  and  $0.40\text{mJ}$ , the intensity of HH11

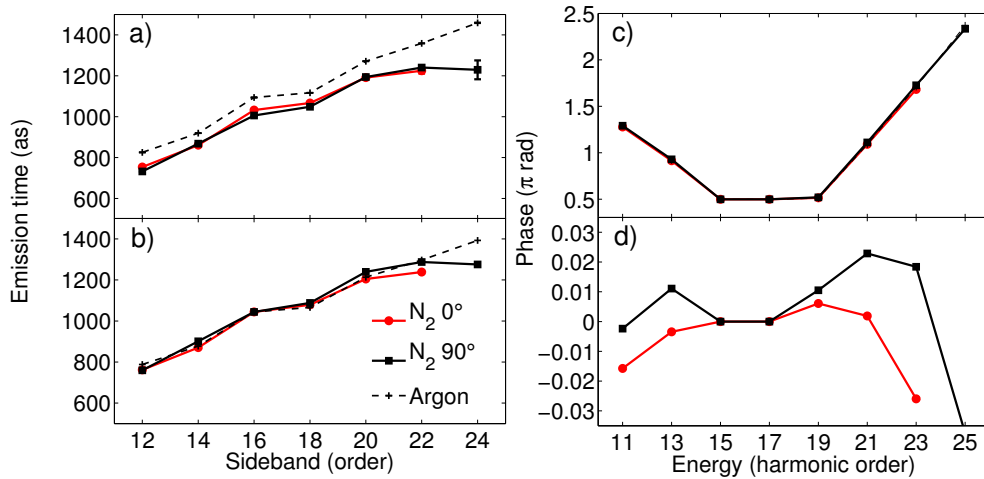


Figure 5.5: The steps of data analysis: from the measured emission times to the DME phase. Emission times as measured a), Emission times with normalized absolute timing b), phase obtained by integrating the emission times c),  $N_2$ -phases normalized by the argon phase d). Error bars are omitted for clarity except a); they are smaller than the size of the symbols except the last order.

is flat versus the alignment angle, while that of the others keep the general trend. If we further decrease the energy to  $0.37\text{mJ}$  and  $0.32\text{mJ}$ , the intensity of HH11 follows the other harmonic orders: all the harmonics have the same variation with the angle then.

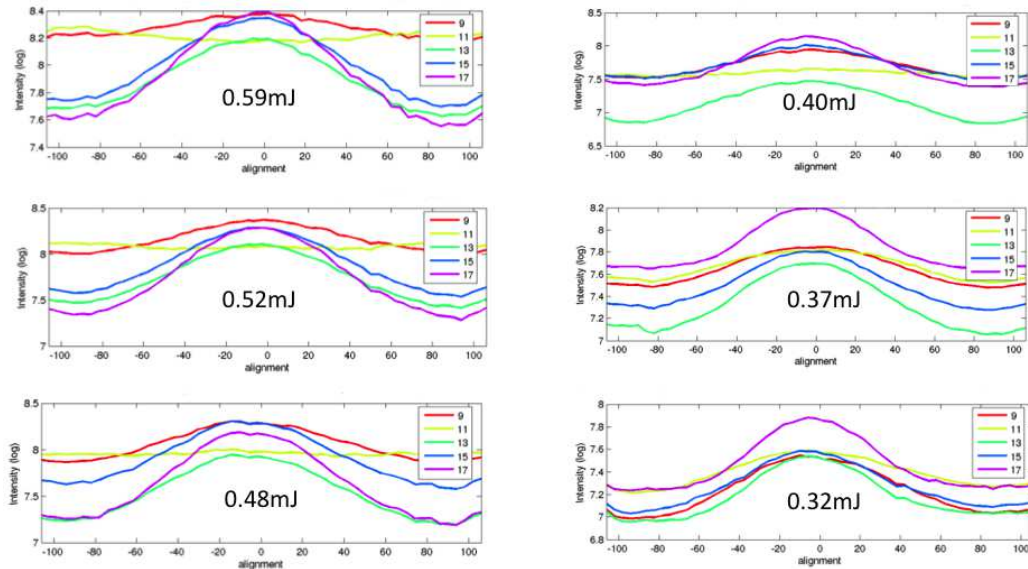


Figure 5.6: Harmonic intensity as a function of alignment angle by using two-source interferometry for different generation energies.

The corresponding phase variation for each harmonic order at different generation energies is shown in Figure 5.7. The phase of HH13 is flat with the alignment angle for the

high energies. Only at low energy  $0.37mJ$  and  $0.32mJ$ , we see a clear positive variation from  $0^\circ$  to  $90^\circ$ . The angular dependence of HH15 is very small for all the energies, which is the reason why we normalize the emission time to SB16 for  $0^\circ$  and  $90^\circ$ . For HH17, the phase is maximized at  $0^\circ$  and decreases slowly until  $90^\circ$  at the highest energy  $0.59mJ$ . By decreasing the energy, the phase is less angular dependent as shown for  $0.52mJ$ ,  $0.48mJ$  and  $0.40mJ$ . At the lowest energy  $0.37mJ$  and  $0.32mJ$ , the phase is then minimized at  $0^\circ$  and increases until  $90^\circ$ . The reason for the intensity dependence of phase may be due to multi-orbital contributions to HHG. Now let us concentrate on the first two harmonic orders HH09 and HH11, which is the region close to the ionization threshold. For HH09, the phase varies negatively from  $0^\circ$  to  $90^\circ$  for all the energies. The phase deviation with angle is bigger and bigger when decreasing the energy except at the lowest energy at  $0.32mJ$ . And the phase of HH11 is flat with respect to the angle for all the energies except for  $0.32mJ$ , at which energy the phase varies negatively from  $0^\circ$  to  $90^\circ$ .

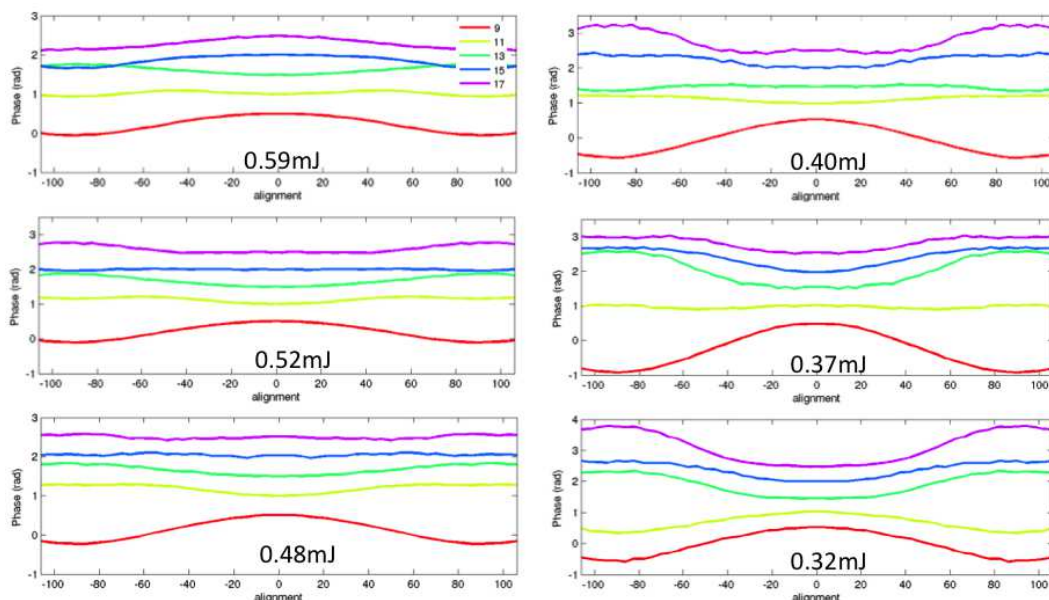


Figure 5.7: Harmonic phase as a function of alignment angle by using two-source interferometry for different generation energies.

Now we can make comparison between the amplitude and phase measured by the two methods. The alignment revival scans in Figure 5.2, 5.3, 5.4 show the measurements of the harmonic intensity as a function of the time delay between the two beams. The TSI measures the intensity as a function of alignment angle by fixing the time delay at  $4ps$ . Thus we can directly compare the intensity measured by using MBES at the delay of  $4ps$  to the measurement of TSI at  $0^\circ$ . In both measurements, the intensity of all the harmonic orders except HH11 are in the same trend that they are reaching the maximum at  $0^\circ$  at the time delay of  $4ps$ . Only HH11 presents unusual behavior, whose intensity arrives at minimum for high generation energies, is flat for intermediate energies and reaches its maximum

for low energies. Since the phase characterization by RABBIT and TSI are performed in two different dimensions, the comparison of phase has to be done after connecting these two dimensions. In RABBIT, we assume the phase angular variation is 0 for HH15 at high generation energy. The phase of HH09 and HH11 is almost flat between  $0^\circ$  and  $90^\circ$  as shown in Figure 5.5 d), which is comparable to the TSI measurement in Figure 5.7 at the highest generation energy. Note that the absolute values of the energies in the RABBIT and TSI measurements can not directly be compared because the corresponding experiments were performed on two different laser systems, one in Saclay (RABBIT) and one in CELIA (TSI). We are here more interested in the general trend of the variation with energy.

The unusual behavior of the intensity and phase for HH11 may be due to the presence of a resonance, which is an autoionizing state belonging to the Rydberg series converging to the  $B^2\Sigma_u^+(3d\sigma_g)^1\Sigma_u^+$  Hopfield state of the ion [193]. This resonance has been studied experimentally [30] and theoretically [191] by Photoionization in  $N_2$ . But there were not thorough investigations by using HHG. Soifer et al. [190] only performed harmonic intensity measurement without studying the harmonic phase, which always provides more detailed information. And Soifer et al. [190] also pointed out that the occurrence of resonances depends on the alignment angle that determines the allowed symmetry of the intermediate excited states. Caillat et al. [191] mentioned that the resonance state mostly couples to the X ionization channel. By considering the symmetries of the autoionizing state and X state, the HHG at  $0^\circ$  should be optimized instead of minimized. Therefore, the investigations we made by using two different methods provide fruitful experimental elements for theoretical study of the presented resonance. Moreover, we accessed to the harmonic order below the ionization potential, which also offers useful information to test the validity of different theory models for this specific spectral region. We will gain a deeper understanding of the origin of high harmonics near the ionization threshold.

## 5.2 HHS in hydrocarbon molecules

Extending HHS to more complex organic molecules is challenging in several ways. First, precise alignment of the molecules needs to be achieved, which is difficult to reach normally for hydrocarbons due to the small polarizability [194]. Second the relatively low ionization potential of the molecules limits the intensity that can be applied, thus the efficiency and the spectral range of high harmonic generation. Furthermore in these molecules, not only the HOMO, but also some of the lower but closely lying orbitals may be ionized. The molecular ion is then left in a coherent superposition of the ground and excited states. This "hole" wave packet evolves on an attosecond timescale during the electron excursion in the continuum and is probed at the recollision: the dynamic behavior influences the recombination process, and this information is encoded in the intensity, phase and polarization of the emitted high harmonic radiation. These very interesting dynamical effects were studied in



Chapter 4 for  $\text{CO}_2$  and  $\text{N}_2\text{O}$ . Extended studies in more complex hydrocarbons could reveal a variety of dynamics due to the huge number of closely lying orbitals. Up to now, only harmonic intensity measurements have been performed for some hydrocarbon molecules [178][194]. We will perform an advanced characterization of the harmonic emission including measurements of the harmonic phase employing the RABBIT technique in this section.

### Methane ( $\text{CH}_4$ )

The shape of methane is like a pyramid as shown in Figure 5.8, which is impossible to align by using linear polarized light due to its small polarizability. Therefore, we directly measure the intensity and phase of nonaligned molecular samples and make a comparison to the reference atom. The difference of binding energies between HOMO ( $12.65\text{eV}$ ) and HOMO-1 ( $12.95\text{eV}$ ) is very small, only  $0.3\text{eV}$ [195]. The ionization from HOMO-1 cannot be ignored. By comparing the harmonic emission from methane and reference atom krypton ( $13.9\text{eV}$ ), we can expect to see differences due to the interference of harmonic signal between the contributing ionization channels.

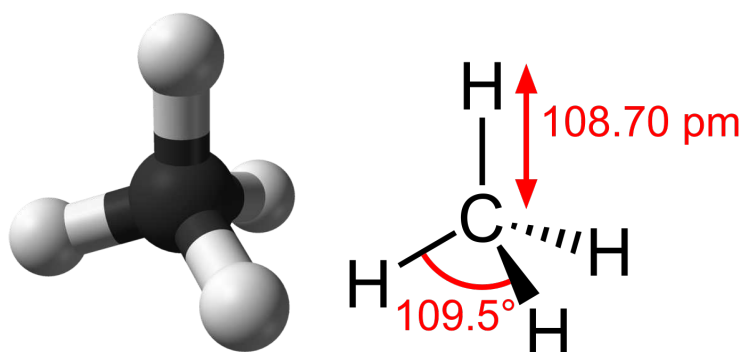


Figure 5.8: The structure of a methane molecule.

First, we measure harmonic intensity generated from  $\text{CH}_4$  and krypton separately by converting the XUV signal to electron signal through Photoionization. The detection gas we used in MBES is argon. In order to study multi-orbital dynamics, we implement the measurements at different generation energies. The results are shown in Figure 5.9, different colors correspond to different energies. The harmonic intensity generated from  $\text{CH}_4$  is presented in a) and that generated from krypton is shown in b). The intensity ratio between  $\text{CH}_4$  and krypton is in c). The harmonic intensity of both  $\text{CH}_4$  and krypton decreases towards high photon energy. Due to the small  $I_p$ , we are limited in the varying range of the generation energy. The cutoff position is not influenced by changing the energy in a) and b), probably because we are already close to the saturation intensity for ionization. In the intensity ratio, we can see a local minimum at HH19 but it is not depending on the generation energy.

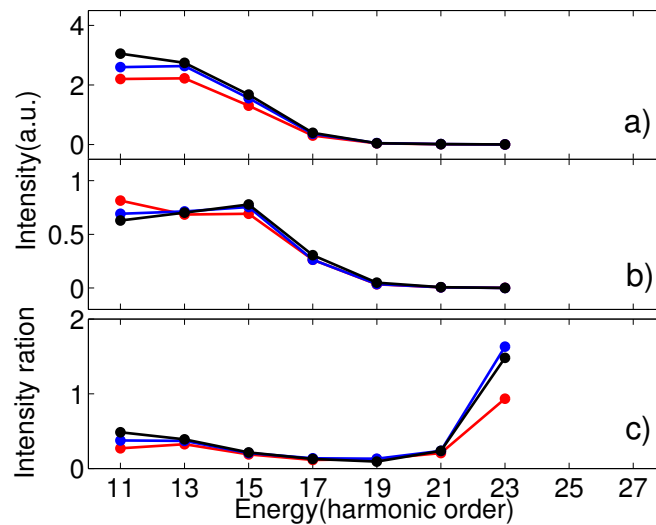


Figure 5.9: Harmonic intensity generated from  $CH_4$  a) and krypton b) as a function of photon energy. Intensity ratio of  $CH_4$  and krypton c). Generation energy of  $0.8mJ$  is in red,  $0.9mJ$  is in blue and  $1.0mJ$  is in black.

The emission time and the phase is shown in Figure 5.10. The solid lines are for  $CH_4$  and the dash lines are for krypton. Different color stands for different generation energies.  $0.8mJ$  is in red,  $0.9mJ$  is in blue and  $1.0mJ$  is in black. The raw emission time is shown in a). b) is the emission time after removing the absolute timing fluctuation by normalizing to SB12. For both  $CH_4$  and krypton, the slope is inversely proportional to the laser intensity, meaning the generation intensity in the interaction region is indeed changed. The phase in c) then can be obtained by integrating the emission time. d) is the phase for  $CH_4$  after subtracting that of krypton. As we can see, the phase is not changing much by varying the generation intensity.

### Ethane ( $C_2H_6$ )

The structure of ethane molecule is shown in Figure 5.11. It has a very small value of polarization anisotropy  $\Delta\alpha = 0.78$  leading to very limited alignment. The binding energy of its HOMO is  $11.56eV$ , for HOMO-1 it is  $13.8eV$  and  $15.2eV$  for HOMO-2 [196]. Here, we make the same measurements as we did in last section in order to study multi-orbital dynamics. Since the  $I_p$  of ethane is smaller than methane, we change the reference atom to xenon, whose  $I_p$  is  $12.1eV$

The harmonic intensity is shown in Figure 5.12. The harmonic intensity of  $C_2H_6$  is in a), while that of xenon is in b). From red, blue to black, the generation energy increases. Similar to methane, the cutoff position is not really changing by varying the generation energy for ethane a) and xenon b) because of the small range of generation intensity limited by the ionization potential. The calibrated  $C_2H_6$  intensity by xenon is in c). There is no real

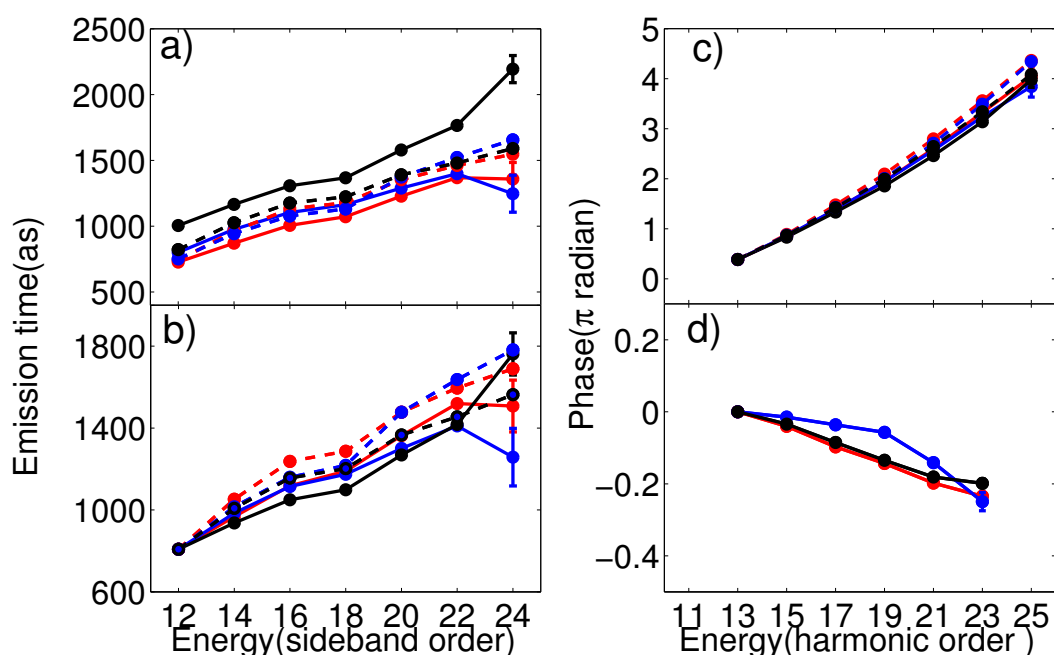


Figure 5.10: From the measured emission times to the calibrated phase. Emission times as measured a), Emission times with normalized absolute timing b), phase obtained by integrating the emission times c),  $\text{CH}_4$ -phases normalized by the krypton phase d). Solid lines stand for the measurement of  $\text{CH}_4$ , while the dash lines are for krypton. Different colors correspond to different generation energies (0.8 mJ red, 0.9 mJ blue and 1.0 mJ black). The last order is removed in d) due to the big error bar.

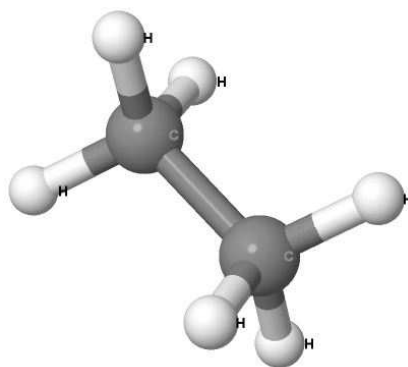


Figure 5.11: The structure of the ethane molecule.

minimum in the measured spectral range except for the case of 0.9 mJ.

Next, let us have a look of the harmonic phase, which is shown in Figure 5.13. The measured emission time can be found in a) where dash lines represent the measurements for xenon and solid lines account for the data of  $\text{C}_2\text{H}_6$ . They are all normalized to SB12 in b). Then we obtain the phase for each measurement in c). Eventually, we reach the calibrated harmonic phase of  $\text{C}_2\text{H}_6$  by xenon in d). However, the phase for different generation

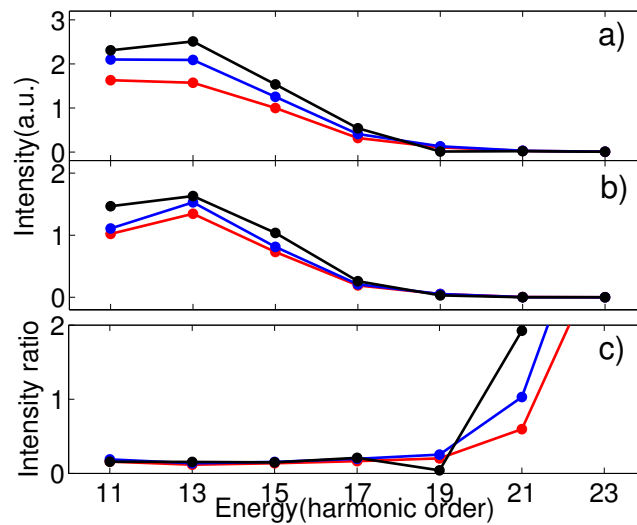


Figure 5.12: Harmonic intensity generated from  $C_2H_6$  a) and xenon b) as a function of photon energy. Intensity ratio of  $C_2H_6$  and xenon c). Generation energy of  $0.63mJ$  is in red,  $0.77mJ$  is in blue and  $0.9mJ$  is in black.

energies is not varying much.

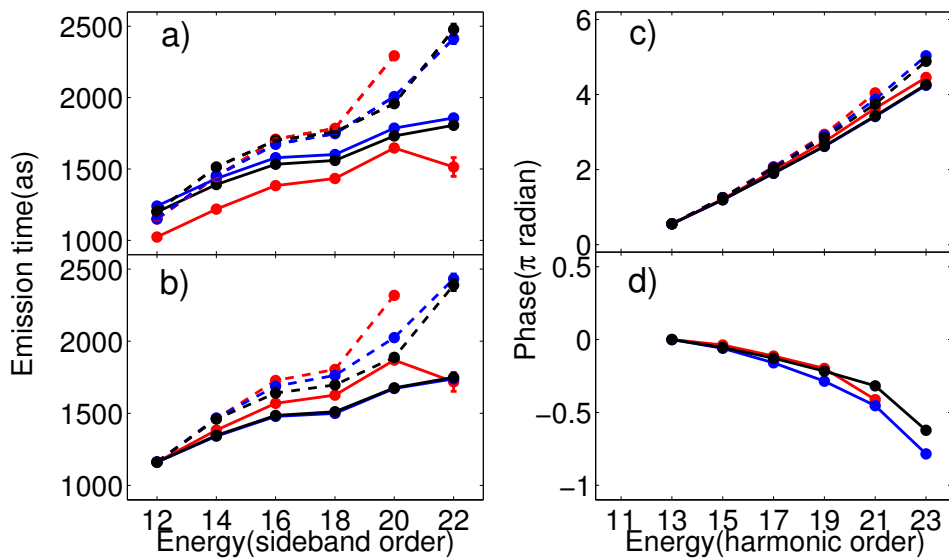


Figure 5.13: From the measured emission times to the calibrated phase. Emission times as measured a), Emission times with normalized absolute timing b), phase obtained by integrating the emission times c),  $C_2H_6$ -phases normalized by the xenon phase d). Solid lines stand for the measurement of  $C_2H_6$ , while the dash lines are for xenon. Different color corresponds to different generation energy ( $0.63mJ$  red,  $0.77mJ$  blue and  $0.9mJ$  black).

In conclusion, we have made advanced characterization of nonaligned methane and ethane molecules in both intensity and phase. But we did not observe clear fingerprint

of the molecular dynamics left in the measurements. The reason that we did not observe energy dependent harmonic emission (multi-orbital contribution) may be due to the small  $I_p$  difference between HOMO and HOMO-1, which results in a small continuum phase difference variation  $\Delta I_p \tau$  ( $\sim 0.24\pi \text{ rads}$  for methane and  $\sim 1.1\pi \text{ rads}$  at the cutoff position) that is not very sensitive on the intensity. In the experiment, we are limited by the tuning range of the laser intensity since the saturation of the ionization of the molecules with small  $I_p$  is easy to reach. Moreover, the small spectrum range we can access may not cover the region where the phase jump or minimum takes place. Now we will continue by the study of the harmonic generation from some aligned hydrocarbon molecules.

### Ethylene ( $\text{C}_2\text{H}_4$ )

Ethylene has the formula  $\text{C}_2\text{H}_4$  or  $\text{H}_2\text{C}=\text{CH}_2$ , and is the simplest alkene (a hydrocarbon with carbon-carbon double bonds). Its molecular structure is shown in Figure 5.14 top. And its polarizability anisotropy  $\Delta\alpha = 2.02$  [194], which is large enough for impulsive alignment to be achieved. The electronic structures of the orbitals are presented in Figure 5.14 bottom. From their structures, we can expect more ionization for HOMO aligned at  $90^\circ$  compared to  $0^\circ$ . The ionization is suppressed at  $0^\circ$  and  $90^\circ$  for HOMO-1 due to the nodal planes. As for HOMO-2, it can contribute at  $0^\circ$  and  $90^\circ$ . The binding energy for HOMO, HOMO-1 and HOMO-2 orbitals are  $10.5\text{eV}$ ,  $12.4\text{eV}$  and  $14.4\text{eV}$ , respectively [196]. The energies are not so far away and molecular alignment may balance the contribution to HHG for each orbital at specific angle, thus ethylene is a good candidate to study multi-orbital contributions to HHG.

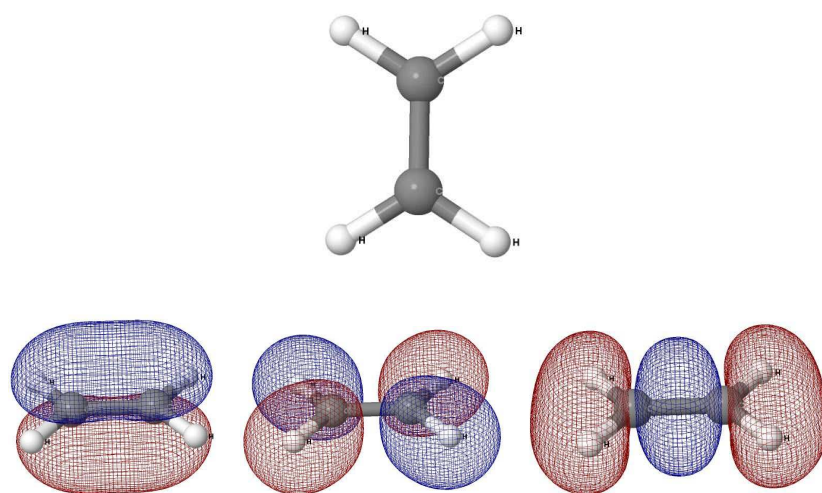


Figure 5.14: The structure of the ethylene molecule (top). The HOMO, HOMO-1 and HOMO-2 orbitals are shown from left to right in the bottom.

Figure 5.15 shows an intensity measurement when changing the delay between pump (alignment beam) and probe (generation beam) for HH19. The molecules are aligned im-

mediately along the laser polarization after the alignment beam passes, which is so called prompt alignment. Ethylene is an asymmetric top and possesses irregularly spaced rotational energy levels, and strong axis alignment is only observed immediately after the aligning laser pulse, with no later revivals. Therefore, the measurements are taken at prompt alignment (0.25 ps); at this time the alignment is maximum and is already field-free as the aligning pulse has just passed. Vozzi et al. [194] and Kajumba et al. [197] performed their measurements at the same position.

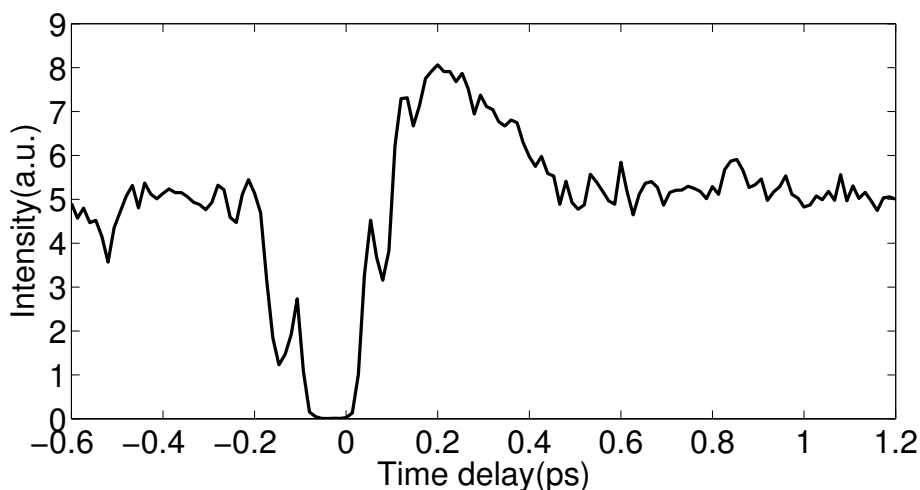


Figure 5.15: Harmonic intensity of HH19 as a function of time delay between the aligning and HH generating pulses for ethylene.

Due to the small  $I_p$  of ethylene, we have very limited range for changing the generation intensity. In the experiment, we do not see a shift of cutoff position in the spectrum when changing the energy in the limited range. Increasing the intensity more, the saturation of the ionization is soon reached. This suggests that we are not able to really vary the effective generation intensity in the interaction region. A laser system with a shorter pulse duration or at longer wavelength may fulfill the requirement, but it is beyond the ability of the current laser system. Therefore, the measurements are performed at a single intensity.

We use argon as the detection gas in MBES. The harmonic orders recorded range from HH11 to HH21. In order to study the modulation in harmonic signal caused by the alignment of the molecules, the harmonic spectra were recorded for different alignment angles. The harmonic intensity measured at prompt alignment as a function of photon energy and molecular alignment angle is shown in Figure 5.16 for ethylene itself a) and calibrated by xenon b). The tomographic harmonic intensities present angular dependence patterns both in a) and b). A strong suppression at  $0^\circ$  is observed, likely due to the nodal plane in the highest occupied molecular orbital HOMO wave function. For all the harmonic orders, the intensity is increasing from  $0^\circ$  to  $90^\circ$ , which is the same as reported by Kajumba [197].

Now let us have a look at the harmonic phase. We get the emission time from the RAB-

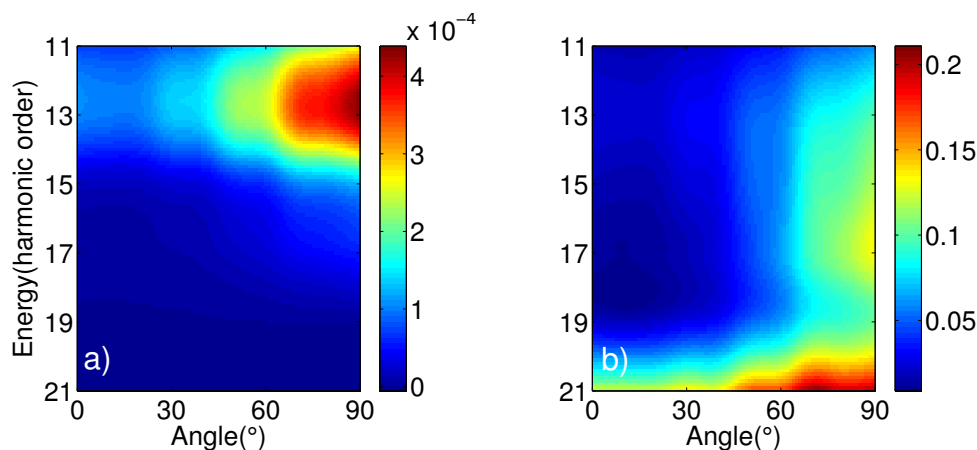


Figure 5.16: Harmonic signal generated from ethylene a) and the ratio of harmonic signal between ethylene and xenon as a function of photon energy (harmonic order) and alignment angle.

BIT scans for different alignment angles from parallel to perpendicular alignment with a step of  $10^\circ$ . The same procedure as methane and ethane is applied to the measured emission time to get the phase as shown in Figure 5.17 a) to d). The phase is flat for low alignment angles at  $0^\circ$  and  $10^\circ$ . The phase deviates more and more from  $10^\circ$  to  $40^\circ$ , which is close to  $0.15\pi rad$  for HH21. Then the phase becomes flatter from  $50^\circ$  to  $90^\circ$  except for  $70^\circ$ . Presumably there is an artifact at  $70^\circ$ . The other angles show a clear evolution with a maximum deviation at  $30 - 40^\circ$ . These are the angles where a maximum contribution from the HOMO-1 orbital is expected (see Figure 5.14). By changing the molecular alignment angle in this specific region, we may switch the main contributing channels to HHG.

### Acetylene ( $C_2H_2$ )

Acetylene has the formula  $C_2H_2$ . It is a hydrocarbon and the simplest alkyne. The carbon-carbon triple bond places all four atoms in the same straight line, with CCH bond angles of  $180^\circ$ , as shown in Figure 5.19 top. The electronic structures of the orbitals are presented in Figure 5.19 bottom. From their structures, we can expect bigger ionization for HOMO aligned at  $90^\circ$  compared to  $0^\circ$ , while for HOMO-2 the ionization is optimized at  $0^\circ$ . As for HOMO-1, it can contribute at both  $0^\circ$  and  $90^\circ$ . The binding energy for HOMO, HOMO-1 and HOMO-2 orbitals are  $11.4eV$ ,  $16.4eV$  and  $18.7eV$ , respectively [198]. The energy differences are relatively larger as compared to the molecules previously studied. Therefore, it is an ideal molecule to investigate the boundary of structural and dynamical interference.

Acetylene is a good candidate among hydrocarbons for field-free alignment due to its relatively big polarizability ( $\Delta\alpha = 2.69$ ). A typical intensity scan when changing the time delay between pump and probe is presented in Figure 5.19, which is covering the full revival of Acetylene. The measurements were performed at the molecular alignment at half revival

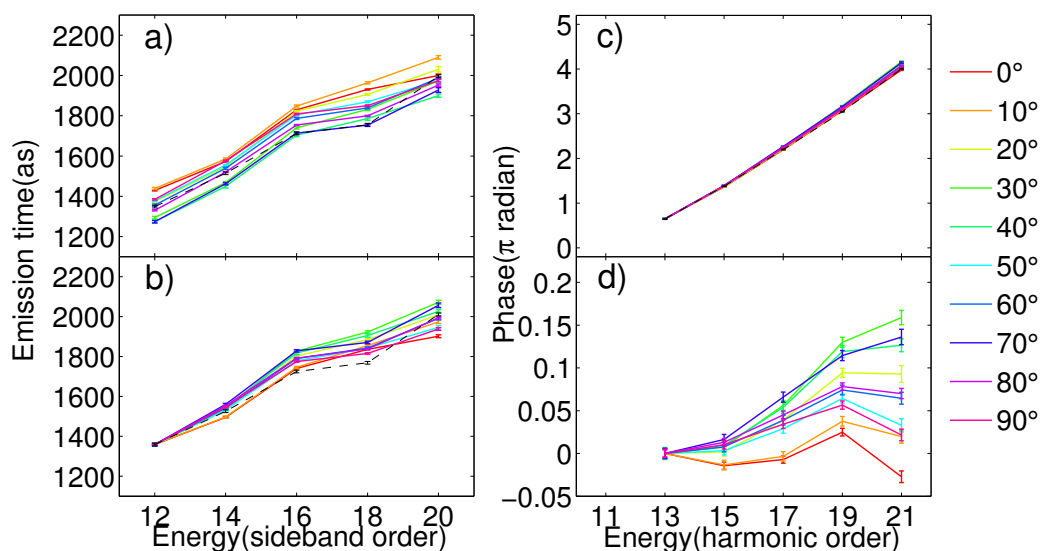


Figure 5.17: From the measured emission times to the calibrated phase. Emission times as measured a), Emission times with normalized absolute timing b), phase obtained by integrating the emission times c),  $C_2H_4$ -phases normalized by the xenon phase d). Solid lines stand for the measurement of  $C_2H_4$ , while the dash lines are for xenon. Different colors correspond to different molecular alignment angles. Black dash line indicates the reference scan of xenon.

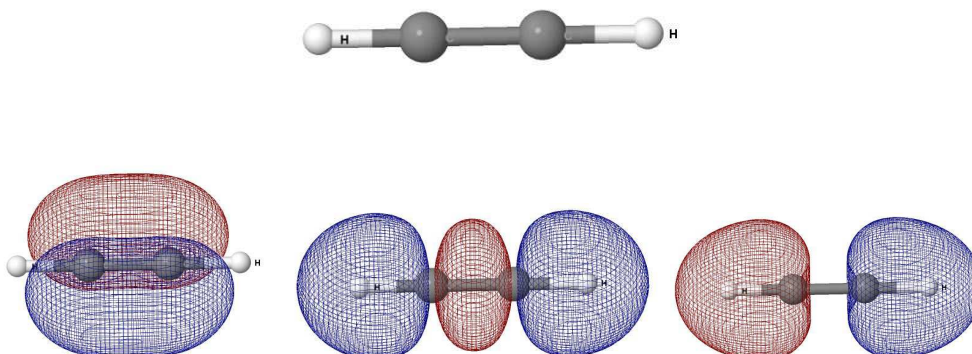


Figure 5.18: The structure of a acetylene molecule (top). The HOMO, HOMO-1 and HOMO-2 orbitals are shown from left to right in the bottom.



(6.8ps). Due to the low ionization potential, the effective intensity in the generation region could not be changed significantly, as in the case of the other hydrocarbons. Therefore the measurements were performed at the same intensity.

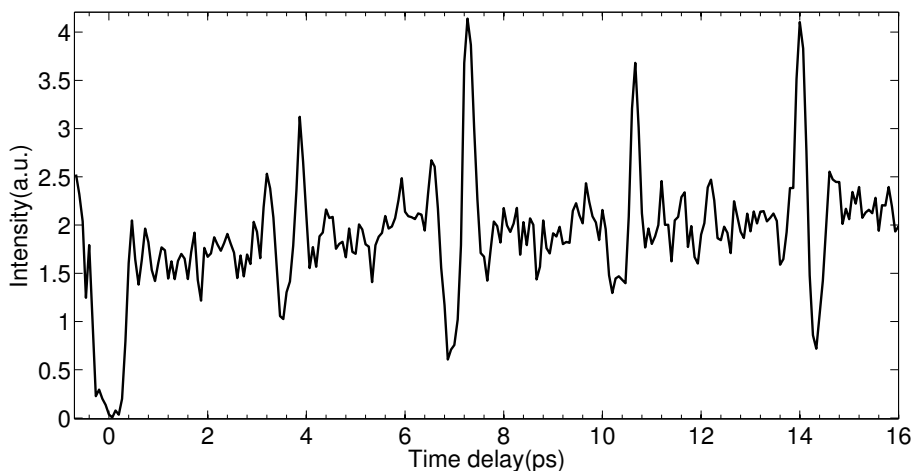


Figure 5.19: Harmonic intensity of HH19 as a function of time delay between the aligning and HH generating pulses for acetylene. The full revival is at 14.38ps [199].

The detection gas used in MBES is argon. The spectrum is recorded for different molecular alignment angles from  $0^\circ$  to  $90^\circ$  by turning the polarization of the alignment beam. The harmonic intensity as a function of photon energy and alignment angle is plotted in Figure 5.20. The raw intensity generated from acetylene is shown in a), while a calibrated intensity of acetylene with a reference of xenon is presented in b). The harmonic intensity for each order is increasing from  $0^\circ$  to  $90^\circ$ , similar results are reported by many groups[178][194][197][199]. Torres et al observed a spectral minimum at  $46eV$  at  $0^\circ$  by using a mid-IR laser [178]. In our measurement, we can see the harmonic signal continuously decreasing towards high photon energy, but we cannot reach that region.

The emission time and the phase is shown in Figure 5.21. As we can see in the calibrated phase in d), the spectral phase is varying in a sequence from  $90^\circ$  to  $0^\circ$ . The phase is flat at  $80^\circ$  and  $90^\circ$ . And it starts to deviate at  $50^\circ$  to  $70^\circ$ . Decreasing the alignment angle further, the phase is deviating more, until it reaches a maximum deviation at  $0 - 10^\circ$ . However this deviation is quite small:  $0.1\pi rad$ . This may be the onset of the phase jump that is expected at  $46eV$  if this is indeed the position of a destructive interference.

So far, we have performed the characterization of the harmonic emission from aligned ethylene and acetylene molecules. Especially, we made harmonic phase measurements which had never been performed in hydrocarbons. We observe neither structural nor dynamical interference in the spectral range that we could access. The limitation is the low ionization potential of hydrocarbons. A laser system with a longer wavelength can be used to overcome this limitation. However, we could already see clear differences when varying

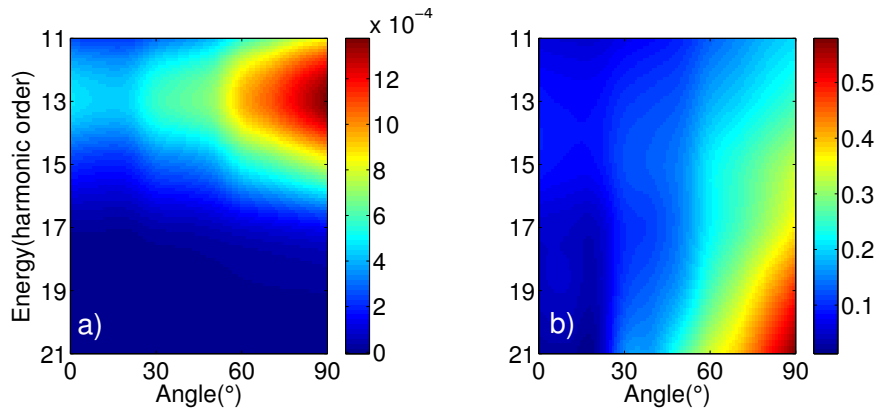


Figure 5.20: Harmonic signal generated from acetylene a) and the ratio of harmonic signal between acetylene and xenon as a function of photon energy (harmonic order) and alignment angle.

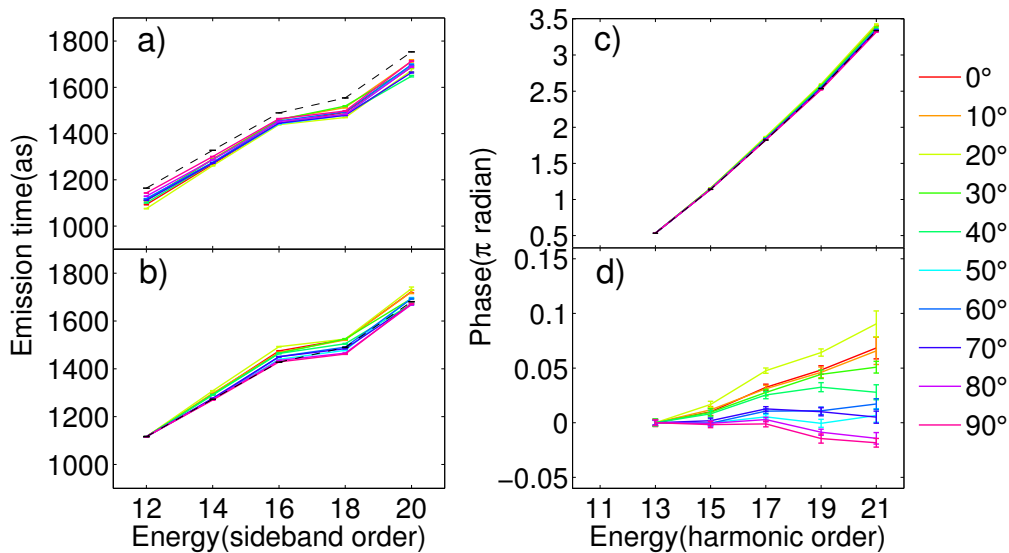


Figure 5.21: From the measured emission times to the calibrated phase. Emission times as measured a), Emission times with normalized absolute timing b), phase obtained by integrating the emission times c),  $C_2H_2$ -phases normalized by the xenon phase d). Solid lines stand for the measurement of  $C_2H_2$ , while the dash lines are for xenon. Different colors correspond to different alignment angles.

the alignment angle. The harmonic intensity is increasing from parallel to perpendicular alignment while the harmonic phase also presents angular dependence. Further studies will be needed to determine whether these phase evolutions are related to a variation of the RDM phase or to a dynamical interference. However, our results already prove the ability of our method for studying the harmonic emission from complex molecules.

### Probing Proton Dynamics in CH<sub>4</sub>

High-order harmonic generation in molecular gases is accompanied by short-time evolution of the nuclear vibrational wave function. HHG can be used as an attosecond probe of vibrational dynamics as first proposed by Manfred Lein [200]. And later observed in H<sub>2</sub> and D<sub>2</sub> [51][53], as well as in CH<sub>4</sub> and CD<sub>4</sub> [51]. Haessler et al. made the first phase measurements for H<sub>2</sub> and D<sub>2</sub> [54]. The small difference in the harmonic phase between H<sub>2</sub> and D<sub>2</sub> calculated theoretically by using a strong-field approximation theory that includes nuclear dynamics is consistent with the experimental results. However, the proton rearrangement in methane upon ionization results in a large isotopic effect, as shown by Baker [51] and later investigated theoretically by Patchkovskii [201]. The phase of the nuclear vibrational wave function for CH<sub>4</sub> has never been addressed. Here, we will study the nuclear vibration in CH<sub>4</sub> and CD<sub>4</sub> during HHG process from the advanced characterization of the HHG emission both in intensity and phase.

The harmonic intensity for CH<sub>4</sub> and CD<sub>4</sub> as a function of harmonic order is shown in Figure 5.22 (top) red and black line, respectively. The harmonic intensities are approximately proportional to the squared modulus of the nuclear autocorrelation function [200]. Since CD<sub>4</sub> is heavier than CH<sub>4</sub>, its nuclear dynamics will be much slower and thus the nuclear autocorrelation function will be close to 1. Therefore, the general harmonic intensity is bigger in CD<sub>4</sub> in the graph. The intensity ratio CD<sub>4</sub> / CH<sub>4</sub> is shown in Figure 5.22 (bottom). As we can see, the intensity ratio is increasing towards high photon energy. This is because higher harmonic orders are associated with longer excursion times of the EWP in the continuum (for the short trajectories) so that the protons of CH<sub>4</sub> have more time to vibrate, thus making the intensity ratio bigger and bigger with increasing harmonic order.

Then the emission time and the phase are shown in Figure 5.23. We get the harmonic phase for CD<sub>4</sub> calibrated by CH<sub>4</sub> as a function of harmonic order in d). We can see the phase is increasing slightly with the harmonic order. This small deviation was reproduced in another set of data. It may correspond to the variation of the phase of the nuclear autocorrelation function between CH<sub>4</sub> and CD<sub>4</sub>.

The measurements we performed thus show the ability of our technique for studying the nuclear vibration on the sub-cycle timescale. Moreover, further comparison between the theory and the experimental results will provide very fruitful information for deeply understanding the vibration process on attosecond time scale.

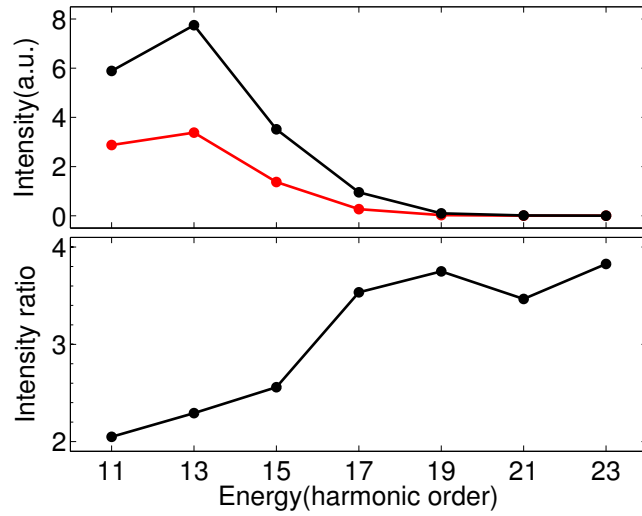


Figure 5.22: Harmonic intensity of  $CH_4$  (red) and  $CD_4$  (black) as a function of harmonic order (top). The intensity ratio between  $CD_4$  and  $CH_4$  as a function of harmonic order (bottom).

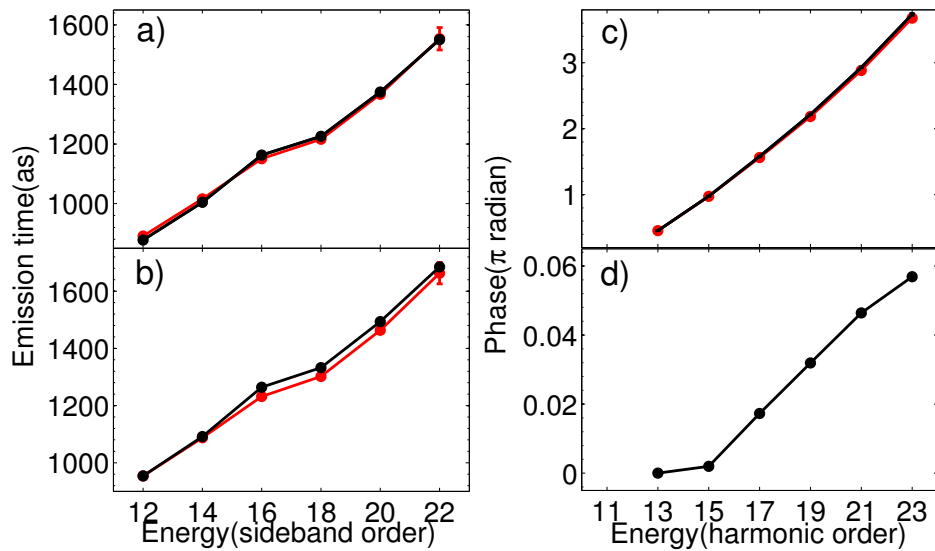


Figure 5.23: From the measured emission times to the calibrated phase. Emission times as measured a), Emission times with normalized absolute timing b), phase obtained by integrating the emission times c),  $CD_4$  phases normalized by  $CH_4$  phase d). Red line stands for the measurement of  $CH_4$ , while the black line is for  $CD_4$ .

### **5.3 HHS in SF<sub>6</sub>**

This part is written in the form of an article, reproduced below.

# High harmonic spectroscopy of the SF<sub>6</sub> molecule, a study of the spectral amplitude and phase of the emitted photons

Bastian Manschwetus<sup>1</sup>, Nan Lin<sup>1</sup>, Jan Rothhardt<sup>3</sup>, Roland Guichard<sup>2</sup>, Antoine Camper<sup>1</sup>, Thierry Ruchon<sup>1</sup>, Jeremie Caillat<sup>2</sup>, Richard Taïeb<sup>2</sup>, Bertrand Carré<sup>1</sup> and Pascal Salières<sup>1</sup>

<sup>1</sup> CEA-Saclay, IRAMIS, Service des Photons, Atomes et Molécules, 91191 Gif-sur-Yvette, France,

<sup>2</sup> UPMC Univ. Paris 06, UMR 7614, Laboratoire de Chimie Physique-Matière et Rayonnement, 11 rue Pierre et Marie Curie, 75231 Paris Cedex 05, France

<sup>3</sup> Friedrich-Schiller-University Jena, Institute of Applied Physics, Albert-Einstein-Str. 15, 07745 Jena, Germany

**Abstract.** We present measurements of the attosecond pulse train emitted from SF<sub>6</sub> molecules irradiated by strong laser pulses. In the emitted spectrum is a minimum observed at the high harmonic order 17 of the 800 nm driving field and a corresponding distortion in the spectral phase. We compare our results with measurements of the attosecond emission of Argon, which has a similar ionization potential, under the same driving laser conditions. To interpret our experimental data we developed a multi-center interference model focusing on the effects from the structure of the SF<sub>6</sub> molecule. Finally we compare our experimental data to an advanced simulation of the high harmonic generation process taking into account multichannel contributions and the photo ionization cross section for each channel.

The discovery of the high harmonic generation process and the application of the process for the generation of attosecond pulse trains and single attosecond pulses opened the way to study molecular structures and dynamics of molecular bound states and continuum states on a sub-femtosecond time scale. The process of high harmonic generation (HHG) can be described by an intuitive three step model developed by Paul Corkum and Ken Schafer [1, 2]. The atom or molecule is ionized by a tunnel process through the potential barrier formed by the interaction of the atomic coulomb potential with the strong laser field. After ionization the continuum state electron is accelerated in the oscillating laser field, and for linear laser polarisation the electron is driven back to the ion and can recombine with the ion. The excess energy of the electron is then emitted as a XUV photon. The photon energy depends on the laser intensity and wavelength and as well on the ionization potential of the target atom or molecule; for Titanium:Sapphire lasers at approximately 800 nm wavelength photon energies up to 150 eV are commonly achieved [3], for an infrared source of 4  $\mu\text{m}$  wavelength the generation of coherent x-rays up to 1.5 keV energy has been recently reported [4]. But the high harmonic generation process can also serve as a probe to investigate the structure and dynamics of the emitting target. The time and space resolution of this probe are defined by the properties of the recolliding continuum electron which encodes the information in the emitted XUV light bursts. The whole process takes place within one half cycle of the laser field, which is 1.3 fs for an 800 nm laser source. This allows probing dynamics with an attosecond time resolution [5]. The spatial resolution of the electron is given by its de-Broglie wavelength, for typical electron kinetic energies of several 10 eV this wavelength is of the order of 1  $\text{\AA}$ , similar to the size of small molecules [6]. These unique characteristics of the high harmonic generation process open new possibilities to investigate atoms and molecules. In 2010 V. Strelkov published a refined version of the three step model which includes a resonant state above the ionization limit [7]. In this model the recombination of the returning electron with the ground state is split into two steps, first the trapping of the electron into the continuum state and afterwards the stimulated decay into the ground state. In his calculation the presence of the resonant continuum state enhances the recombination probability of the electron and the XUV emission at the energy of the resonance dramatically. Experimentally this resonantly enhanced high harmonic radiation was observed in the high harmonic generation from tin plasma plumes, where the harmonic 17 of the 800 nm driving laser was enhanced by a factor 100 [8]. This raises questions such as: is the attosecond pulse structure of the high harmonic emission preserved in this process and can we observe similar features in the high harmonic generation from molecules? To answer this question we have studied the attosecond pulse trains generated by  $\text{SF}_6$  molecules irradiated by femtosecond pulses with 800nm wavelength. In the  $\text{SF}_6$  molecule several well-known shape resonances exist, which were already studied extensively in photo ionization experiments [9, 10, 11, 12]. The ionization potential (IP) of  $\text{SF}_6$  is 15.7 eV very close to the IP of Ar at 15.76 eV, which should allow us to generate efficiently high harmonic radiation and also to use the HHG in Ar as a reference signal.

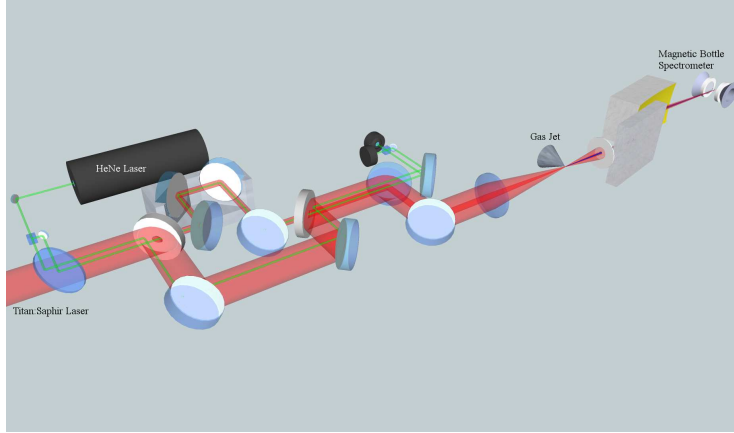


**Figure 1.** Schematics of the optical setup for the RABBIT measurements.

## Experimental setup

We characterized the attosecond emission from  $\text{SF}_6$  and Ar with the RABBIT method for different generation intensities and different backing pressures of the gas jet target. The RABBIT method allows measuring the spectral phase of the emitted attosecond pulse train based on the two-color photoionization of a target gas by the XUV radiation in the presence of a weak infrared field [13]. The photoelectron energy spectrum for pure XUV photo ionization consists of a set of lines at the odd multiples of the laser photon energy. It reflects the spectral intensity of the attosecond pulse train multiplied by the ionization cross section of the target gas, in our case Argon. Adding the IR dressing beam results in the appearance of two-photon XUV+IR processes: the kinetic energy of some of the ionized photo electrons is modified due to the addition or subtraction of one IR photon and they appear in the spectrum as sidebands at even orders between the photo electrons from the single XUV photon ionization. For the  $q$ -th sideband order there are two possible pathways, either the absorption of the  $(q-1)$ -th-harmonic photon plus one IR photon or the absorption of the  $(q+1)$ -th-harmonic photon and emission of one IR photon. These two pathways interfere with each other depending on the phase difference between the IR and the XUV light and the relative phase difference between the two harmonic lines. When the delay  $\tau$  between the IR and the XUV is changed, oscillations of the sideband intensity with a period of  $2\omega_0$  are observed, where  $\omega_0$  denotes the central frequency of the IR laser.

$$S_q(t) \propto \cos(2\omega_0\tau + \phi_{(q+1)} - \phi_{(q-1)} - \Delta\phi_q^{at}) \quad (1)$$

The phase of the oscillations is given by the phase difference between the two contributing HHG lines plus an atomic phase factor coming from the photoionization process. This factor is small and usually it can be neglected. Nevertheless for simple target gases as Neon or Argon, it can be calculated and we corrected for it in the experimental data. From the phase difference extracted from a RABBIT scan the XUV



group delay or emission time can be calculated. It is the frequency derivative of the spectral phase  $\phi(\omega)$  at the sideband number  $q$ .

$$t_{em}(q\omega_0) = \left. \frac{d\phi(\omega)}{d\omega} \right|_{(q\omega_0)} \approx \frac{\phi_{(q+1)} - \phi_{(q-1)}}{2\omega_0} \quad (2)$$

By integrating the phase difference over the whole spectrum the spectral phase of the average pulse of the attosecond pulse train can be retrieved. This spectral phase is mainly given by the phase of the continuum electron plus the phase of the recombination dipole moment, but it encodes as well information about possible sub-fs multi-orbital dynamics occurring in the molecule in the high harmonic generation process. This information can be extracted from the data when the continuum phase and recombination dipole phase contributions are known from a reference gas or from calculations.

The experiments were performed at the PLFA Laser Facility at the CEA Saclay in France. The laser system delivers 13 mJ pulses of 40 fs pulse length with a repetition rate of 1 kHz. The central wavelength of the laser is 804 nm. An overview of the used experimental setup is shown in Figure 1. The high harmonic radiation was generated by focusing laser pulses of 0.6 to 1.5 mJ energy into a pulsed supersonic gas jet of SF<sub>6</sub> or Argon, reaching peak intensities in the focal spot of  $0.6 \times 10^{14} \text{ W/cm}^2$  to  $1 \times 10^{14} \text{ W/cm}^2$ . The backing pressure of the gas jet was chosen between 0.5 bar and 3 bar. After the harmonic generation the XUV light is refocused by a gold coated toroidal mirror (f=50cm) into the detection area of a magnetic bottle spectrometer, where it crosses an effusive jet of Argon gas and produces photoelectrons. The photoelectrons are detected with a magnetic bottle spectrometer of a length of 50 cm. From their time of flight the photoelectron energy spectrum is calculated. The spectrum of the XUV radiation is then calculated by dividing the measured photoelectron spectrum with the known photoionization cross section of Argon [14]. For implementing the RABBIT technique we split the laser beam before the high harmonic generation into a strong beam for the high harmonic generation and a weak beam for the XUV-IR cross correlation by a drilled mirror with an 8 mm hole. Each beam propagates over one arm of a Michelson interferometer before the recombination of the two beams which is done also by a drilled mirror with an 8 mm hole. The generation laser beam is reflected on the outer ring, whereas the weak IR beam used for the RABBIT technique is transmitted through the central hole of the mirror. The annular beam for the high harmonic generation is easily blocked after the generation with an iris, which allow us to work without metallic filters for the XUV light. The path-length difference of the two interferometer arms is controlled with sub-10 nm precision by a piezo actuator and actively stabilized by copropagating a green He-Ne laser beam in each arm. The two He-Ne beams are split of from the IR beams by a dichroic mirror and overlaid in a beam splitter cube. The resulting interference pattern is detected with two photodiodes. From this signals the pathway difference in the interferometer is calculated in a PC with a precision of less than 10 nm modulo the laser wavelength of 543.5 nm. The measured pathway difference

is then stabilized with a PID control loop, which acts back on the piezo actuator in the interferometer.

## Results

With our experimental setup we could measure the intensity and the spectral phase for the high harmonic orders 11 to 27 generated in SF<sub>6</sub>. For each measurement a scan of the photoelectron spectrum versus the delay between the IR and the XUV pulses was taken with a range of 30 fs around the peak of the IR pulse, a typical scan is shown in Figure 2 a) and the corresponding spectrum integrated over the delay in Figure 2 b). The overall signal of SF<sub>6</sub> was approximately a factor 50 smaller than the signal from Argon, really pushing our signal to noise ratio to the limit in the RABBIT scans. The low signal also limited the range in which we could change the generation laser intensity. The harmonic amplitude of the  $q$ -th order emitted by a single molecule can be described by three complex factors according to the Lewenstein model [15], describing the tunnel ionization  $\gamma_{\text{ion}}$ , the continuum propagation  $\mathbf{a}_{\text{cont}}$  and the recombination  $\mathbf{d}_{\text{rec}}$  of the electron wave packet with the ion.

$$\mathbf{D}_{\text{HHG}}(q, \theta, \varphi) = \gamma_{\text{ion}}(q, \theta, \varphi) \times \mathbf{a}_{\text{cont}}(q) \times \mathbf{d}_{\text{rec}}(q, \theta, \varphi) \quad (3)$$

The angle between the molecular axis and the laser polarization is given by  $\theta$  and  $\varphi$  in spherical coordinates. To extract the single molecular response from our measured data, we used the high harmonic generation from Argon under the same generation conditions as a reference for the calibration of the high harmonic generation process and the spectral efficiency of the detection system. We assume that the continuum propagation of the electron for a given generation intensity is independent of the ion properties and the molecular alignment and that the spectral dependence for the tunnel ionization  $\gamma_{\text{ion}}^{\text{SF}_6}(q, \theta, \varphi)$  of SF<sub>6</sub> is the same as for the tunnel ionization  $\gamma_{\text{ion}}^{\text{Ar}}(q)$  of Ar, since both gases have the same ionization potential. Also we neglect here any influence from the HHG phase matching. By calculating now the spectral intensity ratio between SF<sub>6</sub> and Ar three factors are removed, the spectral response of the detection system, the continuum propagation factor of the high harmonic generation process and the spectral component of the tunnel ionization factor  $\gamma_{\text{ion}}^{\text{Ar}}$ .

$$\frac{\mathbf{D}_{\text{SF}_6}(q, \theta, \varphi)}{\mathbf{D}_{\text{Ar}}(q)} = \frac{\gamma_{\text{ion}}^{\text{SF}_6}(q, \theta, \varphi) \times \mathbf{a}_{\text{cont}}(q) \times \mathbf{d}_{\text{rec}}^{\text{SF}_6}(q, \theta, \varphi)}{\gamma_{\text{ion}}^{\text{Ar}}(q) \times \mathbf{a}_{\text{cont}}(q) \times \mathbf{d}_{\text{rec}}^{\text{Ar}}(q)} \quad (4)$$

As we can not fix the axis of SF<sub>6</sub> with respect to the laser polarization, we can only extract the SF<sub>6</sub> emission integrated over all possible molecular orientations from the experimental data.

$$\frac{\mathbf{D}_{\text{SF}_6}(q)}{\mathbf{D}_{\text{Ar}}(q)} \times \mathbf{d}_{\text{rec}}^{\text{Ar}}(q) = \int \gamma_{\text{ion}}^{\text{SF}_6}(\theta, \varphi) \times \mathbf{d}_{\text{rec}}^{\text{SF}_6}(q, \theta, \varphi) d\theta d\varphi \quad (5)$$

As the IR dressing field in the RABBIT scan is too weak to generate photoelectrons directly, the photoelectron intensity is proportional to the XUV intensity for each harmonic order, which allows to extract the spectral intensity of the different harmonic

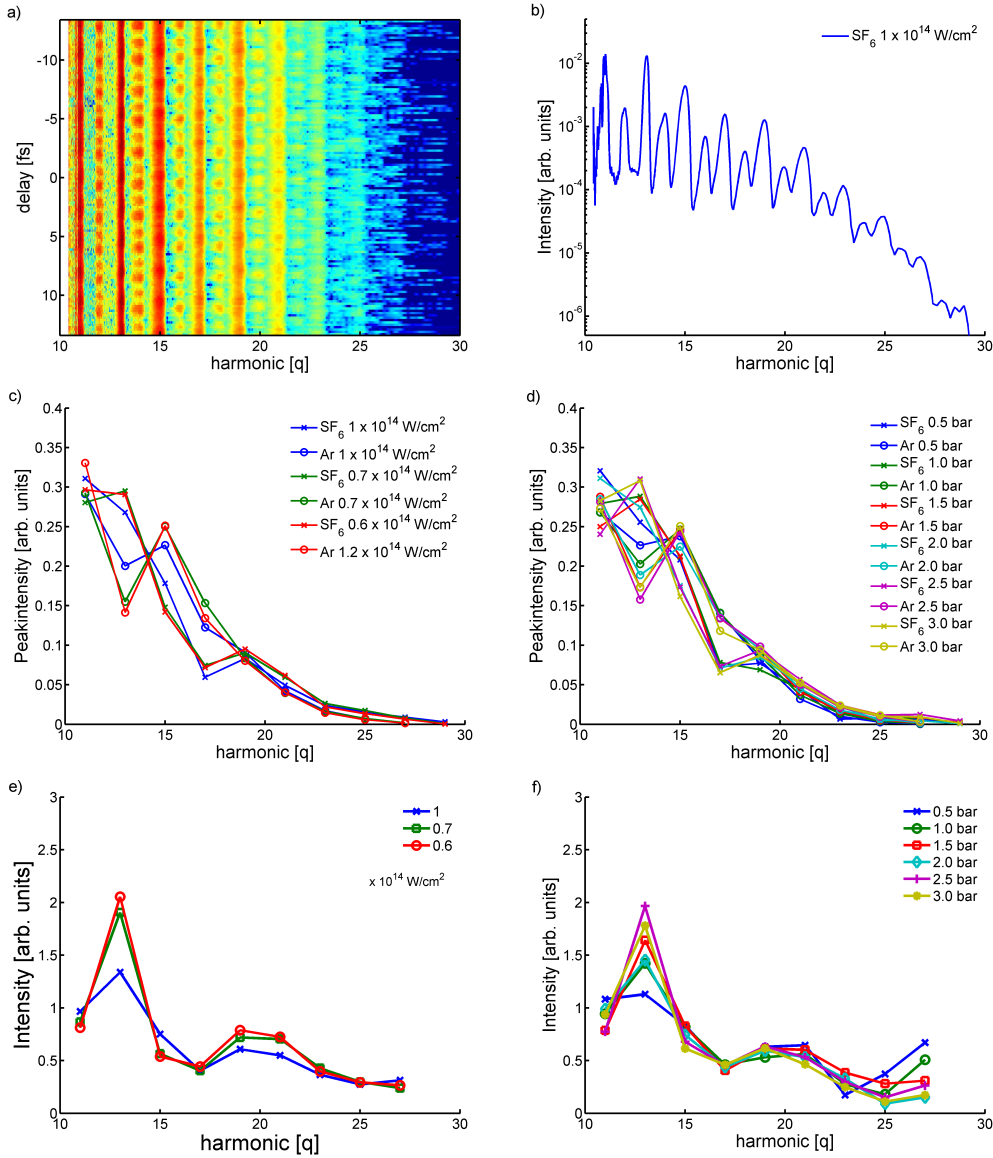


**Figure 2.** RABBIT trace a) of the high harmonics generated in SF<sub>6</sub> at a laser intensity of  $1 \times 10^{14} \text{ W/cm}^2$  on a logarithmic color scale and b) spectral intensity of the RABBIT trace in a) integrated over the delay. As the infrared dressing field can not photoionize the Argon atoms used in the detection, the relative spectral intensity of the harmonic lines can be extracted from this spectrum. Comparison of the spectral intensities of the high harmonic peaks on a linear scale extracted from different RABBIT scans at c) three generation intensities from  $0.6 \times 10^{14} \text{ W/cm}^2$  to  $1 \times 10^{14} \text{ W/cm}^2$  and d) six backing gas pressures from 0.5 bar to 3 bar. The total intensity for all harmonic orders in one spectrum is normalized to one. The spectra are still convoluted with the spectral response of the beam line, the detector and of the Ar reference. A detailed description of the calibration procedure is given in the main text. The calibrated spectral intensity of the high harmonic emission of SF<sub>6</sub> is shown in e) for the three different generation intensities and in f) for the six different gas pressures of the generation medium.

orders  $q$  from the recorded RABBIT scans after integrating over the time delay. In a last step we have to multiply the intensity ratio with the known Argon photoionization cross section to correct for the spectral response of the Ar reference, as it is not flat over the measured spectral range. In the harmonic orders above HH23 the onset of the well-known Ar Cooper minimum [14] is observed. Finally we retrieve the calibrated HHG spectral response of our SF<sub>6</sub> sample, which are shown in Figure 2 e) and f) for three different generation laser intensities  $0.6 \times 10^{14} \text{W/cm}^2$ ,  $0.7 \times 10^{14} \text{W/cm}^2$  and  $1 \times 10^{14} \text{W/cm}^2$  at a backing pressure of 2 bar and for six backing gas pressures of 0.5 bar to 3 bar at a laser intensity of  $1 \times 10^{14} \text{W/cm}^2$ . The generation intensity was deduced by comparing the measured spectral phase for Ar to SFA calculations, it is a factor two lower than the intensity we calculated from the generation beam energy and beam diameter. All high harmonic spectra show a pronounced maximum of the spectral intensity at HH13 followed by a minimum around the harmonic order 17 and a general decrease of the spectral intensity after HH 21. For the two intensities  $0.6 \times 10^{14} \text{W/cm}^2$  and  $0.7 \times 10^{14} \text{W/cm}^2$  the two spectra are very similar, whereas for the laser intensity of  $1 \times 10^{14} \text{W/cm}^2$  the maximum at HH13 and at HH 19 is smaller and the HH15 is slightly higher than in the other two spectra. We made also RABBIT measurements at different backing gas pressure (0.5 to 3 bar) of the generation gas. In the pressure dependence we see an evolution of the spectral shape mainly at the maximum at HH 13, which is relative small for a backing pressure of 0.5 bar and increases for the higher gas pressures. The intensities of the HH orders 23, 25 and 27 show a small decrease with the change in gas pressure. A careful analysis of the HH order 15 revealed a slight decrease of its spectral intensity with increasing gas pressure, which might result from an increase of the reabsorption of the XUV radiation in the gas jet.

From the RABBIT scans we extracted the phase difference between the harmonic lines and calculated the emission times according to Eq. (2). In Figure 3 a,b) the emission times for the generated high harmonics are shown for the same data sets as above, in red for the HHG in Argon and in blue for the HHG in SF<sub>6</sub>. In our experiment we have access to the absolute value of the emission time with respect to the phase of the generation field, thanks to the active stabilization of the interferometer. This absolute emission time allows a direct comparison between the two gases without an arbitrary renormalization of the emission time at one sideband. We extract the absolute emission time from oscillations of the total HHG intensity caused by the overlap of the generation and the dressing pulse in the generation medium. Their phase difference causes destructive or constructive interference of the electric fields depending on the delay  $\tau$  and therefore a modulation of the total high harmonic signal with a frequency of  $\omega$ , which is observed in the RABBIT scans Figure 2a). In all measurements we find that the emission times of the SF<sub>6</sub> high harmonics are shifted by an offset of approximately -200 as with respect to the corresponding Ar reference. In Figure 3 c) we calibrated all emission times by the linear slope, which is in first approximation the Atto-Chirp of the continuum electron wavepacket, extracted from the Ar reference scans. This is important for the calibration, as Ar has an autoionizing resonance close to HH17 [14],

which slightly affects the emission time of SB18. After the calibration only the phase changes of the generated high harmonics caused by the molecular influence remain. In the SF<sub>6</sub> emission times we always find a deviation from the Atto-Chirp at the SB 16 and 18 close to the energy of the spectral minimum at HH 17. The change is small but very reproducible around -150 as. When changing the generation intensity the emission time of the SB 18 remains unchanged but the emission time deviation at SB 16 vanishes for a generation intensity of  $1 \times 10^{14} \text{W/cm}^2$ . From the corrected emission times we can retrieve by a simple integration the spectral phase of the emitted high harmonic light, shown in Figure 3 e). The phases are all normalized to zero at HH 11. Due to the vertical offset in emission times between SF<sub>6</sub> and Ar, the spectral phase of SF<sub>6</sub> drops roughly linearly over our spectral range. The slope of this drop in the spectral phase is intensity dependent, and decreases with increasing generation intensity. The intensity dependent emission time of SB 16 leads to a small phase deviation at HH 17, at the position where we also observe the minimum in the spectral intensity. Shown in Figure 3 d) and f) are the corrected emission time and the corresponding spectral phase for the different backing gas pressures 0.5 to 3 bar at an intensity of  $1 \times 10^{14} \text{W/cm}^2$ , this data set shows also the emission time deviation mainly at SB 18 for this intensity and the general drop of the spectral phase. The SF<sub>6</sub> measurement at 1 bar backing pressure does not follow the same trend as all the other SF<sub>6</sub> measurements; we attribute this to a problem with the extraction of the absolute emission time for this RABBIT scan. All the other SF<sub>6</sub> measurements are very similar. The values for the SB 26 and 28 fluctuate strongly with large error bars due to the low signal to noise ratio. There is no pressure dependence of the measured emission times visible. Our observations raise several points which we will discuss in the following: the overall low HHG efficiency in SF<sub>6</sub>, the possible influence of the SF<sub>6</sub> shape resonance, the spectral minimum at HH 17 and the deviation in the emission times at this energy and finally the observed 200 as shift of the emission times with respect to the Ar reference.

### Phasematching and pressure dependance

In order to have an observable high harmonic signal the XUV emission over the whole gas sample should add up coherently. This condition enforces that the phases of the XUV photons of all emitters through the sample have to be matched. This phase matching is usually spectral dependent, which can modify the observed HHG spectrum strongly from the single atomic or molecular emission [16]. The main parameters for the HHG phase matching are the geometrical phase slip in the focal point, the intrinsic dipole phase variation across the medium and the dispersion caused by the neutral gas and the produced free electrons. By choosing the focus position with respect to the jet, the gas density and the generation intensity a good phase matching over the whole spectral range can be achieved. As we are interested in the HHG response from the single atom or molecule, we have to verify that our observations are robust against changes in the phase matching conditions. The easiest way is usually to change the gas density in the

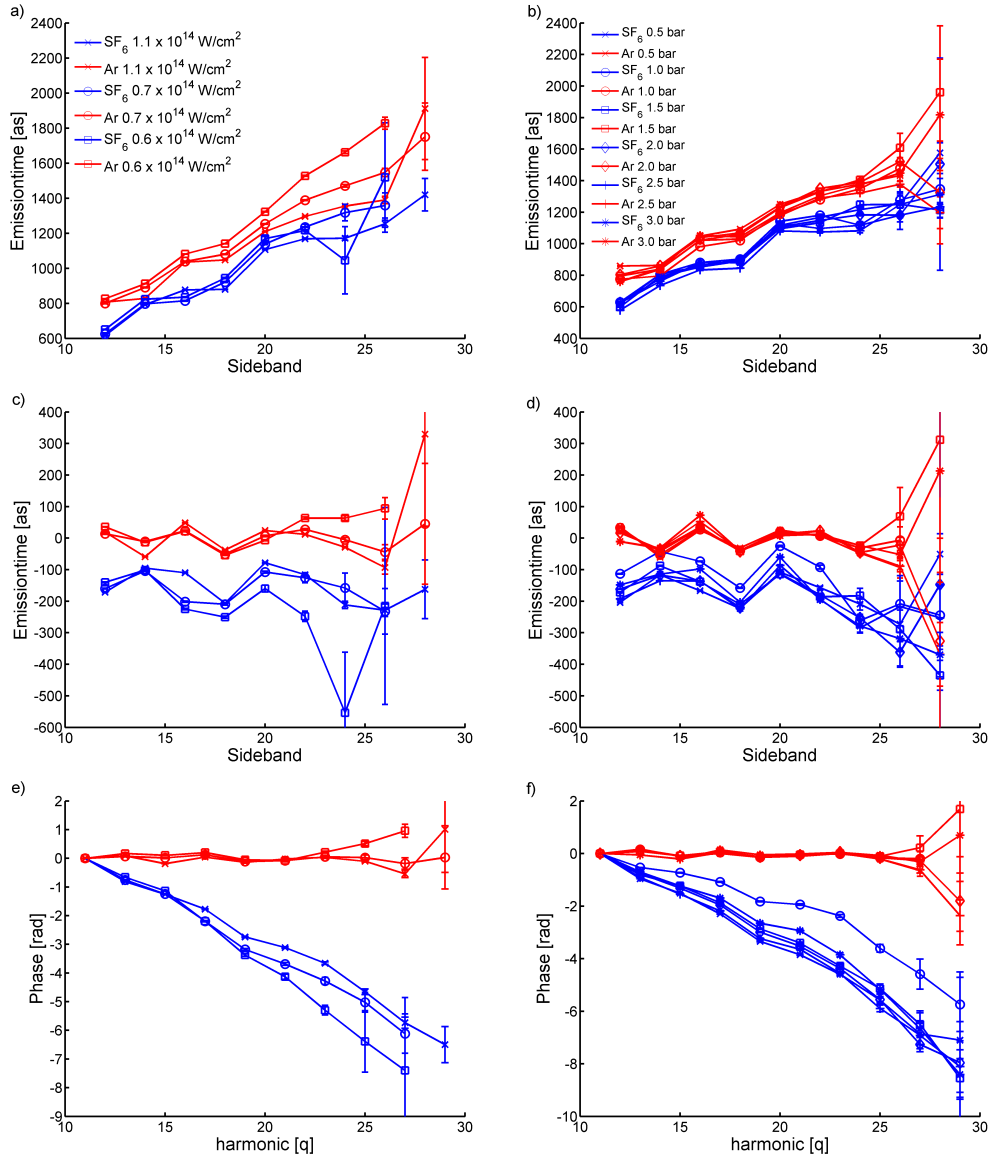


**Figure 3.** High harmonic emission times of SF<sub>6</sub> (blue) and Ar (red) for a) three laser intensities from  $0.6 \times 10^{14} \text{ W/cm}^2$  to  $1 \times 10^{14} \text{ W/cm}^2$  and b) for six backing gas pressure from 0.5 bar to 3 bar. c,d) Difference between the measured emission times for SF<sub>6</sub> and Ar and the linear fit to the argon emission times for the three intensities shown in a) and the six pressures shown in b). The black arrows mark the emission time shift of the SB 16 and 18 from the low to the high generation intensity. e,f) The spectral phase calculated from the emission time differences shown in c,d)

jet.

We were using a pulsed expansion of the gas through a hole with 200 $\mu$ m diameter with an electronic opening time of the piezo valve for 130  $\mu$ s. The interaction region of the gas with the laser focus was as close as possible to the nozzle approximately 0.5 mm downstream. For an estimation of the gas density in the interaction region we applied the formalism for the free jet expansion of an ideal gas described by David R. Miller [17]. For SF<sub>6</sub> at 20 °C and 2 bar backing pressure we calculated a density of  $3 \times 10^{17}$  molecules/cm<sup>3</sup> and for Ar  $1 \times 10^{18}$  molecules/cm<sup>3</sup> in the center line of the jet. The absorption length of the XUV light at the maximum of the photoionization cross section is for SF<sub>6</sub> 0.2 mm and for Ar 0.3 mm at these gas densities. This is of the same order as the effective length of the interaction volume in the gas jet, therefore we might have absorption effects in the high harmonic spectrum. Therefore we performed measurements at different backing gas pressures to verify experimentally that our observations are independent of the gas density in the interaction volume. We varied the backing gas pressure from 0.5 bar to 3 bar, this corresponds to gas densities between  $0.8 \times 10^{17}$  molecules/cm<sup>3</sup> and  $5 \times 10^{17}$  molecules/cm<sup>3</sup> for SF<sub>6</sub> and between  $2 \times 10^{17}$  molecules/cm<sup>3</sup> and  $15 \times 10^{17}$  molecules/cm<sup>3</sup> for Ar. We see a small pressure dependance in the intensity of the HH 13 in the Ar spectra, which decreases with increasing gas pressure, the physical effect behind this observation is so far unclear for us. The spectral intensity of the HHG in SF<sub>6</sub> does not show a strong dependance of the gas pressure also the emission times of the HHG in SF<sub>6</sub> and Ar are within the experimental error independent of the gas pressures. The offset of the SF<sub>6</sub> emission time at a pressure of 1 bar was not reproducible in a second measurement. Therefore we assume that the high harmonic phase matching and the reabsorption in the gas medium can be neglected in the further interpretation of our data.

## Multi-Center Interference Model

We will first investigate whether the observed trends result from structural interferences. To explain the features of the high harmonic emission from aligned linear molecules sometimes a simple model of two-center interference of the returning electron wave packet recolliding with a two-center molecule has been proposed, as a typical case of structural interference [18, 19]. In the following, we generalize this two-center model to a multi-center interference model. In this model the interaction of the plane wave electron with the molecular ion is reduced to the interaction with n point centers located at the positions  $\mathbf{r}_j$ , where each  $\mathbf{r}_j$  is given by the position of the atom j in the molecule.

$$A = \sum_{j=1}^n A_j \exp(i\mathbf{k}(\mathbf{r} - \mathbf{r}_j) + i\phi_j) \quad (6)$$

$$|\mathbf{k}| = \frac{2\pi}{h} \sqrt{2mE_{HHG}} \quad (7)$$

The magnitude of the electron momentum  $\mathbf{k}$  is calculated from the high harmonic energy without taking into account the ionization potential of the molecule, this allows a first

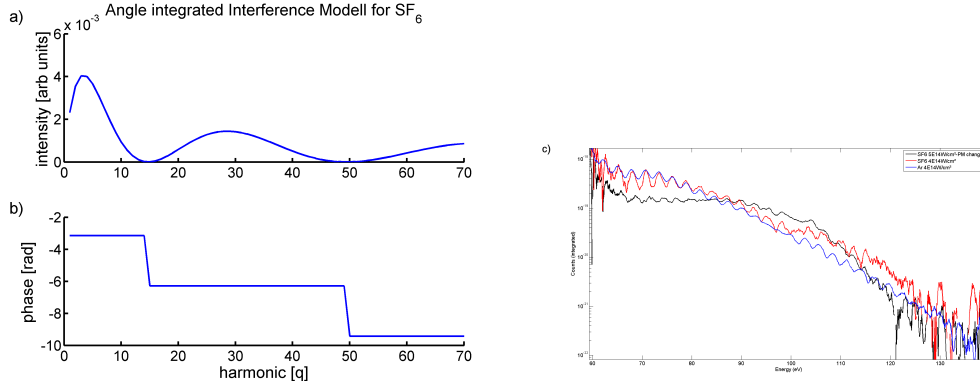


**Figure 4.** Calculated Harmonic spectral intensity (a) and phase (b) using the multi-center interference model. Two intensity minima with corresponding pi phase jumps are visible at the HH orders 15 (23.25 eV) and 49 (76.0 eV). c) Experimental high harmonic spectra of SF<sub>6</sub> (red) and Ar (blue) taken in the high energy range from 60 to 130 eV with a pulse of 950 nm wavelength and 6.5 fs duration.

order correction for the coulomb field of the ion, which accelerates the electron before the recombination. The phase  $\phi_j$  of the atomic centers is given by a global constant plus the phase difference between the centers, which reflects the symmetry with respect to the molecular axis of the Hartree-Fock orbital that is modeled by the multi-centers. In high harmonic generation we never observe the emission of a single molecule but always the macroscopic emission of an ensemble of randomly or partly aligned molecules. To include this in the model the interference structure is coherently averaged over all molecular alignment angles weighted with a possible alignment distribution.

The highest occupied molecular orbital (HOMO) of SF<sub>6</sub> is shown in Table 1. It is three times degenerate with p-orbitals localized at the fluorine atoms in the x-y, x-z and y-z plane. Each of the orbitals is anti-symmetric around the center of the molecule. The calculated spectral intensity and phase for the interference of a plane wave with randomly oriented SF<sub>6</sub> molecules is shown in Figure 4 a) and b). Two very pronounced minima are visible in the intensity at the harmonic orders 15 and 49, they are connected to sharp  $\pi$ -jumps in the spectral phase. This result is surprising since usually the interference structure is smoothed for unaligned molecular samples. In the case of SF<sub>6</sub>, due to the high symmetry of the molecule, the interference structure remains visible. This could thus be an explanation for the minimum observed at HH17 in the measured harmonic spectrum (such a simple model using plane waves cannot predict the exact position of the structural interference). We do not claim that the minimum can be fully interpreted by the 6-center interference minimum, but our model might give an indication that the structure of the SF<sub>6</sub> Orbitals may be surprisingly important even in the unaligned gas sample. This should be considered in a more complete theoretical modeling of the high harmonic generation in SF<sub>6</sub>. An experimental check if the second minimum at HH 49 or energy of 76 eV exists in the High harmonic spectrum of SF<sub>6</sub> was not possible with our Ti:Sa laser system. We are not able to generate high harmonics



above HH 27 in SF<sub>6</sub> due to ionization saturation of the medium. But Jan Rothhardt, who is working in the group of Jens Limpert at the University Jena, was able to perform some measurements in this high spectral range with their laser system based on optical parametric amplification [20]. They can produce pulses of 6.5 fs duration at 950 nm wavelength, which allows extending the high harmonic cut off in SF<sub>6</sub> and Ar to 100 eV. Their experimental spectra from 60 to 130 eV are shown in Figure 4 c). The HHG spectra of both gases show a well-developed plateau up to 80 eV and a cutoff up to 120 eV. From 60 eV to 100 eV the shape of the spectrum is very similar for Ar and SF<sub>6</sub>, at 100 eV SF<sub>6</sub> shows a knee structure and the spectral cutoff of SF<sub>6</sub> becomes slightly higher by approximately 4 eV. A pronounced minimum at 76 eV as predicted by the multi-center interference model for SF<sub>6</sub> is not visible. This model seems to be too simple for explaining the high harmonic generation in SF<sub>6</sub>. A more detailed description including also additional valence states could be the more appropriate way to interpret the experimental data. A surprising feature in the experimental data of SF<sub>6</sub> is the knee structure at 100 eV. Two explanations are possible for this structure. Either it can be explained by the contribution of inner valence states of SF<sub>6</sub> to the high harmonic generation [5] or by a change in the phase matching of the high harmonic radiation due to the tight focusing geometry used in these experiments [3]. The energy of the emitted high harmonic radiation from a single emitter is determined by the energy of the recolliding electron wave packet plus the binding potential of the ionized molecular state. The shape of the electron wave packet produces the typical plateau and cutoff shape of the emitted high harmonic radiation. In SFA the shape of the continuum electron wave packet is only given by the laser parameters, therefore it is approximately the same for all ionization channels. The contribution of an inner valence state to high harmonic radiation becomes visible in the cutoff region of the spectrum when the dominating contribution of the outer state is suppressed. It manifests itself as a second cutoff structure at a higher energy. The difference in the cut off position is given by the difference of the binding potentials of the two molecular states. The second possibility for this structure is a changed phase matching condition, since the measurement with the 950 nm wavelength laser system are done in a tight focusing geometry for the high harmonic generation. Anne l’Huillier et al. already showed in the paper from 1993 [3] that for this geometry the single atomic response cutoff law of  $E_{cutoff} = I_p + 3.17U_p$  is modified to  $E_{cutoff} = I_p + 2U_p$  due to a phase mismatch generated by the geometrical phase slip acquired through the focus. The coherence length of the high harmonic radiation can be written in this case in a simple form.

$$L_{coh} = \frac{\pi b}{2(q - 1)} \quad (8)$$

With  $b$  the confocal parameter of the laser focus and  $q$  the harmonic order. The high harmonic generation is limited by the focusing, if the length  $L$  of the medium is bigger than the coherence length  $L_{coh}$ . In a region between these two limiting cases both cutoffs become visible in the spectrum, first the single atomic cutoff and then due to the increasing phase matching of the harmonics the second cutoff. For the presented

measurements done with the 800 nm wavelength laser, this geometrical phase matching is not a limitation. The confocal parameter is  $b=0.04$  for a beam waist of 70  $\mu\text{m}$ , this allows geometrical phase matching up to the 199 harmonic.

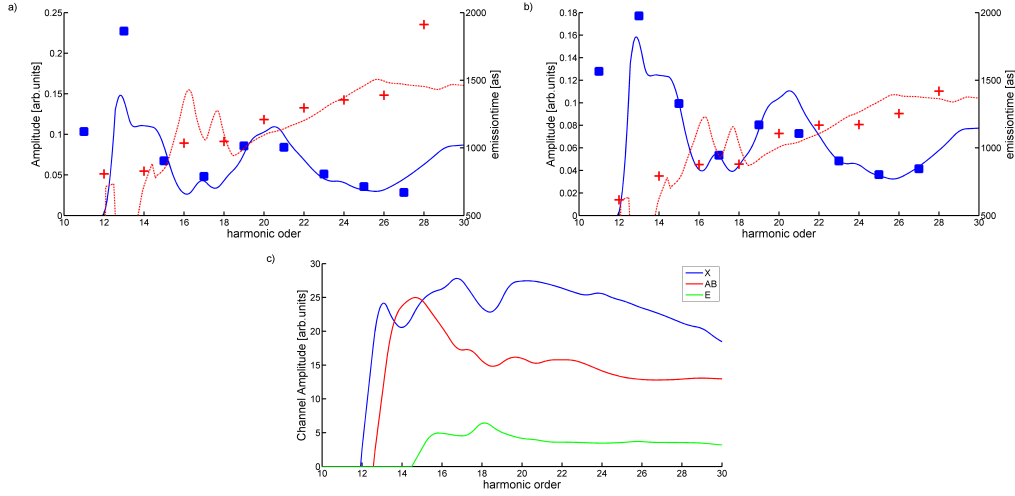
### **The emission time offset**

One very prominent feature in our measurements is the difference of 200 as in the absolute emission times for all harmonic orders between the HHG in  $\text{SF}_6$  and Ar, shown in Figure 3 c. and d.). After integration this offset transforms into the linear drop of the spectral phase for the  $\text{SF}_6$  high harmonic emission, shown in Figure 3 e. and f.). Such an offset in the emission times of the high harmonics can be an effect from the phase matching of the high harmonic radiation in the two different gases. The offset is within our experimental range independent of the backing gas pressure and therefore from the particle density. It is thus not related to the dispersion in the  $\text{SF}_6$  gas.

An other possibility is that the emission time shift is the result of HHG contribution from deeper valence states. The emitted photon energy is the sum of the kinetic energy of the electron and the binding energy of the contributing atomic or molecular state. As the returning electron has for a specific emission time always the same kinetic energy, the recombination to a stronger bound valence state will require less kinetic energy of the continuum electron for the same final photon energy. The emission times for the high harmonic orders in the plateau spectral range depend approximately linearly on the electron kinetic energy, due to the Atto-Chirp of HHG [15]. The contribution from an inner valence state will reduce the emission times for all HH orders and increase the spectral cut-off. Following this argument we can explain the observed emission time difference of 200 as between the HHG in Ar and in  $\text{SF}_6$ , if we assume that the HHG in  $\text{SF}_6$  is dominated by an inner valence state with a binding energy around 22 eV. That is the energy of the E ionization channel of  $\text{SF}_6$  which has an ionization potential of 22.5 eV. In this argumentation we focused on the behavior of a single ionization channel. As the  $\text{SF}_6$  molecule has six outer valence states, the selection of a single state, especially an inner valences state, might be too much simplified. Instead we should consider the contribution of all valence states to describe our experimental data in more detail.

### **Multiple ionization channels**

For rare-gas atoms the high harmonic generation process is dominated by the highest valence state due to the exponential decrease of the tunnel ionization rate with increasing binding potential of the electron. In molecules this general dependence is modified by the non-spherical symmetry of the molecular orbitals and the different valence states have a much smaller difference in binding energy. These two effects can lead to significant contributions of inner valence states as shown for  $\text{N}_2$ ,  $\text{CO}_2$  and  $\text{N}_2\text{O}$  [5, 6]. The  $\text{SF}_6$  molecule now has six valence states within 10 eV below the ionization threshold, their symmetry and ionization potentials are given in Table 1. The highest occupied molecular

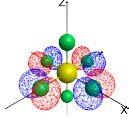
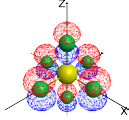
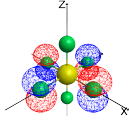
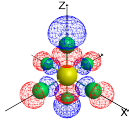
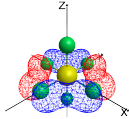
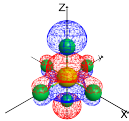
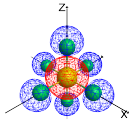


**Figure 5.** Comparison of the calculated HHG amplitude (blue) and emission times (red) for the superposition of the X, A, C, D and E ionization channels of SF<sub>6</sub> and the measured spectral amplitude (■) and emission time (+) for a generation intensity of  $0.7 \times 10^{14} \text{W/cm}^2$  (a) and  $1 \times 10^{14} \text{W/cm}^2$  (b). The sharp drop in the emission times below order 14 result from a calculation artefact, the SFA ionization channels of the A, B and C valence states are closing at these energies. c) The amplitude of the X, A and E ionization channel contributions in the multi-channel calculation for  $1 \times 10^{14} \text{W/cm}^2$ .

orbital (HOMO) is the  $1t_{1g}$  state. In addition we have to consider that in our spectral range two shape resonances are known from photo ionization experiments[12], they result from transitions from the bound states to the  $t_{2g}$  continuum state at +5.0 eV and to the  $e_g$  continuum state at +15.2 eV. Both shape resonances in SF<sub>6</sub> have gerade symmetry and are therefore not dipole coupled to the  $1t_{1g}$  HOMO state, but to the  $5t_{1u}$  HOMO-1 state, which has a slightly higher binding energy of 16.9 eV. We are therefore expecting to observe an effect of these resonances at 21.9 eV and 32.1 eV, which correspond approximately to the high harmonic orders 15 and 21, but only when the HOMO-1 is contributing significantly to the high harmonic process. We describe now the emission of the  $q$ -th high harmonic by the coherent superposition of the contribution of all channels. Each channel  $k$  is described within the Lewenstein model [15] by its tunnel ionization rate  $\gamma_{ion}^k$  times the continuum propagation of the electron  $e^{i\phi_c^k(q)}$  times the recombination dipole moment  $d_{rec}^k(q) \times e^{i\phi_{rec}^k(q)}$ .

$$D_{HHG}(q) = \sum_{k=1}^6 \gamma_{ion}^k \times e^{i\phi_c^k(q)} \times d_{rec}^k(q) \times e^{i\phi_{rec}^k(q)} \quad (9)$$

S. Patchkovski calculated the tunnel ionization rate  $\gamma^k$  of the SF<sub>6</sub> valence state  $k$  for a  $1/2$  cycle laser pulse at a wavelength of 800 nm and an intensity of  $1 \times 10^{14} \text{W/cm}^2$ [21]. The molecular orbitals have a very complex structure, which modifies the tunnel ionization rates significantly compared to the normally used atomic ADK ionization rates [22]. The values are given in Table 1. The  $5t_{1u}$  and the  $3e_g$  states dominate the total ionization rate, whereas the  $1t_{1g}$ , which is the one with the lowest binding energy,

	State	Hartree-Fock Orbital	Ip [eV]	Tunnel ionization rate at $1 \times 10^{14} \text{W/cm}^2$
X	$1t_{1g}$		15.7	2.70
A	$5t_{1u}$		16.9	7.94
B	$1t_{2u}$		17.3	1.73
C	$3e_g$		18.6	5.21
D	$1t_{2g}$		19.7	1.06
E	$4t_{1u}$		22.5	
F	$5a_{1g}$		26.8	

**Table 1.** The  $\text{SF}_6$  valence states with their Hartree-Fock orbitals and the experimental binding potentials [12]. The tunnel ionization rates are calculated S. Patchkowski [21].

is strongly suppressed. But all six ionization channels have ionization rates within one order of magnitude and none of them can be neglected, when modeling the high harmonic emission from the  $\text{SF}_6$  molecule. The continuum phase  $\phi_c^k$  the electron acquires during its continuum propagation is calculated for each state from the Lewenstein Model for the corresponding binding potential. If we neglect the electric field of the laser, the electron recombination of the returning electron wave packet and the following emission of a XUV photon is the inverse process of the normal photo ionization. Following basic principles

Generation intensity Ionization channel	$0.7 \times 10^{14}\text{W}/\text{cm}^2$		$1 \times 10^{14}\text{W}/\text{cm}^2$	
	$\gamma$	$\phi_{rec}$	$\gamma$	$\phi_{rec}$
X	1	0	1	0
AB	0.63	-0.6	0.62	-0.6
C	0	0	0	0
D	0	0	0	0
E	0.32	0	0.28	0

**Table 2.** Parameter used in the multichannel HHG calculation equation (6)

of quantum mechanics the recombination dipole moment is then the complex conjugate of the photoionization dipole moment. Therefore the amplitude of the recombination dipole moment  $d_{rec}^k(q) = \sqrt{\sigma^k(q)}$  can be calculated from the photoionization cross section for the different ionization channels, which are known from synchrotron measurements [23, 12]. In the experimental cross sections the A and B ionization channels of SF<sub>6</sub> are almost degenerate and only a combined cross section can be extracted from the data. In the calculation we used this combined cross section, which we will refer to as AB ionization channel in the following. The only unknown variable in our calculation is the phase of the recombination dipole moment. We assume that for all states this phase is independent of the harmonic order. This approximation is quite rough considering the several resonances in the SF<sub>6</sub> molecule, but to our knowledge nobody ever published theoretical calculations for the spectral phase of the photoionization matrix elements of SF<sub>6</sub>. To match the calculation to our measured HHG amplitude spectrum we used a least-square fit procedure of the recombination phase value and the tunnel ionization rate value for each of the five ionization channels X, AB, C, D and E. The result is shown in Figure 5 for the two intensities  $0.7 \times 10^{14}\text{W}/\text{cm}^2$  and  $1 \times 10^{14}\text{W}/\text{cm}^2$ . In both cases the agreement between the measured and calculated amplitudes is quite good. The maximum at HH 13 and the minimum at HH 17 are reproduced. Still for the HH orders 11 and 13 the agreement is worse than for the higher harmonic orders. This might be due to the high harmonic generation from bound excited states, which become relevant in this energy range and are not included in the calculation. The calculated emission times are always around 1000 as for HH 11, which is about 200 as higher than in the Ar measurements and about 400 as higher than in the SF6 measurements. The calculation could not reproduce the delay in absolute emission time for both gases. The reason for this discrepancy is not clear for us at the moment. A phase matching effect should depend on the gas pressure, but we could not observe any change in the observed absolute timing when changing the backing gas pressure. As the shift appears in all measurements we did, it seems to be a systematic error between the calculation and our experiment. If we remove this vertical shift from the experimental emission times, then the calculated emission times agree well with the experimental data. The emission times are dominated by the linear slope due to the atto-chirp. And there are three deviations visible at SB 16 and 18 and between SB 14 and 12. The maxima at SB

16 and SB 18 match in the position to the spectral minimum at HH 17, but they are more pronounced than the small effect visible in the experimental data. The strong drop in the emission time between SB 12 and 14 is a calculation artifact due to the closing of the A and C ionization channels. The spectral intensity of these channels is set to zero below the ionization threshold. This discontinuity causes the observed artifact. The extracted factors for the tunnel ionization and the recombination phase are listed in Table 2. Only three ionization channels are required to match the calculation to the experimental data, the X channel is the dominant one with smaller contributions from the AB and the E channel. This does not agree with the tunnel ionization rate calculations, which predict a strong contribution for the C ionization channel and a dominant contribution for the AB ionization channel. In the amplitude of the X channel are two minima visible, one at order 14 and one at order 18. The contribution of the AB channel has a strong peak at order 15, which is caused by the shape resonance from the  $5t_{1u}$  state to the  $2t_{2g}$  state. The E ionization channel shows also a resonance peak at the harmonic order 18, this is the transition from the  $4t_{1u}$  state to the  $2t_{2g}$  state.

## Conclusion

We have presented a detailed study of the high harmonic emission in intensity and spectral phase from randomly aligned  $\text{SF}_6$  molecules using 800 nm wavelength laser pulses. The overall signal of the HHG in  $\text{SF}_6$  is much lower than in Argon for the same generation conditions, which we attribute to a reduced tunnel ionization probability of the  $\text{SF}_6$  molecule, as the molecular orbitals have many lobes whose ionization destructively interfere and reduce the amplitude of the outgoing electron wave packet. The emission times of the high harmonic orders generated in  $\text{SF}_6$  show a vertical offset of -200 as compared to the emission times of the Ar reference. The offset is independent of the backing gas pressure but depends on the generation laser intensity. It causes a linear drop of the spectral phase of the high harmonic emission in  $\text{SF}_6$ . We discussed two possible explanations for this observation, which can be caused either by a macroscopic effect due to the propagation of the light pulses in different gases or by the contribution of lower molecular states contributing to the high harmonic generation process in  $\text{SF}_6$ .

At the harmonic order 13 we observed a maximum of the spectral intensity of the XUV radiation generated in  $\text{SF}_6$ , there is no phase distortion visible at this energy. At the Harmonic 17 (photon energy of 26.35 eV) a minimum and a corresponding deviation in the measured emission time of SB 16 and 18 of approximately 250 as are reported. The position and amplitude of these features is well reproduced for different backing gas pressures. For increasing generation laser intensities from  $0.6 \times 10^{14} \text{W/cm}^2$  to  $1 \times 10^{14} \text{W/cm}^2$  the minimum move slightly from in between HH15 and HH 17 to directly HH 17, the phase deviation moved accordingly from SB 16 and SB 18 to only SB 18, whereas the maximum at HH 13 decreases. Due to the low signal from  $\text{SF}_6$  and long pulses of our laser system we could not study the behavior of the spectral features on

a bigger generation intensity range. We investigated two possible explanations, either a multi-center interference of the recolliding electron at the SF<sub>6</sub> octahedral structure or the contribution of multiple ionization channels in the SF<sub>6</sub> molecule. Both approaches lead to a spectral minimum around the HH 17, but both fail to explain fully our experimental data. The multi-center interference model shows a  $\pi$  phase jump at HH 17, which is not found in the experimental spectral phase, also it predicts a second minimum at HH 50, which was not found in additional measurements done by Jan Rothhardt with a few cycle OPCPA laser source. The agreement of the data with the multi-channel contribution model is better. The maximum at HH 13 and the minimum are qualitatively reproduced and the predicted emission times show a clear deviation around HH 17. It cannot explain the 200 as offset we observed between the SF<sub>6</sub> emission times and the Ar reference without assuming unrealistic high contributions to the high harmonic generation from deep valence states. Nevertheless we expect that this multichannel approach is the right way to go for the interpretation of our data, but the input for the calculation has to be significantly improved. The main drawback in it is the lack of the spectral dependence of the phase of the recombination dipole element. The amplitude of the recombination element can be extracted from photoionization experiments, but the spectral phase is not accessible in these experiments. We assumed it to be constant over the whole spectral range. This assumption is not justified since several well-known resonances lie in our measurement range; they will have certainly an effect on the spectral phase of the recombination dipole element. Finally, we assumed independent channels but they could be coupled by the laser field, resulting in additional coupled channels that could play a role in the total emission. Further theoretical work is thus needed to uncover the rich physics underlying HHG from SF<sub>6</sub> molecules.

## References

- [1] P. B. Corkum. Plasma perspective on strong-field multiphoton ionization. *Phys. Rev. Lett.*, **71**:1994, 1993.
- [2] K. J. Schafer, B. Yang, L. F. DiMauro, and K. C. Kulander. Above threshold ionization beyond the high harmonic cutoff. *Phys. Rev. Lett.*, **70**:1599, 1993.
- [3] A. L’Huillier, M. Lewenstein, P. Salières, Ph. Balcou, M. Yu. Ivanov, J. Larsson, and C. G. Wahlström. High-order harmonic generation cutoff. *Phys. Rev. A*, **48**:R3433, 1993.
- [4] Tenio Popmintchev, Ming-Chang Chen, Dimitar Popmintchev, Paul Arpin, Susannah Brown, Skirmantas Ališauskas, Giedrius Andriukaitis, Tadas Balčiunas, Oliver D. Mücke, Audrius Pugzlys, Andrius Baltuška, Bonggu Shim, Samuel E. Schrauth, Alexander Gaeta, Carlos Hernández-García, Luis Plaja, Andreas Becker, Agnieszka Jaron-Becker, Margaret M. Murnane, and Henry C. Kapteyn. Bright coherent ultrahigh harmonics in the kev x-ray regime from mid-infrared femtosecond lasers. *Science*, **336**(6086):1287–1291, 2012.
- [5] Olga Smirnova, Yann Mairesse, Serguei Patchkovskii, Nirit Dudovich, David Villeneuve, Paul Corkum, and Misha Yu. Ivanov. High harmonic interferometry of multi-electron dynamics in molecules. *NATURE*, **460**(7258):972–977, AUG 20 2009.
- [6] S. Haessler, J. Caillat, W. Boutu, C. Giovanetti-Teixeira, T. Ruchon, T. Auguste, Z. Diveki, P. Breger, A. Maquet, B. Carre, R. Taieb, and P. Salieres. Attosecond imaging of molecular electronic wavepackets. *NATURE PHYSICS*, **6**(3):200–206, MAR 2010.

- [7] V Strelkov. Role of autoionizing state in resonant high-order harmonic generation and attosecond pulse production. *Physical Review Letters*, 104(12):123901, 2010.
- [8] S Haessler, LB Elouga Bom, O Gobert, JF Hergott, F Lepetit, M Perdrix, B Carré, T Ozaki, and P Salières. Femtosecond envelope of the high-harmonic emission from ablation plasmas. *Journal of Physics B: Atomic, Molecular and Optical Physics*, 45(7):074012, 2012.
- [9] JL Dehmer. Evidence of effective potential barriers in the x-ray absorption spectra of molecules. *The Journal of Chemical Physics*, 56:4496, 1972.
- [10] Dan Dill and JL Dehmer. Electron-molecule scattering and molecular photoionization using the multiple-scattering method. *The Journal of Chemical Physics*, 61:692, 1974.
- [11] VI Nefedov. Quasistationary states in x-ray absorption spectra of chemical compounds. *Journal of Structural Chemistry*, 11(2):272–276, 1970.
- [12] DMP Holland, MA MacDonald, P Baltzer, L Karlsson, M Lundqvist, B Wannberg, and W Von Niessen. An experimental and theoretical study of the valence shell photoelectron spectrum of sulphur hexafluoride. *Chemical physics*, 192(3):333–353, 1995.
- [13] P. M. Paul, E. S. Toma, P. Breger, G. Mullot, F. Augé, Ph. Balcou, H. G. Muller, and P. Agostini. Observation of a Train of Attosecond Pulses from High Harmonic Generation. *Science*, **292**:1689, 2001.
- [14] JAR Samson and Wayne C Stolte. Precision measurements of the total photoionization cross-sections of he, ne, ar, kr, and xe. *Journal of electron spectroscopy and related phenomena*, 123(2):265–276, 2002.
- [15] M. Lewenstein, Ph. Balcou, M.Yu. Ivanov, A. L’Huillier, and P. B. Corkum. Theory of high-order harmonic generation by low-frequency laser fields. *Phys. Rev. A*, 49:2117, 1994.
- [16] M. Schnürer, Z. Cheng, M. Hentschel, G. Tempea, P. Kálmán, T. Brabec, and F. Krausz. Absorption-Limited Generation of Coherent Ultrashort Soft-X-Ray Pulses. *Phys. Rev. Lett.*, 83:722, 1999.
- [17] David R Miller. Free jet sources, 1988.
- [18] C Vozzi, F Calegari, E Benedetti, J-P Caumes, G Sansone, S Stagira, M Nisoli, R Torres, E Heesel, N Kajumba, et al. Controlling two-center interference in molecular high harmonic generation. *Physical review letters*, 95(15):153902, 2005.
- [19] Robynne M. Lock, Xibin Zhou, Wen Li, Margaret M. Murnane, and Henry C. Kapteyn. Measuring the intensity and phase of high-order harmonic emission from aligned molecules. *Chemical Physics*, 366(1-3):22 – 32, 2009. Attosecond Molecular Dynamics.
- [20] Steffen Hädrich, Stefan Demmler, Jan Rothhardt, Christoph Jocher, Jens Limpert, and Andreas Tünnermann. High-repetition-rate sub-5-fs pulses with 12 gw peak power from fiber-amplifier-pumped optical parametric chirped-pulse amplification. *Optics letters*, 36(3):313–315, 2011.
- [21] Yann Mairesse. High harmonic spectroscopy of  $\text{sf}_6$  molecules. In *523rd WE-Heraeus Seminar High harmonic spectroscopy*, 2013.
- [22] M. V. Ammosov, N. B. Delone, and V. P. Krainov. Tunnel ionization of complex atoms and atomic ions by an alternating electromagnetic field. *Sov. Phys. JETP*, 64:1191–1194, 1986.
- [23] BM Addison Jones, KH Tan, GM Bancroft, and F Cerrina. A comparison of shape resonant behavior in the inner-shell photoabsorption and valence-level photoelectron spectra of sulfur hexafluoride, sulfur chloride fluoride and selenium hexafluoride ( $\text{sf}_6$ ,  $\text{sf}_5\text{cl}$  and  $\text{sef}_6$ ). *Chem. Phys. Lett.*, 129:468–474, 1986.



## 5.4 Conclusions

In this chapter, we have shown our ability to extend High Harmonic Spectroscopy to more complicated molecules based on our advanced characterization of HHG in intensity and phase. The measurements in  $N_2$ , hydrocarbons and  $SF_6$  are presented. (i) We found that the harmonic intensity of HH11 in  $N_2$  presented an opposite behavior compared to the other harmonic orders at high driving laser intensity. By decreasing the generation intensity, we could continuously change the harmonic intensity of HH11 from the opposite to the same as the other harmonic orders. However, there was no big evolution of the phase spectrally or angularly observed from the measurement of RABBIT or TSI, respectively. (ii) We implemented the first characterization of both intensity and phase of HHG for hydrocarbon molecules. Although we were limited by the narrow spectral range due to the small ionization potential of hydrocarbons, we could observe angular dependent behavior for both the harmonic intensity and phase of aligned ethylene and acetylene. (iii) The comparison we made for  $CH_4$  and  $CD_4$  revealed the nuclear dynamics after the ionization. We measured the relative phase  $CD_4/CH_4$  for the first time. And a slight spectral phase deviation is obtained. (iv) In the emitted spectrum of  $SF_6$ , a minimum is observed at the high harmonic order 17 of the 800 nm driving field and a corresponding distortion in the spectral phase. We performed an analysis based on the HOMO structure of  $SF_6$  molecules and on the multichannel contributions issuing from lower lying orbitals.

All the measurements in this chapter prove that HHS can be applied to complex molecules and reveal many results which were not reported by any other method. Moreover, the fruitful information we obtained in this chapter can be used to test the existing theories as well as lead to a deeper understanding of many physical phenomena with attosecond resolution, i.e. resonance, nuclear motion, electronic structure and dynamics.

---

# THE APPLICATION OF ATTOSECOND PULSES: TWO-COLOR MULTI-PHOTON IONIZATION

---

In Chapters 4 and 5, we have given examples of studies using high harmonic spectroscopy. The attosecond emission serves as a probe of the structure and dynamics in the radiating molecular system, in particular when the dynamics has been excited by the laser driving field itself ("self-probing" scheme). High harmonic spectroscopy is a smart concept which has great potential: it reveals fine features of structure and dynamics, especially encoded in the spectral phase over a broad spectral range.

However, high harmonic spectroscopy has limitations. In particular, it may be difficult to study the excited systems, which have been independently excited by a pump pulse and are further probed by HHG. In order to resolve the contribution of the excited systems to HHG, and to discriminate it from the usually dominant one of the unexcited systems, it is necessary to make use of elaborate techniques such as excitation grating [202][203]. Moreover, when several excited states contribute to HHG, it may be not straightforward to make an unambiguous link between the attosecond emission and the different excited states. This requires in general an accurate theoretical description of the system interacting with the strong field.

In parallel with nonlinear spectroscopy, HHG provides a source of extreme ultraviolet (XUV) pulses with unique properties of ultrafast duration, temporal and spatial coherence, perfect synchronization with the driving field, controlled polarization, etc.. Moreover, it offers a table top XUV source as an alternative to large scale facilities. The ultrashort pulses from HHG are very helpful in time-resolved studies of the pump-probe type, in particular when the fine delay or phase relation between the pump and the probe plays a crucial role in the dynamics and should be tuned with sub-cycle, i.e., attosecond accuracy. This is the case in the photoionization (PI) of atoms and molecules in the gas phase by multiple pulses, e.g., XUV and laser pulses, as illustrated in the RABBIT technique. In this Chapter, we will present the multi-photon, multi-color PI studies in rare gas atoms that we have performed

---

in collaboration with the group of Alain Huetz and Yan Picard at the Institut des Sciences Moléculaires d'Orsay (ISMO).

## RÉSUMÉ DU CHAPITRE

*En parallèle de la spectroscopie non-linéaire, la génération d'harmonique apporte une source d'impulsions XUV avec des propriétés uniques : durée ultracourte, cohérence spatiale et temporelle, synchronisation parfaite avec le champ laser de génération, polarisation contrôlée, etc. . . De plus, cela permet d'avoir une source XUV compacte étant ainsi une alternative aux sources de grande échelle telle que les lasers à électrons libres. Les impulsions ultra courtes de la génération d'harmoniques sont vraiment utiles pour les études résolues en temps de type pompe-sonde, en particulier quand le délai fin ou la relation de phase entre la pompe et la sonde joue un rôle crucial dans la dynamique et doit être réglé avec une précision sub-cycle optique (i.e précision attoseconde). C'est le cas de la photoionisation (PI) d'atomes et de molécules en phase gazeuse par plusieurs impulsions (e.g XUV et impulsions lasers), comme illustré par la méthode RABBIT. Dans ce chapitre, nous présenterons les études de PI à plusieurs couleurs/plusieurs photons dans des gaz rares d'atomes, effectuées en collaboration avec le groupe d'Alain Huetz et Yan Picard de l'Institut des Sciences Moléculaires d'Orsay (ISMO).*

*Dans la Section 6.1, nous discutons d'abord de la photoionisation à plusieurs couleurs/plusieurs photons dans deux régimes d'intensité différentes. Ensuite, nous présentons l'étude de la distribution angulaire des photoélectrons (PAD), qui apporte des informations riches sur le processus en question. Après ça, nous mettons en évidence les faiblesses des expériences précédentes effectuées au laboratoire, où le «jitter» femtoseconde du délai a empêché l'observation de la dépendance PAD avec le délai XUV/IR à l'échelle attoseconde.*

*Dans la Section 6.2, nous indiquons les progrès techniques réalisés pour résoudre ce problème. Le résultat majeur de notre nouvelle expérience est la différence frappante entre la PAD des pics satellites et celle des raies principales. La PAD normalisée des pics satellites, en  $\cos^4 \theta$ , où  $\theta$  est l'angle polaire par rapport à l'axe de polarisation de l'XUV/IR, dépend très légèrement du délai  $\tau$  entre l'IR et l'XUV. Par contre, la PAD normalisée des pics principaux est fortement dépendante de ce délai. Nous avons obtenu un bon accord entre les résultats mesurés et la PAD simulée en utilisant la théorie dite «soft-photon». Il est clair que les interférences entre les canaux à un photon et 3 photons sont très sensibles à la phase relative entre les champs XUV et IR. Les PAD des pics principaux sont donc une observable particulièrement utile pour étudier les propriétés du train d'impulsions attosecondes. De plus amples détails peuvent être trouvés dans le papier I.*

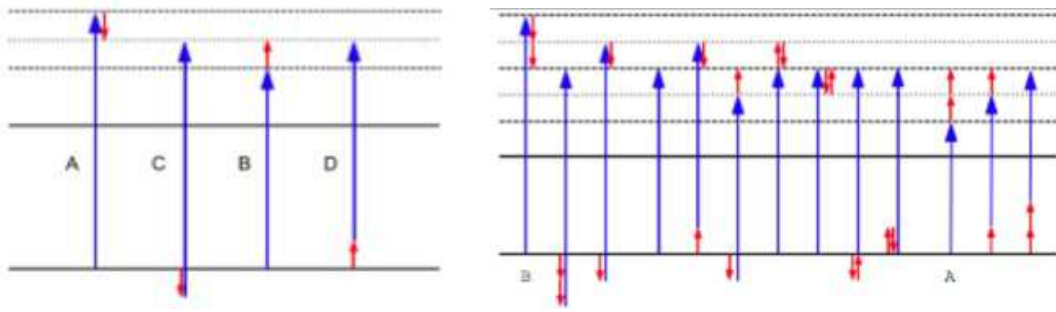


Figure 6.1: The possible quantum path of Two-color two photon ionization (left) and one and three photon ionization (right). The blue arrow lines indicate the transition induced by the XUV photons, while the red arrow line presents the transitions created by the IR photons. The horizontal thick dash lines are the odd orders transitions and the horizontal dotted lines are for the even order transitions (sidebands).

### 6.1 Multi-photon and multi-color photoionization of rare gas atoms

The two-color photoionization process is of fundamental interest by itself, e.g., to validate theoretical predictions from the time dependent Schrödinger equation. On account of their finely controlled delay, the XUV field generated via HHG and the fundamental IR field are ideal tools for this purpose. The RABBIT technique, that we have used to characterize the attosecond emission, is based on the two-color two-photon  $XUV + IR$  PI, with an IR field of weak intensity,  $I \approx 10^{11} W/cm^2$ . In this case, the photoionization occurs by the two channels  $(q\omega_0 + \omega_0, (q+2)\omega_0 - \omega_0)$  which lead to the same final state in the continuum and therefore interfere. They produce the sidebands in the photoelectron spectrum (at energy corresponding to PI by "even harmonic-like"  $(q+1)\omega_0$  photons), as shown in Figure 6.1 (left).

In the present experiment, we investigate multi-color, multi-photon PI in argon and helium in the general case where the IR intensity ranges between the RABBIT ( $I \approx 10^{11} W/cm^2$ ) and the strong-field ( $I \approx 10^{12} W/cm^2$ ) regimes, where three-photon transitions can take place as shown in Figure 6.1 (right). There are several possible paths to the final continuum state of energy  $(q\omega_0)$ , corresponding to the main line of energy  $(q\omega_0 - I_p)$  in the photoelectron spectrum. They include the direct one-photon ( $q\omega_0$ ) channel, the three  $((q-2), +1, +1)\omega_0$  (with all permutations of the photon absorption/emission), the six  $(q, +1, -1)\omega_0$ , and the three  $((q+2), -1, -1)\omega_0$  three-photon channels, which therefore interfere. So far, the photoionization has been studied extensively by means of photoelectron yield integrated over the angular distribution. Indeed, the photoelectron angular distribution (PAD) – or the electron momentum distribution – carries a rich, physically significant information on the process [204][205]. The theoretical calculation of the PAD, performed in the group of Pr. Alfred Maquet at LCPMR and using the soft-photon theory [206], predicts a dramatic pe-

riodical evolution of the photoelectron angular distribution as a function of the delay  $\tau$  between the IR field (maximum of the field) and the XUV pulse (maximum of the attosecond pulse envelope), with a frequency  $2\omega_0$ . This strongly suggests that the photoelectron angular distribution could be used to monitor the temporal structure of attosecond pulses and pulse trains.

In a first experiment performed in 2007, on the PLFA laser at CEA-Saclay, the ISMO and SPAM Attophysics groups have measured the PAD in multi-color, multi-photon PI in He, using the electron/ion spectrometer CIEL of ISMO, based on Cold Target Recoil Ion Momentum Spectrometry (COLTRIMS) in the coincidence mode. The experiment is very demanding at the 1kHz repetition rate of the PLFA laser: it requires that the temporal and spatial overlap of the XUV and laser pulses is controlled in the source volume of the CIEL spectrometer, during long acquisition times of the order of hour. The control of the temporal overlap should be compatible with definite conditions of interference between the different PI channels, i.e., fluctuations of the XUV/IR delay  $\tau \ll 500\text{as}$  (optical path fluctuations  $\ll 100\text{nm}$ ). Simultaneously, it is crucial that the spatial overlap be maintained so that the relative phase-shift of the two pulses be homogeneous over the beam wavefronts.

The XUV and IR pulses were superimposed using a Mach-Zehnder type interferometer, which arms were of  $\approx 4\text{m}$  length. Without active control, a significant timing jitter between IR and XUV pulses, of the order of  $1\text{fs}$  ( $\approx 300\text{nm}$ ), was caused by mechanical instabilities or vibrations in the experimental setup. As a result, it was not possible to accurately fix the interference conditions which were averaged. The experimentally measured PAD in the main lines of the PI process (at kinetic energy  $q\omega_0 - I_p$  in the photoelectron spectrum) could only be compared with the theoretical distributions averaged over the XUV/IR delay at the  $1\text{fs}$  scale [207]. In this frame, a remarkable agreement was nevertheless obtained between the measured and calculated PAD (thick line in Figure 6.2), the latter described with the soft-photon theory [206].

## 6.2 The 2012 experiment

In the experiment performed on PLFA in 2012, the main objective is thus to measure the photoelectron angular distribution, in both the main lines and the sidebands of the photoionization, as a function of the attosecond timing  $\tau$  between XUV and IR pulses. Such a measurement should allow for a more detailed understanding of the photoionization process and a refined comparison to theory. In addition, the sensitivity of the PAD to the characteristics of the attosecond pulses, e.g., the variation of the spectral phase from one to another harmonic, may find practical applications to an accurate monitoring of the coherent XUV sources (HHG, Free Electron Laser) in the future.

The experimental setup, derived from the RABBIT setup, is shown in Figure 2.11. The laser arm for molecular alignment has been removed. The heart of the setup is, i) the Mach-

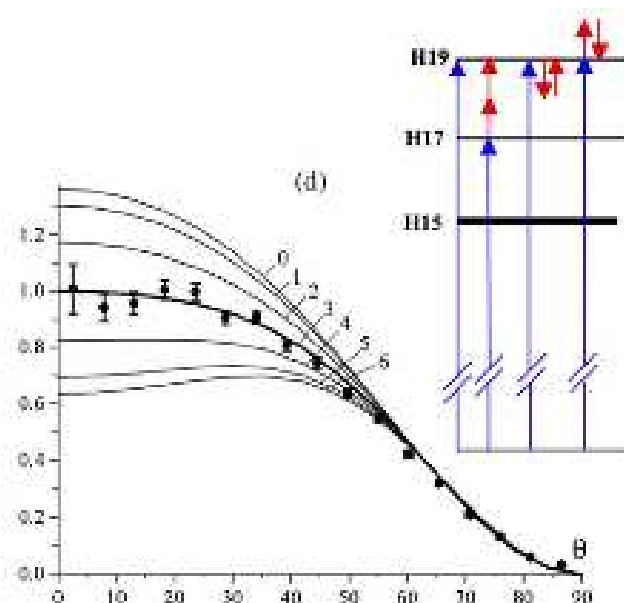


Figure 6.2: Angular momentum distribution of the electrons with an energy corresponding to ionization by H19. Calculations are shown for various values of the relative delay, ranging from 0 to 10 units of time, as indicated on each thin line curve (one unit of time is 4 atomic units or 96.756 as). The curve averaged over the delay is shown as a thick line. The dominant photon pathways are displayed on the right hand side. [207].

Zehnder type interferometer already used in RABBIT, and ii) the CIEL electron/ion spectrometer of the COLTRIMS type. In the interferometer, drilled mirrors separate the annular generating beam (outer diameter cut to 13 mm by an iris), which contains most of the energy ( $\sim 1mJ$ ), and the weak central part (up to  $\sim 150\mu J$  energy, diameter  $\approx 4mm$ ). The outer part of the laser beam is employed for high harmonic generation. The inner part serves as the dressing beam for RABBIT measurements (see below) and for the two-color XUV+IR photoionization in CIEL. The latter can be delayed by a piezoelectric translation stage with interferometric stability, i.e., the stability of the optical path difference between the two interferometer arms has to be  $\sim 50nm$ . In the COLTRIMS reaction microscope (CIEL) [208], the full three-dimensional momentum distribution of the photoelectrons (and ions) produced in helium or argon is measured in the coincidence mode (number of events per pulse  $\leq 0.1$ ). The initial momentum of the photoelectron is accurately determined from the (time, position) measurement of its impact on a time-position 2D-detector (delay line), and by de-convoluting its trajectories in parallel electric and magnetic fields. Typical measured momentum distributions are displayed in Figure 6.3 as cuts in the momentum space.

In parallel to the measurement in CIEL, we have chosen to implement the RABBIT technique. The objective is to finely monitor the delay  $\tau$  between IR and XUV pulses in fast RABBIT scan, prior to or during the long acquisition in CIEL. To that purpose, the additional magnetic bottle electron spectrometer (MBES) is implemented in the beam line,

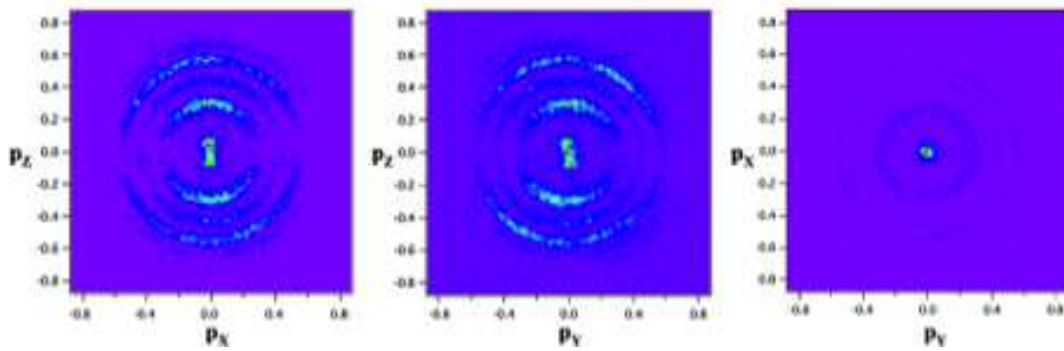


Figure 6.3: Cuts in momentum space (atomic units are used) for  $P_Y$ ,  $P_X$  and  $P_Z = 0 \pm 0.17$  [207].

between the HHG chamber and the CIEL spectrometer as illustrated in Figure 2.11. For RABBIT measurement, the IR dressing intensity is reduced to ( $I \approx 10^{11} \text{W/cm}^2$ ) by close an diaphragm, without changing the other experimental conditions.

In addition, several significant improvements have been introduced with respect to the 2007 experiment:

i) As above mentioned, it is necessary to nicely overlap the wavefronts of the XUV and IR beams in the interaction volume of CIEL, in order to achieve homogeneous phase shift and a clear sideband oscillation (good contrast). To make the dressing beam focal spot bigger than that of the generating beam should help : a 4 mm-hole drilled mirror was used, instead of the 8 mm-hole one, for combining the generating and dressing beam collinearly. We also need slightly higher energy in the dressing arm compare to the RABBIT case, to induce multiphoton ionization : the drilled mirror for splitting the beam at the *entrance* of the interferometer was replaced by a beam splitter and a telescope was added in the dressing path for confining more energy in the hole. The dressing energy was increased to  $\approx 150 \mu\text{J}$ . In the same time, the telescope has another benefit as it partially compensates the beam astigmatism. As a result, the max/min contrast of the sideband oscillation was increased to  $\sim 6$  instead of  $\sim 3$ , which was never reached before.

ii) To improve the timing stabilization which was not sufficient for attosecond control in the 2007 experiment [207], an active stabilization scheme has been worked out and installed (work of Martin Bottcher, Thierry Ruchon and Bastian Manschwetus) [209], which guarantees attosecond stability during COLTRIMS acquisition. The principle is that two cw beams from a He:Ne laser are co-propagated with the driving and dressing IR beams along the two arms of the Mach-Zehnder interferometer, and further recombined, so that the optical path difference can be monitored from the He:Ne fringe pattern; a correction error in a feedback loop is then applied to the XUV/IR delay line. In somewhat more details, the 543.5 nm Helium:Neon (HeNe) laser is divided into two sub-beams by a beam-splitter

cube. The sub-beams are shifted away by 1 cm from each other by a silver mirror, so that they can co-propagate collinearly with the driving/XUV and dressing beams along the two arms in the interferometer. The two He:Ne beams are then recombined with a sequence of 1) a drilled mirror which makes the two beams quasi-collinear, 2) a dielectric mirror with a spectral bandwidth from 750 to 950 nm, transmitting most of the He:Ne light, 3) a beam-splitter cube. By introducing a small angle between the beams (drilled mirror), we produce an interference field in the beam splitter, depending on the path difference, so that the horizontal fringe pattern is split in two. Each of the two interference fields (fraction of a fringe) is monitored by a apertured photodiode. The positions of the photodiodes are chosen so that they monitor two parts  $90^\circ$  relatively out of phase, respectively (a maximum on the one corresponds to a rising or falling intensity on the other). The phase  $\phi$  of the interference pattern can be extracted from the  $I_1, I_2$  outputs of the photodiodes. From the phase the path difference between the two arms of the delay line is calculated and a Proportional-Integral-Derivative (PID) loop acting on the piezo position allows stabilizing the delay  $\tau$  within an error of  $\pm 60$  as rms. The PAD measurement in Ar and He are performed stepwise. First, a fast RABBIT scan is performed using the MBES. It allows to choose the  $\tau$  value to either maximize (minimize), or conversely minimize (maximize) the sideband (main line) amplitude for a given  $(q + 1)$  order, or any other intermediate setting of the sideband oscillation. Second, the  $\tau$  delay is taken as the setpoint of the active stabilization loop, whereas a long acquisition is performed in the CIEL spectrometer. The experimental results and their theoretical description are reported in paper I, submitted to the Phys Rev Lett.

The measurements are performed in Ar and He at intensity close to  $10^{12} \text{W/cm}^2$  for two main delays  $\tau$ , which respectively maximize and minimize the sidebands. The major result of our study is the striking difference between the PAD of the sidebands (*SB14* in Ar, *SB20* in He) and mainline (*H13* in Ar, *H19* in He). The normalized PAD of the sidebands, in  $\cos^4\theta$  where  $\theta$  is the polar angle referred to the XUV/IR polarization axis, depends only slightly of the delay  $\tau$ . In contrast, the normalized PAD of the mainlines are strongly dependent on the delay, as shown in Fig. 4 in paper I. The PAD have been simulated by R. Taïeb and collaborators at LCPMR, using the *soft-photon theory*[206].

The numerical solution of the TDSE for a multi-electron system is beyond the present-day computers capability. Most TDSE treatments rely on the use of single active electron model-potentials[210][211]. In addition, when discussing the physical content of the numerical results (and of the experimental data), it is instructive to compare them to the quantitative predictions of simplified analysis. That is why we advocate the use of the *soft-photon theory*, which applies when the photon energy  $\hbar\omega_0$  is small, as compared to the kinetic energy  $E_k$  of the photoelectron. In the context of IR-XUV ionization, the formalism has been described in [206] and paper I. Indicated by the calculation, if the phase shifts are constant in the energy interval considered, the angular dependence for the sidebands can be written in a simplified form that is dependent on the phase  $\Delta\phi(\tau) = 2\omega_0\tau - \Delta\phi_{2q}$ , where



$\Delta\phi_{2q}$  is the harmonic phase difference (see Eq. 6 in paper I). The change of  $\Delta\phi(\tau)$  results in the change of  $\cos[\Delta\phi(\tau)]$  in Eq. 6, which only influences the magnitude of the sideband without affecting the angular distribution. However, unlike the sidebands, the angular distributions for the mainlines varies significantly when changing  $\tau$ . A general expression for the mainlines will be reported later in R. Taïeb et al. to be submitted.

The agreement between measured and simulated PAD is good (see Fig. 4 in paper I). It makes clear that the interference between the one-photon, twelve three-photon channels are very sensitive to the relative phase of the XUV/IR fields. The PAD of the main lines should be therefore considered as a useful track to investigate the attosecond pulses train properties.

---

## CONCLUSIONS AND OUTLOOK

---

This thesis mainly concentrated on the application of attosecond pulses to High Harmonic Spectroscopy of a variety of molecules. The advanced characterization of the attosecond emission brings plenty of useful information about both the molecular properties and the ultrafast processes occurring in harmonic generation. Another part of the thesis is dedicated to the 'direct scheme' of using HHG as an XUV light source. Here, we give a general summary of the experimental results and theoretical analysis. The perspectives that are opened by this work are also discussed.

### **High Harmonic Spectroscopy**

The studies of High Harmonic Spectroscopy in different molecules were presented in Chapters 4 and 5. In Chapter 4, we implemented two different methods (RABBIT and TSI) for the advanced characterization of the attosecond emission from aligned molecules ( $\text{N}_2\text{O}$  and  $\text{CO}_2$ ). Characterizing the harmonic emission in two different dimensions (spectrally and angularly) allows testing the assumptions made by each method, as well as checking the consistency of the two techniques. More importantly, the two measurements lead to a full mapping of the harmonic intensity and phase. We found clear signatures of destructive interferences due to multi-orbital contributions to HHG in both molecules by changing the intensity of the generating laser beam in the interaction region. In addition, we performed a detailed investigation for aligned  $\text{N}_2\text{O}$  and  $\text{CO}_2$  under the same generation conditions. Striking differences between the two measurements were observed for both methods. We developed a simple model in order to understand the underlying physics. It provides excellent agreement with our experimental results as well as explains the differences between  $\text{N}_2\text{O}$  and  $\text{CO}_2$ : they are due to the different contribution ratio to the harmonic emission from the lower lying orbitals. Interestingly, we demonstrate in  $\text{N}_2\text{O}$  a stronger harmonic emission from HOMO-1 than from HOMO. Moreover, we showed our ability to control the temporal shape of the XUV emission with attosecond precision in a simple way of turning the molecular alignment angle. In Chapter 5, the High Harmonic Spectroscopy is extended

---

to bigger molecules, including SF<sub>6</sub> and various hydrocarbons, where we found many unreported behaviors. Their interpretation requires advanced theoretical analysis. From all these studies, we can draw the following concluding remarks and outlooks:

(i) The harmonic phase contains more detailed information than the intensity. The phase measurements of N<sub>2</sub>O and CO<sub>2</sub> in chapter 4 are sensitive enough to observe significant differences between them even though they have similar electronic and orbital structures. These measurements may even give access to the contribution ratio to HHG between the channels involved in the generation process, which has never been obtained by intensity measurements. Besides the techniques presented in the thesis, there exist other methods giving access to the harmonic phase, i.e. gas mixture [159][184] and transient grating spectroscopy [212]. It will be interesting to compare the results from these different techniques in order to find out their technical limitations and relative precision.

(ii) The full mapping of the harmonic dipole is crucial for molecular orbital tomography. It requires combining at least two characterization techniques exploring the phase variation in two different dimensions. The first full mapping of the harmonic phase for N<sub>2</sub>O by using TSI and RABBIT was shown in Chapter 4. However, these measurements were not performed simultaneously, therefore the comparison and combination of both had to be done carefully since the experimental results are highly dependent on the experimental conditions. In N<sub>2</sub>O, the experimental conditions can be easily checked thanks to the clear signature of the destructive interference from multi-orbital contributions. Once we obtain the same position of the destructive interference and further of the cutoff position from both techniques, the experimental conditions should be comparable. However, to generalize the full mapping technique for harmonic dipole, one has to implement both measurements at the same time. Another PhD student Antoine Camper in our group has implemented a new technique allowing a quick switching between RABBIT and TSI measurement for N<sub>2</sub>, keeping the experimental conditions unchanged. This technique will allow a very precise investigation of various molecular targets. Let us add that recently, Bertrand et al. linked the phase characterization using TSI with the gas mixture for aligned Br<sub>2</sub> [161]. This provides the angular phase relative to the reference gas, which is all the information needed for the orbital tomography. However, it does not give access to the spectral phase (except if the spectral phase of the reference atom is assumed) and thus it does not allow the reconstruction of the attosecond emission.

(iii) To fully characterize the harmonic dipole, the polarization of the harmonic emission should be measured. Indeed, even though the generating laser pulse has a linear polarization, the symmetry may be broken by the molecular alignment, so that the harmonic electric field may present a component orthogonal to the laser polarization. Several polarization experiments were performed, following the first study in aligned molecules (Levesque et al. [213]). Significant amplitude for the perpendicular component was measured in O<sub>2</sub> and CO<sub>2</sub> and even a dephasing resulting in elliptical polarization for aligned N<sub>2</sub> molecules

[181][214]. We have performed a full mapping of the parallel component. It will have to be extended to the perpendicular component. Let us note that such advanced characterization will involve extensive data acquisition time. A full set of RABBIT measurements from  $0^\circ$  to  $90^\circ$  takes  $\sim 50$  minutes at 1 kHz rep-rate. The recent plan of upgrading PLFA system to 10 kHz will further increase the acquisition efficiency.

(iv)  $\text{N}_2\text{O}$  is an asymmetric molecule, therefore it is important to orient it instead of aligning it to avoid the averaging over the two opposite molecular orientations. The orientation of CO molecules has been reported [215]. But the attempt for  $\text{N}_2\text{O}$  was not successful perhaps due to its weak polarity [179]. Recently, the quality of molecular orientation has improved thanks to a bipulse scheme in Prof. Wörner's group in ETH-Zurich (not published yet). Maybe it will be possible to increase the orientation quality for  $\text{N}_2\text{O}$  now. Together with the technique proposed for molecular tomography of asymmetric molecules [216], it may pave the way to the extension of High Harmonic Spectroscopy to polar molecules.

(v) The spectral phase deviation from  $0^\circ$  to  $90^\circ$  is larger in  $\text{N}_2\text{O}$  than in  $\text{CO}_2$ , therefore the corresponding distortion in the temporal domain is stronger too. It results in a flexible control for the spectral phase by just turning the molecular axis with respect to the laser polarization. In addition, the development of XUV multilayer mirrors [186] gives the freedom of controlling the relative intensity for different spectral regions. Thus, the combination of both techniques (amplitude and phase control) has great potential for the shaping of attosecond pulses.

(vi) In High Harmonic Spectroscopy, the amount of information we can extract highly depends on the spectral range we can access. The use of Mid-infrared lasers results in a larger harmonic spectrum, that will allow a deeper investigation in particular in molecules with low ionization potential like hydrocarbons. Moreover, Rupenyan et al. showed that they observed a switching between a regime dominated by multi-channel dynamics to a regime dominated by the HOMO structural interference by increasing the laser wavelength [179][180]. Therefore, either structural or dynamical interferences could be investigated by varying both the generation intensity and wavelength. Finally, longer wavelength means larger excursion time of the EWP trajectories, so that the nuclear dynamics get more time to develop. The channel dependent vibration could also be investigated. These are a few of the many opportunities opened by mid-IR driving lasers.

(vii) The photodissociation of  $\text{N}_2\text{O}$  can be induced by irradiation with a photon of energy  $E \geq 3.5\text{eV}$ :  $\text{N}_2\text{O} \rightarrow \text{N}_2 + \text{O}$ . By changing the delay between the photoionizing beam and the generating beam, in principle one could follow the evolution of the non dissociated orbital structure into the dissociating one. Such a time-resolved molecular orbital tomography is obviously highly challenging but would open the way to real-time imaging of frontier orbitals during chemical reactions.

---

## Direct application of attosecond pulses

In Chapter 6 and paper I, we discussed the direct application of attosecond pulses: combining XUV and infrared (IR) photons from the same femtosecond laser source gives access to few-photon, two-color ionization of rare gas atoms. The angular distribution of the Photoionization lines was measured as a function of the attosecond timing between XUV and IR pulses. We evidence marked differences in the measured angular distributions of the photoelectrons, depending on the number of IR photons exchanged. Joined to a theoretical analysis, these observations bring new insight in the dynamics of this class of two-color photoionization processes that are a key step towards studying photoionization in the time domain, with attosecond time resolution.

This thesis also involved the investigation of isolated attosecond pulse generation (Chapter 1.6). The development of the post pulse compression by using hollow core fiber has been performed together with the SLIC laser team. The first measurements indicated the production of 13.3 fs pulses with output energy of 1.4 mJ after chirped mirror compression from a 45 fs, 4 mJ seeding. With a more stable fiber mounting design as well as the newly tested fibers with 95% transmission efficiency, we can expect a stable output pulse with higher energy. Different optical gating methods were also compared. A linear version of Generalized Double Optical Gating was proposed to gate out a small linear polarized pulse to generate spectral continuum. It has many advantages, i.e. easy to implement, less expensive and more energy efficient. Meanwhile, the laser team has developed a shot-to-shot CEP measurement. All these developments will allow high-energy isolated attosecond pulse generation on the EquipeX ATTOLAB laser beamlines.

In conclusion, High Harmonic Spectroscopy is a promising tool to determine both molecular structure and dynamics. Together with direct application of the generated attosecond pulses, it opens wide prospects for the study of the fastest molecular dynamics with attosecond resolution.

---



---

## ATOMIC UNITS

---



---

Atomic units greatly simplify formulae and render typical values appearing in calculations on atomic-scale systems more computer-friendly. In atomic units, the four fundamental quantities *electron rest mass*,  $m_e$ , *elementary charge*,  $e$ , the *reduced Planck's constant*,  $\hbar$ , and *Coulomb's constant*,  $1/4\pi\epsilon_0$ , are set to unity:

$$m_e = e = \hbar = 4\pi\epsilon_0 = 1.$$

This means, that one atomic unit, (a.u.), of the following quantities correspond in SI units to:

---



---

Angular momentum, Action	$\hbar$	=	$1.054\,571\,68 \times 10^{-34} \text{ J s}$
Mass	$m_e$	=	$9.109\,383 \times 10^{-31} \text{ kg}$
Charge	$e$	=	$1.602\,176\,53 \times 10^{-19} \text{ C}$
Length	$a_0 = \frac{4\pi\epsilon_0\hbar^2}{m_e e^2}$	=	$5.291\,772\,06 \times 10^{-11} \text{ m} = 0.53 \text{ \AA}$
Velocity	$v_B = \frac{e^2}{4\pi\epsilon_0\hbar}$	=	$2.187\,691\,26 \times 10^6 \text{ m s}^{-1}$
Momentum	$m_e v_B$	=	$1.992\,851\,66 \times 10^{-24} \text{ kg m s}^{-1}$
Time	$\tau_0 = \frac{a_0}{v_B}$	=	$2.418\,884\,30 \times 10^{-17} \text{ s} = 24.2 \text{ as}$
Frequency	$\tau_0^{-1}$	=	$4.134\,137\,38 \times 10^{16} \text{ Hz}$
Energy	$E_h = \frac{m_e e^4}{(4\pi\epsilon_0)^2 \hbar^2}$	=	$4.359\,744\,2 \times 10^{-18} \text{ J} = 27.2 \text{ eV}$
Electric field	$\mathcal{E}_0 = \frac{e}{4\pi\epsilon_0 a_0^2}$	=	$5.142\,206\,51 \times 10^{11} \text{ V m}^{-1}$
Intensity	$\frac{1}{2}\epsilon_0 c \mathcal{E}_0^2$	=	$3.509\,445\,2 \times 10^{16} \text{ W cm}^{-2}$

---



---



# SYMMETRY PROPERTIES OF THE FOURIER TRANSFORM: ODDNESS AND IMAGINARITY

The Fourier transformation,  $\mathcal{F}$ , between a complex valued function  $f(\mathbf{r})$  in real space with the Cartesian coordinates  $\mathbf{r} = (x, y, z)$  and the function  $F(\mathbf{k})$  in frequency space of wave vectors  $\mathbf{k} = (k_x, k_y, k_z)$  is defined as

$$F(\mathbf{k}) = \mathcal{F}_{\mathbf{r} \rightarrow \mathbf{k}}[f(\mathbf{r})] = \frac{1}{\sqrt{2\pi}} \int_{-\infty}^{\infty} d\mathbf{r} f(\mathbf{r}) e^{-i\mathbf{k} \cdot \mathbf{r}}, \quad (\text{B.1})$$

$$f(\mathbf{r}) = \mathcal{F}_{\mathbf{k} \rightarrow \mathbf{r}}[F(\mathbf{k})] = \frac{1}{\sqrt{2\pi}} \int_{-\infty}^{\infty} d\mathbf{k} F(\mathbf{k}) e^{i\mathbf{k} \cdot \mathbf{r}}. \quad (\text{B.2})$$

It will be sufficient to discuss properties of a one-dimensional case since  $\mathcal{F}$  in a higher dimensional space can simply be written as a series of one-dimensional transforms, e.g.

$$F(\mathbf{k}) = \frac{1}{\sqrt{2\pi}} \int_{-\infty}^{\infty} dz \left\{ \int_{-\infty}^{\infty} dy \left[ \int_{-\infty}^{\infty} dx f(x, y, z) e^{-ik_x x} \right] e^{-ik_y y} \right\} e^{-ik_z z}. \quad (\text{B.3})$$

Splitting  $f(x)$  in its real and imaginary part:

$$f(x) = a(x) + ib(x) \quad : a(x), b(x) \in \mathbb{R} \forall x, \quad (\text{B.4})$$

and using the Euler's formula  $e^{\pm i\phi} = \cos \phi \pm i \sin \phi$ , equation B.1 writes:

$$F(k_x) = \frac{1}{\sqrt{2\pi}} \int_{-\infty}^{\infty} dx [a(x) \cos(k_x x) + b(x) \sin(k_x x)] + \frac{i}{\sqrt{2\pi}} \left\{ \int_{-\infty}^{\infty} dx [b(x) \cos(k_x x) - a(x) \sin(k_x x)] \right\}. \quad (\text{B.5})$$

Taking a close look at equation B.5 and bearing in mind that the integrals vanish for integrands odd in  $x$ , one is readily convinced of the following handy symmetry properties of the Fourier transform:

$f(x) \dots$	$\Leftrightarrow$	$F(k_x) \dots$
real valued and even in $x$	$\Leftrightarrow$	is real valued and even in $k_x$
real valued and odd in $x$	$\Leftrightarrow$	is imaginary valued and odd in $k_x$
imaginary valued and even in $x$	$\Leftrightarrow$	is imaginary valued and even in $k_x$
imaginary valued and odd in $x$	$\Leftrightarrow$	is real valued and odd in $k_x$
real valued	$\Leftrightarrow$	has an even real part and an odd imaginary part
imaginary valued	$\Leftrightarrow$	has an odd real part and an even imaginary part



## B.1 Considering the Plane Wave dipole for N<sub>2</sub>O

This part tells what to expect from the plane-wave (PW) dipole associated to an asymmetric orbital (e.g. the HOMO of the linear triatomic N<sub>2</sub>O).

### The Fourier Transform in 1D

Let's begin with the properties of the Fourier transform in 1D. Any function  $f(x)$  can be written in terms of its odd and even components,

$$f(x) = f_+(x) + f_-(x) \quad (\text{B.6})$$

where

$$f_{\pm}(x) = \frac{1}{2}[f(x) \pm f(-x)] \quad (\text{B.7})$$

If  $f(x)$  is a real valued function, then

- $\Re\{\text{FT}_{x \rightarrow k}[f]\} = \text{FT}_{x \rightarrow k}[f_+] =: \tilde{f}_+(k)$  is even in  $k$ ;
- $\Im\{\text{FT}_{x \rightarrow k}[f]\} = -i\text{FT}_{x \rightarrow k}[f_-] =: -i\tilde{f}_-(k)$  is odd in  $k$ .

If  $f(x)$  is a imaginary valued function, then

- $\Re\{\text{FT}_{x \rightarrow k}[f]\} = \text{FT}_{x \rightarrow k}[f_-] =: \tilde{f}_-(k)$  is odd in  $k$ ;
- $\Im\{\text{FT}_{x \rightarrow k}[f]\} = -i\text{FT}_{x \rightarrow k}[f_+] =: -i\tilde{f}_+(k)$  is even in  $k$ .

If  $f(x)$  is complex, just apply the above mentioned rules to each of its real and imaginary parts.

### And now the dipole

For simplicity, we will stick here to 2D. We will consider real wave functions  $\psi(x, y)$  (These are actually wave-function integrated along the  $z$  axis) and the associated PW dipoles

$$\vec{d}(\vec{k}) = \int dx \int dy [\psi(x, y)]^* \binom{n}{k} \exp(ik_x x + ik_y y) \quad (\text{B.8})$$

Just to make sure:

- Even(odd) in  $k_x$  means (anti)symmetric with respect to the orientations  $\theta = \pm\pi/2$  rad;
- Even(odd) in  $k_y$  means (anti)symmetric with respect to the orientations  $\theta = 0, \pi$  rad.

Below, we see how the asymmetry of  $\psi(x, y)$  reflects into the PW dipole in the case of HOMO of N<sub>2</sub>O. The reasoning can be applied to any asymmetric orbital.

### HOMO of N<sub>2</sub>O

As shown in Fig. 4.1, the  $\pi_y$  HOMO of N<sub>2</sub>O is asymmetric in  $x$  (the axis parallel to the molecular axis) and odd in  $y$  (antisymmetric with respect to the internuclear axis  $x$ ). We define here the even and odd components as

$$\psi_{\pm}(x, y) = \frac{1}{2}[\psi(x, y) \pm \psi(-x, y)] \quad (\text{B.9})$$

In order to go from the wave-function to the PW dipole, it is more convenient to perform the integration in  $y$ , where the symmetry is well defined, first.

\*  $x$ -component:  $x \times \psi(x, y)$  is nearly even in  $x$ , odd in  $y$ .

1. Integration over  $y$ : The intermediate integrated function

$$x \times g(x, k_y) = x \times \int dy \psi(x, y) \exp(ik_y y) \quad (\text{B.10})$$

$$= x \times \text{FT}_{y \rightarrow k_y}[\psi] \quad (\text{B.11})$$

is purely imaginary valued, nearly even in  $x$  and odd in  $k_y$ .

2. Integration over  $x$ : This brings us to the PW dipole's  $x$ -component:

$$d_x(k_x, k_y) = \int dx x \times g(x, k_y) \exp(ik_x x) \quad (\text{B.12})$$

the real and imaginary parts of which are respectively odd and even in  $k_x$ .

3. Therefore:

- $\Re\{d_x\}$  is odd in both  $k_x$  and  $k_y$ ;
- $\Im\{d_x\}$  is even in  $k_x$  and odd in  $k_y$ ;
- $\Im\{d_x\}$  dominates over  $\Re\{d_x\}$ .

\*  $y$ -component:  $y \times \psi(x, y)$  is nearly odd in  $x$ , even in  $y$ .

1. Integration over  $y$ : The intermediate integrated function

$$h(x, k_y) = \int dy y \times \psi(x, y) \exp(ik_y y) \quad (\text{B.13})$$

$$= \text{FT}_{y \rightarrow k_y}[y \times \psi] \quad (\text{B.14})$$

is purely real valued, nearly odd in  $x$  and even in  $k_y$ .

2. Integration over  $x$ : This brings us to the PW dipole's  $y$ -component:

$$d_y(k_x, k_y) = \int dx h(x, k_y) \exp(ik_x x) \quad (\text{B.15})$$

the real and imaginary parts of which are respectively even and odd in  $k_x$ .

3. Therefore:

- $\Re\{d_y\}$  is even in both  $k_x$  and  $k_y$ ;
- $\Im\{d_y\}$  is odd in  $k_x$  and even in  $k_y$ ;
- $\Im\{d_y\}$  dominates over  $\Re\{d_x\}$ .

An important outcome is that, although asymmetry makes the dipole complex (rather than purely real or imaginary), it turns out that the imaginary part is 10 times bigger than the real part, because the orbital is dominantly antisymmetric. This becomes a factor 100 if one things of the spectrum (dipole squared).



# ACKNOWLEDGMENTS

---

At the end of this thesis, I express my gratefulness to all the people who are most responsible for making sure this thesis was complete successfully.

First and foremost I would like to express my deeply gratitude to my supervisor, Dr. Pascal Salières, for his excellent guidance, advice and constant support. Pascal was always patient and enthusiastic to help and explain to me clearly what I did not understand. He set an example for how I hope to interact with colleagues in the future. His solid knowledge and infinite inspiration that made science both interesting and exciting. Also, his rigorous attitude on science influenced and will influence me in a right way through my entire life.

I would like to extend my heartfelt appreciation to the chef of the group, Bertrand Carré, for his insight and guidance. He always gave wise remarks that inspired me. Even though he has the burden of huge amount of work, he has been always staying late with us in the lab, bringing us dinner, switching off the laser and driving me home.

I was very fortunate to have had the opportunity to work in the attophysics group in CEA. I would like to thank:

Bastian Manschwetus, who has spend the vast majority of his time together with me in the lab, explaining me so well every single detail of the experimental apparatus. Jan Rothhardt, who helped me to understand well the experimental data. Antoine Camper and Vincent Gruson who helped me whenever my French is not enough or need transportation. Zsolt Diveki, who kept on answering my questions even after he moved in London. Thierry Ruchon, who created the best RABBIT analysis programme. Sébastien Weber for sharing the molecular alignment knowledge with me. Thierry Auguste for calculating the amplitude of the continuum once and once again for me. Romain Généaux, who amazed me by his experience in China. Emmanouil Skantzakis, who is half physicist and half artist. Tahir Shaaran for his interest on my work and theoretical comments. Christian Cornaggia for his insisting on training my French. Pierre Breger, Marie Géléoc, Elizabeth English and Arthur Hardiagon for their kindness and help in my work;

The group of Coherent Diffraction Imaging, Hamed Merdji, Xunyou Ge, Fan Wang, David Gauthier, Willem Boutu, Ana Borta, Mathieu Ducouso, Bianca Iwan, Julien Samaan and Aura Inés Gonzalez for the support and friendship;

Marc Billon and Gilles Le Chevallier for fixing all the technical problems. Didier and André

for creating or modifying every component which are needed for the experiments.

High tribute shall be paid to our theoretician colleagues, Richard Taïeb, Roland Guichard, Jérémie Caillat and Alfred Maquet for constructive criticism and valuable suggestions for the remaining problems.

I wish to thank my close collaborators in Imperial College London, Amelle Zaïr, Christopher Hutchison, Sarah Houver, Felicity McGrath and Jon Marangos and all of the amazingly talented people there, for making the experiments fluent and exciting, as well as my collaborators in Paris-Sud University, Alain Huetz, Yan Picard, Elena-Magdalena Staicu-Casagrande and Danielle Dowek, for teaching me how the COLTRIMS works.

I would like to thank the laser experts in SLIC team, Jeff, Olivier, Michel, Fabien and Delphine for providing me the robust laser in the world so that I could finish my experiments.

Special thanks should go to my thesis reviewers, Valérie Blanchet and Pierre Agostini, who have put considerable time and effort into their comments on the draft, as well as my jury members, Anne Klisnick, Amelle Zaïr and Philippe Zeitoun for all the valuable feedback. It is my privilege to have such a wonderful dissertation committee.

Thanks the Marie Curie fellowship (ATTOFEL), which support my study in France within the last three years.

Finally, my thanks would go to my beloved parents for their loving considerations and great confidence in me all through these years. Also my fiancée, for her constant encouragement and love. She has been trying hard to cheer me up from Sweden to France when the experiments were not working as expected.

Thank you all!

Nan

# REFERENCES

---

- [1] Ahmed H Zewail. Femtochemistry: Atomic-Scale Dynamics of the Chemical Bond . *The Journal of Physical Chemistry A*, 104(24):5660–5694, June 2000.
- [2] Pierre Agostini and Louis F Dimauro. The physics of attosecond light pulses. *Reports on progress in physics.*, 67(6):813–855, 2004.
- [3] F. J. McClung and R. W. Hellwarth. Giant Optical Pulsations from Ruby. *Journal of Applied Physics*, 33(3):828, 1962.
- [4] a. J. DeMaria. Self Mode-Locking of Lasers With Saturable Absorbers. *Applied Physics Letters*, 8(7):174, 1966.
- [5] C. V. Shank. Subpicosecond kilowatt pulses from a mode-locked cw dye laser. *Applied Physics Letters*, 24(8):373, 1974.
- [6] R L Fork, C H Cruz, P C Becker, and C V Shank. Compression of optical pulses to six femtoseconds by using cubic phase compensation. *Optics letters*, 12(7):483–5, July 1987.
- [7] G. Steinmeyer. Frontiers in Ultrashort Pulse Generation: Pushing the Limits in Linear and Nonlinear Optics. *Science*, 286(5444):1507–1512, November 1999.
- [8] Ferenc Krausz and Misha Y Ivanov. Attosecond physics. *Reviews of Modern Physics Mod. Phys.*, 81:163, 2009.
- [9] T Brabec and F Krausz. Intense few-cycle laser fields: Frontiers of nonlinear optics. *Reviews of Modern Physics*, 72(2):545, 2000.
- [10] M Ferray, A L’Huillier, and XF Li. Multiple-harmonic conversion of 1064 nm radiation in rare gases. *Journal of Physics B: . . .*, 31, 1988.
- [11] A McPherson, G Gibson, H Jara, and U Johann. Studies of multiphoton production of vacuum-ultraviolet radiation in the rare gases. *Journal of Optical Society of America*, 4(4):595–601, 1987.
- [12] Tenio Popmintchev, Ming-Chang Chen, Dimitar Popmintchev, Paul Arpin, Susannah Brown, Skirmantas Alisauskas, Giedrius Andriukaitis, Tadas Balciunas, Oliver D Mücke, Audrius Pugzlys, Andrius Baltuska, Bonggu Shim, Samuel E Schrauth, Alexander Gaeta, Carlos Hernández-García, Luis Plaja, Andreas Becker, Agnieszka Jaron-Becker, Margaret M Murnane, and Henry C Kapteyn. Bright coherent ultrahigh harmonics in the keV x-ray regime from mid-infrared femtosecond lasers. *Science (New York, N.Y.)*, 336(6086):1287–91, June 2012.
- [13] P B Corkum. Plasma Perspective on Strong-Field Multiphoton Ionization. *Physical Review Letters*, 71(13):1994–1997, 1993.
- [14] KJ Schafer, B Yang, Lf DiMauro, and Kc Kulander. Above threshold ionization beyond the high harmonic cutoff. *Physical review letters*, 70(11):1599–1602, March 1993.
- [15] M Lewenstein, Ph. Balcou, M.Yu. Ivanov, A L’Huillier, and P B Corkum. Theory of high-order harmonic generation by low-frequency laser fields. *Physical Review A*, 49:2117, 1994.
- [16] G Lambert, T Hara, D Garzella, T Tanikawa, M Labat, B Carré, H Kitamura, T Shintake, M Bougeard, S Inoue, Y Tanaka, P Salières, H Merdji, O Chubar, O Gobert, K Tahara, and M E Couprie. Injection of harmonics generated in gas in a free-electron laser providing intense and coherent extreme-ultraviolet light. *Nature Physics*, 4(4):296–300, 2008.
- [17] G Lambert, T Hara, M Labat, T Tanikawa, Y Tanaka, M Yabashi, D Garzella, B Carré, and M E Couprie. Seed level requirement for improving the temporal coherence of a Free-Electron Laser. *EuroPhysics Letters*, 88:54002, 2009.
- [18] D Gauthier, M Guizar-Sicairos, X Ge, W Boutu, B Carré, J R Fienup, and H Merdji. Single-shot Femtosecond X-Ray Holography Using Extended References. *Physical Review Letters*, 105(9):93901, August 2010.

- [19] A.-S. Morlens, R López-Martens, O Boyko, Ph. Zeitoun, Ph. Balcou, K Varjú, E Gustafsson, T Remetter, A L'Huillier, S Kazamias, J Gautier, F Delmotte, and M.-F. Ravet. Design and characterization of extreme-ultraviolet broadband mirrors for attosecond science. *Opt. Lett.*, 31:1558, 2006.
- [20] A Ravasio, D Gauthier, F Maia, M Billon, J-P. Caumes, D Garzella, M. Géléoc, O Gobert, J-F. Hergott, A-M. Pena, H Perez, B. Carré, E Bourhis, J Gierak, A Madouri, D Mailly, B Schiedt, M Fajardo, J Gautier, P Zeitoun, P. Bucksbaum, J Hajdu, and H Merdji. Single-Shot Diffractive Imaging Using Table-Top Femtosecond Soft X-Ray Laser-Harmonics Source. *Physical Review Letters*, 103(2):28104, July 2009.
- [21] Richard Sandberg, Ariel Paul, Daisy Raymondson, Steffen Hädrich, David Gaudiosi, Jim Holtsnider, Raanan Tobey, Oren Cohen, Margaret Murnane, Henry Kapteyn, Changyong Song, Jianwei Miao, Yanwei Liu, and Farhad Salmassi. Lensless Diffractive Imaging Using Tabletop Coherent High-Harmonic Soft-X-Ray Beams. *Physical Review Letters*, 99(9):098103, August 2007.
- [22] G Farkas and C Toth. Proposal for attosecond light pulse generation using laser induced multiple-harmonic conversion processes in rare gases. *Physics Letters A*, 168:447–450, 1992.
- [23] P M Paul, E S Toma, P Breger, G Mullot, F Auge, P Balcou, H G Muller, and P Agostini. Observation of a train of attosecond pulses from high harmonic generation. *Science (New York, N.Y.)*, 292(5522):1689–92, June 2001.
- [24] M Hentschel, R Kienberger, Ch Spielmann, G Reider, N Milosevic, T Brabec, P Corkum, U Heinzmann, M Drescher, and F Krausz. Attosecond metrology. *Nature*, 414(6863):509–513, 2001.
- [25] P Salières, a Maquet, S Haessler, J Caillat, and R Taïeb. Imaging orbitals with attosecond and Ångström resolutions: toward attochemistry? *Reports on progress in physics. Physical Society (Great Britain)*, 75(6):062401, June 2012.
- [26] I. J. Sola, E. Mével, L. Elouga, E. Constant, V. Strelkov, L. Poletto, P. Villoresi, E. Benedetti, J.-P. Caumes, S. Stagia, C. Vozzi, G. Sansone, and M. Nisoli. Controlling attosecond electron dynamics by phase-stabilized polarization gating. *Nature Physics*, 2(5):319–322, April 2006.
- [27] M Uiberacker, Th Uphues, M Schultze, A Verhoef, V Yakovlev, M Kling, J Rauschenberger, N Kabachnik, H Schroder, M Lezius, K Kompa, H G Muller, M Vrakking, S Hendel, U Kleineberg, U Heinzmann, M Drescher, and F Krausz. Attosecond real-time observation of electron tunnelling in atoms. *Nature*, 446(7136):627–632, 2007.
- [28] P Eckle, a N Pfeiffer, C Cirelli, a Staudte, R Dörner, H G Muller, M Büttiker, and U Keller. Attosecond ionization and tunneling delay time measurements in helium. *Science (New York, N.Y.)*, 322(5907):1525–9, December 2008.
- [29] J Mauritsson, P Johnsson, E Mansten, M Swoboda, T Ruchon, A L'Huillier, and K Schafer. Coherent Electron Scattering Captured by an Attosecond Quantum Stroboscope. *Physical Review Letters*, 100(7):73003, 2008.
- [30] S Haessler, B Fabre, J Higuette, J Caillat, T Ruchon, P Breger, B Carré, E Constant, A Maquet, E Mével, P Salières, R. Taïeb, and Y Mairesse. Phase-resolved attosecond near-threshold photoionization of molecular nitrogen. *Physical Review A*, 80(1):11404, July 2009.
- [31] M. Swoboda, T. Fordell, K. Klünder, J. M. Dahlström, M. Miranda, C. Buth, K. J. Schafer, J. Mauritsson, a. L'Huillier, and M. Gisselbrecht. Phase Measurement of Resonant Two-Photon Ionization in Helium. *Physical Review Letters*, 104(10):103003, March 2010.
- [32] K. Klünder, J. M. Dahlström, M. Gisselbrecht, T. Fordell, M. Swoboda, D. Guénot, P. Johnsson, J. Caillat, J. Mauritsson, a. Maquet, R. Taïeb, and a. L'Huillier. Probing Single-Photon Ionization on the Attosecond Time Scale. *Physical Review Letters*, 106(14):143002, April 2011.
- [33] G Sansone, F Kelkensberg, J F Pérez-Torres, F Morales, M F Kling, W Siu, O Ghafur, P Johnsson, M Swoboda, E Benedetti, F Ferrari, F Lépine, J L Sanz-Vicario, S Zherebtsov, I Znakovskaya, a L'huillier, M Yu Ivanov, M Nisoli, F Martín, and M J J Vrakking. Electron localization following attosecond molecular photoionization. *Nature*, 465(7299):763–6, June 2010.
- [34] F Rosca-Pruna and M J J Vrakking. Experimental Observation of Revival Structures in Picosecond Laser-Induced Alignment of I<sub>2</sub>. *Physical Review Letters*, 87(15):153902, 2001.
- [35] Tamar Seideman. Revival Structure of Aligned Rotational Wave Packets. *Physical Review Letters*, 83(24):4971–4974, 1999.
- [36] Henrik Stapelfeldt. Colloquium: Aligning molecules with strong laser pulses. *Reviews of Modern Physics*, 75(2):543–557, April 2003.
- [37] R Velotta, N Hay, M B Mason, M Castillejo, and J P Marangos. High-Order Harmonic Generation in Aligned Molecules. *Physical Review Letters*, 87(18):183901, 2001.
- [38] N Hay, R Velotta, M Lein, R de Nalda, E Heesel, M Castillejo, and J P Marangos. High-order harmonic generation in laser-aligned molecules. *Physical Review A*, 65(5):53805, 2002.

- [39] M. Lein, N. Hay, R. Velotta, J. Marangos, and P. Knight. Role of the Intramolecular Phase in High-Harmonic Generation. *Physical Review Letters*, 88(18):1–4, April 2002.
- [40] M Lein, N Hay, R Velotta, J P Marangos, and P L Knight. Interference effects in high-order harmonic generation with molecules. *Physical Review A*, 66(2):23805, 2002.
- [41] J Itatani, J Levesque, D Zeidler, Hiromichi Niikura, H Pépin, J C Kieffer, P B Corkum, and D M Villeneuve. Tomographic imaging of molecular orbitals. *Nature*, 432(7019):867–71, December 2004.
- [42] S. Haessler, J. Caillat, W. Boutu, C. Giovanetti-Teixeira, T. Ruchon, T. Auguste, Z. Diveki, P. Breger, a. Maquet, B. Carré, R. Taïeb, and P. Salières. Attosecond imaging of molecular electronic wavepackets. *Nature Physics*, 6(3):200–206, January 2010.
- [43] C. Vozzi, M. Negro, F. Calegari, G. Sansone, M. Nisoli, S. De Silvestri, and S. Stagira. Generalized molecular orbital tomography. *Nature Physics*, 7(10):822–826, June 2011.
- [44] Tsuneto Kanai, Shinichirou Minemoto, and Hirofumi Sakai. Quantum interference during high-order harmonic generation from aligned molecules. *Nature*, 435(7041):470–474, 2005.
- [45] C. Vozzi, F. Calegari, E. Benedetti, J.-P. Caumes, G. Sansone, S. Stagira, M. Nisoli, R. Torres, E. Heesel, N. Kajumba, J. Marangos, C. Altucci, and R. Velotta. Controlling Two-Center Interference in Molecular High Harmonic Generation. *Physical Review Letters*, 95(15):1–4, October 2005.
- [46] W. Boutu, S. Haessler, H. Merdji, P. Breger, G. Waters, M. Stankiewicz, L. J. Frasinski, R. Taïeb, J. Caillat, a. Maquet, P. Monchicourt, B. Carre, and P. Salières. Coherent control of attosecond emission from aligned molecules. *Nature Physics*, 4(7):545–549, May 2008.
- [47] Olga Smirnova, Yann Mairesse, Serguei Patchkovskii, Nirit Dudovich, David Villeneuve, Paul Corkum, and Misha Yu Ivanov. High harmonic interferometry of multi-electron dynamics in molecules. *Nature*, 460(7258):972–7, August 2009.
- [48] Olga Smirnova, Serguei Patchkovskii, Yann Mairesse, Nirit Dudovich, and Misha Yu Ivanov. Strong-field control and spectroscopy of attosecond electron-hole dynamics in molecules. *Proceedings of the National Academy of Sciences of the United States of America*, 106(39):16556–61, September 2009.
- [49] Brian K McFarland, Joseph P Farrell, Philip H Bucksbaum, and Markus Gühr. High harmonic generation from multiple orbitals in N<sub>2</sub>. *Science (New York, N.Y.)*, 322(5905):1232–5, November 2008.
- [50] H. J. Wörner, J. B. Bertrand, P. Hockett, P. B. Corkum, and D. M. Villeneuve. Controlling the Interference of Multiple Molecular Orbitals in High-Harmonic Generation. *Physical Review Letters*, 104(23):233904, June 2010.
- [51] S Baker, J S Robinson, C a Haworth, H Teng, R a Smith, C C Chirila, M Lein, J W G Tisch, and J P Marangos. Probing proton dynamics in molecules on an attosecond time scale. *Science (New York, N.Y.)*, 312(5772):424–7, April 2006.
- [52] S. Baker, J. S. Robinson, M. Lein, C. C. Chiril, R. Torres, H. C. Bandulet, D. Comtois, J. C. Kieffer, D. M. Villeneuve, J. W. G. Tisch, and J. P. Marangos. Dynamic Two-Center Interference in High-Order Harmonic Generation from Molecules with Attosecond Nuclear Motion. *Physical Review Letters*, 101(5):053901, July 2008.
- [53] Tsuneto Kanai, Eiji J Takahashi, Yasuo Nabekawa, and Katsumi Midorikawa. Observing the attosecond dynamics of nuclear wavepackets in molecules by using high harmonic generation in mixed gases. *New Journal of Physics*, 10(2):025036, February 2008.
- [54] S Haessler, W Boutu, M Stankiewicz, L J Frasinski, S Weber, J Caillat, R Taïeb, a Maquet, P Breger, P Monchicourt, B Carré, and P Salières. Attosecond chirp-encoded dynamics of light nuclei. *Journal of Physics B: Atomic, Molecular and Optical Physics*, 42(13):134002, July 2009.
- [55] KC Kulander and BW Shore. Calculations of Multiple-Harmonic Conversion of 1064-nm Radiation in Xe. *Physical review letters*, 62(5):30–32, 1989.
- [56] JL Krause, KJ Schafer, and KC Kulander. High-Order Harmonic Generation from Atoms and Ions in the High Intensity Regime. *Physical Review Letters*, 68(24):3535–3538, 1992.
- [57] KC Kulander, KJ Schafer, and JL Krause. Theoretical model for intense field high-order harmonic generation in rare gases. *Laser Physics*, 3(2):359–364, 1993.
- [58] Serguei Patchkovskii, Zengxiu Zhao, Thomas Brabec, and D M Villeneuve. High Harmonic Generation and Molecular Orbital Tomography in Multielectron Systems: Beyond the Single Active Electron Approximation. *Physical Review Letters*, 97(12):123003–123004, 2006.
- [59] Serguei Patchkovskii, Zengxiu Zhao, Thomas Brabec, and D M Villeneuve. High harmonic generation and molecular orbital tomography in multielectron systems. *The Journal of chemical physics*, 126(11):114306, March 2007.



- [60] Robin Santra and Ariel Gordon. Three-Step Model for High-Harmonic Generation in Many-Electron Systems. *Physical Review Letters*, 96(7):73906, 2006.
- [61] L V Keldysh. Ionization in the Field of a Strong Electromagnetic Wave. *Sov. Phys. JETP*, 20:1307–1314, 1965.
- [62] Bing Shan and Zenghu Chang. Dramatic extension of the high-order harmonic cutoff by using a long-wavelength driving field. *Physical Review A*, 65(1):011804, December 2001.
- [63] J. Tate, T. Augustine, H. Muller, P. Salières, P. Agostini, and L. DiMauro. Scaling of Wave-Packet Dynamics in an Intense Midinfrared Field. *Physical Review Letters*, 98(1):013901, January 2007.
- [64] T Popmintchev, M-C. Chen, A Bahabad, M Gerrity, P Sidorenko, O Cohen, I Christov, M Murnane, and H Kapteyn. Phase matching of high harmonic generation in the soft and hard X-ray regions of the spectrum. *Proc. Natl Acad. Sci. USA*, 106(26):10516–10521, 2009.
- [65] A D Shiner, C Trallero-Herrero, N Kajumba, H.-C. Bandulet, D Comtois, F Legare, M Giguere, J-C. Kieffer, P B Corkum, and D M Villeneuve. Wavelength Scaling of High Harmonic Generation Efficiency. *Physical Review Letters*, 103(7):73902, 2009.
- [66] Tenio Popmintchev, Ming-Chang Chen, Paul Arpin, Margaret M. Murnane, and Henry C. Kapteyn. The attosecond nonlinear optics of bright coherent X-ray generation. *Nature Photonics*, 4(12):822–832, December 2010.
- [67] P. Salières, B. Carré, L. Le Déroff, F. Grasbon, G. G. Paulus, H. Walther, R. Kopold, W. Becker, D. B. Milosevic, A. Sanpera, and M. Lewenstein. Feynmans Path-Integral Approach for Intense-LaserAtom Interactions. *Science (New York, N.Y.)*, 292(May):902–905, 2001.
- [68] E Priori, G Cerullo, M Nisoli, and S Stagira. Nonadiabatic three-dimensional model of high-order harmonic generation in the few-optical-cycle regime. *Physical Review A*, 61:1–8, 2000.
- [69] G Sansone, C Vozzi, S Stagira, and M Nisoli. Nonadiabatic quantum path analysis of high-order harmonic generation: Role of the carrier-envelope phase on short and long paths. *Physical Review A*, 70(1):13411, 2004.
- [70] Jing Zhao and Manfred Lein. Determination of Ionization and Tunneling Times in High-Order Harmonic Generation. *Physical Review Letters*, 111(4):043901, July 2013.
- [71] ZSOLT DIVEKI. *GENERATION AND APPLICATION OF ATTOSECOND PULSES*. PhD thesis, 2011.
- [72] K. Varjú, Y. Mairesse, B. Carré, M. B. Gaarde, P. Johnsson, S. Kazamias, R. López-Martens, J. Mauritsson, K. J. Schafer, Ph. Balcou, A. L’huillier, and P. Salières. Frequency chirp of harmonic and attosecond pulses. *Journal of Modern Optics*, 52(2-3):379–394, January 2005.
- [73] M.V.Amosov, N.B.Delone, and V.P.Krainov. Tunnel ionization of complex atoms and of atomic ions in an alternating electromagnetic field. *Sov.Phys.JETP*, 64(1191), 1986.
- [74] D. Milošević and W. Becker. Role of long quantum orbits in high-order harmonic generation. *Physical Review A*, 66(6):063417, December 2002.
- [75] Yong-Chang Han and Lars Bojer Madsen. Comparison between length and velocity gauges in quantum simulations of high-order harmonic generation. *Physical Review A*, 81(6):63430, 2010.
- [76] A D Bandrauk, S Chelkowski, D J Diestler, J Manz, and K.-J. Yuan. Quantum simulation of high-order harmonic spectra of the hydrogen atom. *Physical Review A*, 79(2):23403, 2009.
- [77] Ariel Gordon and Franz Kärtner. Quantitative Modeling of Single Atom High Harmonic Generation. *Physical Review Letters*, 95(22):223901, 2005.
- [78] C. C. Chiril and M. Lein. Assessing different forms of the strong-field approximation for harmonic generation in molecules. *Journal of Modern Optics*, 54(7):1039–1045, May 2007.
- [79] J C Baggesen and L B Madsen. On the dipole, velocity and acceleration forms in high-order harmonic generation from a single atom or molecule. *Journal of Physics B: Atomic, Molecular and Optical Physics*, 44(11):115601, 2011.
- [80] Philippe Antoine, DB Milošević, and A L’Huillier. Generation of attosecond pulses in macroscopic media. *Physical Review A*, 56(6):4960–4969, 1997.
- [81] T Ruchon, C P Hauri, K Varjú, E Mansten, M Swoboda, R López-Martens, and a L’Huillier. Macroscopic effects in attosecond pulse generation. *New Journal of Physics*, 10(2):025027, February 2008.
- [82] Nguyen Shon, Akira Suda, Yusuke Tamaki, and Katsumi Midorikawa. High-order harmonic and attosecond pulse generations: Bulk media versus hollow waveguides. *Physical Review A*, 63(6):063806, May 2001.
- [83] Nenad Milosevic, Armin Scrinzi, and Thomas Brabec. Numerical Characterization of High Harmonic Attosecond Pulses. *Physical Review Letters*, 88(9):093905, February 2002.

- [84] Anne L'Huillier, Kenneth J Schafer, and Kenneth C Kulander. Theoretical aspects of intense field harmonic generation. *Journal of Physics B: Atomic, Molecular and Optical Physics*, 24(15):3315–3341, 1991.
- [85] Philippe Balcou, P Salières, A L'Huillier, and Maciej Lewenstein. Generalized phase-matching conditions for high harmonics: The role of field-gradient forces. *Physical Review A*, 55(4):3204–3210, 1997.
- [86] Pascal Salières, Anne L'Huillier, and Maciej Lewenstein. Coherence Control of High-Order Harmonics. *Physical Review Letters*, 74(19):3776–3779, 1995.
- [87] A L'Huillier, K. J. Schafer, and K C KULANDER. High-Order Harmonic Generation in Xenon at 1064 nm: The Role of Phase Matching. *Physical Review Letters*, 66(17):2200–2203, 1991.
- [88] A L'Huillier, Philippe Balcou, and S Candel. Calculations of high-order harmonic-generation processes in xenon at 1064 nm. *Physical Review A*, 46(5):2778, 1992.
- [89] P Balcou and A L'Huillier. Phase-matching effects in strong-field harmonic generation. *Physical Review A*, 47(2):1447–1459, 1993.
- [90] J Peatross and Dd Meyerhofer. Intensity-dependent atomic-phase effects in high-order harmonic generation. *Physical Review A*, 52(5):3976–3987, November 1995.
- [91] A Rundquist, C G Durfee III, Z Chang, C Herne, S Backus, M Murnane, and H C Kapteyn. Phase matched generation of coherent soft X-rays. *Science*, 280(5368):1412, 1998.
- [92] Stefan Haessler and Marko Swoboda. Optimization and Application of High-order Harmonics of an Ultra-short Terawatt Laser. Lund Reports on Atomic Physics LRAP-324, Lund Institute of Technology, Sweden, 2004.
- [93] O Svelto. *Principles of Lasers*. Plenum Press, New York, 1998.
- [94] P Salières, L Le Déroff, T Auguste, P Monot, P D'Oliveira, D Campo, J F Hergott, H Merdji, and B Carré. Frequency-Domain Interferometry in the XUV with High-Order Harmonics. *Physical Review Letters*, 83(26):5483–5486, 1999.
- [95] T Ruchon, C P Hauri, K Varjú, E Mansten, M Swoboda, R López-Martens, and a L'Huillier. Macroscopic effects in attosecond pulse generation. *New Journal of Physics*, 10(2):025027, February 2008.
- [96] Y Mairesse, a de Bohan, L J Frasinski, H Merdji, L C Dinu, P Monchicourt, P Breger, M Kovacev, R Taïeb, B Carré, H G Muller, P Agostini, and P Salières. Attosecond synchronization of high-harmonic soft x-rays. *Science (New York, N.Y.)*, 302(5650):1540–3, November 2003.
- [97] G Doumy, J Wheeler, C Roedig, R Chirla, P Agostini, and L F DiMauro. Attosecond Synchronization of High-Order Harmonics from Midinfrared Drivers. *Physical Review Letters*, 102(9):93002, 2009.
- [98] N Dudovich, O Smirnova, J Levesque, Y Mairesse, Ivanov, D Villeneuve, and P Corkum. Measuring and controlling the birth of attosecond XUV pulses. *Nature Physics*, advanced o(11):781–786, 2006.
- [99] E Goulielmakis, M Schultze, M Hofstetter, V S Yakovlev, J Gagnon, M Uiberacker, A L Aquila, E M Gullikson, D T Attwood, R Kienberger, F Krausz, and U Kleineberg. Single-Cycle Nonlinear Optics. *Science*, 320(5883):1614–1617, 2008.
- [100] Philippe Antoine, Anne L'Huillier, and Maciej Lewenstein. Attosecond Pulse Trains Using High-Order Harmonics. *Physical Review Letters*, 77(7):1234–1237, 1996.
- [101] Kenneth Schafer, Mette Gaarde, Arne Heinrich, Jens Biegert, and Ursula Keller. Strong Field Quantum Path Control Using Attosecond Pulse Trains. *Physical Review Letters*, 92(2):023003, January 2004.
- [102] P. Johnsson, R. López-Martens, S. Kazamias, J. Mauritsson, C. Valentin, T. Remetter, K. Varjú, M. Gaarde, Y. Mairesse, H. Wabnitz, P. Salières, Ph. Balcou, K. Schafer, and a. L'Huillier. Attosecond Electron Wave Packet Dynamics in Strong Laser Fields. *Physical Review Letters*, 95(1):013001, June 2005.
- [103] A Baltuška, T Udem, and M Uiberacker. Attosecond control of electronic processes by intense light fields. *Nature*, 421(February), 2003.
- [104] C. V. Shank, R. L. Fork, R. Yen, R. H. Stolen, and W. J. Tomlinson. Compression of femtosecond optical pulses. *Applied Physics Letters*, 40(9):761, 1982.
- [105] G Sansone, E Benedetti, F Calegari, C Vozzi, L Avaldi, R Flammini, L Poletto, P Villoresi, C Altucci, R Velotta, S Stagira, S De Silvestri, and M Nisoli. Isolated single-cycle attosecond pulses. *Science (New York, N.Y.)*, 314(5798):443–6, October 2006.
- [106] BEA Saleh and MC Teich. *Fundamentals of photonics (Second Edition)*. 2007.
- [107] C.P. Hauri, W. Kornelis, F.W. Helbing, a. Heinrich, a. Couairon, a. Mysyrowicz, J. Biegert, and U. Keller. Generation of intense, carrier-envelope phase-locked few-cycle laser pulses through filamentation. *Applied Physics B*, 79(6):673–677, September 2004.

- [108] M. Nisoli, S. De Silvestri, and O. Svelto. Generation of high energy 10 fs pulses by a new pulse compression technique. *Applied Physics Letters*, 68(20):2793, 1996.
- [109] M Nisoli, S De Silvestri, O Svelto, R Szpöcs, K Ferencz, Ch. Spielmann, S Sartania, and F Krausz. Compression of high-energy laser pulses below 5 fs. *Optics Letters*, 22(8):522–524, 1997.
- [110] M. Nisoli, S. Stagira, S. De Silvestri, O. Svelto, S. Sartania, Z. Cheng, G. Tempea, C. Spielmann, and F. Krausz. Toward a terawatt-scale sub-10-fs laser technology. *IEEE Journal of Selected Topics in Quantum Electronics*, 4(2):414–420, 1998.
- [111] C Fourcade Dutin, A Dubrouil, S Petit, E Mével, E Constant, and D Descamps. Post-compression of high-energy femtosecond pulses using gas ionization. *Optics Letters*, 35(2):253–255, January 2010.
- [112] S Ghimire, B Shan, C Wang, and Z Chang. High-Energy 6 . 2-fs Pulses for Attosecond Pulse Generation. *Laser Physics*, 15(6):838–842, 2005.
- [113] A L Cavaliere, E Goulielmakis, B Horvath, W Helml, M Schultze, M Fieß, V Pervak, L Veisz, V S Yakovlev, M Uiberacker, A Apolonski, F Krausz, and R Kienberger. Intense 1.5-cycle near infrared laser waveforms and their use for the generation of ultra-broadband soft-x-ray harmonic continua. *New Journal of Physics*, 9(7):242, 2007.
- [114] Akira Suda, Masatoshi Hatayama, Keigo Nagasaka, and Katsumi Midorikawa. Generation of sub-10-fs, 5-mJ-optical pulses using a hollow fiber with a pressure gradient. *Applied Physics Letters*, 86(111116):5–7, 2005.
- [115] Samuel Bohman, Akira Suda, Masanori Kaku, Muhammad Nurhuda, Takuya Kanai, Shigeru Yamaguchi, and Katsumi Midorikawa. Generation of 5 fs, 0.5 TW pulses focusable to relativistic intensities at 1 kHz. *Optics express*, 16(14):10684–10689, 2008.
- [116] Samuel Bohman, Akira Suda, Tsuneto Kanai, Shigeru Yamaguchi, and Katsumi Midorikawa. Generation of 5.0 fs, 5.0 mJ pulses at 1kHz using hollow-fiber pulse compression. *Optics letters*, 35(11):1887–9, June 2010.
- [117] X Chen, A Malvache, A Ricci, A Jullien, and R Lopez-Martens. Efficient hollow fiber compression scheme for generating multi-mJ, carrier-envelope phase stable, sub-5 fs pulses. *Laser Physics*, 21(1):198–201, 2011.
- [118] Govind P Agrawal. *Nonlinear Fiber Optics*. Springer-Verlag Berlin Heidelberg, 2nd edition, 2000.
- [119] C. Vozzi, M. Nisoli, G. Sansone, S. Stagira, and S. De Silvestri. Optimal spectral broadening in hollow-fiber compressor systems. *Applied Physics B*, 80(3):285–289, December 2004.
- [120] E. A. J. Marcatili and R. A. Schmeltzer. Hollow Metallic and Dielectric Wave-guides for Long Distance Optical Transmission and Lasers. *Bell System Technical Journal*, 43:1783–1809, 1964.
- [121] M Nurhuda, A Suda, M Kaku, and K Midorikawa. Optimization of hollow fiber pulse compression using pressure gradients. *Applied Physics B: Lasers and Optics*, 89(2):209–215, 2007.
- [122] Hamed Merdji, Thierry Auguste, Willem Boutu, J.-Pascal Caumes, Bertrand Carré, Thomas Pfeifer, Aurélie Jullien, Daniel M Neumark, and Stephen R Leone. Isolated attosecond pulses using a detuned second-harmonic field. *Optics Letters*, 32(21):3134–3136, November 2007.
- [123] Thomas Pfeifer, Lukas Gallmann, Mark J Abel, Phillip M Nagel, Daniel M Neumark, and Stephen R Leone. Heterodyne Mixing of Laser Fields for Temporal Gating of High-Order Harmonic Generation. *Physical Review Letters*, 97(16):163901, 2006.
- [124] Ph. Antoine, A L’Huillier, M Lewenstein, P Salières, and B Carré. Theory of high-order harmonic generation by an elliptically polarized laser field. *Physical Review A*, 53:1725, 1996.
- [125] Zenghu Chang. Controlling attosecond pulse generation with a double optical gating. *Physical Review A*, 76(5):51403, November 2007.
- [126] Ximao Feng, Steve Gilbertson, Hiroki Mashiko, He Wang, Sabih D Khan, Michael Chini, Yi Wu, Kun Zhao, and Zenghu Chang. Generation of Isolated Attosecond Pulses with 20 to 28 Femtosecond Lasers. *Physical Review Letters*, 103(18):183901, October 2009.
- [127] P. Tzallas, E. Skantzakis, C. Kalpouzos, E. P. Benis, G. D. Tsakiris, and D. Charalambidis. Generation of intense continuum extreme-ultraviolet radiation by many-cycle laser fields. *Nature Physics*, 3(12):846–850, October 2007.
- [128] M Born and R Oppenheimer. Zur Quantentheorie der Molekeln. *Annalen der Physik*, 1927.
- [129] S Haessler. *Generation of Attosecond Pulses in Atoms and Molecules*. PhD thesis, 2009.
- [130] I V Litvinyuk, Kevin F Lee, P W Dooley, D M Rayner, D M Villeneuve, and P B Corkum. Alignment-Dependent Strong Field Ionization of Molecules. *Physical Review Letters*, 90(23):233003, 2003.
- [131] B Zimmermann, M Lein, and J Rost. Analysis of recombination in high-order harmonic generation in molecules. *Physical Review A*, 71(3):33401, 2005.

- [132] Misha Y Ivanov, Thomas Brabec, and Neal Burnett. Coulomb corrections and polarization effects in high-intensity high-harmonic emission. *Physical Review A*, 54(1):742–745, 1996.
- [133] X. M. Tong, Z. X. Zhao, and C. D. Lin. Theory of molecular tunneling ionization. *Physical Review A*, 66(3):1–11, September 2002.
- [134] Bing Shan, Xiao M Tong, Zengxiu Zhao, Zenghu Chang, and C D Lin. High-order harmonic cutoff extension of the O<sub>2</sub> molecule due to ionization suppression. *Physical Review A*, 66(6):61401, 2002.
- [135] Ryan Murray, Wing-Ki Liu, and Misha Yu. Ivanov. Partial Fourier-transform approach to tunnel ionization: Atomic systems. *Physical Review A*, 81(2):23413, 2010.
- [136] Ryan Murray. Tunnel Ionization in Strong Fields in atoms and molecules and its applications. 2011.
- [137] Ryan Murray, Michael Spanner, Serguei Patchkovskii, and Misha Ivanov. Tunnel Ionization of Molecules and Orbital Imaging. *Physical Review Letters*, 106(17):173001, April 2011.
- [138] Domagoj Pavičić, Kevin F. Lee, D. M. Rayner, P. B. Corkum, and D. M. Villeneuve. Direct Measurement of the Angular Dependence of Ionization for N<sub>2</sub>, O<sub>2</sub>, and CO<sub>2</sub> in Intense Laser Fields. *Physical Review Letters*, 98(24):243001, June 2007.
- [139] Serguei Patchkovskii. Nuclear Dynamics in Polyatomic Molecules and High-Order Harmonic Generation. *Physical Review Letters*, 102(25):253602, 2009.
- [140] Serguei Patchkovskii, Zengxiu Zhao, Thomas Brabec, and D M Villeneuve. High harmonic generation and molecular orbital tomography in multielectron systems. *The Journal of chemical physics*, 126(11):114306, March 2007.
- [141] RR Lucchese, Georges Raseev, and V McKoy. Studies of differential and total photoionization cross sections of molecular nitrogen. *Physical Review A*, 25(5), 1982.
- [142] Z Chang. *Fundamentals of attosecond optics*. Taylor & Francis Group, 2011.
- [143] Bretislav Friedrich and Dudley Herschbach. Alignment and Trapping of Molecules in Intense Laser Fields. *Physical Review Letters*, 74(23):4623, 1995.
- [144] Sune Svanberg. *Atomic and Molecular Spectroscopy*. Springer-Verlag Berlin Heidelberg, fourth, re edition, 2004.
- [145] Muller H. G. Reconstruction of attosecond harmonic beating by interference of two-photon transitions. *Applied Physics B: Lasers and Optics*, 74:17, 2002.
- [146] V Vénier, R Taïeb, and A Maquet. Phase dependence of (N+1)-color (N<sub>l</sub>1) ir-uv photoionization of atoms with higher harmonics. *Physical Review A*, 54(1):721–728, July 1996.
- [147] Rick Trebino, Kenneth W. DeLong, David N. Fittinghoff, John N. Sweetser, Marco A. Krumbugel, Bruce A. Richman, and Daniel J. Kane. Measuring ultrashort laser pulses in the time-frequency domain using frequency-resolved optical gating. *Review of Scientific Instruments*, 68(9):3277–3295, 1997.
- [148] J Mauritsson, P Johnsson, R López Martens, K Varjú, W Kornelis, J Biegert, U Keller, M B Gaarde, K J Schafer, and A Lchar39huillier. Measurement and control of the frequency chirp rate of high-order harmonic pulses. *Physical Review A*, 70(2):21801, 2004.
- [149] K Varjú, P Johnsson, and R Lopez-Martens. Experimental studies of attosecond pulse trains. *Laser physics*, 15(6):888–898, 2005.
- [150] P Kruit and F H Read. Magnetic field paralleliser for 2 $\pi$  electron-spectrometer and electron-image magnifier magnifier. *Journal of physical E*, 16:313, 1983.
- [151] Raoul Zerne, Carlo Altucci, Marco Bellini, Mette Gaarde, T. Hänsch, Anne L’Huillier, Claire Lyngå, and C.-G. Wahlström. Phase-Locked High-Order Harmonic Sources. *Physical Review Letters*, 79(6):1006–1009, August 1997.
- [152] M Kovacev, S V Fomichev, E Priori, Y Mairesse, H Merdji, P Monchicourt, P Breger, J Norin, A Persson, A L’Huillier, C G Wahlstrom, B Carre, and P Salieres. Extreme ultraviolet fourier-transform spectroscopy with high order harmonics. *Physical Review Letters*, 95(22):223903, 2005.
- [153] M Bellini, C LyngåTozzi, A, M B Gaarde, C Delfin, T W Hänsch, A L’Huillier, and C.-G. Wahlström. Temporal coherence of ultrashort high-order harmonic pulses. *Physical Review Letters*, 81:297, 1998.
- [154] Chiara Corsi, Angela Pirri, Emiliano Sali, Alessandra Tortora, and Marco Bellini. Direct Interferometric Measurement of the Atomic Dipole Phase in High-Order Harmonic Generation. *Physical Review Letters*, 97(2):023901, July 2006.
- [155] D Descamps, C Lynga, J Norin, A L’Huillier, C.-G. Wahlström, J.-F. Hergott, H Merdji, P Salières, M Bellini, and T W Hänsch. Extreme ultraviolet interferometry measurements with high-order harmonics. *Optics Letters*, 25:135, 2000.

- [156] Xibin Zhou, Robynne Lock, Wen Li, Nick Wagner, Margaret Murnane, and Henry Kapteyn. Molecular Recollision Interferometry in High Harmonic Generation. *Physical Review Letters*, 100(7):1–4, February 2008.
- [157] Robynne M Lock, Xibin Zhou, Wen Li, Margaret M Murnane, and Henry C Kapteyn. Measuring the intensity and phase of high-order harmonic emission from aligned molecules. *Chemical Physics*, 366(1-3):22–32, 2009.
- [158] Nicholas Wagner, Xibin Zhou, Robynne Lock, Wen Li, Andrea Wuest, Margaret Murnane, and Henry Kapteyn. Extracting the phase of high-order harmonic emission from a molecule using transient alignment in mixed samples. *Physical Review A*, 76(6):61403, 2007.
- [159] Tsuneto Kanai, Eiji J Takahashi, Yasuo Nabekawa, and Katsumi Midorikawa. Observing molecular structures by using high-order harmonic generation in mixed gases. *Physical Review A*, 77(4):41402, 2008.
- [160] B. McFarland, J. Farrell, P. Bucksbaum, and M. Gühr. High-order harmonic phase in molecular nitrogen. *Physical Review A*, 80(3):033412, September 2009.
- [161] J. B. Bertrand, H. J. Wörner, P. Salières, D. M. Villeneuve, and P. B. Corkum. Linked attosecond phase interferometry for molecular frame measurements. *Nature Physics*, 9(3):174–178, February 2013.
- [162] S Haessler, J Caillat, and P Salières. Self-probing of molecules with high harmonic generation. *Journal of Physics B: Atomic, Molecular and Optical Physics*, 44(20):203001, October 2011.
- [163] Anh T Le, R R Lucchese, M T Lee, and C D Lin. Probing Molecular Frame Photoionization via Laser Generated High-Order Harmonics from Aligned Molecules. *Phys. Rev. Lett.*, 102(20):203001, 2009.
- [164] Peter Puschnig, Stephen Berkebile, Alexander J Fleming, Georg Koller, Konstantin Emtsev, Thomas Seyller, John D Riley, Claudia Ambrosch-Draxl, Falko P Netzer, and Michael G Ramsey. Reconstruction of molecular orbital densities from photoemission data. *Science (New York, N.Y.)*, 326(5953):702–6, October 2009.
- [165] W.-H. Soe, C. Manzano, a. De Sarkar, N. Chandrasekhar, and C. Joachim. Direct Observation of Molecular Orbitals of Pentacene Physisorbed on Au(111) by Scanning Tunneling Microscope. *Physical Review Letters*, 102(17):176102, May 2009.
- [166] Leo Gross, Nikolaj Moll, Fabian Mohn, Alessandro Curioni, Gerhard Meyer, Felix Hanke, and Mats Persson. High-Resolution Molecular Orbital Imaging Using a p-Wave STM Tip. *Physical Review Letters*, 107(8):086101, August 2011.
- [167] Anh T Le, Della, P Fainstein, D Telnov, M Lein, and C Lin. Theory of high-order harmonic generation from molecules by intense laser pulses. *Journal of Physics B: Atomic, Molecular and Optical Physics*, 41(8):81002, 2008.
- [168] Anh T Le, Toru Morishita, and C D Lin. Extraction of the species-dependent dipole amplitude and phase from high-order harmonic spectra in rare-gas atoms. *Physical Review A*, 78(2):23814, 2008.
- [169] Cheng Jin, Anh T Le, and C D Lin. Retrieval of target photorecombination cross sections from high-order harmonics generated in a macroscopic medium. *Physical Review A*, 79(5):53413, 2009.
- [170] Cheng Jin, Anh-Thu Le, and C D Lin. Medium propagation effects in high-order harmonic generation of Ar and N<sub>2</sub>. *Physical Review A*, 83(2):23411, 2011.
- [171] Cheng Jin, Anh-Thu Le, and C. D. Lin. Analysis of effects of macroscopic propagation and multiple molecular orbitals on the minimum in high-order harmonic generation of aligned CO<sub>2</sub>. *Physical Review A*, 83(5):053409, May 2011.
- [172] Cheng Jin, Hans Jakob Wörner, V Tosa, Anh-Thu Le, Julien B Bertrand, R R Lucchese, P B Corkum, D M Villeneuve, and C D Lin. Separation of target structure and medium propagation effects in high-harmonic generation. *Journal of Physics B: Atomic, Molecular and Optical Physics*, 44(9):095601, May 2011.
- [173] Anh-Thu Le, R. R. Lucchese, and C. D. Lin. Polarization and ellipticity of high-order harmonics from aligned molecules generated by linearly polarized intense laser pulses. *Physical Review A*, 82(2):023814, August 2010.
- [174] Lagmago Kamta and A D Bandrauk. Three-dimensional time-profile analysis of high-order harmonic generation in molecules: Nuclear interferences in H<sub>2</sub><sup>+</sup>. *Physical Review A*, 71(5):53407–53419, 2005.
- [175] C C Chiril and M Lein. Explanation for the smoothness of the phase in molecular high-order harmonic generation. *Physical Review A*, 80(1):13405, 2009.
- [176] P H Bucksbaum M Ghr McFarland J .P. Farrell. High Harmonic Generation from Multiple Orbitals in N<sub>2</sub>. *Science*, 322:1232–1235, 2008.
- [177] R. Torres, T. Siegel, L. Brugnera, I. Procino, Jonathan G. Underwood, C. Altucci, R. Velotta, E. Springate, C. Froud, I. C. E. Turcu, S. Patchkovskii, M. Yu. Ivanov, O. Smirnova, and J. P. Marangos. Revealing molecular structure and dynamics through high-order harmonic generation driven by mid-IR fields. *Physical Review A*, 81(5):051802, May 2010.

- [178] R Torres, T Siegel, L Brugnera, I Procino, Jonathan G Underwood, C Altucci, R Velotta, E Springate, C Froud, I C E Turcu, M Yu Ivanov, O Smirnova, and J P Marangos. Extension of high harmonic spectroscopy in molecules by a 1300 nm laser field. *Optics express*, 18(3):3174–80, February 2010.
- [179] A. Rupenyan, P. M. Kraus, J. Schneider, and H. J. Wörner. Quantum interference and multielectron effects in high-harmonic spectra of polar molecules. *Physical Review A*, 87(3):031401, March 2013.
- [180] A. Rupenyan, P. M. Kraus, J. Schneider, and H. J. Wörner. High-harmonic spectroscopy of isoelectronic molecules: Wavelength scaling of electronic-structure and multielectron effects. *Physical Review A*, 87(3):033409, March 2013.
- [181] Y Mairesse, J Higuët, N Dudovich, D Shafir, B Fabre, E Mével, E Constant, S Patchkovskii, Z Walters, M Yu. Ivanov, and O Smirnova. High Harmonic Spectroscopy of Multichannel Dynamics in Strong-Field Ionization. *Physical Review Letters*, 104(21):213601, 2010.
- [182] R M Lock, S Ramakrishna, X Zhou, H C Kapteyn, M M Murnane, and T Seideman. Extracting continuum electron dynamics from high harmonic emission from molecules. *Physical review letters*, 108(13):133901, March 2012.
- [183] J Muth-Bohm, a Becker, and Fh Faisal. Suppressed molecular ionization for a class of diatomics in intense femtosecond laser fields. *Physical review letters*, 85(11):2280–3, September 2000.
- [184] Tsuneto Kanai, Eiji Takahashi, Yasuo Nabekawa, and Katsumi Midorikawa. Destructive Interference during High Harmonic Generation in Mixed Gases. *Physical Review Letters*, 98(15):153904, April 2007.
- [185] Anthony E. Siegman. *Lasers*. 1986.
- [186] C Bourassin-Bouchet, Z Diveki, S de Rossi, E English, E Meltchakov, O Gobert, D Guénot, B Carré, F Delmotte, P Salières, and T Ruchon. Control of the attosecond synchronization of XUV radiation with phase-optimized mirrors. *Optics express*, 19(4):3809–3817, 2011.
- [187] H J Worner, J B Bertrand, P Hockett, P B Corkum, and D M Villeneuve. Controlling the Interference of Multiple Molecular Orbitals in High-Harmonic Generation. *Physical Review Letters*, 104(23):233904, 2010.
- [188] Z Diveki, a Camper, S Haessler, T Auguste, T Ruchon, B Carré, P Salières, R Guichard, J Caillat, a Maquet, and R Taïeb. Spectrally resolved multi-channel contributions to the harmonic emission in N<sub>2</sub>. *New Journal of Physics*, 14(2):023062, February 2012.
- [189] Z. Diveki, R. Guichard, J. Caillat, A. Camper, S. Haessler, T. Auguste, T. Ruchon, B. Carré, A. Maquet, R. Taïeb, and P. Salières. Molecular orbital tomography from multi-channel harmonic emission in N<sub>2</sub>. *Chemical Physics*, April 2012.
- [190] H. Soifer, P. Botheron, D. Shafir, a. Diner, O. Raz, B. D. Bruner, Y. Mairesse, B. Pons, and N. Dudovich. Near-Threshold High-Order Harmonic Spectroscopy with Aligned Molecules. *Physical Review Letters*, 105(14):143904, September 2010.
- [191] Jérémie Caillat, Alfred Maquet, Stefan Haessler, Baptiste Fabre, Thierry Ruchon, Pascal Salières, Yann Mairesse, and Richard Taïeb. Attosecond resolved electron release in two-color near-threshold photoionization of N<sub>2</sub>. *Physical review letters*, 106(9):93002, 2011.
- [192] GH Lee, HT Kim, JY Park, and CH Nam. Revival Strictures of Linear Molecules in a Field-Free Alignment Condition as Probed by High-Order Harmonic Generation. *Journal of the Korean Physical Society*, 49(1):337–341, 2006.
- [193] P M Dehmer, P J Miller, and W A Chupka. Photoionization of N<sub>2</sub> X 1Σ<sup>+</sup><sub>g</sub>, v=0 and 1 near threshold. Preionization of the WorleyJenkins Rydberg series. *The Journal of Chemical Physics*, 80(3):1030, 1984.
- [194] C. Vozzi, R. Torres, M. Negro, L. Brugnera, T. Siegel, C. Altucci, R. Velotta, F. Frassetto, L. Poletto, P. Villoresi, S. De Silvestri, S. Stagira, and J. P. Marangos. High harmonic generation spectroscopy of hydrocarbons. *Applied Physics Letters*, 97(24):241103, 2010.
- [195] M Stano, S Matejcik, J D Skalny, and T D Mark. Electron impact ionization of CH<sub>4</sub>: ionization energies and temperature effects. *Journal of Physics B: Atomic, Molecular and Optical Physics*, 36:261, 2003.
- [196] D W Turner. *Molecular Photoelectron Spectroscopy*. John Wiley & Sons, 1970.
- [197] N Kajumba, R Torres, Jonathan G Underwood, J S Robinson, S Baker, J W G Tisch, R De Nalda, W a Bryan, R Velotta, C Altucci, I Procino, I C E Turcu, and J P Marangos. Measurement of electronic structure from high harmonic generation in non-adiabatically aligned polyatomic molecules. *New Journal of Physics*, 10(2):025008, February 2008.
- [198] D. Lynch, M.-T. Lee, R. R. Lucchese, and V. McKoy. Studies of the photoionization cross sections of acetylene. *The Journal of Chemical Physics*, 80(5):1907, 1984.
- [199] R Torres, N Kajumba, Jonathan Underwood, J Robinson, S Baker, J Tisch, De R Nalda, W Bryan, R Velotta, C Altucci, I Turcu, and J Marangos. Probing Orbital Structure of Polyatomic Molecules by High-Order Harmonic Generation. *Physical Review Letters*, 98(20):203007, 2007.

- [200] Manfred Lein. Attosecond Probing of Vibrational Dynamics with High-Harmonic Generation. *Physical Review Letters*, 94(5):53004, 2005.
- [201] Serguei Patchkovskii. Nuclear Dynamics in Polyatomic Molecules and High-Order Harmonic Generation. *Physical Review Letters*, 102(25):253602, June 2009.
- [202] H J Wörner, J B Bertrand, B Fabre, J Higuët, H Ruf, a Dubrouil, S Patchkovskii, M Spanner, Y Mairesse, V Blanchet, E Mével, E Constant, P B Corkum, and D M Villeneuve. Conical intersection dynamics in NO<sub>2</sub> probed by homodyne high-harmonic spectroscopy. *Science (New York, N.Y.)*, 334(6053):208–12, October 2011.
- [203] H Ruf, C Handschin, a Ferré, N Thiré, J B Bertrand, L Bonnet, R Cireasa, E Constant, P B Corkum, D Descamps, B Fabre, P Larregaray, E Mével, S Petit, B Pons, D Staedter, H J Wörner, D M Villeneuve, Y Mairesse, P Halvick, and V Blanchet. High-harmonic transient grating spectroscopy of NO<sub>2</sub> electronic relaxation. *The Journal of chemical physics*, 137(22):224303, December 2012.
- [204] O Guyétand, M Gisselbrecht, a Huetz, P Agostini, R Taïeb, V Vénier, a Maquet, L Antonucci, O Boyko, C Valentin, and D Douillet. Multicolour above-threshold ionization of helium: quantum interference effects in angular distributions. *Journal of Physics B: Atomic, Molecular and Optical Physics*, 38(22):L357–L363, November 2005.
- [205] K Varjú, P Johnsson, J Mauritsson, T Remetter, T. and Ruchon, Y Ni, F Lépine, M Kling, J Khan, K J Schafer, M J J Vrakking, and A L'Huillier. Angularly resolved electron wave packet interferences. *Journal of Physics B: Atomic, Molecular and Optical Physics*, 39(18):3983–3991, 2006.
- [206] Alfred Maquet and Richard Taïeb. Two-colour IR + XUV spectroscopies: the soft-photon approximation. *Journal of Modern Optics*, 54(13-15):1847–1857, September 2007.
- [207] O Guyétand, M Gisselbrecht, a Huetz, P Agostini, R Taïeb, a Maquet, B Carré, P Breger, O Gobert, D Garzella, J-F Hergott, O Tcherbakoff, H Merdji, M Bougeard, H Rottke, M Böttcher, Z Ansari, and P Antoine. Evolution of angular distributions in two-colour, few-photon ionization of helium. *Journal of Physics B: Atomic, Molecular and Optical Physics*, 41(5):051002, March 2008.
- [208] M. Gisselbrecht, a. Huetz, M. Lavollee, T. J. Reddish, and D. P. Seecombe. Optimization of momentum imaging systems using electric and magnetic fields. *Review of Scientific Instruments*, 76(1):013105, 2005.
- [209] F.M. Böttcher, B. Manschwetus, H. Rottke, N. Zhavoronkov, Z. Ansari, and W. Sandner. Interferometric long-term stabilization of a delay line: a tool for pump-probe photoelectron-photoion-coincidence spectroscopy on the attosecond time scale. *Applied Physics B*, 91(2):287–293, April 2008.
- [210] ES Toma and HG Muller. Calculation of matrix elements for mixed extreme-ultraviolet-infrared two-photon above-threshold ionization of argon. *Journal of Physics B: Atomic, Molecular and Optical Physics*, 35:3435–3442, 2002.
- [211] M Swoboda, T Fordell, K Klünder, J M Dahlström, M Miranda, C Buth, K J Schafer, J Mauritsson, A. L'Huillier, and M Gisselbrecht. Phase Measurement of Resonant Two-Photon Ionization in Helium. *Physical Review Letters*, 104(10):103003, March 2010.
- [212] H J Wörner, J B Bertrand, D V Kartashov, P B Corkum, and D M Villeneuve. Following a chemical reaction using high-harmonic interferometry. *Nature*, 466(7306):604–7, July 2010.
- [213] Jérôme Levesque, Yann Mairesse, Nirit Dudovich, Henri Pépin, Jean-Claude Kieffer, P. Corkum, and D. Villeneuve. Polarization State of High-Order Harmonic Emission from Aligned Molecules. *Physical Review Letters*, 99(24):243001, December 2007.
- [214] Xibin Zhou, Robynne Lock, Nick Wagner, Wen Li, Henry C Kapteyn, and Margaret M Murnane. Elliptically Polarized High-Order Harmonic Emission from Molecules in Linearly Polarized Laser Fields. *Physical Review Letters*, 102(7), 2009.
- [215] E. Frumker, C. T. Hebeisen, N. Kajumba, J. B. Bertrand, H. J. Wörner, M. Spanner, D. M. Villeneuve, a. Naumov, and P. B. Corkum. Oriented Rotational Wave-Packet Dynamics Studies via High Harmonic Generation. *Physical Review Letters*, 109(11):113901, September 2012.
- [216] Y. J. Chen, L. B. Fu, and J. Liu. Asymmetric Molecular Imaging through Decoding Odd-Even High-Order Harmonics. *Physical Review Letters*, 111(7):073902, August 2013.

---





**Attosecond evolution of energy- and angle-resolved  
photoemission spectra in two-color (IR + XUV)  
ionization of rare gases**

Y.J. Picard, B. Manschwetus, M. Géléoc, M. Böttcher, E.M. Staicu  
Casagrande, N. Lin, T. Ruchon, B. Carré, J.-F. Hergott, F. Lepetit, R.  
Taïeb, A. Maquet and A. Huetz.

*Submitted to Physical Review A xx, xxx (2013).*



## Attosecond evolution of energy- and angle-resolved photoemission spectra in two-color (IR + XUV) ionization of rare gases

Y.J. Picard<sup>1</sup>, B. Manschwetus<sup>2</sup>, M. Géléoc<sup>2</sup>, M. Böttcher<sup>1</sup>, E.M. Staicu Casagrande<sup>1</sup>, N. Lin<sup>2</sup>, T. Ruchon<sup>2</sup>, B. Carré<sup>2</sup>, J.-F. Hergott<sup>2</sup>, F. Lepetit<sup>2</sup>, R. Taïeb<sup>3</sup>, A. Maquet<sup>3</sup> and A. Huetz<sup>1</sup>

<sup>1</sup>*ISMO, UMR 8214, Université Paris-Sud, Bâtiment 350, Orsay Cedex, France.*

<sup>2</sup>*CEA-Saclay, IRAMIS, Service des Photons, Atomes et Molécules, 91191 Gif-sur-Yvette, France and*

<sup>3</sup>*UPMC, Université Paris 06, CNRS, UMR 7614, LCPMR, 11 rue Pierre et Marie Curie, 75231 Paris Cedex 05, France*

(Dated: October 3, 2013)

We have analyzed the angular distributions of the photoelectrons emitted upon photoionization of rare gases by a comb of harmonics in the extreme ultra violet (XUV) range, in the presence of a “dressing” infrared (IR) field with controlled delay  $\tau$ , stabilized down to about  $\pm 60$  as. The measurements have been performed with the help of the coincidence momentum imaging technique. We evidence marked differences in the measured angular distributions of the photoelectrons, depending on the number of IR photons exchanged. Joined to a theoretical interpretation, these observations bring new insights in the dynamics of this class of two-color photoionization processes that are a key step towards studying photoionization in the time domain, with attosecond time resolution.

Photoionization of atoms or molecules in the simultaneous presence of attosecond pulses of extreme ultra violet (XUV) coherent radiation, together with an infrared (IR) laser “dressing” field with controlled time delay is the cornerstone of the so-called “attophysics”. The analysis of the photoemission spectra obtained under these conditions provides the physical basis to follow in real time the paradigmatic process of photoionization, with attosecond resolution [1–5]. We emphasize that the presence of the IR field, with typical cycle duration of about 2.6 fs (Ti:Sapph. laser), is essential to clock the photoionization process on the attosecond scale. In particular, for specific intensities and durations of the two pulses, the so-called RABBIT (Reconstruction of Attosecond Beating By Interference of Two-photon transitions), as dubbed by Muller, [6, 7], has been successfully implemented to characterize harmonic radiation and to explore photoionization, notably in the time domain [1, 2, 4, 8]. The technique relies on a low intensity “dressing” field and implies the exchange of only *one* IR photon. Then, the analysis is concentrated on the photoelectron lines, or sidebands, lying in-between the so-called harmonic peaks that mainly result from the absorption of only one XUV photon. At much higher IR intensities, the “dressing” field can be used to “streak” the energy and angular distributions of the photoelectrons generated through XUV photoionization [9]. Here, we investigate the range of *intermediate* IR intensities for which the exchange of *few* IR photons can take place. As we shall show, valuable informations can be derived also from the angular dependences of the harmonic peaks.

An exact treatment of time-dependent processes with finite duration pulses, such as photoionization in poly-electronic species, is out of reach of the present computers capabilities. Most Time-Dependent Schrödinger Equation (TDSE) treatments rely on the use of single-active electron model-potentials [10–13]. To interpret the data

a more simplified description of the physics of the process is often required. Here, we shall advocate the use of the so-called “soft-photon approximation”, as discussed below [14, 15].

We have shown, in preliminary studies in Helium, that the angular distributions of the photoelectrons provides more detailed information than the angle-integrated cross sections used in standard RABBIT studies [1, 2, 4]. In particular, they depend on both the phases of the continuum wave functions of the ejected electrons, and on the intrinsic phases of the second-order transition matrix elements which account for the “dressing” of the photoelectron by the IR field [6, 10, 15, 16]. In an attophysics context, these phases, which are notoriously difficult to determine, play an essential role to achieve a complete description of photoionization, notably in the time domain [17].

The determination of simultaneous energy- and angle-resolved spectra requires sophisticated techniques, such as Velocity Map Imaging (VMI) as used by Aseyev *et al.* [12] or Cold Target Recoil Ion Momentum Spectroscopy (COLTRIMS). Here, we have chosen to use a COLTRIMS-like device as described in Ref. [18]. The latter, based on the coincidence technique between electrons and ions, has the advantage of (i) eliminating background electrons and (ii) being selective of the physical process involved. The price to pay is that the counting rates are significantly reduced, compared for instance to VMI. Thus, one of the crucial points when performing such experiments is to maintain a long term stability of the synchronization between the XUV and IR fields [19]. Here we report stabilized delay accuracy in the 60 as range, over more than one hour. This represents a significant improvement as compared to previous measurements, where the time jitter between the two pulses was either fixed or not accurately controlled [15, 16].

While not essential to measure the angular distribu-

tions in single-photon ionization, the use of coincidence with stabilized delay lines, as in our experiment, paves the way to more complex studies, where multiple ionization channels could be open.

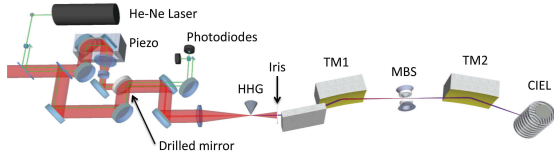


FIG. 1. Scheme of the experimental set-up. The incoming IR beam is divided into two branches by a beam splitter, one for the high harmonic generation (HHG) and the other for the “dressing”. The latter goes through a piezo controlled delay line and a 2:1 telescope. The two beams are recombined by a drilled mirror with a central hole of 4 mm diameter. The two IR beams are then focused by a 75 cm lens into a pulsed gas jet of argon where the annular beam with pulse energy of 2 mJ is used to generate high harmonics. Then the generation beam is blocked by an iris and only the XUV and the “dressing” IR are transmitted and focused by a first toroidal mirror (TM1) in the detection volume of a magnetic bottle spectrometer (MBS) and refocused by a second toroidal mirror (TM2) in the center of the COLTRIMS apparatus (CIEL).

The femtosecond laser PLFA [20], delivering up to 13 mJ, 40 fs pulses at 801.4 nm and 1 kHz, has been used to generate simultaneously a comb of harmonics at an intensity of approximately  $1.2 \times 10^{14}$  W cm<sup>-2</sup> and the “dressing” IR beam. A scheme of the used experimental setup is shown in Fig. 1. The Magnetic Bottle Spectrometer (MBS) is used to monitor the whole experiment while recording coincidence data. For each value of the delay  $\tau$  between the “dressing” IR and the XUV pulses, the acquisition takes typically one hour. The electric and magnetic fields were 4 V cm<sup>-1</sup> and 5.6 Gauss respectively, allowing to record ion-electron coincidence events with  $4\pi$  detection of the electrons up to kinetic energy of 10 eV. For the long acquisition times the delay  $\tau$  must be very stable. We use a He-Ne laser which propagates collinearly to the IR beams through the interferometer. After recombination the two He-Ne beams produce a pattern of interference fringes, which are measured by two photodiodes. From this pattern the path difference between the two arms of the delay line is calculated and a proportional-integral-derivative loop acting on the piezo position allows stabilizing the delay  $\tau$  within an error of  $\pm 60$  as rms. A similar method was used earlier for active stabilization in attosecond experiments using the COLTRIMS technique [19].

When recombining the XUV harmonics with the IR beam onto target atoms, the dominant photoionization process is associated to the absorption of one XUV photon accompanied with the exchange of IR photons. In the intensity range chosen here ( $I_{IR} \approx 10^{12}$  W cm<sup>-2</sup>),

the ionization process is dominated by the exchange of one or two IR photons via stimulated transitions. Representative photoelectron spectra are shown in Fig. 2 for He and Ar targets, as measured after integration over angles. The odd-labelled “dressed harmonics” lines, denoted H( $2q \pm 1$ ), result dominantly from absorption of a single XUV harmonic photon of order ( $2q \pm 1$ ), alone or accompanied by the exchange (absorption+stimulated emission) of two IR photons. The even-labelled “sideband” lines, denoted SB( $2q$ ), are dominantly associated to the absorption of one harmonic photon with the exchange of only one IR photon. It is known that, in comparison with pure XUV spectra (not shown here), IR+XUV photoelectron spectra are shifted towards lower energy by the ponderomotive shift  $U_p = F_{IR}^2 / (4\omega_{IR}^2)$ , where  $F_{IR}$  is the IR field strength. The measured shifts are  $(79 \pm 13)$  in Ar and  $(47 \pm 19)$  meV in He, indicating IR intensities of  $(1.2 \pm 0.2)$  and  $(0.7 \pm 0.3) \times 10^{12}$  W cm<sup>-2</sup> respectively. In the following, we have not considered the SB16 and H17 peaks of He which are known to be affected by a resonant process through the 1s3p excited state [13, 15].

Previous studies have shown that the magnitude of a sideband SB( $2q$ ) varies with the delay  $\tau$  as:  $\cos(2\omega_{IR}\tau - \Delta\phi_{2q} - \Delta\theta_{2q})$ . Here,  $\Delta\phi_{2q} = \phi_{2q+1} - \phi_{2q-1}$  is the phase difference between consecutive harmonics H( $2q + 1$ ) and H( $2q - 1$ ) and  $\Delta\theta_{2q}$  is the phase difference between the atomic amplitudes associated to the interfering quantum paths leading to SB( $2q$ ), [6]. On the top line in Fig. 2 (a and c), the values of the XUV-IR delay  $\tau$  have been fixed and stabilized to maximize the cosine term given above, and thus the magnitude of the sideband peaks. On the bottom line they have been incremented by T/4 (660 as), where T is the IR period, so that the sidebands peaks are close to their minima, Fig.2 (b and d).

The angular distributions (ADs) show the photoelectron emission probability for a given polar angle  $\theta$  between its momentum vector and the laser polarization vector. The distributions have been obtained by integration over the azimuthal angle  $\phi$  of the recorded data. For pure XUV (not shown here) they are proportional to  $[1 + \beta P_2(\cos(\theta))]$ , with the Legendre polynomial  $P_2(\cos(\theta)) = \frac{1}{2}(3\cos^2(\theta) - 1)$ . Our data are fully consistent with  $\beta = 2$  for He, while for Ar, a fit of the data yields  $\beta = 0.17, 0.76$ , and 1.16 for H11, H13 and H15 respectively. All values are in excellent agreement with synchrotron data [21].

For XUV+IR, the ADs are shown in Fig. 3 and 4 for selected peaks of Fig. 2. Fig. 3 shows the ADs of the sidebands SB14 in Ar (a) and SB20 in He (b). When the delay IR-XUV  $\tau$  is changed by a quarter of an IR period, it appears clearly that the shape of their ADs does not vary significantly, although their magnitudes change as shown in Fig. 2. This behavior is in sharp contrast with the “dressed” harmonic peaks, which exhibit strong variations when changing  $\tau$ . This is illustrated in Fig. 4,

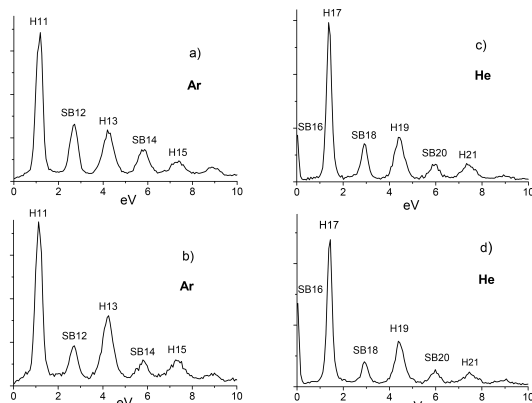


FIG. 2. Photoelectron spectra: (a,b) in Ar; (c,d) in He. The odd and even labelled peaks correspond to dressed harmonics and sidebands respectively. The XUV-IR delay  $\tau$  is tuned to maximize the sidebands in a) and c). From a) to b) and from c) to d)  $\tau$  is incremented by 660 as, *i.e.* a quarter IR laser period.

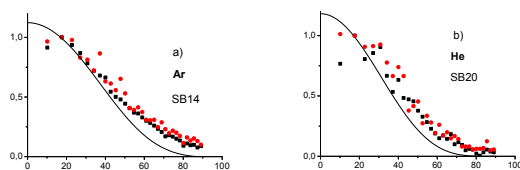


FIG. 3. Normalized ADs of representative sideband lines at two different IR-XUV delays  $\tau$ , see text: a) AD of SB14 in Ar: squares (black) and circles (red) from spectra 2a and 2b respectively; b) AD of SB20 in He, from spectra 2c and 2d respectively. Thin lines: “soft-photon” approximation. The x axis gives the values of the polar angle  $\theta$  in degrees. The polarization direction is at  $\theta = 0^\circ$ .

which displays the ADs of H13 for Ar (a) and H19 for He (b). Such an evolution, which has been predicted theoretically in the case of He [15], is observed here for the first time experimentally. The ADs corresponding to the minima of the sideband peaks of Fig. 2 are close to the pure XUV ones, but those corresponding to the maxima are changed as the probability of emission is significantly decreased at low values of  $\theta$ , close to the polarization axis.

We show now that this complex behavior can be interpreted with the help of the “soft-photon” approximation [14]. The essence of the model is contained in the following factorized form of a two-photon (XUV+IR) transition amplitude. Here, it is written for the second-order  $S$ -matrix component, associated to a transition leading to SB(2q) reached via simultaneous absorption of one

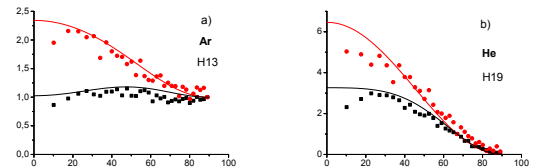


FIG. 4. Normalized ADs of representative harmonic lines. Conditions are the same as for Fig. 3, but a): AD of H13 in Ar; b): AD of H19 in He.

XUV harmonic  $H(2q\pm 1)$  with vector potential  $\vec{A}_\pm$  and the exchange of one IR photon, with field vector amplitude  $\vec{F}_0$ :

$$S_{2q}^{(\pm)}(\vec{k}_\pm, \tau) = -2\pi i J_{\mp 1}(\vec{\alpha}_0 \cdot \vec{k}_\pm) e^{-i(\phi_{H(2q\pm 1)} + \omega_{IR}\tau)} \times \langle \chi_{\vec{k}_\pm} | \vec{A}_\pm \cdot \vec{p} | \varphi_{n,\ell,m} \rangle \quad (1)$$

Here,  $S_{2q}^{(\pm)}(\vec{k}_\pm, \tau)$  is given for a photoelectron with final momentum  $\vec{k}_\pm = \hat{k}_\pm \sqrt{2[(2q\pm 1)\omega_{IR} - I_p - U_p]}$  and an IR-XUV delay  $\tau$ .  $J_n(z)$  is a Bessel function,  $\vec{\alpha}_0 = \vec{F}_0/\omega_{IR}^2$  is the classical excursion vector of the photoelectron embedded within the IR laser field and  $\phi_{H(2q\pm 1)}$  is the intrinsic phase of  $H(2q\pm 1)$ . The matrix element  $\langle \chi_{\vec{k}_\pm} | \vec{A}_\pm \cdot \vec{p} | \varphi_{n,\ell,m} \rangle$  is associated to the dipole transition between the atomic bound state  $|\varphi_{n,\ell,m}\rangle$  and a final continuum state with wave function  $|\chi_{\vec{k}_\pm}\rangle$ . The Bessel function arises from approximating the absorption of the additional IR photon as a dipole transition between Volkov states of the photoelectron [14].

To illustrate the approach, we present the main steps of the calculation leading to the expression we have used to model the angular distributions of the sidebands SB(2q). Here it is adapted to the case where the initial atomic state is a  $p$ -state. Assuming equally populated magnetic sub-levels, the one-photon ionization differential cross section for the absorption of  $H(2q\pm 1)$  is proportional to:

$$\frac{d\sigma^{(1,\pm)}}{d\Omega(\hat{k}_\pm)} \propto \frac{1}{3} \sum_{m=-1}^{m=+1} \left| \langle \chi_{\vec{k}_\pm} | \vec{A}_\pm \cdot \vec{p} | \varphi_{n,\ell=1,m} \rangle \right|^2 \propto \sigma^{(1,\pm)} [1 + \beta_\pm P_2(\cos\theta)] \quad (2)$$

where

$$\sigma^{(1,\pm)} = \frac{|A_\pm|^2}{12\pi} [|T_{(0,\pm)}|^2 + 2|T_{(2,\pm)}|^2] \quad \text{and} \quad \beta_\pm = \frac{1 - 2\cos(\Delta_\pm)|T_{(0,\pm)}/T_{(2,\pm)}|}{1 + |T_{(0,\pm)}|^2/(2|T_{(2,\pm)}|^2)} \quad (3)$$

where  $T_{(0,\pm)}$  and  $T_{(2,\pm)}$  are real radial amplitudes associated respectively to the dipole transitions  $p \rightarrow s$  and  $p \rightarrow d$  upon absorption of either  $H(2q\pm 1)$ . The phase  $\Delta_\pm = \delta_{(0,\pm)} - \delta_{(2,\pm)}$  accounts for the difference between

the phase shifts of the continuum states in the corresponding channels.

The photoelectrons collected in SB(2q) originate from the simultaneous absorption of H(2q-1) and H(2q+1) in the presence of the IR field. The differential cross section can be factorized:

$$\frac{d\sigma_{SB2q}^{(2)}}{d\Omega(\hat{k}_{2q})} \propto |J_1(\vec{\alpha}_0 \cdot \vec{k}_{2q})|^2 \left\{ \frac{d\sigma^{(1,+)}}{d\Omega(\hat{k}_+)} + \frac{d\sigma^{(1,-)}}{d\Omega(\hat{k}_-)} + \frac{\tilde{\sigma}_{\text{tot}}}{4\pi} [1 + \tilde{\beta} P_2(\cos \theta)] \right\} \quad (4)$$

Within the braces, the first two terms are differential cross sections for one-(XUV) photon absorption, while the third term is a phase-dependent interference contribution, with  $\tilde{\sigma}_{\text{tot}}$  given by:

$$\tilde{\sigma}_{\text{tot}} = A_+ A_- [T_{(0,-)} T_{(0,+)} \cos[\delta_{(0,-)} - \delta_{(0,+)} - \Delta\phi(\tau)] + 2T_{(2,-)} T_{(2,+)} \cos[\delta_{(2,-)} - \delta_{(2,+)} - \Delta\phi(\tau)] \quad (5)$$

where the phase  $\Delta\phi(\tau) = 2\omega_{IR}\tau - \Delta\phi_{2q}$  depends on both the IR-XUV delay  $\tau$  and on the harmonic phase difference. Regarding the asymmetry parameter  $\tilde{\beta}$ , it can be expressed in terms of the radial amplitudes  $T_{(0,\pm)}$ ,  $T_{(2,\pm)}$  and oscillating terms such as:  $\cos[\delta_{(0,-)} - \delta_{(0,+)} - \Delta\phi(\tau)]$  which depend also on the photoelectron phase-shifts. The developed expression of  $\tilde{\beta}$  is too intricate and will be reported in a forthcoming publication [22].

We mention the interesting fact that, if the phase-shifts were constant in the energy interval considered, and if the one-(XUV) photon differential cross sections vary smoothly, the overall angular dependence can be written in a much simplified form:

$$\frac{d\sigma_{SB2q}^{(2)}}{d\Omega(\hat{k}_{2q})} \propto |J_1(\vec{\alpha}_0 \cdot \vec{k}_{2q})|^2 \frac{d\sigma^{(1)}}{d\Omega(\hat{k}_{2q})} \times \cos[\Delta\phi(\tau)] \quad (6)$$

where the  $\tau$ -dependent  $\cos[\Delta\phi(\tau)]$  factor *only* changes the magnitude of the sideband, without affecting the shape of the angular distribution. Moreover, in the IR intensity regime explored here, one recovers an overall  $\cos^4 \theta$  angular dependence of the angular distributions, as already reported for helium [15].

The case of the odd-numbered harmonic peaks is more involved. A closed form of the transition amplitudes involving the stimulated exchange of two IR photons can be derived in the soft-photon approximation. Its general expression will be reported elsewhere [22]. We should emphasize that, unlike the sideband transition case, its  $\tau$ -dependence cannot be factorized in any manner. It follows, in particular, that the global shape of the ADs changes significantly when varying  $\tau$ .

The main features of the observed ADs are well reproduced by the calculations, which are shown by thin lines in Figs. 3 and 4. The computations have been performed for IR intensities of 1.3 and  $0.8 \times 10^{12}$  W cm<sup>-2</sup>

for Ar and He respectively, in agreement with the observed ponderomotive shifts. As we focus on the shapes of these ADs, a normalization of all curves has been applied in each case at a given angle (17° in Fig. 3, 90° and 67° in Fig. 4 a and b respectively). In Fig. 3 a and b only single (black) curves have been drawn, which are very close to a  $\cos^4 \theta$  shape, and do not depend significantly on  $\tau$ , in full agreement with the data. It should be emphasized that, although the ADs for harmonics under pure XUV are strongly different in Ar and He, the ADs of their respective sidebands are similar, with a maximum along the polarization axis and a minimum at 90°. The slight discrepancies between theory and experiment, in the vicinity of 90°, are likely to result from the soft-photon approximation, which forbids the exchange of one IR-photon when the photoelectron momentum is orthogonal to the IR polarization vector. This translates into a zero-valued argument in the Bessel function of Eq. (4).

As for the dressed harmonics in Fig. 4 the agreement is especially impressive for Ar, knowing that the calculations do not include any adjustable parameter, and is still very good for He. Again, the angular distributions of H13 (in Ar) and H19 (in He) under pure XUV being noticeably different, this supports the generality of the soft-photon theory and its validity down to low energy, in the [4-7 eV] range considered here.

In conclusion, since the early 2000s, the intensities of the sidebands and their periodic variations have been extensively used, in RABBIT-like measurements, to probe the ionization dynamics in the time domain. Here, we have shown that the shape of the angular distributions of the sidebands brings few additional information, while those of the harmonic peaks constitute a sensitive tool to determine the intrinsic phases of the “dressed” photoelectrons wave functions, that are essential to study photoionization in the time domain.

On the experimental side, our study demonstrates that in two-color photoionization, the coincidence method between electrons and ions, although requiring long periods of acquisition time, can be combined with time delay stabilization down to attosecond accuracy. This opens the route for future two-color experiments with attosecond accuracy on other physical processes such as photo-double ionization of rare gases [18] or dissociative ionization of molecules [23].

We are very grateful to the staff of the PLFA laser at SLIC facility for efficient and constant support and to Pascal Salières for permanent encouragement during this experiment. We acknowledge financial support from the Triangle de la Physique network under contracts DYN-ELEC 2008-046T and 2009-008T, and from the French ANR ATTOWAVE contract ANR-09-BLAN-0031-01.

- 
- [1] P.M. Paul *et al.*, Science **292**, 1689 (2001).
- [2] Y. Mairese *et al.*, Science **302**, 1540 (2003).
- [3] M. Schultze *et al.*, Science **328**, 1658 (2010).
- [4] C. Klünder *et al.*, Phys. Rev. Lett. **106**, 143002 (2011).
- [5] J. M. Dahlström, A. L'Huillier and A. Maquet, J. Phys. B: Atom. Molec. and Opt. Phys. **45**, 183001 (2012).
- [6] V. Véniard, R. Taïeb and A. Maquet, Phys Rev A **54**, 721 (1996).
- [7] H. G. Muller, Applied Phys. B, **74** S17 (2002).
- [8] M. Dahlström *et al.*, Chem. Phys. **414**, 53 (2013).
- [9] E. Goulielmakis *et al.*, Science **305**, 1267 (2004) and references therein.
- [10] E.S. Toma and H.G. Muller, J. Phys. B: Atom. Molec. and Opt. Phys. **35**, 3435 (2002).
- [11] J. Norin, *et al.*, Phys. Rev. Lett. **88**, 193901 (2002).
- [12] S. A. Aseyev, *et al.*, Phys. Rev. Lett. **91**, 223902 (2003).
- [13] M. Swoboda *et al.*, Phys. Rev. Lett. **104**, 103003 (2010).
- [14] A. Maquet and R. Taïeb, J. Mod. Opt. **54**, 1847 (2007)
- [15] O. Guyétand, *et al.*, J. Phys. B: Atom. Molec. and Opt. Phys. **41**, 051002 (2008).
- [16] O. Guyétand, *et al.*, J. Phys. B: Atom. Molec. and Opt. Phys. **38**, L357 (2005).
- [17] D. Guénot *et al.*, Phys Rev A **85**, 053424 (2012).
- [18] O. Guyétand, *et al.*, J. Phys B: Atom. Molec. and Opt. Phys. **41**, 065601 (2008).
- [19] M. Böttcher, *et al.*, Appl. Phys. B **91**, 287 (2008).
- [20] PLFA is a laser line of the Saclay Laser-matter Interaction Center- SLIC- of the Commissariat à l'Energie Atomique et aux Energies Alternatives -CEA- at Saclay (France).
- [21] R.G. Houlgate, *et al.*, J. Mol. Spect **9**, 205 (1976).
- [22] R. Taïeb, *et al.*, to be published (2013).
- [23] P. Billaud, *et al.*, J. Phys. B: Atom. Molec. and Opt. Phys. **45**, 194013 (2012).





**Electron trajectory control of odd and even ordered harmonics in high harmonic generation using an orthogonally polarised second harmonic field**

C. Hutchison, S. Houver, N. Lin, D.J. Hoffmann, F. McGrath, T. Siegel, D.R. Austin, A. Zaïr, P. Salières, and J.P. Marangos.

*Submitted to Journal of Modern Optics xx, xxx (2013).*



## Paper

### Electron trajectory control of odd and even order harmonics in high harmonic generation using an orthogonally polarised second harmonic field

C. Hutchison<sup>a\*</sup>, S. Houver<sup>a</sup>, N. Lin<sup>b</sup>, D.J. Hoffmann<sup>a</sup>, F. McGrath<sup>a</sup>, T. Siegel<sup>a</sup>, D.R. Austin<sup>a</sup>, A. Zair<sup>a</sup>,  
P. Salières<sup>b</sup> and J.P. Marangos<sup>a</sup>

<sup>a</sup>*Blackett Laboratory, Imperial College London, Prince Consort, London SW7 2AZ, United Kingdom;*

<sup>b</sup>*CEA-Saclay, IRAMIS, Service des Photons, Atomes et Molecules, 91191 Gif-sur-Yvette, France*

(v0.1 made October 25, 2013)

We investigate quantum trajectory control in high-order harmonic generation using an additional orthogonally polarised second harmonic field. By controlling the relative phase between this field and fundamental we are able to suppress & enhance particular electron trajectories which results in a modulation of the harmonic emission. We observe a phase shift of the modulation between the short and long trajectories that is different for adjacent odd and even harmonics. These results have good agreement with a full propagation calculation where the single atom response was obtained from SFA.

**Keywords:** Attosecond; High Harmonic Generation; Multi-colour fields; Coherent control;

## 1. Introduction

Over the last two decades high-order harmonic generation (HHG) has been shown to be versatile strong field technique that is capable of generating coherent soft x-rays and attosecond pulses [1], and measuring ultra fast molecular dynamics [2]. HHG spectroscopic investigations usually involve the use of only a single laser field, however the presence of additional fields with different wavelengths can greatly influence the HHG process. A great deal of work has been done both theoretically [3–6] and experimentally [7–10] on HHG using multiple fields. Most of this was focused on the use of a second field to improve the HHG efficiency. It was postulated [11, 12] that the use of a perpendicularly polarised field in HHG can provide quantum control of the electron trajectories. In particular this has been done by controlling the relative phase between the fundamental ( $\omega$ ) and its second harmonic ( $2\omega$ ) when they are focused together in HHG, as this is experimentally convenient. For instance it has been recognised that this can allow different electron recombination angles to probe the cation. The first experimental result that showed a two colour field could be used to control electron trajectories in the continuum in order to probe an atomic system was performed by Shafir *et al.*[13]. Two colour fields have also been used to shorten the attosecond pulses generated using HHG [14, 15].

Our investigations aimed to control electron trajectories in HHG through the use of two colour perpendicularly polarised fields. This builds on the previous work of L. Brugnera *et al.*[16], where differential control of short and long trajectory contributions to the harmonic spectrum were observed in a similar experimental configuration. They showed that the second colour field

---

\*Corresponding author. Email: christopher.hutchison05@imperial.ac.uk

could be used as a gate for selecting which electron trajectories recombine and dominate the harmonic emission. Here we sought to better quantify the dependence of the gating on the second harmonic field intensity and harmonic order, with particular emphasis on any differences between odd and even ordered harmonics. We also sought to provide quantitative comparison with a numerical model.

To understand the effect of the second field on HHG we must first briefly reprise the mechanism of HHG in a single colour field. In the semi-classical three step model of HHG [17], an electron is tunnel ionised by a intense laser pulse near to the peak of the electric field. Once free of the parent ion the electron is driven away by the strong field. When the electric field reverses direction the electron is slowed down and driven back and there is a chance that it will recombine with the parent ion. This can result in the emission of a photon with energy equal to the kinetic energy gain from the field plus the ionisation potential of the state the electron recombines to. Due to phase-matching and symmetry constraints only emissions that are odd multiples of the fundamental are able to grow to produce macroscopic measurable signals in a single colour field. Electrons can tunnel ionise at any time around the peak of the field which will dictate the trajectory the electron will take in the continuum. Electrons which ionise at  $17^\circ$  phase after the driving field peak will recombine with the maximum kinetic energy of  $3.2 U_p$ , where  $U_p$  is the ponderomotive (wiggle) energy the electron gains from the electric field. Trajectories that ionise before or after this critical trajectory give rise to two trajectories sets that are degenerate in energy. Those that ionise earlier spend more time in the continuum and are designated long trajectories while the which ionise after spend less time are referred to as short.

It has been shown that if the second harmonic field is sufficiently weak that it does not significantly alter the ionisation rate. Its dominant effect on the HHG mechanism will be steering of the electron while in the continuum. Classical calculations have shown that by adjustment of the relative phase between the fields it is possible to preferentially select between short and long trajectories [12]. Here we consider only orthogonally polarised fields, in which case the presence of the second harmonic field does not greatly increase the maximum electric field vector as compared to the parallel case. Therefore allowing the second harmonic to be used at appreciable strengths without significantly influencing the rate of tunnel ionisation. The combination of the two fields can be written as

$$\mathbf{E}(t) = \hat{\mathbf{e}}_\omega E_x \cos(\omega t) + \hat{\mathbf{e}}_{2\omega} E_y \cos(2\omega t + \phi) \quad (1)$$

where  $E_x$  and  $E_y$  are the electric field strengths in the x and y axis,  $\hat{\mathbf{e}}_\omega$  and  $\hat{\mathbf{e}}_{2\omega}$  are the polarisations of the fundamental ( $\omega$ ) and second harmonic ( $2\omega$ ) fields respectively and  $\phi$  is the relative phase between the two. As the two fields are orthogonally polarised in our case it is possible to consider the electron displacement in each field axis separately to gain a qualitative understanding of trajectory control.

In order for a trajectory to result in recombination the electron must return to the core. For this to occur the displacement in each of the axis must be the close to zero. Assuming that the fundamental trajectory times are unchanged by the second harmonic field these occur at different points in the cycle for the two fields. The second harmonic field creates a second displacement that will depend on the relative phase between the two fields. For example when the peaks of the two fields are in phase ( $\phi = 0$ ), the short trajectories driven by the fundamental would normally recombine between  $0.3-0.55T$  (where T is period of the fundamental). However the presence of the second field means that at this time of the recombination the electron is most displaced and misses the core, while the long trajectory recombination coincides with approximately zero net displacement by the second field and are generated as they would be in the single colour case. Other choices of  $\phi$  induce the opposite effect i.e the short trajectories being favoured over the long trajectories. In general by controlling the relative phase one can select which trajectories this second harmonic ‘gate’ allow to recombine. The width of the gate will depend on the strength

of second harmonic field, with stronger second harmonic fields causing larger displacements in shorter times making the gate width shorter in time. If the second harmonic field is too weak the electron will not be displaced sufficiently to miss the core and no selection will occur. If the field is too strong it will induce ionisation the selection will become very difficult to interpret.

## 2. Experimental And Theoretical Methods

We performed an HHG experiment to study this gating of the trajectories. The degree to which the trajectories will be gated will depend on the strength of the second field. However, we want the second field to be weak enough so that it does not strongly contribute to ionisation. Having the second field polarised orthogonally is particularly beneficial in ensuring this. Any perturbation of the atomic potential that is a result of the second field will be along a different axis to that induced by the fundamental. Therefore it should not increase or decrease the rate of tunnel ionisation. If the fields were polarised in the same direction this would not be the case.

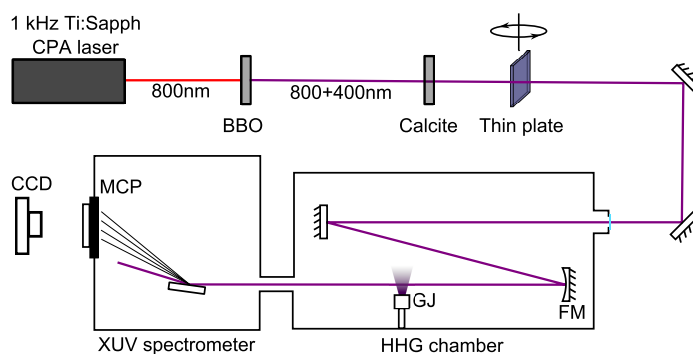


Figure 1. Schematic of the experiment set-up employed. 800 nm 30 fs pulses are used to generate a second harmonic field. The pulses are temporally overlapped using a calcite plate and the relative phase is controlled by rotating a thin glass plate. The two overlapped pulses are focused using a  $f=200$ mm mirror (FM) on to argon gas expanded from a CW gas jet (GJ). Harmonics produced are spectrally sorted using a spatially preserving XUV grating and imaged using an imaging MCP and CCD combination.

The experiment was performed using a 1 kHz repetition rate chirped pulse amplification (CPA) Ti:sapphire laser system (Red Dragon, KML Inc.) which provided up to 8 mJ at a wavelength of 800 nm in 30 fs pulses. To avoid HHG saturation in the Ar gas under the tight focusing conditions used driving pulses of only  $\approx 200 \mu\text{J}$  were used. The second field was generated by frequency doubling the fundamental pulses using a  $500 \mu\text{m}$  thick type I  $\beta$ -barium borate (BBO) crystal (Figure 1). For our particular driving laser's pulse energy and duration the crystal was able to produce conversion efficiencies up to 25%, controlled by varying the crystal orientation. Two different regimes were used in the experiment, with second harmonic energies of 3% and 25% as compared to fundamental, which was maintained at  $\approx 2 \times 10^{14} \text{ Wcm}^{-2}$ . Dispersion inside the generating crystal and subsequent optics leads to the fundamental and the second harmonic pulses not being temporally overlapped in the interaction region. A calcite plate was used to control the coarse delay between the two pulses in order to overlap the peaks of the pulse envelopes.

The presence of the second harmonic field breaks the half-cycle symmetry of HHG allowing for the phase matching and observation of even harmonics. In general the intensities of the even harmonics depended on the strength of the dressing field. Therefore, temporal overlap of the pulse envelopes could be optimised by finding the maximum of the even harmonic signal. The

calcite plate we used had a delay range of 370 – 520 fs over 0–5° angle incidence. Such a large range of the calcite is crucial for overlapping in the interaction region, however rotation of this plate is too coarse to study the sub-cycle (< 2 fs) dynamics of trajectory control. By rotating a 130  $\mu\text{m}$  thick borosilicate glass plate (D263 M, Schott) the induced dispersion gave fine control of the relative delay between the two fields. The advantage of this plate as compared to the fused silica ones used in previous efforts is the delay can be controlled very finely. However requiring such large angles in order to achieve the enough delay to observe modulation mean that there are small changes in reflectivity and hence intensity over the scan. Taking into account refraction and dispersion the delay introduced by such a plate,  $\tau(\theta)$  is given by

$$\tau(\theta) = \frac{d}{c} (n_{2\omega}(\cos A) - n_{\omega}(\cos B)) \quad (2)$$

$$A = \sin^{-1}(\sin(\theta)/n_{2\omega}), \quad B = \sin^{-1}(\sin(\theta)/n_{\omega})$$

where  $c$  is the speed of light in a vacuum,  $d$  is the thickness of the glass plate,  $\theta$  is the angle of incidence. The refractive index of the fundamental ( $\omega$ ) and the second harmonic ( $2\omega$ ) in the plate are  $n_{\omega}$  and  $n_{2\omega}$  respectively.  $A$  and  $B$  are the refracted angles of the second harmonic and fundamental inside the glass plate respectively. Note that (2) describes the total delay introduced by the glass plate, we experimentally compensated for the delay at  $\theta = 0$  using the calcite plate and are therefore only concerned with the change in relative delay,  $\Delta\tau$ .

HHG was performed by focusing the two collinear fields into a jet of argon expanded from supersonic continuous flow gas jet with an aperture of 100  $\mu\text{m}$ . The spherical mirror used had a focal length of 200 mm. The short focal length was beneficial in achieving conditions where the long trajectory as well as short trajectory contributions to the harmonic field were of similar strength and more easily separated. The jet was positioned before the focus to facilitate off-axis phase matching of the long trajectories allowing them to be distinguished from the short trajectories [18]. The harmonics were spectrally separated using an XUV flat-field spectrometer which preserves the harmonics spatial profile in the non-dispersed direction and detected using an imaging micro-channel plate (MCP) and CCD camera. The MCP voltages were 1.7 kV on the plates and 3.5 kV on the phosphor screen.

Delay scan were carried out by rotating the thin glass plate between 0–50° in steps of 1° and while observing the harmonic spectra. This was done for both the 3% and 25% relative intensity cases. We observed the characteristic modulation of the harmonic signal with relative phase indicative of trajectory gating by a second harmonic field.

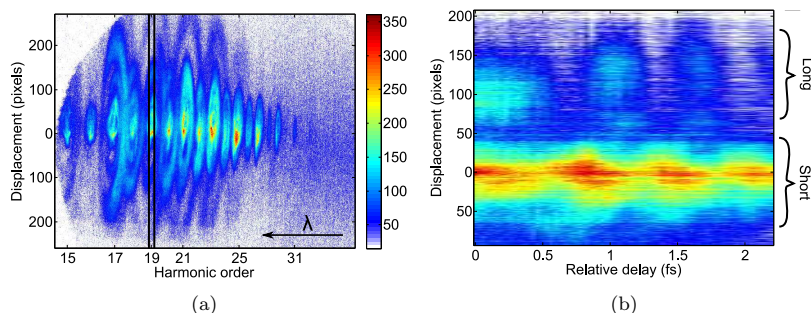


Figure 2. (a) The raw experimental data from the MCP/camera readout for the case of a second harmonic field of 25%. The spectral integration window used to isolate one harmonic is shown in black. Also shown (b) the modulation of from 19<sup>th</sup> harmonic in the 25% case. For clarity only the one side of the long trajectory is shown.

To properly observe the trajectory gating we needed to measure the relative intensities of the

short and long trajectory contributions. A small spectral integration window was used to isolate a single harmonic (Figure 2(a)) while preserving the separation of the trajectories. A simple interpolation method was used to remove the dependence seen in equation 2 to produce plot that was linear with  $\tau$  (Figure 2). The delay scale was then calibrated using (2). An example of this is shown in Figure 2(b). It can be seen that the period of the modulation is approximately one half cycle of the second harmonic field ( $\approx 0.66$  fs). The on axis and off axis signals from the short and long trajectory respectively are then separately integrated. In some situations additional intermediate rings were observed, these are the result of quantum path interference [19] and were excluded from our intergration.

Numerical simulations of the HHG under the conditions of the experiment were also performed [20]. The single-atom dipole response was calculated using a quantum orbit model [21, 22]. This model is a modification of the strong field approximation (SFA) model [23]. It allows the modification of particular trajectories by the presence of the second field to be studied for each half cycle of the pulse. The single atom response was converted into a macroscopic far-field signal similar to that observed experimentally using a propagation method [24]. A full description of the theoretical model that was employed can be found in [25].

### 3. Results And Discussion

We investigated the modulation from the short and long trajectories of odd order and even order harmonics. The intensity of the even harmonics depends on the strength of the second harmonic field (Figure 3). In addition the measured intensity of the long trajectories are typically lower than their short equivalents due to a combination of wavepacket spreading and being more divergent in our focusing geometry. Figures 4(a) & 4(b) show examples of the harmonic spectra from the 3% and 25% cases. It can be seen that in the 3% case, observation of even order long trajectories was not possible due to their low intensity, this meant only comparison of the short trajectories was possible.

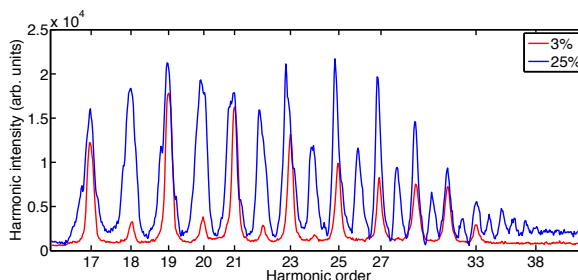


Figure 3. Spatially integrated HHG spectra from argon with 3% and 25% orthogonal second harmonic field.

For the 3% case we compared the modulation of short trajectory harmonic signal against relative delay for two adjacent odd and even harmonics (19<sup>th</sup> & 20<sup>th</sup>). It can be seen that for the 19<sup>th</sup> harmonic (Figure 5(a)) there is no visible modulation in either the short trajectory or long trajectory signals. However for 20<sup>th</sup> harmonic (Figure 5(b)) there is very clear modulation of the short trajectory signal. This comparison was also done for 25% case. We observed modulation of both the short and long trajectories for both the 19<sup>th</sup> (Figure 5(c)) and 20<sup>th</sup> (Figure 5(d)). There was also a phase difference between the short and long trajectory harmonic signal modulations. In the case of the 19<sup>th</sup> the long trajectory signal peaks  $\approx 0.2$  fs before the short, whilst for the 20<sup>th</sup> harmonic the long trajectory modulation peaks  $\approx 0.3$  fs after the short. This phase shift is



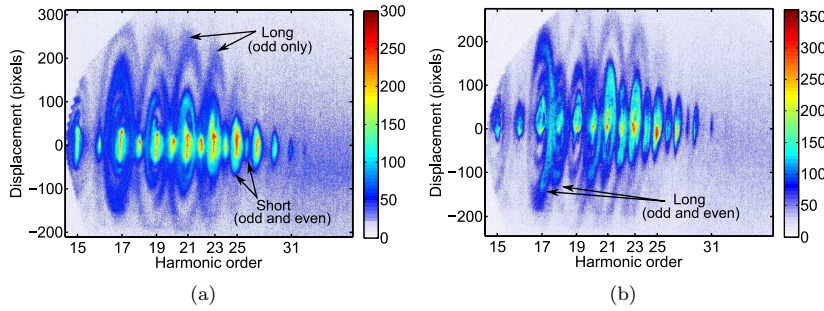


Figure 4. HHG spectra from argon with (a) 3% and (b) 25% orthogonal second harmonic field. The 3% case showing the absence of long trajectories in from even order harmonics.

also visible in the SFA calculation results (Figures 5(e) & 5(f)) which show very similar harmonic intensity modulation as well as phase shift difference between the odd and even orders. There is between agreement with the 19<sup>th</sup> than the 20<sup>th</sup>.

Even ordered harmonics that are produced by the presence of an additional orthogonal second harmonic field are also polarised in that direction. This is due to the fact that the half-cycle symmetry is not broken in the fundamental polarisation ( $\hat{e}_\omega$ ) only the perpendicular polarisation ( $\hat{e}_{2\omega}$ ). In the same way because the symmetry is broken in the  $\hat{e}_{2\omega}$  direction no odd orders harmonics can be macroscopically observed with this polarisation. This allows us to consider the odd order and the even order harmonics separately.

We identify several factors that can lead to modulation of the harmonic signal with varying relative phase of the two fields. They are electron ‘*position*’ and ‘*momentum*’ upon recombination and modification of the ‘*trajectory time*’ The theoretical model accounts for all three factors, here we discuss their physical significance.

The electron position factor is the same as the previously mentioned ‘*trajectory gating*’, wherein the displacement of the electron wavepacket in the  $\hat{e}_{2\omega}$  direction due to the second harmonic field reduces the overlapped with the core at recombination. Smaller overlap results in a lower probability of recombination leading to weaker harmonic signals. This process does not distinguish between adjacent odd and even ordered harmonics as it simply depends on recombination time, which are very similar for neighbouring harmonics from a particular trajectory set. However due to the large difference in timing between short and long trajectories it will gate each at different relative field phases. This process also requires a reasonably strong second harmonic field as if the field is too weak the displacement will be too small cause a measurable reduction in signal as in the case of 3%.

The electron momentum at the point of recombination can be decomposed to  $\mathbf{P} = p_\omega \hat{e}_\omega + p_{2\omega} \hat{e}_{2\omega}$ , i.e. components along the two perpendicular axes. The strength of the even ordered harmonics will depend on the magnitude of  $p_{2\omega}$  while that of the odd harmonics depend on  $p_\omega$ . The ratio of these two gives the angle of recombination of the core, which will dictate the direction in which the dipole acceleration causing harmonic emission occurs. Theoretical calculations have shown that for higher orders harmonics this induces a shift in the optimal relative phases for odd and even ordered short trajectory harmonics [25], which will manifest as a phase shift of the harmonic modulation with  $\phi$  (the field relative phase). The even order harmonics are only produced if  $|p_{2\omega}| \neq 0$ . As a result the harmonic signal is very sensitive to small changes in  $|p_{2\omega}|$ , whereas the odd orders will only be affected if the recombination angle becomes large enough that there is a significant reduction of  $|p_\omega|$  which explains why only modulation of the even orders was visible in the 3% intensity ratio case.

Figure 6 shows a calculation of how the quantum orbits are modified by the presence of a 25% second harmonic field. It can be seen that depending on the relative phase of the field the short and long trajectories experience a shift in their respective excursion times. Altering the

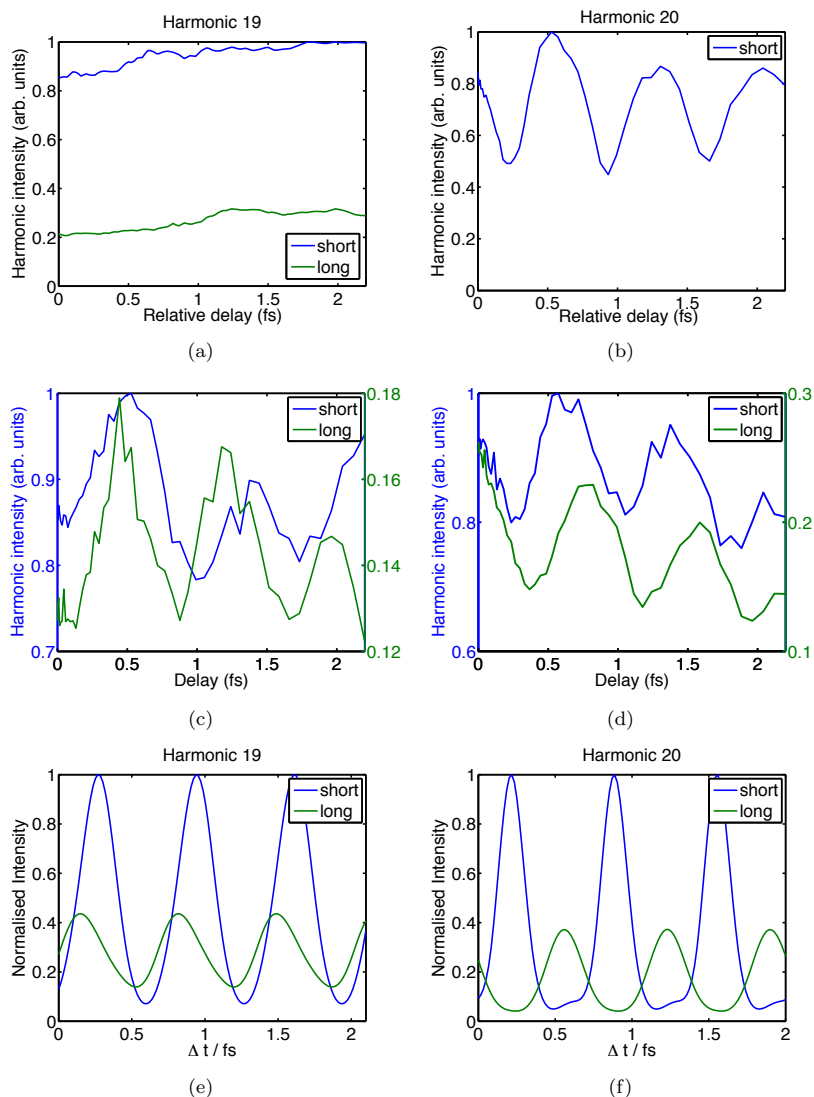


Figure 5. Scans of the relative delay between the fundamental and second harmonic field against intensity of the 19<sup>th</sup> and 20<sup>th</sup> harmonics generated in argon. In (a) & (b) the second harmonic field is 3% of the fundamental and in (c) and (d) it is 25%. Also shown are (e) & (f) the SFA calculation results which was done under the same conditions as the 25% experiment[20]. In the case of (a), (b), (e) & (f) the signal has been normalised to the short trajectory maximum. For (c) and (d) the short and long trajectories are plotted on individual scales to allow clearer comparison of the modulations.

excursion time of a particular harmonic changes the effect of wavepacket spreading will cause with a decrease in harmonic signal if the time is lengthened and vice-versa. As with electron position displacement this process will not cause a variation between adjacent odd and even orders as their trajectory times are not only similar but will be altered a similar amount by the second harmonic field.

The three sources of modulation all induce modulation with a frequency that has a period  $\lambda_{2\omega}/2$  which when combined this will produce an overall phase that is shifted depending on the relative strengths and phases of each effect. We have shown that the relative strength of the two fields has a big effect on which processes contribute, but the effects will also be highly dependant

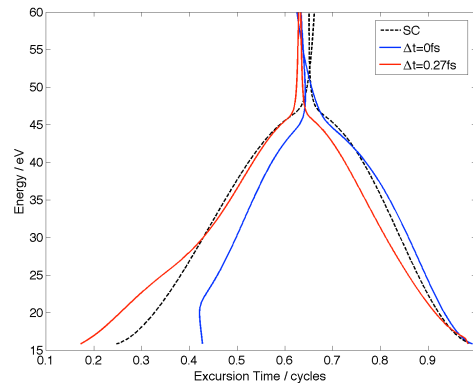


Figure 6. Results of quantum orbit calculations which show the modification of the excursion times as a function emitted photon energy. Two different relative phases ( $\Delta t$ ) between the fundamental and 25% orthogonal second harmonic field are plotted. It can be seen that the short trajectories (left) and long trajectories (right) experience a shift in excursion time at different delays. The single colour (SC) case is also given for reference.

on the absolute intensities of the two fields this can greatly vary the timing of a particular harmonic. This could explain why we observe a slight difference between the experimental and theoretical results of the 25% case as the calculation were made using estimations of laser intensities which are in practice difficult to determine accurately.

#### 4. Conclusion

We have shown that through the use of a second harmonic dressing field the electron trajectories HHG can be altered. Modulation was observed in the short and long trajectories of both the odd and even ordered harmonics when using a 25% field. Further a phase shift in the modulation was seen that is different for odd and even orders which have good agreement with quantum orbit SFA calculations. In order to explain the difference between the odd and even orders we considered several factors that could lead to the harmonic modulation observed. Each process is highly dependent on the absolute and relative intensities of the two fields. We conclude that the difference between odd and even orders is the result of the differing dependence on recombination angle in this orthogonal set-up. We have shown that while the second harmonic field can be used to gate a particular trajectory the full mechanism requires considerations more than just the classical trajectory displacement.

#### Acknowledgements

This work has been supported by EPSRC (UK) grant number EP/I032517/1 and EP/J002348/1. As well as ERC ASTEX project 290467.

#### References

- [1] Krausz, F.; Ivanov, M. Attosecond physics. *Reviews of Modern Physics* **2009**, *81* (1) (Feb.), 163–234.
- [2] Baker, S.; Robinson, J.S.; Haworth, C.A.; Teng, H.; Smith, R.A.; Chiril, C.C.; Lein M. Tisch, J.W.G.; et al. Probing Proton Dynamics in Molecules on an Attosecond Time Scale. *Science* **2006**, *312* (5772), 424–427.
- [3] Perry, M.D.; Crane, J.K. High-order harmonic emission from mixed fields. *Physical Review A* **1993**, *48* (6) (Dec.), R4051–R4054.

- [4] Watanabe, S.; Kondo, K.; Nabekawa, Y.; Sagisaka, A.; et al. Two-Color Phase Control in Tunneling Ionization and Harmonic Generation by a Strong Laser Field and Its Third Harmonic. *Physical Review Letters* **1994**, *73* (20) (Nov.), 2692–2695.
- [5] Kondo, K.; Kobayashi, Y.; Sagisaka, A.; Nabekawa, Y.; et al. Tunneling ionization and harmonic generation in two-color fields. *Journal of the Optical Society of America B* **1996**, *13* (2) (Feb.), 424–429.
- [6] Andiel, U.; Tsakiris, G.D.; Cormier, E.; et al. High-order harmonic amplitude modulation in two-colour phase-controlled frequency mixing. *EPL (Europhysics Letters)* **1999**, *47* (1) (Jul.), 42.
- [7] Eichmann, H.; Egbert, A.; Nolte, S.; Momma, C.; Wellegehausen, B.; Becker, W.; Long, S.; et al. Polarization-dependent high-order two-color mixing. *Physical Review A* **1995**, *51* (5) (May), R3414–R3417.
- [8] Protopapas, M.; Sanpera, A.; Knight, P.L.; et al. High-intensity two-color interactions in the tunneling and stabilization regimes. *Physical Review A* **1995**, *52* (4) (Oct.), R2527–R2530.
- [9] Telnov, D.A.; Wang, J.; Chu, S.I. Two-color phase control of high-order harmonic generation in intense laser fields. *Physical Review A* **1995**, *52* (5) (Nov.), 3988–3996.
- [10] Paulus, G.G.; Becker, W.; Walther, H. Classical rescattering effects in two-color above-threshold ionization. *Physical Review A* **1995**, *52* (5) (Nov.), 4043–4053.
- [11] Ivanov, M.; Corkum, P.B.; Zuo, T.; et al. Routes to Control of Intense-Field Atomic Polarizability. *Physical Review Letters* **1995**, *74* (15) (Apr.), 2933–2936.
- [12] Kitzler, M.; Lezius, M. Spatial Control of Recollision Wave Packets with Attosecond Precision. *Physical Review Letters* **2005**, *95* (25) (Dec.), 253001.
- [13] Shafir, D.; Mairesse, Y.; Villeneuve, D.M.; Corkum, P.B.; et al. Atomic wavefunctions probed through strong-field light-matter interaction. *Nature Physics* **2009**, *5* (6) (Jun.), 412–416.
- [14] Zheng, Y.; Zeng, Z.; Zou, P.; Zhang, L.; Li, X.; Liu, P.; Li, R.; et al. Dynamic Chirp Control and Pulse Compression for Attosecond High-Order Harmonic Emission. *Physical Review Letters* **2009**, *103* (4) (Jul.), 043904.
- [15] Brugnera, L.; Frank, F.; Hoffmann, D.J.; Torres, R.; Siegel, T.; Underwood, J.G.; Springate, E.; Froud, C.; Turcu, E.I.C.; Tisch, J.W.G.; et al. Enhancement of high harmonics generated by field steering of electrons in a two-color orthogonally polarized laser field. *Optics Letters* **2010**, *35* (23) (Dec.), 3994–3996.
- [16] Brugnera, L.; Hoffmann, D.J.; Siegel, T.; Frank, F.; Zar, A.; Tisch, J.W.G.; et al. Trajectory Selection in High Harmonic Generation by Controlling the Phase between Orthogonal Two-Color Fields. *Physical Review Letters* **2011**, *107* (15) (Oct.), 153902.
- [17] Corkum, P.B. Plasma perspective on strong field multiphoton ionization. *Physical Review Letters* **1993**, *71* (13) (Sep.), 1994–1997.
- [18] Lewenstein, M.; Salieres, P.; LHuillier, A. Phase of the atomic polarization in high-order harmonic generation. *Physical Review A* **1995**, *52* (6) (Dec.), 4747–4754.
- [19] Zaïr, A.; Holler, M.; Guandalini, A.; Schapper, F.; Biegert, J.; Gallmann, L.; Keller, U.; Wyatt, A.S.; Monmayrant, A.; Walmsley, I.A.; Cormier, E.; Auguste, T.; Caumes, J.P.; et al. Quantum Path Interferences in High-Order Harmonic Generation. *Physical Review Letters* **2008**, *100* (14) (Apr.), 143902.
- [20] Hoffmann, D.J.; Hutchison, C.; Houver, S.N.; Lin, N.; McGrath, F.; Simpson E Arnold, M.; Zaïr, A.; et al., High Harmonic Trajectory Control in Two-Colour Fields Comparing Odd and Even Trajectories, Poster presented at ATTO2013, 8-12th July 2013, Paris, FRANCE., 2013.
- [21] Kopold, R.; Becker, W.; Kleber, M. Quantum path analysis of high-order above-threshold ionization. *Optics Communications* **2000**, *179* (16) (May), 39–50.
- [22] Milošević, D.B.; Becker, W. Role of long quantum orbits in high-order harmonic generation. *Physical Review A* **2002**, *66* (6) (Dec.), 063417.
- [23] Lewenstein, M.; Balcou, P.; Ivanov, M.Y.; LHuillier, A.; et al. Theory of high-harmonic generation by low-frequency laser fields. *Physical Review A* **1994**, *49* (3) (Mar.), 2117–2132.
- [24] Gaarde, M.B.; Tate, J.L.; Schafer, K.J. Macroscopic aspects of attosecond pulse generation. *Journal of Physics B: Atomic, Molecular and Optical Physics* **2008**, *41* (13) (Jul.), 132001.
- [25] Hoffmann, D.J.; Hutchison, C.; Zaïr, A.; et al. Control of temporal mapping and harmonic intensity modulation using two-colour orthogonally polarized fields. *Accepted in Physical Review A* **2013**.